STRONGLY CORRELATED BAND INSULATORS AND EMERGENT SUPERCONDUCTIVITY: A GENERALIZED GUTZWILLER PROJECTION APPROACH

By

ANWESHA CHATTOPADHYAY

PHYS05201604002

Saha Institute of Nuclear Physics, Kolkata

A thesis submitted to the

Board of Studies in Physical Sciences

In partial fulfillment of requirements

For the Degree of

DOCTOR OF PHILOSOPHY

of

HOMI BHABHA NATIONAL INSTITUTE

July, 2021

Homi Bhabha National Institute

Recommendations of the Viva Voce Committee

As members of the Viva Voce Committee, we certify that we have read the dissertation prepared by **Anwesha Chattopadhyay** entitled **"Strongly correlated band insulators and emergent superconductivity: a generalized Gutzwiller projection approach"** and recommend that it maybe accepted as fulfilling the thesis requirement for the award of Degree of Doctor of Philosophy.

Date: 14/7/21

Chairman - Prof. Prakash Mathews (Dean- Academic (SINP), Physical Sciences for HBNI)

Date: 14/7/21

Guide / Convener - Prof. Arti Garg

Date: 14/07/21

Examiner - Prof. Vikram Tripathi

Date: 14/7/21

Member 1 - Prof. Abhik Basu

Date: 14/07/21

Member 2 - Prof. Kalpataru Pradhan

Date: 14/7/21

Member 3 - Prof. Amit Ghosal

Final approval and acceptance of this thesis is contingent upon the candidate's submission of the final copies of the thesis to HBNI.

I/We hereby certify that I/we have read this thesis prepared under my/our direction and recommend that it may be accepted as fulfilling the thesis requirement.

Date: 14/7/21

Place: KOLKATA

Guide:_____

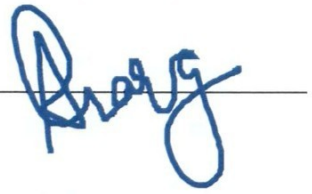

STATEMENT BY AUTHOR

This dissertation has been submitted in partial fulfillment of requirements for an advanced degree at Homi Bhabha National Institute (HBNI) and is deposited in the Library to be made available to borrowers under rules of the HBNI.

Brief quotations from this dissertation are allowable without special permission, provided that accurate acknowledgement of source is made. Requests for permission for extended quotation from or reproduction of this manuscript in whole or in part may be granted by the Competent Authority of HBNI when in his or her judgment the proposed use of the material is in the interests of scholarship. In all other instances, however, permission must be obtained from the author.

Anwesha Chattopadhyay

Arti Garg

Ph.D Supervisor

DECLARATION

I, hereby declare that the investigation presented in the thesis has been carried out by me. The work is original and has not been submitted earlier as a whole or in part for a degree / diploma at this or any other Institution / University.

Anwesha Chattopadhyay

Arti Garg

Ph.D Supervisor

LIST OF PUBLICATIONS ARISING FROM THE THESIS

Journal:

1. "Gutzwiller projection for exclusion of holes: Application to strongly correlated ionic Hubbard model and binary alloys"
   Anwesha Chattopadhyay, Arti Garg
   Phys. Rev. B **97**, 245114 (2018).

2. "Phase diagram of the half-filled ionic Hubbard model in the limit of strong correlations"
   Anwesha Chattopadhyay, Soumen Bag, H. R. Krishnamurthy, Arti Garg
   Phys. Rev. B **99**, 155127 (2019).

3. "Unconventional superconductivity in a strongly correlated band-insulator without doping"
   Anwesha Chattopadhyay, H. R. Krishnamurthy, Arti Garg
   SciPost Phys. Core **4**, 009 (2021).

Others:

1. “Interplay of mass imbalance and frustration in correlated band insulators”

   Anwesha Chattopadhyay

   Phys. Rev. B **103**, 045125 (2021).

Anwesha Chattopadhyay

Arti Garg

Ph.D Supervisor

DEDICATION

To

My parents

who are my first teachers of physics.

ACKNOWLEDGEMENTS

This moment when I am writing the acknowledgement of my thesis has materialized due to the cumulative efforts of many. The first person I want to thank is my supervisor, Arti Garg who has constantly been there for me through ups and downs during my PhD. She has been an extraordinary academic who has made great efforts in training me throughout my PhD tenure. She has helped me with the little things and has taught me with utmost care. Most importantly, she has been a good friend to me. During Covid times, when I was stuck at home the thing I missed most was our interesting group discussions over tea at the canteen. I will always remember how she emphasized the need to get back to the simple known limits of a problem before jumping to the complicated stuff. Another teacher who inspired me a lot was Pradeep Kumar Mohanty, fondly known as P.K. His infectious enthusiasm in science was unmissable and always left me in awe. He taught statistical mechanics in an unconventional way which I liked a lot. Abhik Basu and Kalpataru Pradhan taught me really well during post M.Sc. which helped me a lot in my research. Theory division professors like Palash Baran Pal, Asit De, Kumar Shankar Gupta and others taught me their respective courses amazingly well which helped me grip the basics of quantum mechanics and quantum field theory. I would also like to thank my collaborators H. R. Krishnamurthy and Soumen Bag for their immense support.

I would not have seen this day if it had not been for my teachers at Ramakrishna Mission Vivekananda Educational and Research Institute who reinstilled in me the love for physics when I was going through a very rough phase in life. I also fondly remember my undergraduate days in Jadavpur University which were the most enjoyable days of my life.

Next comes the turn of my friends. I always felt the presence of my childhood friends,

Pallavi and Nodee even though we were miles apart. JU friends Sreetama and Mitali were the best lab partners anyone could hope for. Friends who are or who have been at some point or the other at SINP: Bithika, Aranya, Avik (Paul), Avik (Banerjee), Supriyo, Dipak, Amrita, Soumita, Yogeshwar, Sanjukta di, Indranil, Sandip, Astik, Sudip da and Kausik da have always cheered me up and motivated me to work harder. Special thanks to Aranya and Avik (Banerjee) for helping me out with forms and formats relating to thesis work and educating me about the entire process of thesis submission.

Last but not the least comes the turn of my parents. My parents introduced me to physics and encouraged me in practicing free thinking instead of forcing me to be bound by the norms and rules of the formal education system. My father keeps saying ,“Keep the doors of your mind open while you do science” and indeed that was a great advice from the very beginning. He was the first person who aroused in me the curousity for science at a very young age when he talked about stars, planets and the universe. My mother who herself is a PhD in physics had to leave academia for my sake. It is not possible to repay her debt but I think today she will be a little proud of me. I can not end my acknowledgement without thanking the two bundles of joy who have been a part of my life, my pets, Bushy and Ricky for loving me so selflessly beyond what anyone can fathom.

Anwesha Chattopadhyay

CONTENTS

LIST OF FIGURES

LIST OF TABLES

CHAPTER 5

CONCLUSION

Through the preceeding chapters, we gradually developed the theory for dealing with strong interactions and equally strong inhomogeneties which led to the prediction of a novel high T_c superconductor mediated predominantly by spin-exchange interactions in a strongly correlated band insulator at half-filling. In most of the known unconventional superconductors, superconductivity is obtained only upon doping the parent compound away from half filling, which brings in disorder into the system. Thus, searching for new mechanisms of unconventional superconductivity at half filling in strongly correlated systems is a challenge both from theoretical and experimental point of view. In this thesis we demonstrated that starting from a simple model of a strongly correlated band insulator, it is indeed possible to attain a superconducting phase with a high enough transition temperature mediated mainly by spin exchange couplings, provided the system has enough frustration against the magnetic order.

In this thesis, we also developed a formaslim for treating strong interactions and disorder. The formalism developed in the $U \sim \Delta \gg t$ limit introduces the concept of site

specific hole and doublon projection which can be applied to a broad class of condensed matter systems like ionic Hubbard model (IHM), binary alloy model, Hubbard model with random disorder and even Hubbard model with strong attractive impurities. In this sense the method of projection and the formulation of low energy effective Hamiltonian is quite general. In all these systems competing U and Δ promises the possibility of many exotic phases and is worth exploring. In this thesis, we specifically explored the physics of IHM in the aforesaid limit. The low energy effective Hamiltonian in this case emphasized that the system will not be charge frozen at half-filling unlike the strongly correlated Hubbard model at half-filling. The non-zero low energy hoppings intuitively suggested the possibility of charge dynamic phases like metallic and superconducting phases. Indeed the solution of the renormalized Hamiltonian confirmed that there exists a superconducting phase although metastable. The antiferromagnetic (AF) Mott insulator is energetically stabler than the superconducting phase. There is also a thin sliver of antiferromagnetic half metallic phase very close to the transition line. This is the story in the particle hole symmetric state. The investigation turns more captivating when we make the Hamiltonian particle hole asymmetric by introducing frustration in the form of next neighbor hopping. Superconductivity in both d-wave and extended s-wave channels become stable and it is enveloped by the paramagnetic metallic phase on one side and the ferrimagnetic metallic phase on the other side. The phase diagram is strikingly different from cuprates but has a high T_c and also a pseudogap phase. The most interesting thing about this superconductivity is that it is "clean" as it is devoid of any impurities being at commensurate filling. For experimentalists realizing this kind of superconductivity in real materials is challenging. IHM can possibly be used as a minimal model to understand layered heterostructures like bilayer graphene with a transverse electric field where the electric field can create a staggeredness in the potential or graphene in h-BN substrate where the difference in energies

of boron and nitrogen can act as a staggered potential. The limit of strong correlation and onsite energies can be achieved by straining or twisting the material which will reduce the overlap between the orbitals thus suppressing the tunneling and in turn making $U, \Delta \gg t$.

Interestingly and surprisingly, this seemingly innocent looking model of a correlated band insulator with onsite interaction and staggered potential has turned out to be a storehouse of many exotic phenomena, mainly the unconventional superconductivity without doping, as investigated through these series of works. The competition between two insulating tendencies viz, the AF Mott insulator and the correlated band insulator gives rise to these interesting phases and we are hopeful that many other avenues relating to IHM remains to be investigated. Specially, the particle hole symmetry can also be broken by doping the system instead of adding next neighbor hopping. Our formalism will still hold for low values of doping and infact we hope that the superconducting phase can be relatively broadened if we allow for doping.

SUMMARY

When we add strong e-e repulsive interactions to a metallic system at half-filling, the system becomes an antiferromagnetic (AF) Mott insulator with charge degree of freedom completely frozen. However, the effect of interactions on band insulators have not been explored much in literature. In this thesis, we explore the physics of strongly correlated band insulators. To start with, we develop a formalism for treating strong correlations in the presence of equally strong inhomogeneties. We find the low energy effective Hamiltonian by suitably projecting out doublons from some sites and holes from some other sites through a generalised Schrieffer Wolff transformation. Using a scheme of generalised Gutzwiller renormalized mean field theory, we solve a simple model of a band insulator, i.e., the ionic Hubbard model and explore the physics in strong correlation and strong on-site potential limit. Within this model, we explore the possibility of a correlation driven unconventional superconductor (SC) in the limit of strong e-e interactions and a large band gap. We demonstrate that it is possible to have spin-exchange mediated unconventional SC in a strongly correlated band insulator provided there is enough frustration against the magnetic order. The most striking feature of this SC is that it is realized at commensurate filling. Most of the common unconventional SCs are obtained by chemically doping

a parent Mott insulator away from half-filling with charge carriers as in cuprates. Chemical doping however introduces disorder in the system which makes these systems highly inhomogeneous. A SC at half-filling therefore eliminates the possibility of any disorder in the system. Moreover, the SC obtained is observed to have a high transition temperature comparable to cuprates which can possibly be further enhanced by tuning parameters in the Hamiltonian. It is also found to have a pseudogap phase as in cuprates. But unlike cuprates, this novel SC is enveloped by exotic metallic and half-metallic phases like ferrimagnetic metal, paramagentic metal and AF half-metal, all with potential applications in the field of spintronics.

CHAPTER 1

INTRODUCTION

Strong correlations between electrons play a very crucial role in a large class of materials in condensed matter physics. Many experimental findings can be successfully explained only after including the physics of strong correlations among the basic constituents. Independent electron picture can explain metallicity in systems where kinetic energy is much larger than the interaction strength which in turn can be treated perturbatively. However, this method fails when we try to explain the properties of systems with narrow bandwidths where the interaction scale starts dominating the tunneling between orbitals. Many interesting phases like Mott insulators, antiferromagnets and high temperature superconductivity arise when Coulomb interaction dominate over the kinetic energy. In most of the known unconventional superconductors like cuprates [11], organic superconductors [3], iron-pnictides and chalcogenides [12, 13], and very recently in magic angle twisted bilayer graphene [14, 15], the low temperature phase of the parent compound is either a strongly correlated antiferromagnetic (AF) Mott insulator where charge dynamics is completely frozen, or an AF spin-density-wave (SDW) phase with at least moderately strong correlations. The uncon-

ventional superconductivity in many of these materials can be understood, at least qualitatively, in terms of the strongly correlated limit of the paradigmatic Hubbard model (single or multi band) doped away from half filling [11–16]. But the possibility of a superconducting phase in a strongly correlated band insulator has been explored very little so far, either theoretically or experimentally. In this thesis, we study the effect of e-e interactions on a band insulator and explore the possibility of unconventional superconductivity as an effect of strong correlations in a band insulator.

In the following sections, a few of the key concepts and models involved in the work presented in this thesis have been discussed, and the outline of the thesis is presented at the end of this chapter.

1.1 Strong correlation and uncoventional superconductivity

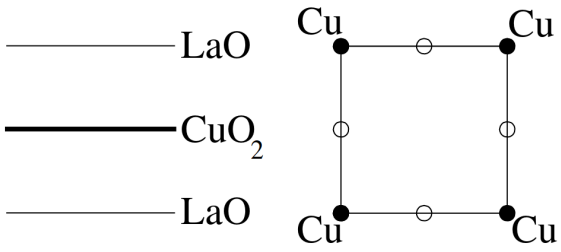

Figure 1.1: Left: Layered structure of La_2CuO_4 along c-axis. Right: Structure of the CuO_2 plane. Adapted from Ref [1].

In this section we discuss different class of materials where unconventional superconductivity is believed to originate from strong Coulomb interaction between electrons in

the material. Superconductivity in Cuprates has been one of the most significant discoveries of the past century. In 1986, Bednorz and Müller for the first time encountered what is well known now as high T_c superconductivity in a certain class of ceramics known as cuprates. The cuprates are layered materials of $Cu - O$ planes coupled weakly to each other (see Fig. 1.1). Although, initially $T_c \sim 35K$ was found in lanthanum barium copper oxide, higher transition temperatures were recorded in different cuprate compounds with the highest of about $133K$ in mercury barium calcium copper oxide compounds.

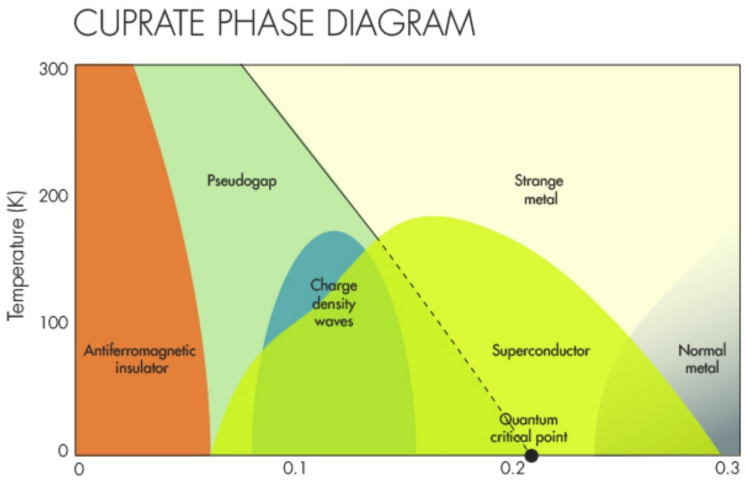

Figure 1.2: Schematic phase diagram of Cuprates where superconductivity arises in close proximity of a parent Mott insulator. Adapted from Quantamagazine.

Fig. 1.2 is a schematic phase diagram of the cuprates which shows that the parent compound is an AF Mott insulator and superconductivity arises upon doping the system with oxygen which induces holes into the Cu-O planes. The basic features of the phase diagram can be understood qualitatively by studying the strongly correlated limit of the one band Hubbard model where in the strong correlation limit, double occupancies are not allowed in the ground state [2, 16]. The famous resonant valence bond (RVB) theory proposed that superconductivity in cuprates can be explained as a resonant state of singlet pairs of electrons where a state of simultaneous superposition of macroscopic wavefunctions of spin singlets

and holes can be realized by Gutzwiller projection of the Bardeen-Cooper-Schrieffer (BCS) wavefunction. Fig. 1.3 represents such a RVB liquid state. These singlet pairs which are basically charged Cooper pairs constitute the supercurrent in the system. The RVB theory could successfully explain the existence of d-wave pairing in cuprates and also indicated the existence of pseudogapped phase.

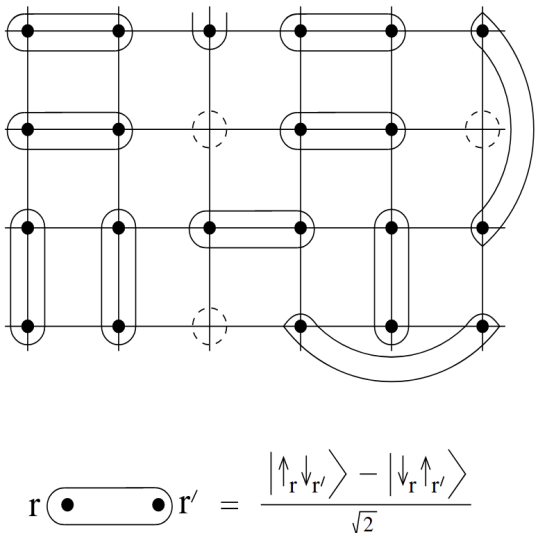

Figure 1.3: Snapshot of singlet pairs of electrons in the background of doped holes. The RVB many body wavefunction is a linear superposition of such resonating valence bond configurations. Adapted from Ref [2].

At half-filling, the charge degree is completely frozen and the system is a quantum Néel ordered RVB solid described by the Heisenberg model. Doping holes into the system melts the Mott insulating phase by introducing quantum fluctuations. Holes frustrate AF order and the resonance in the valence bond liquid state (See Fig. 1.3) stabilizes superconductivity in cuprates. Since superconductivity arises upon doping of charge carriers, and doping induces inhomogeneity in the system, these samples are highly disordered which is clearly seen in scanning tunneling microscopy (STM) data on cuprates [17–20].

Superconductivity with anisotropic gap has also been observed in certain class of lay-

ered organic conductors. A transition temperature of $\sim 33K$ can be obtained in these systems by increasing hydrostatic as well as chemical pressure. Interestingly, the parent compound is again an AF Mott insulator. As pressure is applied, the system remains in the AF Mott insulator phase till a certain value of critical pressure above which superconductivity appears (See Fig. 1.4). Moreover, the chemical substitutions in these compounds play an important role in deciding the ground state of the system at a particular value of pressure. Thus, the transition from AF insulator to superconducting phase can also occur by effectively changing "chemical pressure" of the system by modifying chemical substituents. Pressure plays an important role in these systems since it effectively makes the correlation dominant than the bandwidth of the system and thus unconventional superconductivity in these organic molecular materials are driven by strong correlation. Also, superconductivity in these systems are almost always at finite doping of charge carriers.

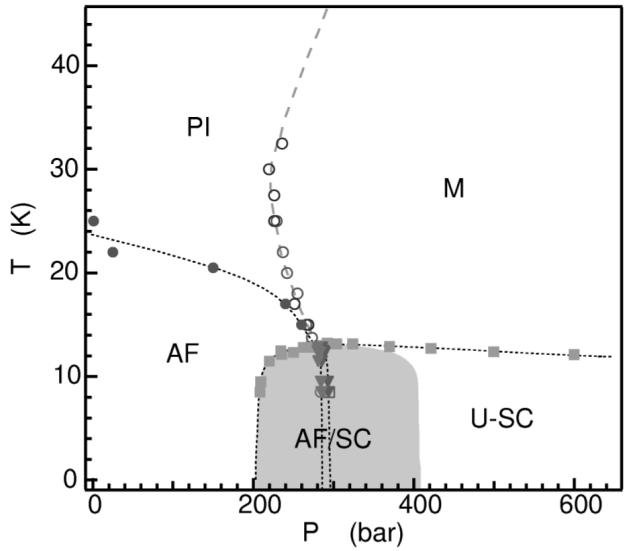

Figure 1.4: Temperature versus pressure phase diagram of an organic superconductor $\kappa - Cl$. Adapted from Ref [3].

Few years ago considerably high superconducting transition temperatures were ob-

served in iron based materials like pnictides and chalcogenides [12, 13]. We know strong correlation can result into magnetically ordered states formed due to the interaction between localized moments. On the other hand, relatively weak interactions drives magnetic ordering due to Fermi surface nesting. In iron based superconductors, the parent compound is a SDW ordered "bad" metal unlike the Cuprates where the parent compound is an AF Mott insulator. This means that the ratio of the correlation and bandwidth is only moderate in these systems incapable of localizing the itinerant electrons. Superconductivity arises upon doping the parent compound which can be done by substituting elements that introduces holes or electrons, e.g., by substituting Fe by Co or Ba by K (See Fig. 1.5). The symmetry of the superconducting sate is $s^{\pm}$ where the gap changes sign between electron and hole pockets. In fact the iron based superconductors are the first examples of electronically driven s-wave superconductivity.

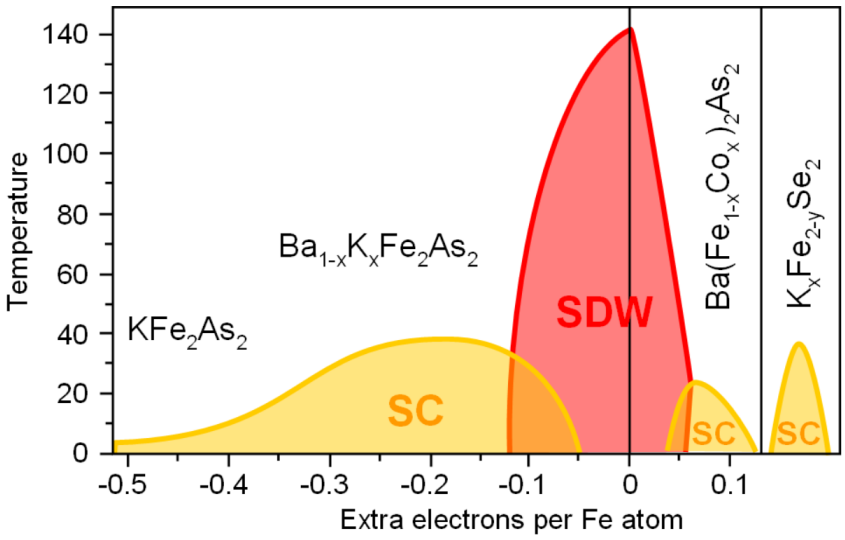

Figure 1.5: Phase diagram of some typical iron based superconductors. Adapted from Wikipedia.

Very recently superconductivity has also been observed in bilayers of graphene twisted at some specific angles known as magic angles [14, 15]. In single layer graphene, the

dispersion is linear near the Dirac cones which means electrons behave relativistically. In large angle twisted bilayers, the layers behave as if they are decoupled and electrons still behave as relativistic particles. However when untwisted, the dispersion is parabolic. So the band structure is basically a function of the twist angle and something remarkable may happen while moving from untwisted to large twist angles. At small magic angles the bands become effectively flat i.e., independent of momentum resulting into the divergence of density of states. In the twisted bilayer, there is a quasi periodicity in the structure on large scales and the pattern so formed is known as moiré pattern (See Fig. 1.6(a)) [14, 15]. The effective falttening of the band makes the ratio of correlation and bandwidth large and hence strong correlation physics play a very important role here like the previous examples. The phase diagram of the magic angle twisted bilayer graphene consists of superconducting domes separated by correlated isulating states at commensurate fillings (See Fig. 1.6(b)).

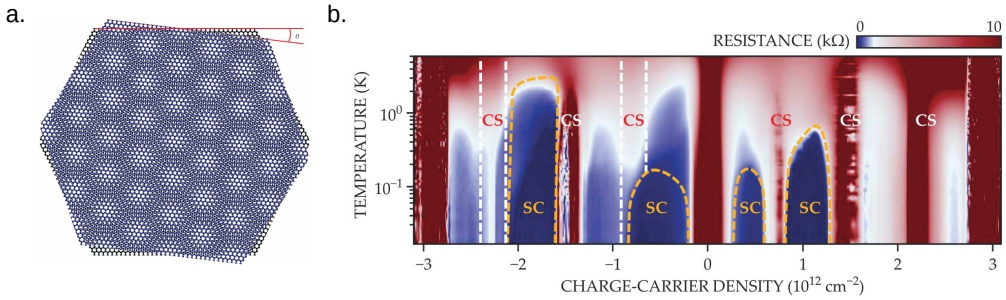

Figure 1.6: (a) Moiré pattern formed by twisting bilayer graphene. Quasiperiodicity occurs at large length scales. (b) Phase diagram of magic angle twisted bilayer graphene as function of carrier concentration. Adapted from Physics Today.

Doping here can be varied by simply tuning the gate voltage and so superconductivity can be obtained relatively easily because the complications of chemical doping are not present here unlike in the cuprates. The superconducting transition temperature is very low in

this system ($\sim 1.7K$ at 1.05° twist angle) which is comparable to BCS superconductors. However, in BCS superconductors (such as Al) the carrier density required for phonon mediated coupling is very large. What is important is the ratio of T_c and carrier density. Since, in twisted bilayer graphene superconductor carrier density is much lower and it is in close proximity to a correlated insulator, unconventional superconductivity originating due to strong correlation holds a valid ground here.

All these examples highlight the importance of strong correlation in driving unconventional superconductivity in materials. At first glance strong Coulomb repulsion between electrons may seem to destabilize the formation of Cooper pairs. And surely onsite s-wave superconductivity as seen in BCS superconductors is not possible here. Frozen singlet pairs which are spatially separated melt into a liquid state upon doping to constitute a supercurrent in these systems. One of the major goal of condensed matter physicists now-a-days is to enhance the T_c to room temperatures. Keeping in mind the exciting development relating to correlation driven superconductivity in the past, it will perhaps not be unjustified to hope for an unconventional correlation driven room temperature superconductor in near future.

1.2 Model for strongly correlated electron systems

The Hubbard model [21–24] is historically one of the most successful models which explains strong correlation physics in many contexts, at least on a qualitative level. It is a good approximation for electrons on a lattice at low temperatures in systems where long range interactions are effectively screened. It has two simple ingredients : one electron hopping term ($\sim t$) and onsite Coulomb repulsion term ($\sim U$) as seen from the model Hamiltonian given by Eq. 1.1. The chemical potential, μ tunes the particle density of the system.

$$\mathcal{H} = -t \sum_{<ij>,\sigma} (c^{\dagger}_{i\sigma} c_{j\sigma} + h.c.) + U \sum_{i} n_{i\uparrow} n_{i\downarrow} - \mu \sum_{i} n_i \tag{1.1}$$

To explain the intricate behavior of real materials, we often extend this simple model either by extending the range of interactions or by treating multiple bands.

The presence of two electrons on the same site which should necessarily be of opposite spins (or else Pauli exclusion principle will be violated) cost an energy U. In the strong correlation limit, this means in the ground state configurations with double occupancies on sites will not be preferred as it is energetically unfavourable. At absolute zero, all sites will hence be singly occupied at commensurate filling and any charge fluctuation is prohibited on energetic grounds. The system is then a Mott insulator with charge degree of freedom completely frozen. Thus the Hubbard model which may have looked like a trivial extension of the tight binding model makes the non trivial prediction of an insulator instead of a band metal when onsite correlations are significantly greater than the kinetic energy. On doping the system with either holes or electrons can however induce charge fluctuations in the system which can give rise to charge dynamic phases like metals or superconductors.

The Hubbard model in one dimension is exactly solvable in the thermodynamic limit by Bethe ansatz method [25]. The problem of solving the stationary Schrödinger equation is transformed into a problem of finding the roots of a set of non-linear coupled algebriac equations, famously known as Lieb-Wu equations. The solutions of these equations contain all the information about the one dimensional Hubbard model. Explicit solutions of the N particle system is not known exactly. However in the thermodynamic limit the distribution of the solutions in the complex plane is what matters and physical quantities can be calculated from solutions of integral equations. The system is metallic at $U = 0$ but for any non zero value of U, it is an insulator highlighting the fact that the insulating property

is interaction induced.

However, the Hubbard model is not exactly solvable for $d \geq 2$. In higher dimensions either one has to resort to numerical methods like quantum Monte Carlo (QMC) [26] or exact diagonalization (ED) [27] or to approximate analytical calculations. The numerical methods give exact answers for finite size systems. The QMC approach which can produce results on much larger systems than ED is further restricted by the "fermion sign problem", and by the problem of analytic continuation of numerical data from imaginary time to the real axis. ED or basically Lanczos diagonalization is limited to small system sizes such that the eigenvalues are sparse and even a metallic phase may appear gapped. The analytical methods include Green's function methods which sum over selected subset of Feynman diagrams (e.g., the random phase approximation) or functional integral approaches which amount to a mean field theory plus fluctuations. Usually such approaches are accurate only in the weak coupling limit.

The other methods one can use to extract information about the Hubbard model are dynamical mean field theory (DMFT) [28] and density matrix renormalization group (DMRG) [29]. DMFT is a non-perturbative technique where the lattice model is mapped to an effective single site Anderson impurity model where the impurity and bath degrees of freedom couple via a hybridization function. The impurity model can be solved by several schemes like iterative perturbation theory (IPT), continuous time Monte Carlo (CTQMC) etc which basically finds the interacting Green's function. This method however approximates the lattice self-energy to be momentum independent i.e., it neglects spatial fluctuations similar to mean field approximations. The hybridization function remains time dependent which allows DMFT to capture the temporal fluctuations owing to e-e interaction. Hence, the name "dynamical" mean field theory. DMRG is a variational technique which can handle large system sizes and give high precision results, specially in one dimension. The de-

grees of freedom are iteratively eliminated leaving behind the ones that are relevant for the ground state.

In the limit $U \gg t$, a perturbative expansion in hopping is used to study the low energy properties of the system. The effective Hamiltonian in this limit is known as the "tJ model" [30, 31].

1.3 tJ model as strong correlation limit of the Hubbard model

In the large U limit, a double occupancy is energetically expensive and is not allowed in the ground state configurations. The low energy Hilbert space then consists of the following spin $1/2$ single site configurations: $|\uparrow\rangle, |\downarrow\rangle, |0\rangle$. The double occupancy $|\uparrow\downarrow\rangle$ forms the high energy sector of the Hilbert space. In the hole doped case, the allowed hopping between two sites is an effective hole hopping as it does not involve a doublon on any site. There are other hopping terms which connect the low and high energy sectors in the sense that they either start or end with a doublon. The effective hopping of doublon however belongs entirely to the high energy sector and will eventually be eliminated when we restrict ourselves to the low energy physics. After doing a similarity tranformation which decouples the low and high energy sectors and confining to the low energy space we get the following Hamiltonian in the doublon projected space which is known as the tJ model,

$$H_{tJ} = \mathcal{P}_d \Bigg(\sum_{<ij>} -t(\sum_{\sigma} c^{\dagger}_{i\sigma} c_{j\sigma} + H.c.) + J\left(S_i.S_j - \frac{n_i n_j}{4}\right) + \text{trimer terms} \Bigg) \mathcal{P}_d, \quad (1.2)$$

where $\mathcal{P}_d = \prod_i (1 - n_{i\uparrow} n_{i\downarrow})$ is the projection operator which projects out doublons. Here $J = \dfrac{4t^2}{U}$ which is the coupling for the spin exchange term. Details of the steps involved in the transformation are given in Appendix A.1.

At half-filling, the low energy hopping term is completely projected out as holes will not be allowed along with doublons and the tJ model reduces to the AF Heisenberg model. The ground state therefore is an AF state without any charge dynamics. The simple components of the tJ model can give us good intuition of the possible phases it hosts. In the strongly correlated limit, even in the presence of holes, the t term is suppressed because of the constraint of no double occupancy. Further, the J term suppresses t more, since it favours singlets. Infact, we know that when J dominates over t, in the sense holes in the system are less, then a macroscopic singlet insulating state is the favoured ground state. However, as we increase doping fraction of holes, t term is favoured over J term and we expect a normal Fermi liquid behavior in this case. But what will happen when t and J compete with each other? Will it give rise to a liquid state of spin singlets? Thus the possibilty of a superconducting state arises in this case.

After obtaining the low energy effective Hamiltonian, we are left with task of solving it and finding the quantities of physical interest. Since the effective Hamiltonian in the projected space is defined in terms of non-canonical operators, we can not use standard Wick's theorem as in usual perturbation theory. One can solve the Schwinger equation of motion for the Greens function of projected electrons [32, 33] and use a systematic perturbation theory in some parameter that controls double occupancy. Other methods are the Variational Monte Carlo (VMC) method, the slave boson mean field theory (SBMFT) and the method of Gutzwiller renormalized mean field theory (RMFT).

1.3.1 Variational Monte Carlo

Variational Monte Carlo (VMC) [1, 34] is a powerful non perturbative method for solving the low energy effective Hamiltonian. The first job in VMC is to make a guess of the starting wavefunction which is known as the variational ansatz. The guess often arises from clues gathered from simple mean field calculations which are used for getting first hand impressions about a problem. The variational ansatz in this case is a doublon projected d-wave BCS wavefunction for a fixed particle number given by,

$$|\psi\rangle = \mathcal{P}_d \sum_{ij} (\phi(i-j) c^\dagger_{i\uparrow} c^\dagger_{j\downarrow})^{N/2} |0\rangle. \tag{1.3}$$

Crux of the problem is to obtain expectation value of quantities like the energy in this quantum state which is nothing but a slater determinant of $\phi(i-j)$'s (known as pair functions) and finally extremize it with respect to the variational parameters which are in this case the pair functions themselves, to obtain the required ground state. But calculation of expectation values requires summation over lattice configurations which are exponentially large in number. Here, comes the role of Monte Carlo. To simplify matters, we visit only those configurations which have high probability of occurance. In other words, this is what is called importance sampling. Using algorithms like Metropolis, two kinds of moves are made: (1) moving an electron to a site if it is empty (2) exchanging of oppositely oriented spins. These moves conserve the double occupancy number to zero, thus always moving in the low energy subspace. However, the VMC calculations are computationally expensive. This makes us look for other alternative routes like slave boson mean field theory or Gutzwiller renormalized mean field theory.

1.3.2 Slave boson mean field theory

In the slave boson formalism [35] one introduces new auxiliary operators : two fermionic operators for $|\uparrow\rangle, |\downarrow\rangle$ and two bosonic operators for $|0\rangle, |\uparrow\downarrow\rangle$. The fermionic operators create σ spin particle with zero charge while the bosonic opeartors create zero spin paticle accompanied with an unit of electronic charge. The Hubbard operators, $(X^{\beta\leftarrow\alpha} = |\beta\rangle\langle\alpha|)$ are expressed in terms of the original c-operators, e.g, $X^{\sigma\leftarrow 0} = c^{\dagger}_{\sigma}|0\rangle$ where the reference state is the empty state $|0\rangle$. However, the latter state is not a convenient starting point in the sense that there is no Wick's theorem for such states and therefore usual quantum field theoretical methods cannot be applied. However, it is possible to express the Hubbard operators exactly in terms of products of fermionic and bosonic operators which obey the canonical anti-commutation/commutation rules. The empty site is now created starting from a vacuum state by operating the bosonic operator $b^{\dagger}$. In the projected space double occupanicies are not allowed so the constraint relation connecting fermionic and bosonic operators become,

$$\sum_{\sigma} f^{\dagger}_{i\sigma} f_{i\sigma} + b^{\dagger}_{i} b_{i} = 1. \tag{1.4}$$

Through this constraint relation the bosonic degrees of freedom are "slaved" as they are not allowed to form macroscopic condensate like free bosons and hence the name slave boson. The tJ model can be rewritten in slave boson language as

$$H_{tJ} = -t \sum_{<ij>,\sigma} f^{\dagger}_{i\sigma} f_{j\sigma} b^{\dagger}_{j} b_{i} + J \sum_{<ij>,\sigma,\sigma'} f^{\dagger}_{i\sigma} f_{i\sigma'} f^{\dagger}_{j\sigma'} f_{j\sigma}. \tag{1.5}$$

The introduction of the slave boson theory however has made the problem complicated by introducing new operators. The complication is also at the level of constraint relations

that one has to follow. However, approximate mean field theories based on the slave boson theory can give insights into the ground state properties of the system. This thesis is however based on the technique of Gutzwiller renormalized mean field theory which will be discussed in details in the next section.

1.4 Gutzwiller Approximation and renormalized mean field theory

For a system with Fermi surface nesting, a metal to insulator transition occurs at $U = 0$ since there is an AF instability for any arbitrarily small value of U due to the nesting property. The system then is a weakly correlated SDW insulator where the insulating property is due to the long range magnetic order. However, this has nothing to do with Mott insulating property which is born out of strong local correaltions. As U is tuned to relatively larger values, the SDW insulator goes over to an AF Mott insulator smoothly without any observable singularity. The absence of the singularity masks the onset of the local correlations crucial for realizing a Mott insulator which we know will set in when $U \sim W$ where W is the bare bandwidth of the system. To understand the Mott physics as arising out of slowly building local correlations the system is constrained to be paramagnetic so that a paramagnetic metal to insulator transition occurs. A popular approach to study this problem is the Gutzwiller variational approach where we start from a variational trial wavefunction,

$$|\psi\rangle = \prod_i (1 - (1 - \eta) n_{i\uparrow} n_{i\downarrow}) |FS\rangle, \tag{1.6}$$

where $0 \leq \eta \leq 1$ is the variational parameter which suppresses the weights of configurations with double occupancies as compared to the metallic Fermi sea $|FS\rangle$. For $\eta = 1$,

we get back the Fermi sea for which $U = 0$. For $\eta = 0$, the weights of many body configurations with even one double occupancy is made to be zero and corresponds to $U = \infty$ which is the Mott insulating state with single occupancies at half-filling. When the density is lesser than unity, the system has charge fluctuations due to the presence of holes and is metallic even at $U = \infty$. For, any $U > 0$ the weights of configurations with double occupancies are suppressed with factors of $\eta < 1$. With this trial wavefunction, the ground state energy is evaluated and minimized with respect to η to find the ground state and hence the double occupancy count for a particular value of U. Although this method captures the physics well at two limiting points, it always predicts a metallic phase in finite dimensions for intermediate values of repulsion. This is beacuse the Gutzwiller wave function misses the inter-site correlation of holons and doublons which are inevitably there at finite values of U. For an insulating state the holons and doublons need to be bound so that under an applied electric field these expensive charge configurations do not constitute a current. Missing spatial correlations always make the state metallic at finite values of U for conventional trial wavefunctions where the starting state is a paramagnetic metallic Fermi sea.

However, when we want to study the effects of correlation only in the strongly correlated limit we resort to the scheme of Gutzwiller approximation [1, 36–40] where the constraints due to strong correlation are treated in an approximate way. Within Gutzwiller approximation, the expectation value of an operator in the fully projected space is related to that in the unprojected space through a statistical weight factor known as Gutzwiller factor which takes into account the projection of doublons in an approximate way as shown here,

$$\langle\psi|\hat{O}|\psi\rangle = g_O\langle\psi_0|\hat{O}|\psi_0\rangle. \tag{1.7}$$

Here, ψ_0 is the unprojected wavefunction which we seek through the renormalized mean field theory calculation . In this section, we will only discuss the method of calculating Gutzwiller factors through phase space counting which will be relevant for comprehension of future chapters. In the context of tJ model, as we go from the projected to unprojected space , we incorporate two Gutzwiller factors: $g_{t\sigma}$ the kinetic energy renormalization factor and g_s the renormalization factor for spin exchange term.

Calculation of $g_{t\sigma}$:

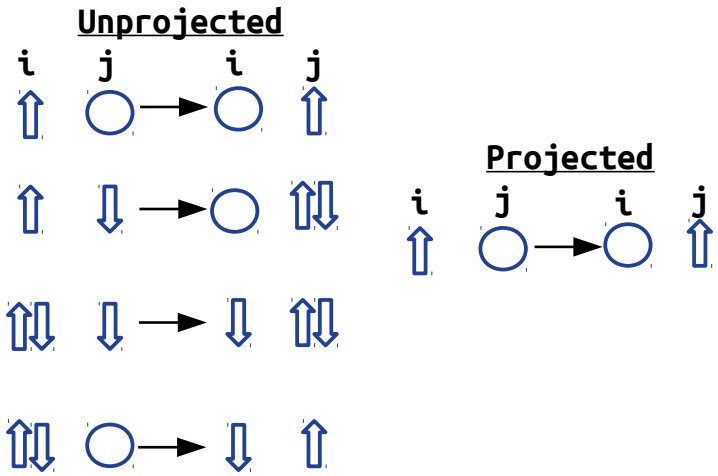

Figure 1.7: In unprojected space there are no constraints on double occupancies and hence hopping can occur by all four processes (as shown on left) whereas hopping in the projected space where doublons are not allowed, is purely a hole hopping (as shown on right).

An up spin particle can hop from $i-th$ site to $j-th$ site in four possible ways in the unprojected space. Here, double occupancies are allowed unlike the projected space where doublons are prohibited. In the projected space, this hopping is basically a hole hopping from $j-th$ site to $i-th$ site. These are shown in Fig. 1.7. The Gutzwiller factor is defined as the square root of the ratio of the probability of the process in the projected space to that in the unprojected space. The probabilities can be calculated in a straightforward way.

First, in the unprojected space, if we look at the initial state, there is always an up spin particle on $i-th$ site and no up spin particle on the $j-th$ site. So, probability of the initial state in the uprojected space is $n_{i\uparrow}(1-n_{j\uparrow})$. On the other hand, in the final state, there is always an up spin particle on the $j-th$ site and no up spin particle on the $i-th$ site which makes the probability of the final state $(1-n_{i\uparrow})n_{j\uparrow}$. The probability of the process in the unprojected space is the product of the probabilities for the final and initial states ,i.e., $n_{i\uparrow}(1-n_{j\uparrow})(1-n_{i\uparrow})n_{j\uparrow}$. In the doublon projected space, the probability for an up spin particle at $i-th$ site is $n_{i\uparrow}$ where as the probability of a hole on $j-th$ site is $(1-n_j)$ which comes from the conservation of probability of configurations in the projected space ($X^{\uparrow\leftarrow\uparrow}+X^{\downarrow\leftarrow\downarrow}+X^{h\leftarrow h}=1$). Then the probability of the process in projected space is $n_{i\uparrow}(1-n_j)(1-n_i)n_{j\uparrow}$. The probabilities are calculated under the approximation that the spin resolved densities before and after projection are equal. The expression of $g_{t\uparrow}$ is then,

$$g_{t\uparrow}=\sqrt{\frac{(1-n_i)(1-n_j)}{(1-n_{i\uparrow})(1-n_{j\uparrow})}}. \tag{1.8}$$

If we put $n_{i\sigma}=(1-x)/2$ (in the spin symmetric case), where x is the hole doping fraction, then $g_t=2x/(1+x)$.

Calculation of g_s:

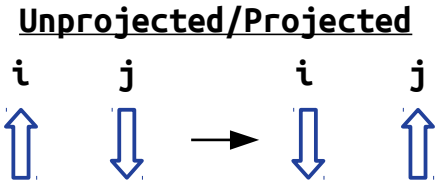

Figure 1.8: Figure shows spin flip term between $i-th$ and $j-th$ sites which corresponds to the same process in unprojected and projected space.

The Heisenberg term in the tJ model is renormalized by the Gutzwiller factor g_s. There

are two parts in the J term: (1) Spin flip part $[\frac{1}{2}(S_i^+ S_j^- + S_i^- S_j^+)]$ (2) Spin preserving part $[S_i^z S_j^z]$. We will calculate the Gutzwiller factor corresponding to the spin flip part and since the Hamiltonian is $SU(2)$ symmetric we will impose that the spin preserving part also has the same scaling factor.

The probability of a σ spin particle in the unprojected space is $n_\sigma(1-n_{\bar{\sigma}})$ and that in the projected space is n_σ. Therefore, the probabilities of the process shown in Fig. 1.8 in the unprojected and projected spaces are $n_{i\uparrow}(1-n_{i\downarrow})n_{j\downarrow}(1-n_{j\uparrow})\times(i \leftrightarrow j)$ and $n_{i\uparrow}n_{j\downarrow}\times(i \leftrightarrow j)$ respectively. Therefore, g_s comes out to be,

$$g_s = \frac{1}{\sqrt{(1-n_{i\uparrow})(1-n_{i\downarrow})(1-n_{j\uparrow})(1-n_{j\downarrow})}}. \tag{1.9}$$

Thus the tJ model can be written in the unprojected space as,

$$H_{tJ} \approx \left(\sum_{<ij>} -t(\sum_\sigma g_{t\sigma} c_{i\sigma}^\dagger c_{j\sigma} + H.c.) + J\left(g_s S_i.S_j - \frac{n_i n_j}{4} \right) \right), \tag{1.10}$$

where the density-density term has a scaling factor of 1. If we put $n_{i\sigma} = (1-x)/2$ (in the spin symmetric case) where x is the hole doping fraction, then $g_s = 4/(1+x)^2$.

The effect of the projection is approximately captured through the Gutzwiller factors in the renormalized tJ Hamiltonian given by Eq. 1.10. This Hamiltonian is now in terms of unprojected normal fermionic operators with the Gutzwiller factors suitably suppressing or enhancing the terms to take into account the effect of projection. In order to solve the Hamiltonian, we treat the quartic terms at the mean field level to make them quadratic. For example to explore superconductivity, one can introduce pairing amplitude, $\tilde{\Delta}_r = \langle c_{i\uparrow}^\dagger c_{i+r\downarrow}^\dagger - c_{i\downarrow}^\dagger c_{i+r\uparrow}^\dagger \rangle_0$ and Fock shift, $\tilde{\xi}_{r\sigma} = \langle c_{i\sigma}^\dagger c_{i+r\sigma} \rangle_0$ as appropriate mean fields and solve them self-consistently to find the approximate ground state of the system. Details of the calculation are given in Appendix A.2.

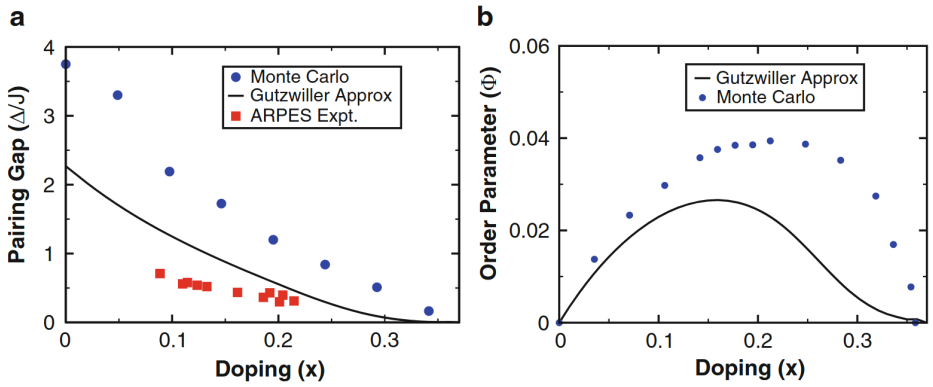

Figure 1.9: (a) Pairing gap Δ as a function of doping, x within VMC and Gutzwiller RMFT calculations and comparison with experimental ARPES data. (b) Order parameter Φ from VMC and Gutzwiller RMFT calculations. Adapted from Ref [4].

Gutzwiller approximation, though is an adhoc technique, has been well tested against more accurate methods like VMC in context of tJ model. Fig. 1.9 shows the pairing gap from VMC calculations, Gutzwiller RMFT and angle resolved photo emmission spectroscopy (ARPES) experimental results. Also shown is the superconducting order parameter (from VMC and RMFT calculations) which captures the off diagonal long range order in the superconducting state and also gives an estimate of T_c. The results are in qualitative agreement in the sense that monotonic decay of gap and non-monotonicity in order parameter are captured well within Gutzwiller approximation.

1.5 Strong e-e correlations in band insulators

In this thesis, we analyze the effects of on-site Coulomb repulsion U on a band insulator, modeled by a tight-binding hopping together with an explicit one-body potential, also

known as the ionic potential, which doubles the unit cell. We start with a band insulator with two bands, one filled and other unfilled, and turn on the on-site Coulomb repulsion, the Hubbard U. This model is also known as ionic Hubbard model (IHM). We show how a spin-exchange mediated superconductivity can be realized without doping in a simple model of a strongly correlated band insulator, where the bare band gap and the e-e interactions both dominate over the kinetic energy.

1.5.1 Ionic Hubbard model

In this section we discuss a variant of the Hubbard model known as the ionic Hubbard model (IHM). The IHM has in adddition to onsite Coulomb repulsion ($\sim U$), a staggered potential ($\sim \Delta$) acting on itinerant electrons. The Hamiltonian is given by,

$$\mathcal{H} = -\sum_{i,j\sigma}(t_{ij}c^{\dagger}_{i\sigma}c_{j\sigma} + h.c.) - \mu\sum_{i} n_i - \frac{\Delta}{2}\sum_{i\in A} n_i + \frac{\Delta}{2}\sum_{i\in B} n_i + U\sum_{i} n_{i\uparrow}n_{i\downarrow} \quad (1.11)$$

where $-\frac{\Delta}{2}$ is the ionic potential on A sites and $\frac{\Delta}{2}$ is the ionic potential on B sites.

In the non-interacting limit ($U = 0$), the Hamiltonian is exactly solvable and the system is a band insulator with a gap equal to Δ as shown in Fig. 1.10. When we introduce U slowly, the gap gets suppressed to $|\Delta - U\delta|$ (where δ is the density difference between the sublattices) which is found within restricted (paramagnetic) Hartree Fock theory for weak values of U and Δ [7]. On the other hand we can gain some insight about the strong correlation limit by looking at the atomic limit of the model where $t = 0$. For $\Delta > U$, $n_A = 2, n_B = 0$ forms the ground state of the system with a gap $\Delta - U$ which decreases with U. While for $\Delta < U$, $n_A = 1, n_B = 1$ is the ground state of the system with

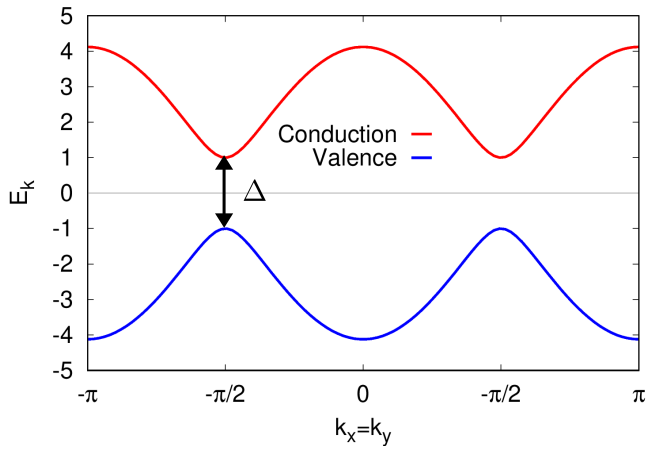

Figure 1.10: $U = 0$ limit of the IHM where the system is a band insulator with gap Δ. Here, the dispersion E_k is shown along the $k_x = k_y$ direction in the full Brillouin zone (FBZ) for $\Delta = 2$.

a gap $U - \Delta$ which increases with U. Exactly at $U = \Delta$, the system is gapless with states $n_A = 2, n_B = 0$ and $n_A = 1, n_B = 1$ being degenerate. Introducing hopping adiabatically, results into a metallic phase between a band insulator and a Mott insulator in the paramagnetic sector [5, 41–44].

In the presence of only nearest neighbor hopping, the Hamiltonian is particle hole symmetric under the transformation $c^\dagger_{A\sigma} \rightarrow c_{B\sigma}$ and $c^\dagger_{B\sigma} \rightarrow -c_{A\sigma}$ with chemical potential $\mu = \dfrac{U}{2}$ at half-filling. But this particle hole symmetry is explicitly broken if we add a next nearest neighbor hopping term as the Hamiltonian is no longer preserved under the transformation. The ionic Hubbard model in $U = 0$ limit in the prsence of t' shows a band insulator to a band metal transition. The non-interacting Hamiltonian is exactly solavable with eigenvalues,

$$\lambda^{\pm} = -\mu - 4t' \cos(k_x) \cos(k_y) \pm \sqrt{\frac{\Delta^2}{4} + t^2 \Gamma_k^2} \tag{1.12}$$

on a square lattice where $\Gamma_k = 2(\cos(k_x) + \cos(k_y))$. For $t' = 0$, the system is a band

insulator with a gap Δ as shown in Fig. 1.10 opening along the Fermi surface $\Gamma_k = 0$ at half-filling. But as soon as we turn on t', the degeneracy on the Fermi surface is broken and the points $K = (\pm\pi/2, \pm\pi/2)$ and $K' = (0, \pm\pi) or (\pm\pi, 0)$ become inequivalent. The conduction band minima $\lambda^+ = \Delta/2$ occurs at K whereas the valence band maxima $\lambda^- = 4t' - \Delta/2$ occurs at K' and there is an indirect band gap of $\Delta - 4t'$ for $\Delta > 4t'$. The system is then a band insulator until $t' = \Delta/4$ when the band gap closes to give an insulator to metal transition.

(A) IHM in low dimensions

IHM was used as a prototypical model for describing neutral-ionic transition in mixed-stack organic compunds [45, 46]. This model was also believed to capture the physics of ferroelectric perovskites [47–51]. There has been quite an extensive study of IHM in 1d in the past [49–57]. Exact diagonaliztion study in the paramagnetic phase at half-filling reported a phase transition from band to Mott insulator with a metallic transition point as U is increased for a given value of Δ [49, 50]. A continuous transition from band insulator to bond ordered wave (BOW) phase and another from BOW to Mott insulator was observed at half-filling within an effective field theory [51]. DMRG studies also supported the existence of these two continuous transitions in 1d at half-filling [55, 56]. In the limit $U, \Delta \gg t$ an effective Hamiltonian was derived for the IHM in 1d where the existence of spontaneously dimerized insulating BOW phase intervening the band and Mott insulator phases was confirmed [57].

(B) Phase diagram of IHM in weak to intermeidate coupling regime

Large U prefers single occupancies and hence an AF Mott insulating state where as large Δ prefers staggered charge density giving rise to a charge density wave (CDW) insula-

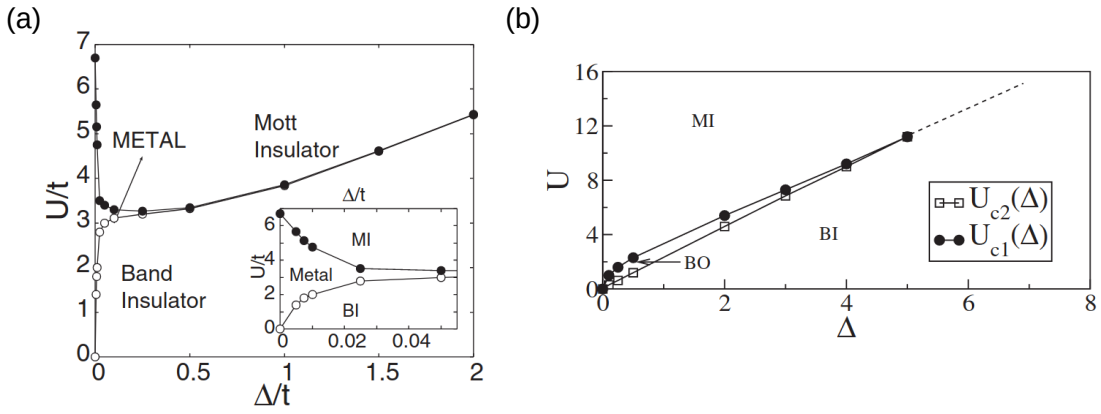

Figure 1.11: (a) Intermediate metallic phase in the IHM on Bethe lattice in the paramagnetic sector. Adapted from Ref [5]. (b) When AF order is allowed, it preempts the formation of metallic phase. An intermediate bond ordered insulating phase is observed in between the AF Mott insulating phase and paramagnetic band insulating phase based on cluster DMFT study. Adapted from Ref [6].

tor. The IHM has been studied theoretically in the past using dynamical mean field theory (DMFT) [5, 7, 43, 58–62], determinantal quantum Monte carlo [41, 42], cluster DMFT [6] and coherent potential approximation [44]. For $\Delta = 0$ we recover the usual Hubbard model and the system is an antiferromagnetic spin density wave insulator for low U values which goes over to an antiferromagnetic Mott insulator as we crank up U. For $U = 0$ the system is a band insulator with a gap Δ (See Fig. 1.10). In the weak to intermediate values of U and Δ, the zero temperature phase diagram shows an intervening correlation induced metallic phase in the paramagnetic sector at half-filling within DMFT [5, 41–44] (See Fig. 1.11(a)). However, when spontaneous symmetry breaking is allowed the transition from paramagnetic band insulator to AF insulator preempts the formation of the metallic phase [6, 59] (See Fig. 1.11(b)), except for a thin sliver of AF half-metallic phase found within DMFT using Iterated Perturbation Theory (IPT) as impurity solver [60]. On doping the IHM a

broad ferrimangetic half-metallic phase [60] is obtained between a weakly correlated paramagnetic metal for small values of U and a strongly correlated metal for larger values of U.

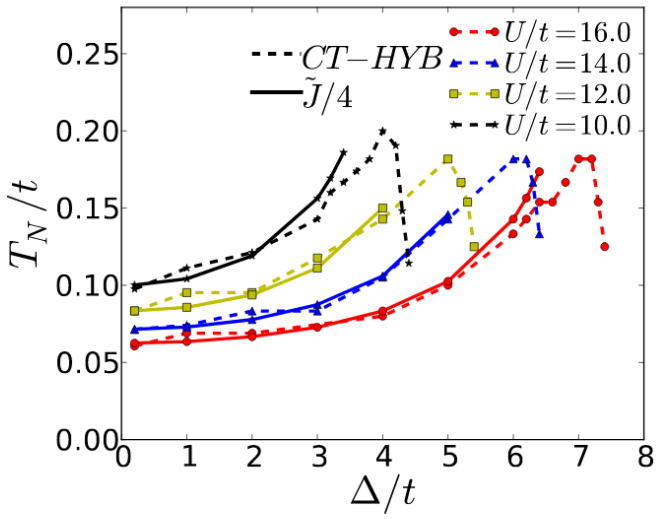

Figure 1.12: The Néel temperature from CTQMC+DMFT calculation follows the coupling of the Heisenberg term of the effective model (in the $U \gg t$ but $\Delta \sim t$ limit) for $\Delta < U$ but beyond that shows deviation from it. Adapted from Ref [7]. (Note that there is a difference in convention used for Δ term in the Hamiltonian in Ref [7] and current Hamiltonian. The two are related by a factor of 2)

(C) Strongly correlated limit of IHM

For $U \gg t$ but $\Delta \sim t$, the IHM maps to a modified tJ model with an additional ionic potential term and with spin-exchange term given by $\tilde{J} = 4t^2U/(U^2 - \Delta^2)$ [7]. Note that in this limit doublons are projected out from the low energy Hilbert space from all sites. In this case the Néel temperature of the AF order should obey $\tilde{J}$ and hence increase as Δ increases. In fact this was observed in DMFT+CTQMC calculation for the IHM at half filling [7] where it was shown that for U as high as $16t$, up to Δ little less than U, $T_N \sim \tilde{J}/4$ (Note that there is a difference in convention used for Δ term in the Hamiltonian

in Ref [7] and current Hamiltonian. The two are related by a factor of 2). But for $\Delta \geq U$ a sudden drop in T_N was observed which could not be explained based on the spin exchange coupling $\tilde{J}$ (See Fig. 1.12).

(D) Limit of strong correlation and strong staggered potential

In this thesis, we explore the limit $U \sim \Delta \gg t$ which has not yet been explored in detail. In this limit, as we will discuss in detail in the following chapters, double occupancies are expensive one one sublattice and holes are expensive on the other sublattice at half-filling. In order to take into account these projection constraints, we do a generalized similarity transformation which eliminates such high energy states from the Hilbert space and yields the low energy effective Hamiltonian. We further generalize Gutzwiller approximation to obtain scaling of various terms in the low energy effective Hamiltonian. Most striking feature of the low energy effective Hamiltonian is the presence non zero hopping terms at half-filling [10] which is unlike the strongly correlated limit of the Hubbard model which is a charge frozen Mott insulator at half-filling. This indicates the possibility of charge dynamic phases like metallic and superconducting phases which is the main motivation of this thesis. In the presence of nearest neighbor hopping only, the superconducting phase we find is meta-stable and it requires sufficient amount frustration in the form of next neighbor hopping to stabilize this unconventional superconductivity. Next neighbor hopping (t') acts as a mechanism of frustration of AF order. In the $U, \Delta \gg t, t'$ limit of the IHM, a perturbation in hopping yields two competing Heisenberg terms:

- $JS_{iA}.S_{jB}$ on nearest neighbor bonds.
- $J'S_{iA}.S_{jA}$ and $J'S_{iB}.S_{jB}$ on the next nearest neighbor bonds.

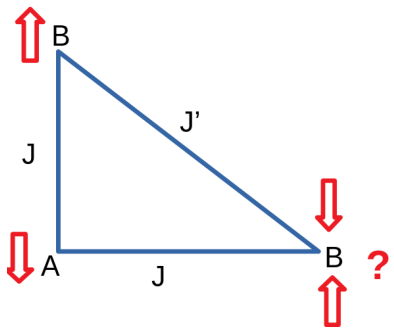

Figure 1.13: Antiferromagnetic interactions J and J' on nearest and next nearest neighbor bonds respectively on a square lattice.

In Fig. 1.13 we take the example of the square lattice where spins on the nearest neighbor bond AB interact antiferromagnetcally through coupling J and those on next nearest neighbor bond BB interact antiferromagnetcally through coupling J'. If spins align antiparallel on the AB bond, the spin on the third site is frustrated. Thus, the next neighbor hopping frustrates the magnetic order and helps in stabilizing the superconductivity even at half filling, which is the main conclusion from this thesis. The IHM in the presence of frustration in the form of next neighbor hopping has been a focus of study in recent times and many interesting phases are possible in such scenario [63–65].

(E) Experimental realizations of IHM

The IHM has been experimentally realized on an optical lattice with honeycomb structure in the recent past where the Mott phase and the charge density wave insulator phase have been observed [8] as shown in Fig. 1.14. Interaction strength was tuned by magnetic Feshbach resonance while the modulation in the potential was achieved by interference of counterpropagating laser beams. Due to the recent developments in layered materials and heterostructures, there can be many scenarios where the IHM can be used as a minimal

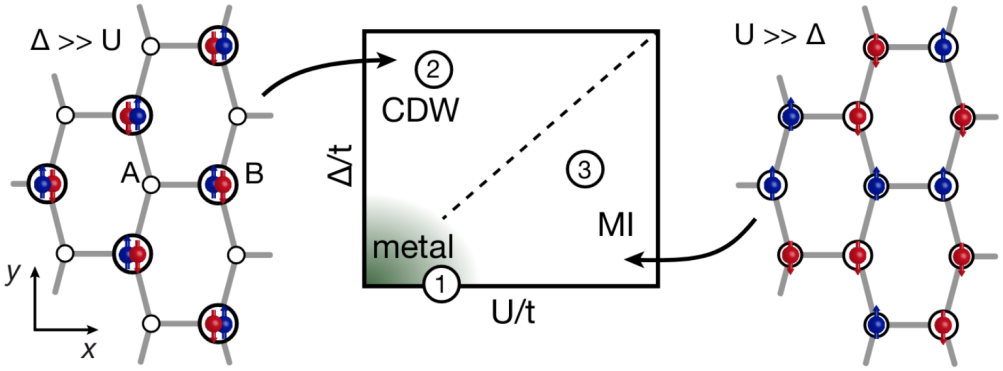

Figure 1.14: Experimental realization of IHM on a tunable optical honeycomb lattice. Adapted from Ref [8].

model, for example, graphene on h-BN substrate and bilayer graphene in the presence of a transverse electric field [66], which plays the role of the staggered potential. The limit of strong correlation, crucial for realizing the superconducting phase, can be achieved in these materials by applying a strain or twist. A strain/twist can suppress the tunneling by reducing overlap between the orbitals which can make $U/t, \Delta/t$ effectively large. Band insulating systems with two inequivalent strongly correlated atoms per unit cell, frustration in hopping and antiferromagnetic exchange, and lack of particle-hole symmetry, are promising candidates in this direction.

1.6 Outline of the thesis

The aim of the thesis is to study the effect of strong correlations in band insulators. Particularly, we show that an unconventional superconductor can be realized at commensurate filling starting from a strongly correlated band insulator.

In Chapter 2 we develop the formalism for treating strong correlations in the presence

of equally strong inhomogeneities at half-filling. Particularly, we study two models: the ionic Hubbard model and the Hubbard model with binary disorder. In both these models for $U \sim \Delta \gg t$, double occupancies are expensive on sites with positive ionic potential and holes are expensive on sites with negative ionic potential at half-filling. Through a generalized Schrieffer Wolff transformation, we do a site dependent projection to derive the low energy effective Hamiltonian. The various couplings in the Hamiltonian are then suitably renormalized using a scheme of generalized Gutzwiller approximation which captures the physics of the site dependent projection approximately. The striking feature of the low energy Hamiltonian is that hopping terms still survive at half-filling unlike the strongly correlated limit of the Hubbard model at half-filling which is a charge frozen Mott insulator. This motivated us to look for charge dynamic phases like metallic and superconducting phases.

In Chapter 3, we study a simple model of band insulator known as the ionic Hubbard model and study the role of interactions in the origin of unconventional superconductivity. In the spin symmetric phase where we force the staggered magnetization to go to zero, we find both d-wave and extended s-wave superconducting phases turn up. However, the d-wave phase is considerably broader and energetically also little lower than the extended s-wave phase. But as soon as we allow for AF order to exist, the superconducting phase becomes metastable with the AF Mott insulator phase being energetically more stable than the superconducting phase. The phase diagram consists of a direct transition from an AF Mott insulator to a paramagnetic band insulator through a sliver of AF half metal phase. This made us think that if we could suppress the AF order by introducing frustration in the system, we would be able to stabilize the superconducting phase.

In Chapter 4, we study the role of frustration in stabilizing unconventional superconductivity in strongly correlated band insulators. Introducing the next nearest neighbor hopping

as a mechanism of frustration not only stabilizes superconductivity which is predominantly d-wave with a small region where d-wave and extended s-wave are very close in energy, but also leads to the emergence of exotic metallic phases like paramagnetic metallic phase, ferrimagnetic metallic phase and AF half metallic phase which envelop the superconducting phase. The superconducting phase like in cuprates has a high T_c as well as a pseudogap phase.

Finally in Chapter 5 we conclude and summarise the work in this thesis.

CHAPTER 2

FORMALISM FOR STRONGLY CORRELATED MODELS WITH LARGE ONSITE POTENTIALS

2.1 Introduction

As mentioned in the chapter 1, strongly correlated systems are of immense interest and importance in condensed matter physics. Strong e-e interactions leads to many interesting phases like high-T_c superconductivity, antiferromagnetically ordered phases and Mott insulators. It is very essential to have a controlled many-body formalism for dealing with strong correlations. Various methods and tools are available for treating strong interactions in Hubbard type models in the limit when the e-e interactions form the largest energy scale. We described some of these methods in the Introduction chapter. In this chapter, we generalize the available formalism for treating strong correlations for the limit where

both the e-e interactions and the one-body potential (like staggered potential in ionic Hubbard model (IHM) or disorder potential in the binary alloy Hubbard model) are dominant and comparable. The method developed here is not only useful in exploring the special strongly correlated limit of the IHM, which is the main focus of this thesis but will also be essential to describe systems where strong impurities are present in the system e.g., Zn or Ni impurities in cuprate superconductors [67, 68].

The Hubbard model is a paradigmatic model in strongly correlated electron systems with two simple ingredients, namely, hopping of electrons ($\sim t$) and on-site Coulomb interaction ($\sim U$). In the limit of large U and finite hole doping, doublons are energetically unfavorable and need to be projected out from the low energy Hilbert space. A regular similarity transformation which projects out double occupancies, gives the effective low energy Hamiltonian which is known as the $t-J$ model [30] and captures many aspects of the physics of high T_c superconducting cuprates [2, 16, 69–74].

The $t-J$ model is defined in the projected Hilbert space and since Wick's theorem does not work for the fermionic operators in the projected Hilbert space, standard many-body physics tools of calculating various order Feynman diagrams for the self-energy [75] can not be used to solve this model. One needs to solve the Schwinger equation of motion for the Green's function of projected electrons [32, 33] and use a systematic perturbation theory in some parameter that controls double occupancy. Numerically, the $t-J$ model can be studied using the variational Monte Carlo method [34] where one starts with a variational wavefunction and then carries out doublon projection from each site explicitly . But because of the computational complexity, another alternative analytical tool most commonly used in the community as an approximate way of implementing the Gutzwiller projection (elimination of double occupancies) is known as the Gutzwiller approximation. The Gutzwiller approximation, as first introduced by Gutzwiller [76,77], was improved and

investigated later by several others [1, 36–40] mainly in the context of the hole-doped $t-J$ model. Under this approximation, the expectation values in the projected state is related to that in the unprojected state by a classical statistical weight factor know as the Gutzwiller factor that accounts for doublon exclusion. As an effect various terms in the Hamiltonian become renormalized by the Gutzwiller factors and the renormalized Hamiltonian can be studied in the unprojected basis.

Though the Gutzwiller projection for exclusion of doublons has been explored in detail in the literature, the Gutzwiller projection of holes from the low energy Hilbert space and its implementation in renormalizing the couplings in the effective low energy Hamiltonian at the level of the Gutzwiller approximation are still completely unexplored. There are models, like the electron doped $t-J$ model, where in the low energy Hilbert space one has to allow for doublons and holes have to be excluded. But in this situation it is not really essential to use the formalism of the Gutzwiller projection for holes as one can simply do particle-hole transformation and map the model to the hole-doped $t-J$ model where the low energy Hilbert space allows for holes excluding doublons. Hence probably the formalism of the Gutzwiller projection of holes has not been explored yet. But there are situations where the Gutzwiller projection of holes becomes crucial to carry out, e.g., in a model where on some of the sites it is energetically favourable to do hole projection while on some other sites doublon projection is required. With this motivation, we provide the basic formalism for the Gutzwiller projection of holes and calculate the Gutzwiller factors for implementing this projection approximately by renormalizing the couplings in the low energy Hamiltonian for a couple of such models.

In this chapter we provide a general formalism for studying variants of the strongly correlated Hubbard model with inhomogeneous onsite potential terms of the same order as U or larger than that. Due to competing effects of onsite potential and U, there are sites at

which holes are the maximum energy states (rather than doublons) and should be projected out from the low energy Hilbert space. We do a systematic extension of the similarity transformation in which the similarity operator itself varies from bond to bond depending upon whether both sites of the bond have doublons projected low energy Hilbert space dominated by large U physics, or both have hole projected low energy Hilbert space or one of the site on the bond has a hole projected and the other site has a doublon projected low energy Hilbert space. We further calculate generalised Gutzwiller approximation factors for various terms in the low energy effective Hamiltonian which are also bond dependent. Gutzwiller factors for bonds where one site requires hole projection and the other has doublon projection or where both the sites have hole projection have not been calculated in the literature earlier and here we derive them under the assumption that spin resolved densities before and after the projection remain the same.

To be specific, we provide details of the formalism for two well studied models, namely, the ionic Hubbard model (IHM) and correlated binary alloys represented by the Hubbard model in the presence of binary disorder. IHM is an interesting extension of the Hubbard model with a staggered onsite potential Δ added onto it. IHM has been studied in various dimensions with a variety of numerical and analytical tools. In one-dimension [51, 78, 79], it has been shown to have a spontaneously dimerized phase, in the intermediate coupling regime, which separates the weakly coupled band insulator from the strong coupling Mott insulator. In higher dimensions ($d > 1$), this model has been studied mainly using dynamical mean field theory (DMFT) [5, 7, 43, 58–62], determinantal quantum Monte Carlo [41, 42], cluster DMFT [6] and the coherent potential approximation [44]. As mentioned in chapter 1, though the solution of DMFT self consistent equations in the paramagnetic (PM) sector at half filling at zero temperature shows an intervening metallic phase [5], in the spin asymmetric sector, the transition from paramagnetic band insulator (PM BI) to

anti-ferromagnetic (AFM) insulator preempts the formation of a para-metallic phase [6,59]. In a recent work, it was shown that upon doping the IHM, one gets a broad ferrimagnetic half-metal phase [60] sandwiched between a PM BI and a PM metal. IHM has also been realised in optical lattices [8] on the honeycomb structure.

Most of these earlier works on IHM are in the limit of weak to intermediate U/t except [7, 61] where the strongly correlated limit of IHM has been studied for $\Delta \leq U$ within DMFT. Recently, [80] the $\Delta \sim U \gg t$ limit of IHM has been studied using slave-boson mean field theory. The Gutzwiller approximation method has been used for studying IHM [81] but in the limit of large U (not extreme correlation limit) where double occupancies are not fully prohibited. To the best of our knowledge, the Gutzwiller approximation formalism for this model has not been developed in the limit $\Delta \sim U \gg t$ which we present here. As we will describe in detail later in this chapter, in the limit of large U and Δ ($U \sim \Delta$), holes are energetically expensive in the sublattice where the staggered potential is $-\Delta/2$ (say, sublattice A) and double occupancies are expensive in the sublattice having potential $\Delta/2$(say, B). Therefore holes are projected out from the A sublattice and doublons from the B sublattice, which gives us the low energy effective Hamiltonian.

The second model for which we provide details of the formalism is the model of correlated binary alloys described by the Hubbard model in the presence of the binary disorder potential. In all correlated electron systems, disorder is almost inevitable due to various intrinsic and extrinsic sources of impurities. In high T_c cuprates, it is the doping of the parent compound (e.g. with oxygen) which results in the random onsite potential along with introducing holes [17]. Another type of common disorder is binary disorder which is for example realized in disulfides ($Co_{1-x}Fe_xS_2$ and $Ni_{1-x}Co_xS_2$) [82–85] in which two different transition metal ions are located at random positions, creating two different atomic levels for the correlated d-electrons. Binary disorder along with interactions among basic

degrees of freedom has also been realised in optical lattice experiments [86, 87]. Hence it becomes crucial to study the interplay of disorder and interactions in order to understand many interesting properties of these systems.

In the correlated binary alloy model, the onsite potential can be $\pm V/2$ at any site of the lattice randomly. The physics of this model has been explored for the intermediate to strong coupling regime mainly using DMFT [88–91]. But the limit of large onsite repulsion as well as strong disorder potential $U \sim V \gg t$, where holes are projected out from sites having potential $-V/2$ (A) sites and double occupancies are projected out from sites having potential $V/2$ (B) sites, has not been explored so far. Though this model has similarity with the IHM mentioned above, but the intrinsic randomness associated with the binary disorder model makes the effective low energy Hamiltonian different from the case of IHM. The interplay of disorder and interaction in this model may lead to very different physics like many-body localization [92–95].

The rest of the chapter is structured as follows. First we provide the basic formalism for hole projection by defining electron creation and annihilation operators in the hole projected Hilbert space. We enlist probabilities of various allowed configurations in the hole projected Hilbert space and calculate the Gutzwiller approximation factors for hopping processes. In the next section, we have derived the effective low energy Hamiltonian for the IHM in the limit of $U \sim \Delta \gg t$ and calculated the corresponding Gutzwiller approximation factors for various terms in the Hamiltonian. Followed by this we have described the similarity transformation and Gutzwiller approximation for correlated binary alloys in the limit of strong interactions and strong disorder. At the end, we also touch upon the case of fully random disorder and randomly distributed attractive impurities in the limit of both interaction and disorder strength being much larger than the hopping amplitude.

2.2 Basic formalism for hole projection

Though the formalism of Gutzwiller projection is well developed for the case of doublon projection in the literature, case of hole projection has not been explored in detail so far. In this section we derive the basic framework by defining new creation and annihilation operators for electrons in a restricted Hilbert space where holes are projected out but which still allows for doublons.

For a system of spin-1/2 fermions, at each site there are four possibilities, namely, $|\uparrow\rangle, |\downarrow\rangle, |\uparrow\downarrow\rangle$ and $|0\rangle$. Consider a model in which the energy cost of having $|0\rangle$ is much more than the other three states e.g., shown in Fig. [2.1]. It may also happen that due to some other constraints e.g. to achieve certain density of particles in the system, one has to retain doublons in the low energy Hilbert space (though the energy cost for doublons might be close to that of holes) and exclude holes. In these situations, the effective creation and annihilation operators for fermions in the low energy Hilbert space need to be modified.

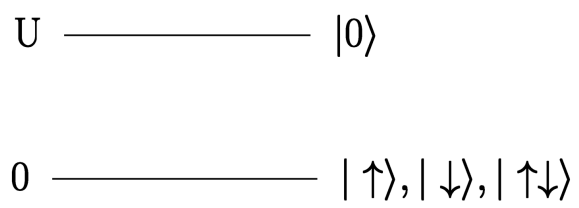

Figure 2.1: Separation in the energy scales of a hole and other states.

The simplest way to see this is the following. A normal electron creation operator can be expressed in terms of local Hubbard operators:

$$c_\sigma^\dagger = X^{\sigma\leftarrow 0} + \eta(\sigma) X^{d\leftarrow\bar{\sigma}}, \tag{2.1}$$

where,

$$X^{b\leftarrow a} = |b\rangle\langle a|. \tag{2.2}$$

Here σ can be $\uparrow$ or $\downarrow$ and d represents a double occupancy and $\eta(\uparrow) = 1$ and $\eta(\downarrow) = -1$. This means one can create a particle either starting from a hole or by annihilating one

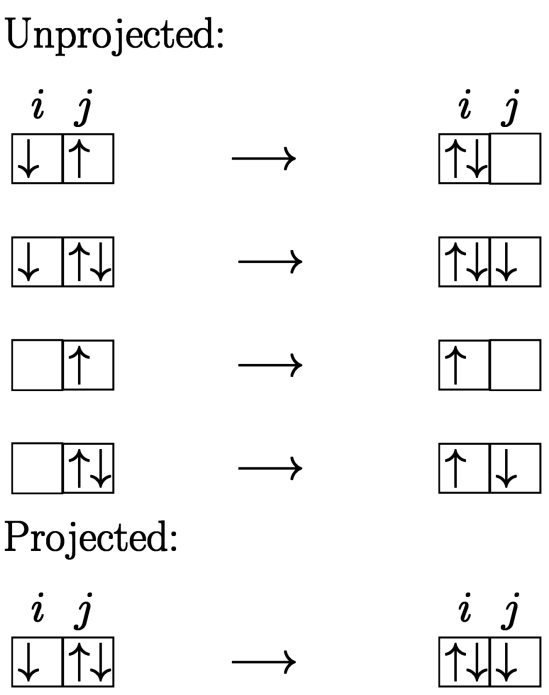

Figure 2.2: Top: Possible nearest neighbor hopping process in full Hilbert space. Bottom: Allowed hopping process in reduced Hilbert space from which hole has been projected out.

particle from a double occupancy. Since, in the present case holes are projected out from the low energy subspace, one can not create an up spin particle starting from a hole; rather we can create an up spin particle only by annihilating a down spin particle from a doublon. Therefore, the projected electron creation operator, which we denote by $\tilde{c}^{\dagger}_{\sigma}$, is:

$$\tilde{c}^{\dagger}_{\sigma} = \eta(\sigma)X^{d\leftarrow\bar{\sigma}} = c^{\dagger}_{\sigma}n_{\bar{\sigma}}, \tag{2.3}$$

with

$$\{\tilde{c}_\sigma, \tilde{c}_\sigma^\dagger\} = n_{\bar{\sigma}}. \tag{2.4}$$

Here, $\eta(\uparrow) = 1$ and $\eta(\downarrow) = -1$. Note that $\tilde{c}_\sigma$ does not satisfy standard Lie algebra of fermions as shown in Eq. 2.4. The corresponding number operator in this reduced Hilbert space is $\tilde{n}_\sigma = n_\sigma n_{\bar{\sigma}}$. Various Hubbard operators in terms of fermionic operators in the hole projected Hilbert space are given as,

$$\begin{aligned} X^{\sigma\leftarrow\sigma} &= \tilde{c}_{\bar{\sigma}}\tilde{c}_{\bar{\sigma}}^\dagger, \\ X^{\sigma\leftarrow\bar{\sigma}} &= -\tilde{c}_{\bar{\sigma}}\tilde{c_\sigma}^\dagger, \\ X^{d\leftarrow d} &= \tilde{c}_\uparrow^\dagger\tilde{c}_\uparrow = \tilde{c}_\downarrow^\dagger\tilde{c}_\downarrow. \end{aligned} \tag{2.5}$$

From the completeness relation of X operators in hole projected Hilbert space we get,

$$\begin{aligned} X^{\uparrow\leftarrow\uparrow} + X^{\downarrow\leftarrow\downarrow} + X^{d\leftarrow d} &= \mathcal{I}, \\ n_\uparrow(1-n_\downarrow) + n_\downarrow(1-n_\uparrow) + n_\uparrow n_\downarrow &= \mathcal{I}, \\ n_\uparrow n_\downarrow &= n - \mathcal{I}. \end{aligned} \tag{2.6}$$

Let us consider hopping of a particle to its nearest neighbor site in this reduced Hilbert space. In the full Hilbert space, which does not have the constraint of hole projection, there are four possible nearest neighbor hopping processes as shown in the top panel of Fig. [2.2]. But the only allowed hopping processes in the low energy Hilbert space of the hole projected system are those which do not have a hole in the initial state and in which no hole is created in the final state as well. This leaves for only one process in which there is a doublon at site j, and a spin $|\sigma\rangle$ at site i. Then a $\bar{\sigma}$ hopes from site j to i resulting in a single occupancy at site j and a doublon at site i as shown in the bottom panel of Fig. [2.2].

Thus effectively only hopping of doublons takes place in the projected space resulting in an overall suppression of the hopping process. The corresponding operator for this hopping process is,

$$\begin{aligned} H_{hopp} &= -t \sum_{<i,j>,\sigma} X_i^{d\leftarrow\bar{\sigma}} X_j^{\bar{\sigma}\leftarrow d} + h.c. \\ &= -t \sum_{<i,j>,\sigma} \tilde{c}_{i\sigma}^{\dagger} \tilde{c}_{j\sigma} + h.c. \end{aligned} \tag{2.7}$$

which is equivalently written in terms of normal fermionic operators as,

$$\begin{aligned} H_{hopp} &= -t \sum_{<i,j>,\sigma} c_{i\sigma}^{\dagger} n_{i\bar{\sigma}} n_{j\bar{\sigma}} c_{j\sigma} + h.c. \\ &= -\mathcal{P}_h (t \sum_{<i,j>,\sigma} c_{i\sigma}^{\dagger} c_{j\sigma} + h.c.) \mathcal{P}_h. \end{aligned} \tag{2.8}$$

Here $\mathcal{P}_h$ stands for the Gutzwiller projection operator for hole projection defined as $\mathcal{P}_h = \prod_i (1 - (1 - n_{i\uparrow})(1 - n_{i\downarrow}))$. We now generalize the concept of the Gutzwiller approximation for hole projected Hilbert space. The expectation value of the hopping process in the hole-projected Hilbert space can be obtained through the Gutzwiller approximation by renormalizing the hopping term in the unprojected basis by a Gutzwiller factor which takes into account of the physics of projection approximately. The Gutzwiller renormalization factor then is defined as the ratio of the expectation value of an operator O in the projected basis to that in the unprojected basis:

$$g = \frac{\langle \psi | \mathcal{P}_h O \mathcal{P}_h | \psi \rangle}{\langle \psi | O | \psi \rangle}, \tag{2.9}$$

where, ψ is the unprojected state.

The Gutzwiller renormalization factors are determined by the ratios of the probabilities

States	Unprojected	Projected
$\vert\uparrow\rangle$	$\mathbf{n}_\uparrow(1-\mathbf{n}_\downarrow)$	$(1-\mathbf{n}_\downarrow)$
$\vert\downarrow\rangle$	$\mathbf{n}_\downarrow(1-\mathbf{n}_\uparrow)$	$(1-\mathbf{n}_\uparrow)$
$\vert\uparrow\downarrow\rangle$	$\mathbf{n}_\uparrow\mathbf{n}_\downarrow$	$(\mathbf{n}-1)$
$\vert 0\rangle$	$(1-\mathbf{n}_\uparrow)(1-\mathbf{n}_\downarrow)$	0

Table 2.1: Probabilities of different states in terms of electron densities in unprojected and hole projected basis.

of the corresponding physical processes in the projected and unprojected bases. Listed in Table 2.1 are the probabilities of states in unprojected and hole projected spaces where the spin resolved unprojected and projected densities have been taken to be equal.

Here $\mathbf{n}_\sigma$ is the electron density with spin σ. Consistently everywhere we use $\mathbf{n}$ for density and n for the corresponding number operator.

The probability of hopping of an $\uparrow$ spin electron in the unprojected basis is $(1-\mathbf{n}_{i\uparrow})\mathbf{n}_{j\uparrow}\mathbf{n}_{i\uparrow}(1-\mathbf{n}_{j\uparrow})$. In the hole projected basis, the corresponding probability is $(\mathbf{n}_j-1)(\mathbf{n}_i-1)(1-\mathbf{n}_{i\uparrow})(1-\mathbf{n}_{j\uparrow})$. Therefore, the Gutzwiller factor for the hopping process comes out to be,

$$g_{t\uparrow}=\sqrt{\frac{(\mathbf{n}_i-1)(\mathbf{n}_j-1)}{\mathbf{n}_{i\uparrow}\mathbf{n}_{j\uparrow}}}. \tag{2.10}$$

With this set up for the hole projected Hilbert space, we describe the strongly correlated limit of IHM and binary alloys.

2.3 Strongly Correlated Limit of Ionic Hubbard Model

IHM has tight-binding electrons on a bipartite lattice (sub-lattices A and B) described by the Hamiltonian,

$$H = -t \sum_{i\in A, j\in B, \sigma} [\, c^{\dagger}_{i\sigma} c_{j\sigma} + h.c\,] - \frac{\Delta}{2}\sum_{i\in A} n_i + \frac{\Delta}{2}\sum_{i\in B} n_i + U\sum_i n_{i\uparrow} n_{i\downarrow} - \mu \sum_i n_i. \quad (2.11)$$

Here t is the nearest neighbor hopping, U the Hubbard repulsion and Δ a one-body staggered potential which doubles the unit cell. The chemical potential is $\mu = U/2$ for the average occupancy per site to be one, that is, $(\langle n_A\rangle + \langle n_B\rangle)/2 = 1$, corresponding to "half-filling".

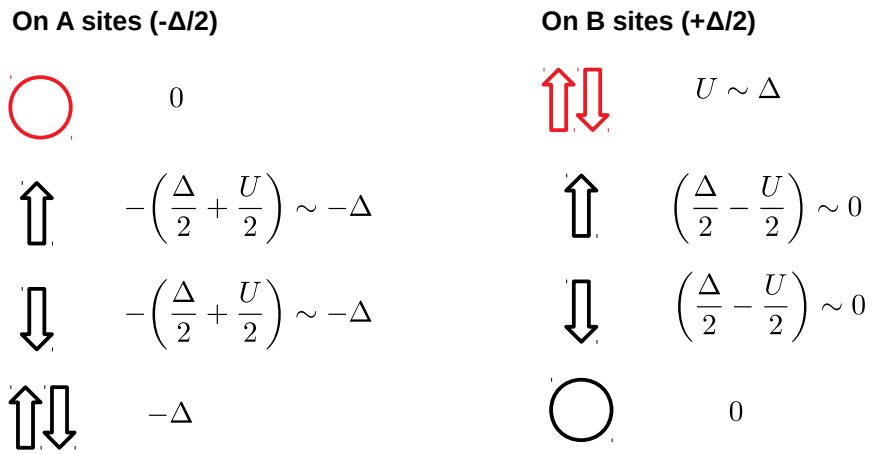

Figure 2.3: Single site sublattice specific energies in the limit $U \sim \Delta \gg t$. On the A sublattice, holes are the highest in energy while the single occupancies and doublons are almost degenerate and form the low energy Hilbert space. On the B sublattice, doublons are the highest in energy and the single occupancies and holes which are almost degenerate form the low energy Hilbert space.

Let us consider the $t = 0$ limit of this model in the regime $U \sim \Delta$. On the A sublattice, single occupancies have energy $-\left(\frac{\Delta}{2}+\frac{U}{2}\right) \sim -\Delta$, the hole has 0 energy and the doublon has energy $-\Delta$. So, among the four choices of occupancy, a hole on A is the highest energy state and should be projected out from the low energy Hilbert space. On the other hand, on the B sublattice, single occupancies cost $\left(\frac{\Delta}{2}-\frac{U}{2}\right) \sim 0$ energy, holes also cost 0 energy, while doublons cost energy $\Delta \sim U$, and therefore, on the B sublattice, doublons should be projected out from the low energy Hilbert space. This is shown in Fig. [2.3].

2.3.1 Low Energy Hamiltonian in the limit $U \sim \Delta >> t$

In the presence of a non-zero hopping term, the following nearest neighbor processes can take place as shown in Fig. [2.4].

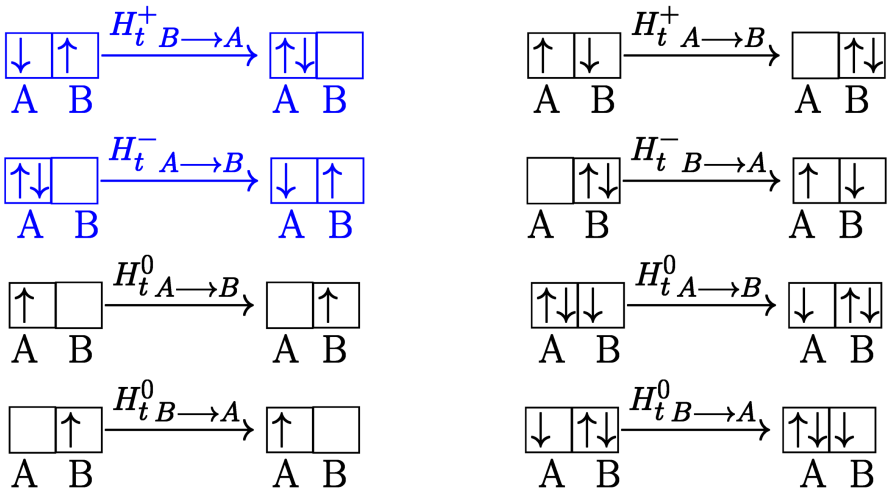

Figure 2.4: Nearest neighbor hopping processes for IHM.

H_t^+ processes involve an increase in double occupancy and hole occupancy by one, H_t^- processes involve a decrease in the double occupancy and hole occupancy by one and H_t^0 processes involve no change in the double occupancy or hole occupancy. Note that

$H^{+}_{tB\to A}$ and $H^{-}_{tA\to B}$ are the only processes which are confined to the low energy sector of the Hilbert space. All other hopping processes mix the high energy and the low energy part of the Hilbert space. The effective low energy Hamiltonian in the limit $U \sim \Delta \gg t$ can be obtained by doing a similarity transformation which eliminates processes which interconnects the high and low energy sectors of the Hilbert space. The effective Hamiltonian is given by,

$$\mathcal{H}_{eff} = e^{iS} H e^{-iS} = H + i[S, H] + \frac{i^2}{2}[S, [S, H]] + ... \tag{2.12}$$

Here, S, the transformation operator is perturbative in t/Δ and $t/(U + \Delta)$ and is given by,

$$iS = \frac{1}{U + \Delta}(H^{+}_{t\ A\to B} - H^{-}_{t\ B\to A}) + \frac{1}{\Delta}(H^{0}_{t\ A\to B} - H^{0}_{t\ B\to A}). \tag{2.13}$$

Higher order ($O(t^2/U)$) terms that arise from $[S, H_t]$ and $[S, [S, H_0]]$ and connects the low energy sector to the high energy sector can be eliminated by including a second similarity transformation $S^{'}$ such that $[S^{'}, H_0]$ cancels those terms. The effective Hamiltonian which does not involve mixing between low and high energy subspaces upto order t^2 is,

$$\begin{aligned}\mathcal{H}_{eff} = H_0 + H_{1,low} + \frac{1}{U + \Delta}[H^{+}_{t\ A\to B}, H^{-}_{t\ B\to A}] \\ + \frac{1}{\Delta}[H^{0}_{t\ A\to B}, H^{0}_{t\ B\to A}] + O(t^3/U^2)...\end{aligned} \tag{2.14}$$

Here $H_0 = U\sum_i n_{i\uparrow}n_{i\downarrow} - \frac{\Delta}{2}\sum_{i\in A} n_i + \frac{\Delta}{2}\sum_{i\in B} n_i$ and $H_{1,low} = H^{+}_{tB\to A} + H^{-}_{tA\to B}$ is the hopping process in the low energy sector. If we now confine to the low energy subspace, $\frac{1}{U+\Delta}[H^{+}_{t\ A\to B}, H^{-}_{t\ B\to A}] \sim -\frac{1}{U+\Delta}H^{-}_{t\ B\to A}H^{+}_{t\ A\to B}$ because the first term in the commutator demands a doublon at site B and a hole at site A which is energetically not favourable. Similarly, $\frac{1}{\Delta}[H^{0}_{t\ A\to B}, H^{0}_{t\ B\to A}] \sim -\frac{1}{\Delta}H^{0}_{t\ B\to A}H^{0}_{t\ A\to B}$ because the first term in the commutator either demands a doublon at B or a hole at A and thus is not allowed

because they belong to the high energy sector.

2.3.2 Low energy Hamiltonian in terms of projected Fermions

Since holes on the A sublattice and doublons on the B sublattice belong to the high energy sector, we have projected them out from the low energy Hilbert space and introduced new projected operators,

$$\tilde{c}^{\dagger}_{A\sigma} = \eta(\sigma) X_A^{d\leftarrow\bar{\sigma}} = c^{\dagger}_{A\sigma} n_{A\bar{\sigma}}, \tag{2.15}$$

$$\tilde{\tilde{c}}^{\dagger}_{B\sigma} = X_B^{\sigma\leftarrow 0} = c^{\dagger}_{B\sigma}(1 - n_{B\bar{\sigma}}). \tag{2.16}$$

Note that $\{\tilde{\tilde{c}}_{\sigma}, \tilde{\tilde{c}}^{\dagger}_{\sigma}\} = 1 - n_{\bar{\sigma}}$.

While writing in terms of normal fermionic operators in the projected space, the order of the terms in the projected basis becomes important for the A and B sublattices. On the A sublattice, $\tilde{c}_{A\sigma}\tilde{c}^{\dagger}_{A\sigma} = \mathcal{P}_h c_{A\sigma} c^{\dagger}_{A\sigma}\mathcal{P}_h$ where as $\tilde{c}^{\dagger}_{A\sigma}\tilde{c}_{A\sigma} \neq \mathcal{P}_h c^{\dagger}_{A\sigma} c_{A\sigma}\mathcal{P}_h$. In the former case, both forms of operators count $\bar{\sigma}$ type single occupancies where as in the later case $\tilde{c}^{\dagger}_{A\sigma}\tilde{c}_{A\sigma}$ count double occupancies while $c^{\dagger}_{A\sigma}c_{A\sigma}$ counts both double occupancies as well as σ type single occupancies in the hole projected space. On the B sublattice, the situation is opposite. $\tilde{c}^{\dagger}_{B\sigma}\tilde{c}_{B\sigma} = \mathcal{P}_d c^{\dagger}_{B\sigma} c_{B\sigma}\mathcal{P}_d$ and $\tilde{c}_{B\sigma}\tilde{c}^{\dagger}_{B\sigma} \neq \mathcal{P}_d c_{B\sigma} c^{\dagger}_{B\sigma}\mathcal{P}_d$. In the former case, both projected and normal fermionic operators count σ type single occupancies where as in the latter case the projected space operators count holes while the normal fermionic representation counts holes as well as $\bar{\sigma}$ type single occupancies in the doublon projected space.

In terms of new projected operators, H_0 in Eq. (2.14) can be written as $U\sum_{i\in A}(n_i - 1) - \frac{\Delta}{2}[\sum_{i\in A} n_i - \sum_{i\in B} n_i]$. Here we have used that on a site $i \in A$, $n_{i\uparrow}n_{i\downarrow} = n_i - 1$ (see Eq. (2.6)). Since doublons have been projected out from the B sublattice, in the low

energy effective Hamiltonian there is no Hubbard term for the B sublattice. The hopping term $H_{1,low}$ in the projected space does not involve holes on sublattice A and doublons on sublattice B. The representation in terms of projected operators is,

$$\begin{aligned} H_{1,low} &= -t \sum_{<ij>,\sigma} \tilde{c}^{\dagger}_{iA\sigma} \tilde{\tilde{c}}_{jB\sigma} + \tilde{\tilde{c}}^{\dagger}_{jB\sigma} \tilde{c}_{iA\sigma} \\ &= -t \sum_{<ij>,\sigma} \mathcal{P}[c^{\dagger}_{iA\sigma} c_{jB\sigma} + h.c.]\mathcal{P}, \end{aligned} \tag{2.17}$$

where,

$$\mathcal{P} = \prod_{i,j} (1 - (1 - n_{iA\uparrow})(1 - n_{iA\downarrow}))(1 - n_{iB\uparrow} n_{iB\downarrow}). \tag{2.18}$$

Here the projection operator $\mathcal{P}$ projects out holes from the Hilbert space corresponding to sublattice A and doublons from the Hilbert space on sublattice B.

$\underline{O(t^2/(U+\Delta))}$ **Dimer Terms**: In terms of Hubbard operators, the dimer term corresponding to $\frac{1}{U+\Delta}[H^{+}_{t\ A\to B}, H^{-}_{t\ B\to A}] \sim -\frac{1}{U+\Delta} H^{-}_{t\ B\to A} H^{+}_{t\ A\to B}$ becomes,

$$H^{1}_{dimer} = -\frac{t^2}{U+\Delta} \sum_{i\in A, j\in B, \sigma} [X^{\sigma\leftarrow\sigma}_{i} X^{\bar{\sigma}\leftarrow\bar{\sigma}}_{j} - X^{\bar{\sigma}\leftarrow\sigma}_{i} X^{\sigma\leftarrow\bar{\sigma}}_{j}]$$

The corresponding process is represented in Fig. [2.5]. In terms of projected fermionic operators, these dimer terms take the following form:

$$= -\frac{t^2}{U+\Delta} \sum_{i,j,\sigma} [\tilde{c}_{iA\bar{\sigma}} \tilde{c}^{\dagger}_{iA\bar{\sigma}} \tilde{\tilde{c}}^{\dagger}_{jB\bar{\sigma}} \tilde{\tilde{c}}_{jB\bar{\sigma}} - \tilde{c}_{iA\sigma} \tilde{c}^{\dagger}_{iA\bar{\sigma}} \tilde{\tilde{c}}^{\dagger}_{jB\sigma} \tilde{\tilde{c}}_{jB\bar{\sigma}}]$$

$$= J_1 \sum_{i,j} \mathcal{P}[S_{iA}.S_{jB} - (2 - n_{iA})n_{jB}/4]\mathcal{P}, \tag{2.19}$$

with $J_1 = \frac{2t^2}{U+\Delta}$.

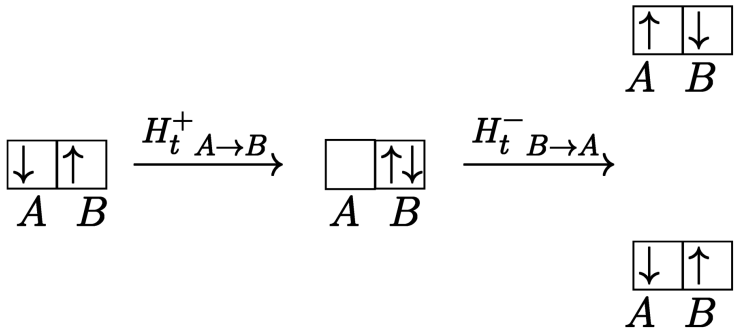

Figure 2.5: Spin exchange and spin preservation dimer terms for IHM.

The dimer term corresponding to $[H^0_{t\ A\to B}, H^0_{t\ B\to A}]$ involves hopping of an electron or a doublon from some site to its nearest neighbor site and back to the initial site as shown in Fig. [2.6].

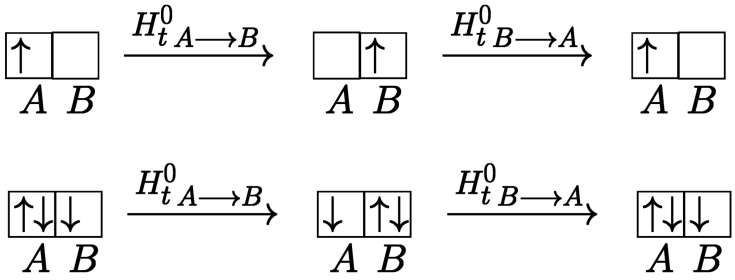

Figure 2.6: Top: Hopping of a single spin to site B and back to site A. Bottom: Hopping of a doublon from A to B and back to A.

This process is of order t^2/Δ and can be written as,

$$H^2_{dimer} = -\frac{t^2}{\Delta} \sum_{\sigma,<ij>} \left[X^{\sigma\leftarrow\sigma}_{iA} X^{0\leftarrow 0}_{jB} + X^{d\leftarrow d}_{iA} X^{\bar{\sigma}\leftarrow\bar{\sigma}}_{jB}\right]$$

In terms of projected operators we get

$$= -\frac{t^2}{\Delta} \sum_{\sigma,<ij>} \left[\tilde{c}_{iA\bar{\sigma}}\tilde{c}^{\dagger}_{iA\bar{\sigma}}\tilde{\tilde{c}}_{jB\sigma}\tilde{\tilde{c}}^{\dagger}_{jB\sigma} + \tilde{c}^{\dagger}_{iA\sigma}\tilde{c}_{iA\sigma}\tilde{\tilde{c}}^{\dagger}_{jB\bar{\sigma}}\tilde{\tilde{c}}_{jB\bar{\sigma}}\right]$$

$$= -\frac{t^2}{\Delta} \sum_{<ij>,\sigma} \mathcal{P}\left[(1-n_{iA\bar{\sigma}})(1-n_{jB}) + (n_{iA}-1)n_{jB\bar{\sigma}}\right]\mathcal{P}. \tag{2.20}$$

$\underline{O(t^2/\Delta)}$ **Trimer terms**:

Trimer terms involve hopping of a doublon or a hole from a site to it's next nearest neighbor site. Effectively there is doublon hopping which is intra A sublattice hopping denoted by H^{AA}_{hopp} where as the hole hopping is intra B sublattice hopping (H^{BB}_{hopp}) as shown in Fig. [2.7, 2.8].

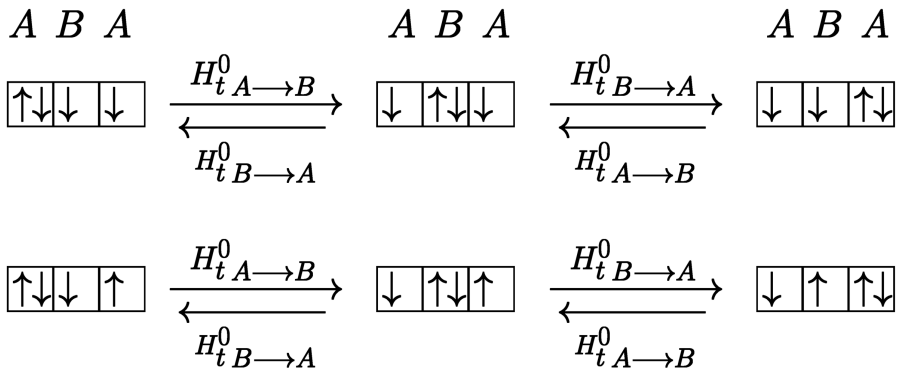

Figure 2.7: Effective next nearest neighbor hopping of a doublon within A sublattice.

In terms of X operators, hopping processes for doublon hopping, which is of $O(t^2/\Delta)$, on the A sublattice are represented as,

$$H^{AA}_{hopp} = -\frac{t^2}{\Delta} \sum_{\sigma,<ijk>} X^{d\leftarrow\bar{\sigma}}_{kA} X^{\bar{\sigma}\leftarrow\bar{\sigma}}_{jB} X^{\bar{\sigma}\leftarrow d}_{iA} + X^{d\leftarrow\sigma}_{kA} X^{\sigma\leftarrow\bar{\sigma}}_{jB} X^{\bar{\sigma}\leftarrow d}_{iA} + h.c.$$

In terms of projected operators, they are represented as,

$$= -\frac{t^2}{\Delta} \sum_{\sigma,<ijk>} (\tilde{\tilde{c}}^{\dagger}_{kA\sigma} \tilde{\tilde{c}}^{\dagger}_{jB\bar{\sigma}} \tilde{\tilde{c}}_{jB\bar{\sigma}} \tilde{c}_{iA\sigma} + \tilde{c}_{iA\bar{\sigma}} \tilde{\tilde{c}}^{\dagger}_{jB\bar{\sigma}} \tilde{\tilde{c}}_{jB\sigma} \tilde{\tilde{c}}^{\dagger}_{kA\sigma})$$

$$= -\frac{t^2}{\Delta} \sum_{\sigma,<ijk>} \mathcal{P}(c^{\dagger}_{kA\sigma} n_{jB\bar{\sigma}} c_{iA\sigma} + c_{iA\bar{\sigma}} c^{\dagger}_{jB\bar{\sigma}} c_{jB\sigma} c^{\dagger}_{kA\sigma})\mathcal{P}. \tag{2.21}$$

Similarly the hopping of holes within the B sublattice, shown in Fig. [2.8], can be written in terms of X operators as,

$$H^{BB}_{hopp} = -\frac{t^2}{\Delta} \sum_{\sigma,<jil>} X^{0\leftarrow\sigma}_{lB} X^{\sigma\leftarrow\sigma}_{iA} X^{\sigma\leftarrow 0}_{jB} + X^{0\leftarrow\bar{\sigma}}_{lB} X^{\bar{\sigma}\leftarrow\sigma}_{iA} X^{\sigma\leftarrow 0}_{jB} + h.c.$$

which can be written in terms of projected operators as,

$$= -\frac{t^2}{\Delta} \sum_{\sigma,<jil>} (\tilde{\tilde{c}}_{lB\sigma} \tilde{c}_{iA\bar{\sigma}} \tilde{c}^{\dagger}_{iA\bar{\sigma}} \tilde{\tilde{c}}^{\dagger}_{jB\sigma} + \tilde{\tilde{c}}^{\dagger}_{jB\sigma} \tilde{c}_{iA\sigma} \tilde{c}^{\dagger}_{iA\bar{\sigma}} \tilde{\tilde{c}}_{lB\bar{\sigma}})$$

$$= -\frac{t^2}{\Delta} \sum_{\sigma,<jil>} \mathcal{P}(c_{lB\sigma}[(1 - n_{iA\bar{\sigma}}) c^{\dagger}_{jB\sigma} + c^{\dagger}_{iA\sigma} c_{iA\bar{\sigma}} c^{\dagger}_{jB\bar{\sigma}}])\mathcal{P}. \tag{2.22}$$

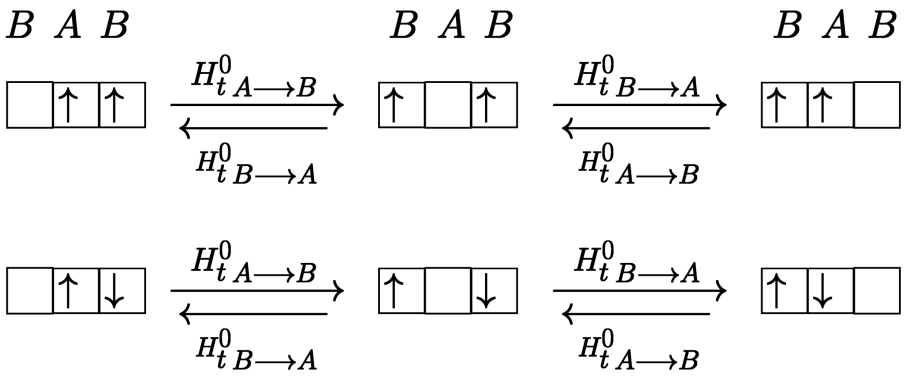

Figure 2.8: Effective next nearest neighbor hopping of hole for IHM.

2.3.3 Gutzwiller approximation

The effective low energy Hamiltonian obtained in the above section can be written as $\mathcal{H}_{eff} = \mathcal{P}\tilde{H}\mathcal{P}$ where $\mathcal{P}$ will project out holes from the A sublattice and doublons from the B sublattice for half-filling and densities close to half-filling. Within the Gutzwiller approximation, the effect of this projection is taken approximately by renormalizing various coupling terms in $\tilde{H}$ by corresponding Gutzwiller factors such that eventually the expectation value of the renormalized Hamiltonian can be calculated in the normal basis. Further we will calculate the Gutzwiller approximation factors under the assumption that the spin resolved densities before and after the projection remain the same which will make Gutzwiller factors equal to 1 for some terms in $\tilde{H}$. The renormalized Hamiltonian can be written as,

$$\tilde{H} = H_0 - t \sum_{\sigma,<ij>} g_{t\sigma}[c^{\dagger}_{iA\sigma}c_{jB\sigma} + h.c.]$$

$$-\frac{t^2}{\Delta}\sum_{<ij>,\sigma}[(1-n_{iA\bar{\sigma}})(1-n_{jB}) + (n_{iA}-1)n_{jB\bar{\sigma}}]$$

$$-\frac{t^2}{\Delta}\sum_{\sigma,<ijk>}(g_{A\sigma}c^{\dagger}_{kA\sigma}n_{jB\bar{\sigma}}c_{iA\sigma} + g^{A}_{2}c_{iA\bar{\sigma}}c^{\dagger}_{jB\bar{\sigma}}c_{jB\sigma}c^{\dagger}_{kA\sigma}) + h.c.$$

$$-\frac{t^2}{\Delta}\sum_{\sigma,<jil>}(g_{B\sigma}c_{lB\sigma}(1-n_{iA\bar{\sigma}})c^{\dagger}_{jB\sigma} + g^{B}_{2}c_{lB\sigma}c^{\dagger}_{iA\sigma}c_{iA\bar{\sigma}}c^{\dagger}_{jB\bar{\sigma}}) + h.c.$$

$$+\frac{2t^2}{U+\Delta}\sum_{<i,j>}\left[g_s S_{iA}.S_{jB} - \frac{1}{4}(2-n_{iA})n_{jB}\right]. \tag{2.23}$$

Here $g_{t,\sigma}$ and g_s are Gutzwiller approximation factors for the nearest neighbor hopping and spin exchange terms. Note that in writing the above renormalized form of the Heisenberg part of the Hamiltonian, we have imposed SU(2) symmetry by hand [1, 36–40, 96–98].

States	Unprojected	Projected
$\vert\uparrow\rangle$	$\mathbf{n}_\uparrow(1-\mathbf{n}_\downarrow)$	$\mathbf{n}_\uparrow$
$\vert\downarrow\rangle$	$\mathbf{n}_\downarrow(1-\mathbf{n}_\uparrow)$	$\mathbf{n}_\downarrow$
$\vert\uparrow\downarrow\rangle$	$\mathbf{n}_\uparrow\mathbf{n}_\downarrow$	0
$\vert 0\rangle$	$(1-\mathbf{n}_\uparrow)(1-\mathbf{n}_\downarrow)$	$(1-\mathbf{n})$

Table 2.2: Probabilities of different states in terms of electron densities in unprojected and doublon projected bases.

Within the simplest approximation of spin resolved densities being same in projected and unprojected states, the Gutzwiller approximation factor for $S^z_{iA}S^z_{jB}$ remains unity while the Gutzwiller factor for the $S^+_{iA}S^-_{jB}+h.c.$ term is g_s. Since the original Hamiltonian is $SU(2)$ symmetric, the renormalized Hamiltonian obtained after taking into account the effect of projection, must also be $SU(2)$ symmetric. Hence we used g_s to be the Gutzwiller factor for the $S^z_{iA}S^z_{jB}$ term as well. Gutzwiller factors of the dimer terms are unity which will be discussed shortly . $g_{A\sigma}$ and g_2^A are Gutzwiller factors for intra sublattice hopping of doublons on the A sublattice and $g_{B\sigma}$ and g_2^B are Gutzwiller factors for the intra sublattice hopping of holes on the B sublattice. As we will demonstrate, some of the Gutzwiller factors are spin symmetric while others might be spin dependent in a spin symmetry broken phase like in antiferromagnetically ordered phases. Below we evaluate them one by one for various processes involved in $\mathcal{H}_{eff}$. We have enlisted below in Table 2.2 the probabilities of different states in the doublon projected basis. Probabilities for various states for the hole projected sublattice were enlisted in Table 2.1.

As we mentioned earlier, this analysis holds at half-filling and for densities not far from half-filling. Even if the system is overall half-filled, the individual sublattices are not, the

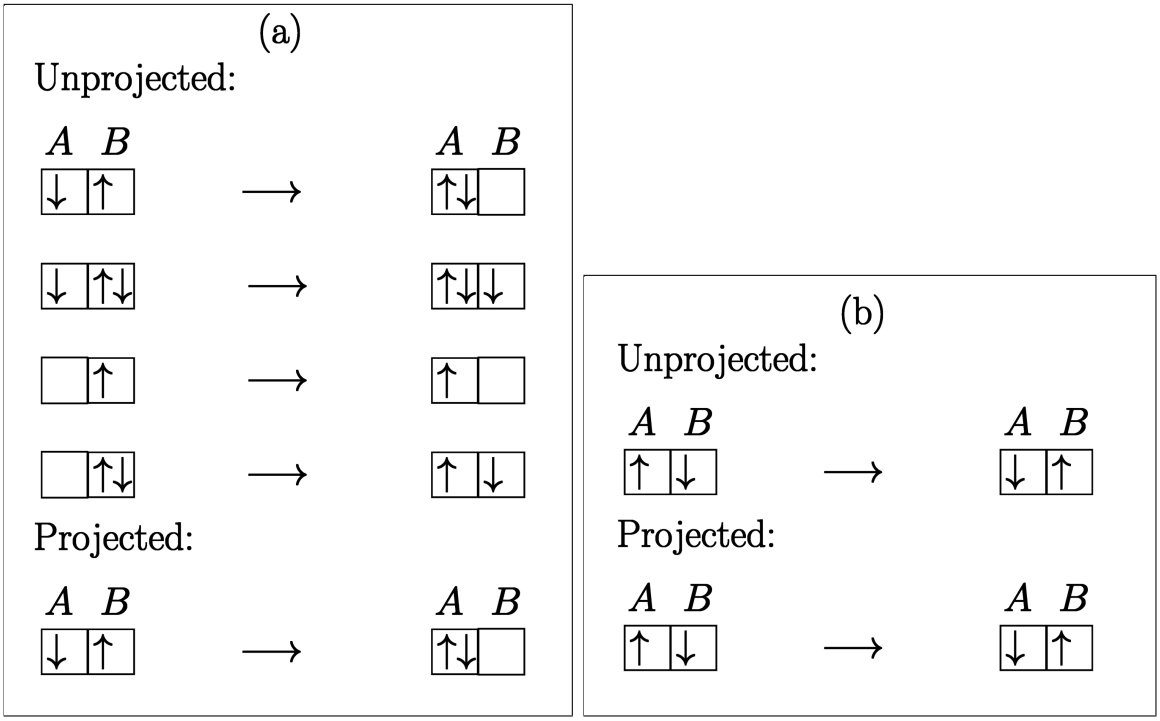

Figure 2.9: (a) Processes involved in the calculation of nearest neighbor hopping renormalization factor, $g_{t,\sigma}$. (b) Processes involved in the calculation of spin exchange renormalization factor g_s.

A subalttice is electron doped where asthe B sublattice is hole doped. At half-filling in the Hubbard model, the Gutzwiller renormalization factor for hopping is zero because the system is an antiferromagnetic Mott insulator where as in the case of IHM, the density difference between the sublattices results in finite $g_{t,\sigma}$. Here, as we will show, the density difference between two sublattices plays the role of doping in the case of the Hubbard model. Also, the trimer terms are present in the half-filled IHM which results in intra sublattice hopping of holes and doublons where as the half-filled Hubbard model has no trimer terms.

Below we first give the general expression for $g_{t,\sigma}$ and g_s at any filling and then evaluate them for the special case of half filling, $\frac{\mathbf{n}_A + \mathbf{n}_B}{2} = 1$. The probability of near-

est neighbor hopping of an $\uparrow$ electron in the unprojected space (shown in Fig. [2.9(a)]) is $(1-\mathbf{n}_{A\uparrow})\mathbf{n}_{B\uparrow}\mathbf{n}_{A\uparrow}(1-\mathbf{n}_{B\uparrow})$ and in the unprojected space it is $(1-\mathbf{n}_{A\uparrow})\mathbf{n}_{B\uparrow}(\mathbf{n}_A-1)(1-\mathbf{n}_B)$. Then, the Gutzwiller renormalization factor,

$$g_{t\uparrow} = \sqrt{\frac{(\mathbf{n}_A-1)(1-\mathbf{n}_B)}{\mathbf{n}_{A\uparrow}(1-\mathbf{n}_{B\uparrow})}}. \tag{2.24}$$

Let $\delta = \dfrac{\mathbf{n}_A - \mathbf{n}_B}{2}$ be the density difference between two sublattices. Then at half-filling, the density of A sublattice is $\mathbf{n}_A = 1+\delta$ and that of the B sublattice is $\mathbf{n}_B = 1-\delta$. Let the magnetization on the A sublattice, $m_A = \mathbf{n}_{\mathbf{A}\uparrow} - \mathbf{n}_{\mathbf{A}\downarrow}$, then at half-filling due to particle-hole symmetry, $m_A = -m_B = m$. One can re-write $g_{t,\sigma} = \dfrac{2\delta}{1+\delta+\sigma m}$ in an antiferromagnetically ordered phase at half-filling. For $m = 0$, g_t takes a form similar to that known for the doped $t-J$ model with δ , the density difference in IHM, playing the role of hole doping in the $t-J$ model.

Now consider the spin exchange process shown in Fig. [2.9(b)]. The probability for this process to take place in the unprojected basis is $\mathbf{n}_{A\uparrow}(1-\mathbf{n}_{A\downarrow})\mathbf{n}_{B\downarrow}(1-\mathbf{n}_{B\uparrow})\mathbf{n}_{A\downarrow}(1-\mathbf{n}_{A\uparrow})\mathbf{n}_{B\uparrow}(1-\mathbf{n}_{B\downarrow})$ where as in the projected basis it is $(1-\mathbf{n}_{A\downarrow})\mathbf{n}_{B\downarrow}(1-\mathbf{n}_{A\uparrow})\mathbf{n}_{B\uparrow}$, resulting in the Gutzwiller factor,

$$g_s = \sqrt{\frac{1}{\mathbf{n}_{A\uparrow}\mathbf{n}_{A\downarrow}(1-\mathbf{n}_{B\uparrow})(1-\mathbf{n}_{B\downarrow})}}. \tag{2.25}$$

Again at half-filling in an AFM ordered phase $g_s = 4/((1+\delta)^2 - m^2)$ which for $m = 0$ again maps to the g_s factor for the doped $t-J$ model with δ playing the role of hole-doping in that case.

The Gutzwiller factors of the dimer terms are 1 because the dimer terms $H^{1,2}_{dimer}$ are the products of densities. Under the assumption that the spin resolved unprojected and

projected densities are the same, the Gutzwiller factors for these terms are 1.

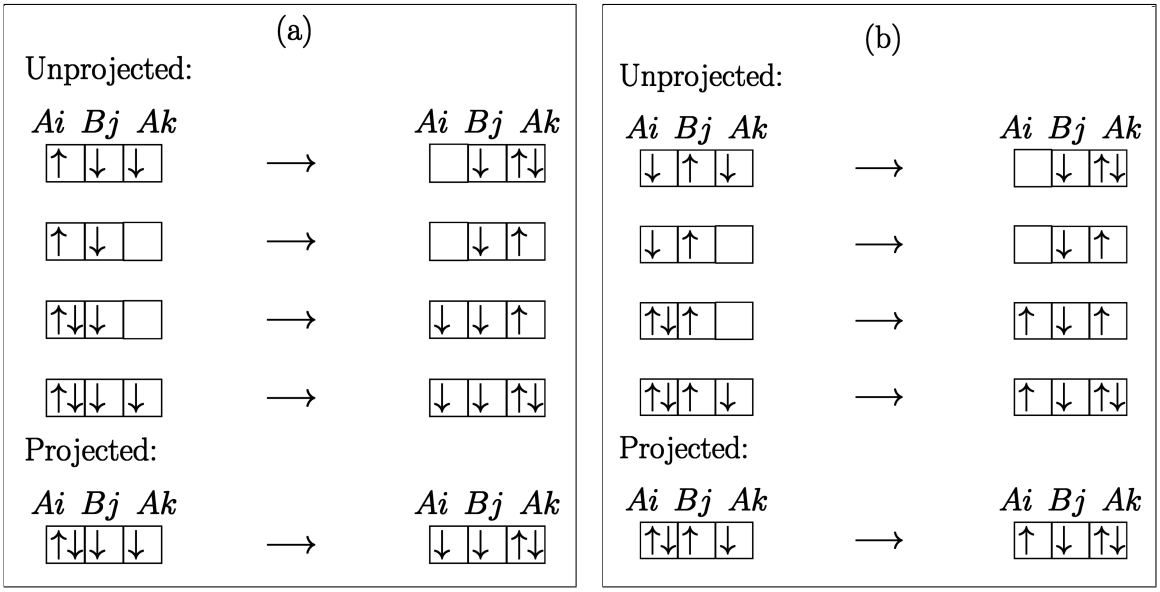

Figure 2.10: (a) Processes involved in the calculation of $g_{A\sigma}$. Similar physical processes with doublon at B site in the unprojected basis are considered in the calculation (but not shown here). (b) Processes involved in the calculation of g_2^A.

Now we will calculate Gutzwiller factors for various trimer terms shown in Fig.[2.7] and Fig. [2.8]. Fig.[2.10(a)] shows hopping of an $\uparrow$ electron within the A sublattice with a spin ($\downarrow$) on the intermediate B site being preserved. In the unprojected basis, the probability for this process to happen is $\mathbf{n}_{A\uparrow}^2(1-\mathbf{n}_{A\uparrow})^2\mathbf{n}_{B\downarrow}^2$. It is to be noted that processes with either a down type particle or a doublon at the intermediate B site have been considered in the unprojected space. Like wise, the probability for the process to happen in the projected basis is $(\mathbf{n}_A-1)^2(1-\mathbf{n}_{A\uparrow})^2\mathbf{n}_{B\downarrow}^2$. Therefore, the Gutzwiller factor for this process is,

$$g_{A\uparrow}=\frac{\mathbf{n}_A-1}{\mathbf{n}_{A\uparrow}}=\frac{2\delta}{1+\delta+m}. \tag{2.26}$$

where the expression on the right most side holds in the case of half-filling for non-zero staggered magnetization. In general one gets $g_{A\sigma}=\frac{\mathbf{n}_A-1}{\mathbf{n}_{A\sigma}}$. Fig. [2.10(b)] depicts hopping

processes on the A sublattice in which spin on the intermediate B site gets flipped. The probability in the unprojected basis for this process to occur is $(1-\mathbf{n}_{A\uparrow})(1-\mathbf{n}_{A\downarrow})\mathbf{n}_{A\uparrow}\mathbf{n}_{A\downarrow}(1-\mathbf{n}_{B\uparrow})(1-\mathbf{n}_{B\downarrow})\mathbf{n}_{B\uparrow}\mathbf{n}_{B\downarrow}$ where as that in the projected basis is $(\mathbf{n}_A-1)^2(1-\mathbf{n}_{A\uparrow})(1-\mathbf{n}_{A\downarrow})\mathbf{n}_{B\uparrow}\mathbf{n}_{B\downarrow}$ resulting in the Gutzwiller factor,

$$g_2^A = \frac{\mathbf{n}_A - 1}{\sqrt{\mathbf{n}_{A\uparrow}\mathbf{n}_{A\downarrow}(1-\mathbf{n}_{B\uparrow})(1-\mathbf{n}_{B\downarrow})}} = \frac{4\delta}{(1+\delta)^2 - m^2}. \tag{2.27}$$

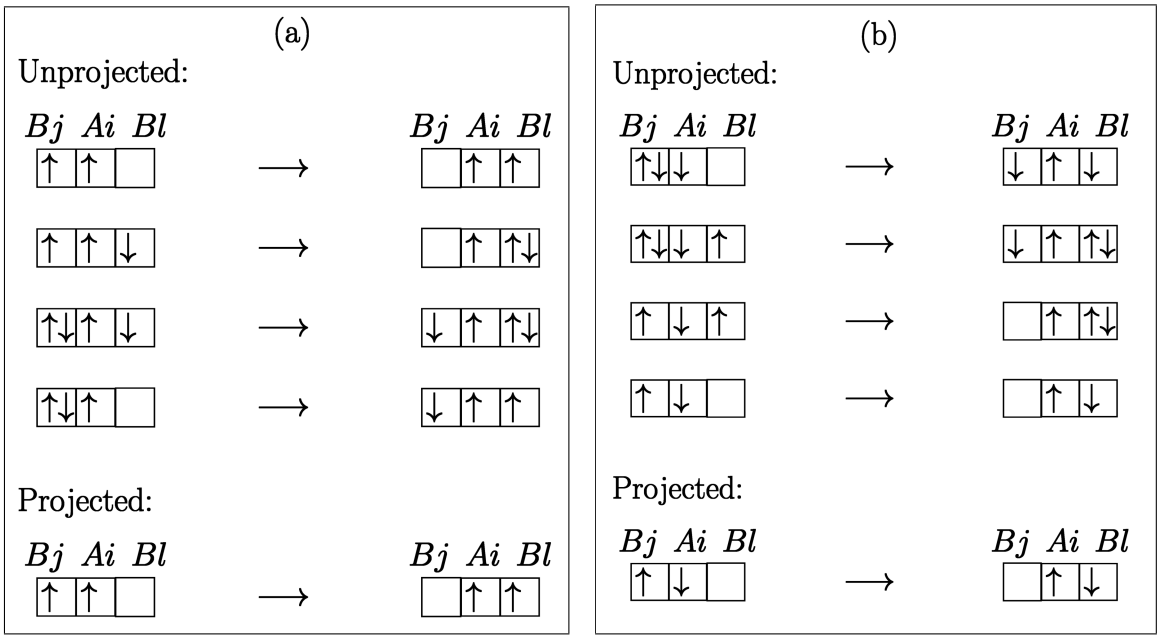

Figure 2.11: (a) Processes involved in the calculation of $g_{B\sigma}$. Similar physical processes with hole at A site in the unprojected basis are considered in the calculation of $g_{B\sigma}$ (but not shown here). (b) Processes involved in the calculation of g_2^B.

Now consider the hopping processes within the B sublattice depicted in Fig. [2.8]. Fig. [2.11(a)] shows hopping of an $\uparrow$ spin particle within the B sublattice such that spin on the intermediate A site is preserved. Here, again it must be noted that processes with either an up particle or a hole at the intermediate A site have been considered in the unprojected basis. In the unprojected basis the probability of this process is $(1-\mathbf{n}_{A\downarrow})^2\mathbf{n}_{B\uparrow}^2(1-\mathbf{n}_{B\uparrow})^2$

and that in the projected basis is $(1-\mathbf{n}_{A\downarrow})^2\mathbf{n}_{B\uparrow}^2(1-\mathbf{n}_B)^2$ leading to the Gutzwiller factor,

$$g_{B\uparrow} = \frac{1-\mathbf{n}_B}{1-\mathbf{n}_{B\uparrow}} = \frac{2\delta}{1+\delta+m}. \tag{2.28}$$

In general, $g_{B\sigma} = (1-\mathbf{n}_B)/(1-\mathbf{n}_{B\sigma})$ is spin dependent.

Another hopping process within the B sublattice is the one in which spin on the intermediate A site gets flipped. The probability for this process to occur in the unprojected basis is $(1-\mathbf{n}_{A\uparrow})(1-\mathbf{n}_{A\downarrow})\mathbf{n}_{A\uparrow}\mathbf{n}_{A\downarrow}(1-\mathbf{n}_{B\uparrow})(1-\mathbf{n}_{B\downarrow})\mathbf{n}_{B\uparrow}\mathbf{n}_{B\downarrow}$ and in the projected space it is $(1-\mathbf{n}_{A\uparrow})(1-\mathbf{n}_{A\downarrow})\mathbf{n}_{B\uparrow}\mathbf{n}_{B\downarrow}(1-\mathbf{n}_B)^2$. The Gutzwiller factor is therefore,

$$g_2^B = \frac{1-\mathbf{n}_B}{\sqrt{\mathbf{n}_{A\uparrow}\mathbf{n}_{A\downarrow}(1-\mathbf{n}_{B\uparrow})(1-\mathbf{n}_{B\downarrow})}} = \frac{4\delta}{(1+\delta)^2-m^2}. \tag{2.29}$$

In cases, even when particle-hole symmetry is broken explicitly, such that sublattice magnetizations are no longer equal and opposite in general, $g_2^A = g_2^B = g_2$. This will be seen in chapter 4.

2.3.4 Results for strongly correlated limit of IHM

In this section we present results for the IHM in the limit $U \sim \Delta \gg t$ at half filling. To be specific, we do mean field decomposition of the renormalized low energy Hamiltonian in Eq. (2.23) giving non zero expectation values to the following mean fields: (i) magnetization on the A sublattice (B sublattice), m_A (m_B) (ii) inter sublattice Fock shift (χ_{AB}) (iii) intra sublattice Fock shifts (iv) Hartree shifts and (v) the density difference between the two sublattices (δ). The quadratic mean field Hamiltonian is solved by appropriate canonical transformation and mean fields are obtained self-consistently. Below we first provide a comparison of our approach with the results obtained from an exact diagonal-

ization (ED) study of this model for a one dimensional chain followed up by the results towards a possible phase diagram of the IHM in the limit of validity of this approach.

2.3.4.1 Comparison with ED results

Below we first benchmark our approach of hole and doublon projection, implemented at the level of the renormalized low energy Hamiltonian via the Gutzwiller approximation, by comparing our results for a 1-d chain with those obtained from exact diagonalization by Anusooya-Pati et. al [9]. Although, renormalized mean field theory is expected to give reliable results for $d \geq 2$, here we have calculated simple quantities like sublattice density for comparison with data available from exact diagonalization study of IHM for a $1d$ chain. Interestingly, it matches quite well in this case.

Since the formalism we have developed in this chapter is valid for the regime of both U and Δ being much larger than the hopping amplitude t we compare our results for the largest value of U for which results are shown in [9]. Fig. [2.12] shows the density on sublattice A as a function of Δ for $U = 10t$ for a $1d$ chain. The ED result, obtained by digitizing the plot from the work of Anusooya-Pati et. al [9], is an extrapolation of finite size chains in the thermodynamic limit. For smaller values of Δ our formalism does not hold and hence the comparison has been shown for $\Delta \geq 7t$. The qualitative trend in both the calculations is the same and as Δ increases better quantitative consistency is observed between the two calculations. Note that there is an overall factor of 2 difference in the ionic potential term in our Hamiltonian and the one used in Anusooya-Pati et.al. After this check to validate our formalism, we provide below the details of the phase diagram of IHM in the limit under consideration.

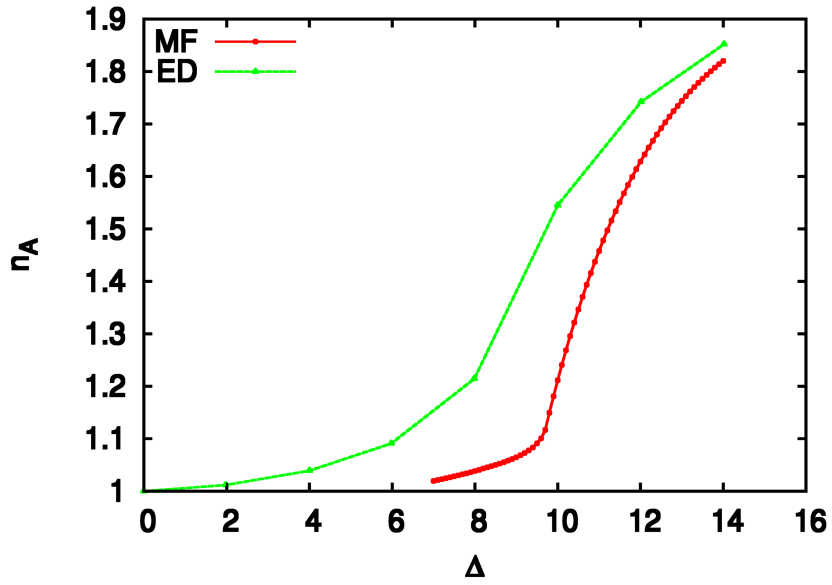

Figure 2.12: Density on sublattice A as a function of Δ for $U = 10t$. ED results shown are obtained from Ref [9].

2.3.4.2 Phase diagram of IHM for $U \sim \Delta \gg t$

The phase diagram of IHM in the limit $U \sim \Delta \gg t$ has not been explored in detail so far. There are a few numerical results available [7, 9] but a complete understanding has been lacking mainly because no perturbative calculation has been developed in this limit so far. One of the reasons is that the formalism for hole projection, which is essential in this limit, was missing so far in the literature. Below we provide details of various physical quantities based on the mean field analysis of our renormalized Hamiltonian for a $1d$ chain and also discuss possible phases in higher dimensional cases. Here, we are not trying to extract any physical understanding from the mean field analysis in $1d$, rather we are calculating some basic quantities which has similarities with higher dimesional results as we will see in the following chapters.

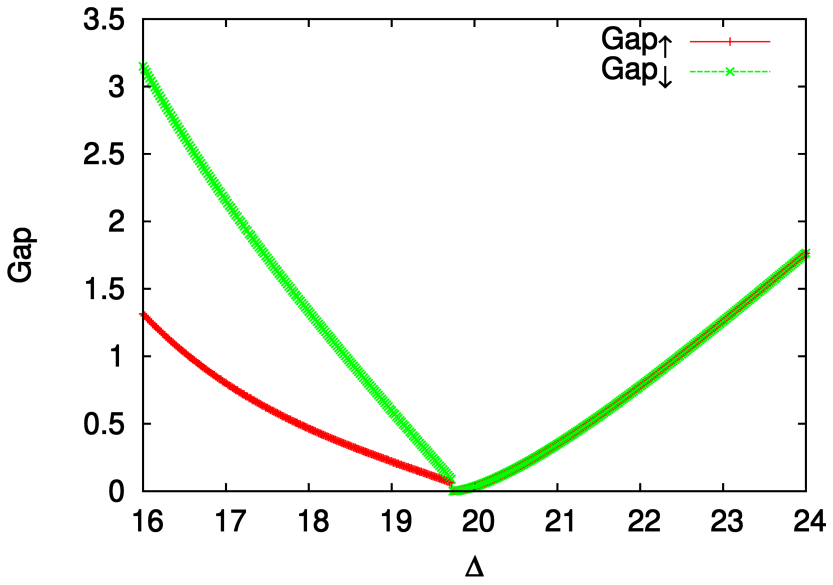

Figure 2.13: The gap in the single particle density of states vs Δ for $U = 20$. For $\Delta < U$, $gap_{\downarrow} > gap_{\uparrow}$ and both decrease with incraese in Δ eventually becoming zero for $\Delta \sim U$. As Δ increases further, the gap opens up again but the gap in the up and down channel are equal in this phase.

Gap in the single particle spectrum: Fig. [2.13] shows the behavior of gap_{σ} as a function of Δ for $U = 20t$. For $U > \Delta$, the gap in the down spin channel is more than that in the up spin channel but both decrease with increase in Δ becoming gapless near $\Delta \sim U$. Further increasing Δ opens up the gap in both channels which is now spin symmetric.

The existence of a metallic phase intervening between the two insulating phases of the IHM has been a debatable issue in the literature. Though the solution of DMFT self consistent equations in the paramagnetic (PM) sector at half filling at zero temperature shows an intervening metallic phase [5], in the spin asymmetric sector, the transition from paramagnetic band insulator (PM BI) to antiferromagnetic (AFM) insulator preempts the formation of a para-metallic phase [6,59]. But determinantal quantum Monte Carlo results demonstrated the presence of a metallic phase even in the spin asymmetric solution [41,42].

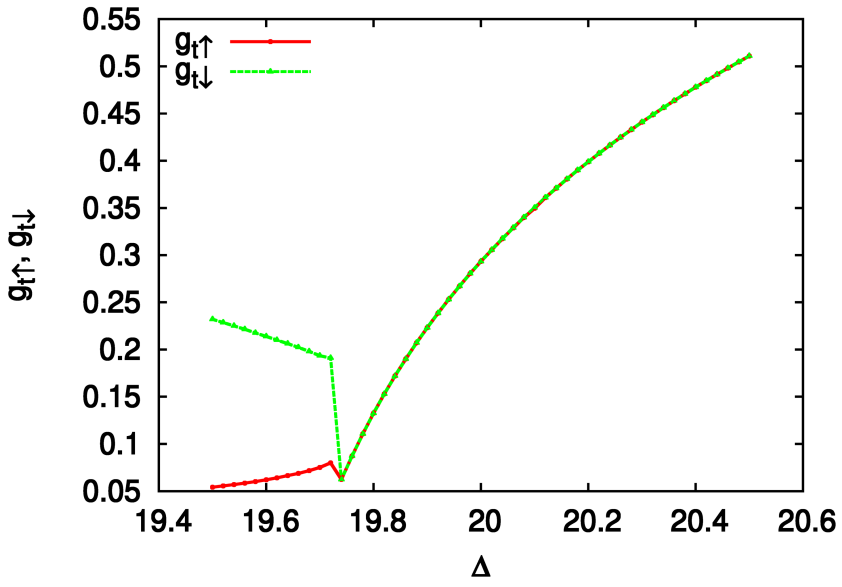

Figure 2.14: Plot of $g_{t\sigma}$ vs Δ for $U = 20$. In the metallic phase $g_{t\sigma}$ provides the quasi-particle weight.

Exact diagonalization for 1d chains [9] has also shown signatures of the presence of a metallic phase via calculation of the charge stiffness. In all the cases, where an intervening metallic phase has been demonstrated, it was also shown that the width of the metallic phase shrinks with increase in U and Δ. A very narrow metallic regime observed in our approach for the IHM at half filling for $U \sim \Delta \gg t$ is completely consistent with these studies.

The renormalized momentum distribution function $n_{\alpha\sigma}(k) = \int d\omega A_{\alpha\sigma}(k,\omega) = g_{t\sigma} n^0_{\alpha\sigma}(k)$, where $n^0_{\alpha\sigma}(k)$ is the momentum distribution function in the unprojected Hilbert space. Thus the quasi-particle weight, which is the jump in the momentum distribution function at the Fermi momentum, is $Z = g_{t\sigma}$. Fig. [2.14] shows $g_{t\sigma}$ vs Δ for $U = 20t$. In the metallic regime, that is, for $\Delta \sim 20t$, $g_{t\uparrow} = g_{t\downarrow} \ll 1$ which indicates that we actually have a *bad* metal, with very heavy quasi-particles, intervening between the two insulators. Note that

in the insulating regime $g_{t\sigma}$ does not carry the meaning of quasi-particle weight.

Magnetisation and staggered density: The staggered magnetization m, defined as $m = (m_A - m_B)/2$, calculated within the renormalized mean field theory is shown in Fig. [2.15]. For a given $U \gg t$, $m = 0$ for $\Delta > U$ but as Δ approaches U, the anti-ferromagnetic order sets in with a jump in m at Δ_c. As Δ decreases further, m increases approaching the saturation value. Note that for very small values of Δ where m might tend to unity, our approach does not work.

The staggered density difference $\delta = (n_A - n_B)/2$ is shown in the green curve in Fig. [2.15] as a function of Δ. As expected for $\Delta > U$, δ is large close to its saturation value and with decrease in Δ, δ reduces monotonically for $\Delta > \Delta_c$. At Δ_c, there occurs a change in slope $\frac{\partial \delta}{\partial \Delta}$. Note that within our approach the system can never attain the saturation values $m = 1$ and $\delta = 0$ at which the Gutzwiller factor for the spin exchange term g_s diverges and the perturbation theory fails.

Possible superconductivity in higher dimensions: Based on the renormalized Hamiltonian in Eq. (2.23) one can see that even at half filling for the overall lattice, there is a finite hopping between A and B sublattices in the projected space as long as the density difference δ is non-zero. This effectively gives a doped $t-J$ model for each sublattice even at half filling. Further there are finite effective next nearest neighbor hopping terms within each sublattice which appear through trimer terms in the Hamiltonian in Eq. (3.9). In this renormalized Hamiltonian there is a possibility that the metallic phase mentioned above can turn into a d-wave superconducting phase or $d + is$ pairing superconducting phase in higher dimensional system. The superconducting phase might survive for a larger range of $U - \Delta$ space compared to the metallic phase with support of trimer terms. This has been explored in the future chapters.

Non-monotonic behavior of Néel temperature with Δ: The renormalized Hamilto-

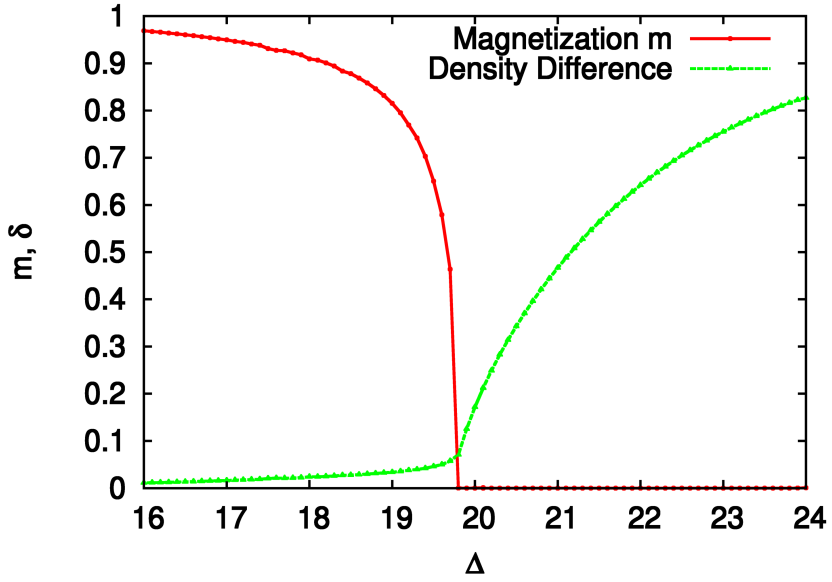

Figure 2.15: Staggered magnetisation m and staggered density δ vs Δ for $U = 20t$. At $\Delta_c \sim 19.8t$, m drops to zero with a discontinuity. At the same point a discontinuity is seen in the slope $\frac{\partial \delta}{\partial \Delta}$.

nian in Eq. (2.23) is illuminating enough to predict the behavior of the Néel temperature for the AFM order in the IHM in the large U and Δ regime at half-filling. For $U \gg t$ but $\Delta \sim t$, the IHM maps to the modified $t - J$ model with an additional ionic potential term and with the spin-exchange term given by $\tilde{J} = 4t^2U/(U^2 - \Delta^2)$ [7]. Note that in this limit doublons are projected out from the low energy Hilbert space from all sites. In this case the Néel temperature of the AFM order should obey $\tilde{J}$ and hence increase as Δ increases. In fact this was observed in DMFT+CTQMC calculation for the IHM at half filling [7] where it was shown that for U as high as $16t$, up to Δ little less than U, $T_N \sim \tilde{J}/4$ (Note that there is a difference in convention used for Δ term in the Hamiltonian in [7] and current Hamiltonian. The two are related by a factor of 2). But for $\Delta \geq U$ a sudden drop in T_N was observed which could not be explained based on the spin exchange coupling $\tilde{J}$.

Our current renormalized Hamiltonian sheds light on this non-monotonic behavior of

T_N since it is valid for the $U \sim \Delta$ as well as for the $\Delta > U$ regime. In this regime the coefficient of spin exchange term is $\tilde{\tilde{J}} = 2t^2/(U+\Delta)$ which decreases with increase in Δ. Hence for $U \gg t$, for small values of $\Delta \leq U$ T_N follows $\tilde{J}$ and hence T_N increases with Δ. As Δ increases further T_N starts to follow the new coupling $\tilde{\tilde{J}}$ and starts decreasing with increase in Δ.

To summarize, in the strongly correlated limit of the ionic Hubbard model, the interplay of U and Δ promises a rich phase diagram, and our formalism of the renormalized Hamiltonian obtained by Gutzwiller projection of holes on one sublattice and doublons on another sublattice, further implemented by the Gutzwiller approximation, is illuminating enough to give insight into this exotic physics.

2.4 Strongly Correlated Binary Alloys

In this section we will discuss the physics of hole projection in the context of the strongly correlated limit of binary alloys, modelled with the Hubbard model in the presence of a binary disorder. The Hamiltonian for this system is,

$$\mathcal{H} = -t \sum_{<ij>} c^{\dagger}_{i\sigma} c_{j\sigma} + U \sum_{i} n_{i\uparrow} n_{i\downarrow} - \sum_{i} (\mu - \epsilon_i) n_i, \tag{2.30}$$

where ϵ_i is the random onsite energy drawn from the probability distribution function,

$$p_{\epsilon}(\epsilon_i) = x\delta\left(\epsilon_i + \frac{V}{2}\right) + (1-x)\delta\left(\epsilon_i - \frac{V}{2}\right). \tag{2.31}$$

Here, x and $1-x$ are the fractions of the lattice sites with energies $-\frac{V}{2}$ and $\frac{V}{2}$ respectively. We label sites with $\epsilon(i) = -V/2$ as A sites and sites with $\epsilon(i) = V/2$ as B sites. At half-

filling, the above Hamiltonian is particle hole symmetric only if the percentages of A and B sites are equal.

Most of the earlier studies have solved this model using variants of DMFT in the weak to intermediate limit of U/t [88–91]. Using DMFT+QMC, this model has also been solved at finite temperature in the limit of sufficiently large U and V [90]. We are interested in the strongly correlated, strongly disordered limit of this model, that is, $U \sim V \gg t$. The single site energetics is similar to IHM, that is, holes are projected out from Hilbert space at A sites and doublons are projected out from Hilbert space at B sites. The difference here is that the hole projected sites and doublon projected sites are randomly distributed on the lattice in each disorder configuration. This makes all three type of nearest neighbor bonds possible: AA, BB and AB. Also in three site processes, as we will show later, there are many more hopping processes possible which do not occur for IHM. Every disorder configuration has a different combination of two site and three site hopping terms due to different environment of a site in each configuration.

2.4.1 Similarity transformation

The nearest neighbor hopping processes between two sites can be classified as follows depending upon which sites are involved in the hopping; AA sites, BB sites, or AB sites and whether the hopping process changes the number of doublons or not:

$$H_t{}^{AA} = H_t^+{}_{A\to A} + H_t^-{}_{A\to A} + H_t^0{}_{A\to A},$$

$$H_t{}^{BB} = H_t^+{}_{B\to B} + H_t^-{}_{B\to B} + H_t^0{}_{B\to B},$$

$$H_t{}^{AB} = H_t^+{}_{A\to B} + H_t^+{}_{B\to A} + H_t^-{}_{A\to B} + H_t^-{}_{B\to A} + H_t^0{}_{A\to B} + H_t^0{}_{B\to A}. \quad (2.32)$$

Since an A type site has doublons allowed in the low energy sectors and holes should be projected out while on B type sites the reverse happens, one needs to do different similarity transformations on the local Hamiltonian depending on whether the bond is AA type, BB type or AB type:

$$iS^{AA} = \frac{1}{U}(H_t^+{}_{A\to A} - H_t^-{}_{A\to A}),$$

$$iS^{BB} = \frac{1}{U}(H_t^+{}_{B\to B} - H_t^-{}_{B\to B}),$$

$$iS^{AB} = \frac{1}{U+V}(H_t^+{}_{A\to B} - H_t^-{}_{B\to A}) + \frac{1}{V}(H_t^0{}_{A\to B} - H_t^0{}_{B\to A}). \quad (2.33)$$

Note that S^{AA} and S^{BB} are perturbative in t/U while S^{AB} has term which are perturbative in $t/(U+V)$ or t/V.

If we consider the commutators of the type $[S^{\alpha\beta}, H_t^{\alpha\beta}]$ and $[S^{\alpha\beta}, [S^{\alpha\beta}, H_0^{\alpha\beta}]]$, we get terms connecting the low energy sector to the high energy sector which must be removed through suitable similarity transformation. The terms that do not interconnect the low energy sector and the high energy sector constitute the effective Hamiltonian. The effective Hamiltonian itself is a function of disorder configuration. In a disorder configuration, dimer

terms in H_{eff} depend on whether bonds are AA, BB or AB type:

$$\begin{aligned}\mathcal{H}_{eff} &= H_0 + H^0_{t\ A\to A} + H^0_{t\ B\to B} + H^+_{t\ B\to A} + H^-_{t\ A\to B} \\ &+\frac{1}{U}[H^+_{t\ A\to A}, H^-_{t\ A\to A}] + \frac{1}{U}[H^+_{t\ B\to B}, H^-_{t\ B\to B}] \\ &+\frac{1}{U+V}[H^+_{t\ A\to B}, H^-_{t\ B\to A}] + \frac{1}{V}[H^0_{t\ A\to B}, H^0_{t\ B\to A}] \\ &+\frac{1}{2}\left(\frac{1}{U}+\frac{1}{V}\right)\left([H^+_{t\ A\to A} + H^+_{t\ B\to B}, H^0_{t\ B\to A}]\right) \\ &-\frac{1}{2}\left(\frac{1}{U}+\frac{1}{V}\right)\left([H^-_{t\ A\to A} + H^-_{t\ B\to B}, H^0_{t\ A\to B}]\right). \end{aligned} \tag{2.34}$$

2.4.2 Effective Low energy Hamiltonian in terms of projected fermions

Now we represent the effective low energy Hamiltonian of Eq. (2.34) in terms of projected fermionic operators on A and B sites as defined in Eq. (2.15) and (2.16). Let us first consider the $\mathcal{O}(t)$ hopping terms which are confined in the low energy Hilbert space and are represented as,

$$\begin{aligned} H^{A_i,A_j}_{1,low} &= H^0_{tA\to A}(i,j) = -t\sum_\sigma [\tilde{c}^\dagger_{iA\sigma}\tilde{c}_{jA\sigma} + h.c.], \\ H^{B_i,B_j}_{1,low} &= H^0_{tB\to B}(i,j) = -t\sum_\sigma [\tilde{\tilde{c}}^\dagger_{iB\sigma}\tilde{\tilde{c}}_{jB\sigma} + h.c.], \\ H^{A_i,B_j}_{1,low} &= H^-_{tA\to B}(i,j) + H^+_{tB\to A}(i,j) = -t\sum_\sigma [\tilde{c}^\dagger_{iA\sigma}\tilde{\tilde{c}}_{jB\sigma} + h.c.]. \end{aligned} \tag{2.35}$$

Here, $H^0_{t\ A\to A}$ involves hopping of a doublon while $H^0_{t\ B\to B}$ involves hopping of a hole:

O(t^2/U) Dimer terms:

Now we consider $\mathcal{O}(t^2/U)$ dimer terms obtained from $\frac{1}{U}[H^+_{t\ \alpha\to\alpha}, H^-_{t\ \alpha\to\alpha}]$ terms with

$\alpha = A, B$. Let us first look at the AA term. $\frac{1}{U}[{H_t^+}_{A\to A}, {H_t^-}_{A\to A}] \sim -\frac{1}{U}{H_t^-}_{A\to A}{H_t^+}_{A\to A}$ since the first term in the commutator requires a hole to start with which lies in the high energy sector for A type sites. The dimer term corresponding to this commutator is,

$$H_{dimer}^{A_i,A_j} = -\frac{t^2}{U}\sum_{\sigma}[{X_{iA}}^{\sigma\leftarrow\sigma}{X_{jA}}^{\bar{\sigma}\leftarrow\bar{\sigma}} - {X_{iA}}^{\sigma\leftarrow\bar{\sigma}}{X_{jA}}^{\bar{\sigma}\leftarrow\sigma} + j \leftrightarrow i] \tag{2.36}$$

This in terms of projected operators can be expressed as,

$$\begin{aligned}&\frac{J}{2}\sum_{\sigma}[\tilde{c}_{iA\bar{\sigma}}\tilde{c}^{\dagger}_{iA\sigma}\tilde{c}_{jA\sigma}\tilde{c}^{\dagger}_{jA\bar{\sigma}} - \tilde{c}_{iA\bar{\sigma}}\tilde{c}^{\dagger}_{iA\bar{\sigma}}\tilde{c}_{jA\sigma}\tilde{c}^{\dagger}_{jA\sigma}]\\ &= J\mathcal{P}_h\bigg(S_{iA}.S_{jA} - \frac{(2-n_{iA})(2-n_{jA})}{4}\bigg)\mathcal{P}_h.\end{aligned} \tag{2.37}$$

with $J = 4t^2/U$. A factor of $4 = 2 \times 2$ comes from spin summation and from hoppings from i to j site first or vice versa. A similar analysis can be extended in the case of B sites. $\frac{1}{U}[{H_t^+}_{B\to B}, {H_t^-}_{B\to B}] \sim -\frac{1}{U}{H_t^-}_{B\to B}{H_t^+}_{B\to B}$ since the first term in the commutator requires a doublon to start with which lies in the high energy sector for B type sites. The dimer term corresponding to this commutator is,

$$H_{dimer}^{B_i,B_j} = -\frac{t^2}{U}\sum_{<ij>,\sigma}[{X_{iB}}^{\sigma\leftarrow\sigma}{X_{jB}}^{\bar{\sigma}\leftarrow\bar{\sigma}} - {X_{iB}}^{\sigma\leftarrow\bar{\sigma}}{X_{jB}}^{\bar{\sigma}\leftarrow\sigma} + j \leftrightarrow i] \tag{2.38}$$

Again, in terms of projected operators it is,

$$\begin{aligned}-\frac{J}{2}\sum_{\sigma}[\tilde{\tilde{c}}^{\dagger}_{iB\sigma}\tilde{\tilde{c}}_{iB\sigma}\tilde{\tilde{c}}^{\dagger}_{jB\bar{\sigma}}\tilde{\tilde{c}}_{jB\bar{\sigma}} - \tilde{\tilde{c}}^{\dagger}_{iB\sigma}\tilde{\tilde{c}}_{iB\bar{\sigma}}\tilde{\tilde{c}}^{\dagger}_{jB\bar{\sigma}}\tilde{\tilde{c}}_{jB\sigma}]\\ = J\mathcal{P}_d\bigg(S_{iB}.S_{jB} - \frac{n_{iB}n_{jB}}{4}\bigg)\mathcal{P}_d.\end{aligned} \tag{2.39}$$

There are also $t^2/(U+V)$ order terms obtained from hopping of a spin-1/2 from site A to B and back. In H_{eff} the corresponding term for this process is $\frac{1}{U+V}[H_t^+{}_{A\to B}, H_t^-{}_{B\to A}]$ which, as explained in the section on IHM, can be expressed as,

$$H_{dimer}^{A_i,B_j} = J_1[S_{iA}.S_{jB} - (2-\hat{n}_{iA})\hat{n}_{jB}/4], \tag{2.40}$$

with $J_1 = \frac{2t^2}{U+V}$. Note that all the above expressions are defined in projected Hilbert space.

The dimer term corresponding to $[H_t^0{}_{A\to B}, H_t^0{}_{B\to A}]$ involves hopping of a particle or a doublon from one site to the nearest neighbor site and back to the initial site as shown in Fig. [2.6]. This process is of order t^2/V and the corresponding expression is given in Eq. (2.20).

O(t^2/U) Trimer terms:

Since on each site there is possibility of having an A type site or B type site, in total there are 8 trimer terms possible arising from various commutators in H_{eff}. Trimer terms from the commutator involving only A type sites $\frac{1}{U}[H_t^+{}_{A\to A}, H_t^-{}_{A\to A}]$ involves hopping of a particle from the intermediate site resulting in the formation of a doublon in the nearest neighbor site and the other doublon unpairs in two ways : one in the spin preserving way, the other in the spin flip way, as shown in Fig. [2.16]. Eventually we get $H_{trimer}^{AAA}(i,j,k)$ as,

$$-\frac{t^2}{U}\sum_\sigma [X_{jA}^{\sigma\leftarrow 0}X_{kA}^{\bar\sigma\leftarrow d}X_{iA}^{d\leftarrow\bar\sigma}X_{jA}^{0\leftarrow\sigma} + h.c.] + \frac{t^2}{U}\sum_\sigma [X_{jA}^{\sigma\leftarrow 0}X_{kA}^{\bar\sigma\leftarrow d}X_{iA}^{d\leftarrow\sigma}X_{jA}^{0\leftarrow\bar\sigma} + h.c.]$$

$$= \frac{t^2}{U}\sum_\sigma [\tilde{c}_{iA\sigma}^\dagger \tilde{c}_{jA\bar\sigma}\tilde{c}_{jA\bar\sigma}^\dagger \tilde{c}_{kA\sigma} - \tilde{c}_{iA\bar\sigma}^\dagger \tilde{c}_{jA\bar\sigma}\tilde{c}_{jA\sigma}^\dagger \tilde{c}_{kA\sigma}] + h.c.$$

$$= \frac{t^2}{U}\sum_\sigma \mathcal{P}_h[c_{iA\sigma}^\dagger(1-\hat{n}_{jA\bar\sigma})c_{kA\sigma} + c_{iA\bar\sigma}^\dagger c_{jA\sigma}^\dagger c_{jA\bar\sigma}c_{kA\sigma} + h.c.]\mathcal{P}_h. \tag{2.41}$$

A similar trimer term on BBB sites is obtained from $\frac{1}{U}[{H_t^+}_{B\to B}, {H_t^-}_{B\to B}]$. In the BBB

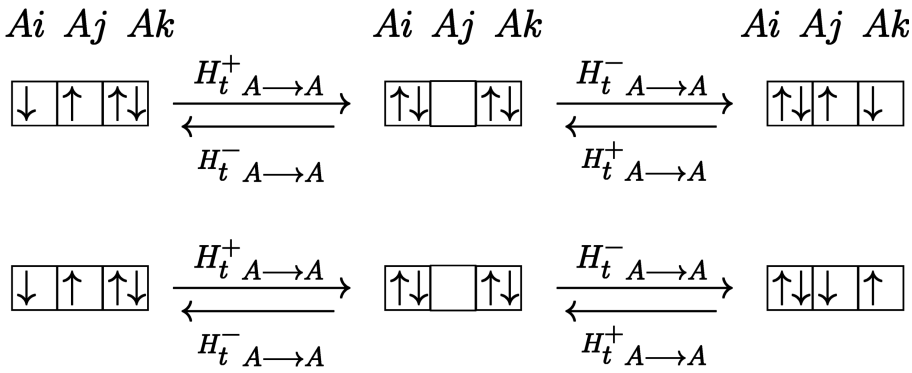

Figure 2.16: Trimer term on AAA sites for correlated binary alloy model.

trimer terms, the effective next nearest neighbor hopping of hole takes place just as in AAA terms it is the effective next nearest neighbor hopping of a doublon which takes place. The corresponding trimer term can be expressed as H_{trimer}^{BBB}

$$= -\frac{t^2}{U}\sum_\sigma [X_{iB}^{\sigma\leftarrow 0}X_{jB}^{\bar\sigma\leftarrow d}X_{jB}^{d\leftarrow\bar\sigma}X_{kB}^{0\leftarrow\sigma} + h.c.] + \frac{t^2}{U}\sum_\sigma [X_{iB}^{\bar\sigma\leftarrow 0}X_{jB}^{\sigma\leftarrow d}X_{jB}^{d\leftarrow\bar\sigma}X_{kB}^{0\leftarrow\sigma} + h.c.]$$

$$= -\frac{t^2}{U}\sum_\sigma [\tilde{\tilde{c}}_{iB\sigma}^\dagger \tilde{\tilde{c}}_{jB\bar\sigma}^\dagger \tilde{\tilde{c}}_{jB\bar\sigma}\tilde{\tilde{c}}_{kB\sigma} - \tilde{\tilde{c}}_{iB\bar\sigma}^\dagger \tilde{\tilde{c}}_{jB\sigma}^\dagger \tilde{\tilde{c}}_{jB\bar\sigma}\tilde{\tilde{c}}_{kB\sigma}]$$

$$= -\frac{t^2}{U}\sum_\sigma \mathcal{P}_d(c_{iB\sigma}^\dagger n_{jB\bar\sigma}c_{kB\sigma} - c_{iB\bar\sigma}^\dagger c_{jB\sigma}^\dagger c_{jB\bar\sigma}c_{kB\sigma} + h.c.)\mathcal{P}_d. \tag{2.42}$$

Then there are ABA and BAB type trimer terms, which are of order t^2/V. Note that similar terms also appeared in IHM and are represented in Fig. [2.7] and Fig. [2.8]. Below we summarize their forms for the case of the binary alloy model,

$$H_{trimer}^{Ai,Bj,Ak} = -\frac{t^2}{V}\sum_\sigma \mathcal{P}(c_{kA\sigma}^\dagger [n_{jB\bar\sigma}c_{iA\sigma} - c_{iA\bar\sigma}c_{jB\bar\sigma}^\dagger c_{jB\sigma}])\mathcal{P}, \tag{2.43}$$

$$H_{trimer}^{Bi,Aj,Bk} = -\frac{t^2}{V}\sum_{\sigma}\mathcal{P}(c_{kB\sigma}[(1-n_{iA\bar{\sigma}})c_{jB\sigma}^{\dagger} + c_{iA\sigma}^{\dagger}c_{iA\bar{\sigma}}c_{jB\bar{\sigma}}^{\dagger}])\mathcal{P}. \tag{2.44}$$

AAB and BBA trimer terms:

Next we consider the remaining trimer terms, namely, $AAB(or BAA)$ and BBA(or ABB) type terms. We would like to emphasize that these terms never appear in strongly correlated limit of IHM presented in earlier section and are characteristic of random arrangement of A and B type sites in the binary alloy model.

The AAB trimer terms, shown in Fig. [2.17], arise from the commutator $\frac{(U+V)}{2UV}[H_{t\ A\to A}^{+}, H_{t\ B\to A}^{0}] \sim -\frac{K}{t^2}H_{t\ B\to A}^{0}H_{t\ A\to A}^{+}$ where we have defined the coupling strength for this term $K = \frac{t^2(U+V)}{2UV}$. This is because the first term of the commutator requires a hole at the intermediate A site to begin with which is energetically unfavourable. As shown in Fig. [2.17], this consists of the usual spin preserving and spin flip terms. In one case, the spin at the intermediate site remains the same as the initial state and in the other case it flips.

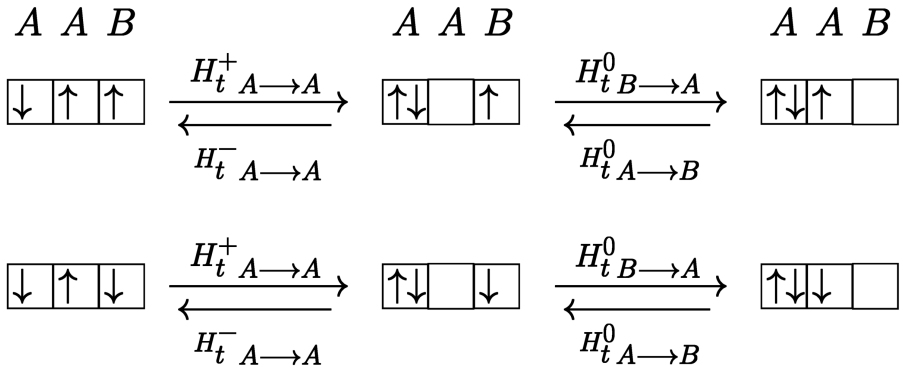

Figure 2.17: AAB trimer processes for correlated binary alloy model.

The fermionic representation of these terms $H_{trimer}^{A_i,A_k,B_j}$ is as follows,

$$-K\sum_{\sigma}\eta(\sigma)[X_{kA}^{\sigma\leftarrow 0}X_{jB}^{0\leftarrow\sigma}X_{iA}^{d\leftarrow\bar{\sigma}}X_{kA}^{0\leftarrow\sigma} + X_{kA}^{\bar{\sigma}\leftarrow 0}X_{jB}^{0\leftarrow\bar{\sigma}}X_{iA}^{d\leftarrow\bar{\sigma}}X_{kA}^{0\leftarrow\sigma}]$$

$$= K \sum_{\sigma} (\tilde{c}^{\dagger}_{iA\sigma} \tilde{c}_{kA\bar{\sigma}} \tilde{c}^{\dagger}_{kA\bar{\sigma}} \tilde{\tilde{c}}_{jB\sigma} - \tilde{c}^{\dagger}_{iA\sigma} \tilde{c}_{kA\sigma} \tilde{c}^{\dagger}_{kA\bar{\sigma}} \tilde{\tilde{c}}_{jB\bar{\sigma}})$$

$$= K \sum_{\sigma} \mathcal{P}(c^{\dagger}_{iA\sigma}(1 - n_{kA\bar{\sigma}}) c_{jB\sigma} + c^{\dagger}_{iA\sigma} c^{\dagger}_{kA\bar{\sigma}} c_{kA\sigma} c_{jB\bar{\sigma}}) \mathcal{P}. \tag{2.45}$$

Similarly, the BBA trimer terms appear from the commutator $\frac{K}{t^2}[{H_t^+}_{B\to B}, {H_t^0}_{B\to A}] \sim -\frac{K}{t^2} {H_t^0}_{B\to A} {H_t^+}_{B\to B}$. The first term in the commutator requires a doublon at the intermediate site B to start with which is energetically unfavourable. As shown in Fig. [2.18], these terms also come in two variants, spin preserving and spin flip at the intermediate site.

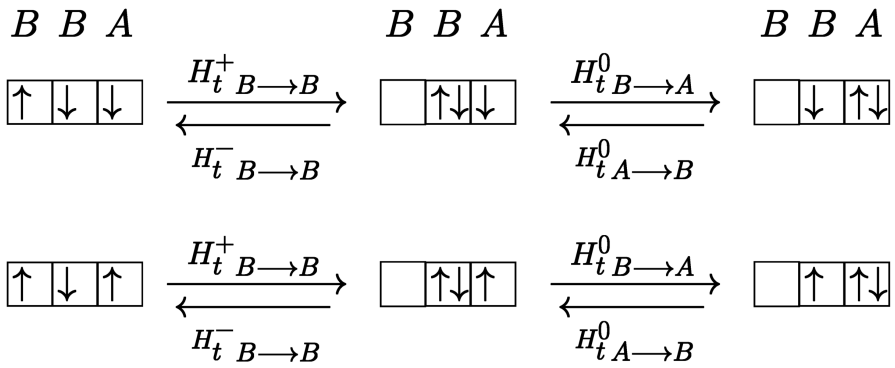

Figure 2.18: BBA trimer processes for correlated binary alloy model.

Below we represent $H_{trimer}^{B_j,B_l,A_i}$ in terms of X operators and then in terms of projected operators as,

$$-K \sum_{\sigma} \eta(\sigma) [X_{iA}^{d\leftarrow\bar{\sigma}} X_{lB}^{\bar{\sigma}\leftarrow d} X_{lB}^{d\leftarrow\bar{\sigma}} X_{jB}^{0\leftarrow\sigma} + X_{iA}^{d\leftarrow\sigma} X_{lB}^{\sigma\leftarrow d} X_{lB}^{d\leftarrow\bar{\sigma}} X_{jB}^{0\leftarrow\sigma}]$$

$$= -K \sum_{\sigma} (\tilde{c}^{\dagger}_{iA\sigma} \tilde{\tilde{c}}^{\dagger}_{lB\bar{\sigma}} \tilde{\tilde{c}}_{lB\bar{\sigma}} \tilde{\tilde{c}}_{jB\sigma} - \tilde{c}^{\dagger}_{iA\sigma} \tilde{\tilde{c}}^{\dagger}_{lB\bar{\sigma}} \tilde{\tilde{c}}_{lB\sigma} \tilde{\tilde{c}}_{jB\bar{\sigma}})$$

$$= -K \sum_{\sigma} \mathcal{P}(c^{\dagger}_{iA\sigma} n_{lB\bar{\sigma}} c_{jB\sigma} - c^{\dagger}_{iA\sigma} c^{\dagger}_{lB\bar{\sigma}} c_{lB\sigma} c_{jB\bar{\sigma}}) \mathcal{P}. \tag{2.46}$$

The terms from the commutators $[{H_t^-}_{A\to A}, {H_t^0}_{A\to B}]$ and $[{H_t^-}_{B\to B}, {H_t^0}_{A\to B}]$ are the hermitian conjugate terms of the trimer terms in Eq. (2.45) and (2.46) and are represented by

the lower arrows in Fig. [2.17] and [2.18].

2.4.3 Gutzwiller Approximation

After finding various terms in the low energy effective Hamiltonian for the strongly correlated binary disorder model, we will now evaluate Gutzwiller factors for various terms in H_{eff} of Eq. (2.34). The low energy effective Hamiltonian for binary alloys consists of certain dimer and trimer terms and for some of these terms we have already found the Gutzwiller factors in the section on IHM. However here, unlike in IHM, the densities on A or B sites are not homogeneous. They are site dependent and depends on the local environment. Let us first consider the hopping process of $O(t)$ between two neighboring sites. Within the Gutzwiller approximation,

$$H_{1,low}^{A_i,A_j} = -t\sum_\sigma \mathcal{P}_h[c_{iA\sigma}^\dagger c_{jA\sigma} + h.c.]\mathcal{P}_h = -t\sum_\sigma g_{t\sigma}^{AA}(i,j)[c_{iA\sigma}^\dagger c_{jA\sigma} + h.c.],$$

$$H_{1,low}^{B_i,B_j} = -t\sum_\sigma \mathcal{P}_d[c_{iB\sigma}^\dagger c_{jB\sigma} + h.c.]\mathcal{P}_d = -t\sum_\sigma g_{t\sigma}^{BB}(i,j)[c_{iB\sigma}^\dagger c_{jB\sigma} + h.c.], \quad (2.47)$$

$$H_{1,low}^{A_i,B_j} = -t\sum_\sigma \mathcal{P}[c_{iA\sigma}^\dagger c_{jB\sigma} + h.c.]\mathcal{P} = -t\sum_\sigma g_{t\sigma}^{AB}(i,j)[c_{iA\sigma}^\dagger c_{jB\sigma} + h.c.].$$

As explained for AB terms in the section on IHM, one can evaluate these Gutzwiller factors by evaluating probability for hopping process on corresponding bonds within the projected and unprojected Hilbert space. By doing an exercise similar to the one explained in the section on IHM, we obtain,

$$g_{t\sigma}^{AA}(i,j) = \sqrt{\frac{(\mathbf{n}_{iA}-1)(\mathbf{n}_{jA}-1)}{\mathbf{n}_{iA\sigma}\mathbf{n}_{jA\sigma}}},$$

$$g_{t\sigma}^{BB}(i,j) = \sqrt{\frac{(1-\mathbf{n}_{iB})(1-\mathbf{n}_{jB})}{(1-\mathbf{n}_{iB\sigma})(1-\mathbf{n}_{jB\sigma})}}, \tag{2.48}$$
$$g_{t\sigma}^{AB}(i,j) = \sqrt{\frac{(\mathbf{n}_{iA}-1)(1-\mathbf{n}_{jB})}{\mathbf{n}_{iA\sigma}(1-\mathbf{n}_{jB\sigma})}}.$$

Next let us consider the renormalization of $O(t^2/U)$ or $O(t^2/U+V)$ dimer terms which are also of three type depending upon the bond under consideration in a given disorder configuration. Within the Gutzwiller approximation, couplings in Eq. (2.37), (2.39) and (2.40) get rescaled with the corresponding Gutzwiller factors to give,

$$\begin{aligned} H_{dimer}^{A_i,A_j} &= Jg_s^{AA}(i,j)\left(S_{iA}.S_{jA} - \frac{(2-n_{iA})(2-n_{jA})}{4}\right), \\ H_{dimer}^{B_i,B_j} &= Jg_s^{BB}(i,j)\left(S_{iB}.S_{jB} - \frac{n_{iB}n_{jB}}{4}\right), \\ H_{dimer}^{A_i,B_j} &= J_1 g_s^{AB}(i,j)\left(S_{iA}.S_{jB} - \frac{(2-n_{iA})n_{jB}}{4}\right). \end{aligned} \tag{2.49}$$

The corresponding Gutzwiller factors are obtained, as explained for an AB term in the section on IHM, to be,

$$\begin{aligned} g_s^{AA}(i,j) &= \frac{1}{\sqrt{\mathbf{n}_{iA\uparrow}\mathbf{n}_{iA\downarrow}\mathbf{n}_{jA\uparrow}\mathbf{n}_{jA\downarrow}}}, \\ g_s^{BB}(i,j) &= \frac{1}{\sqrt{(1-\mathbf{n}_{iB\uparrow})(1-\mathbf{n}_{iB\downarrow})(1-\mathbf{n}_{jB\uparrow})(1-\mathbf{n}_{jB\downarrow})}}, \\ g_s^{AB}(i,j) &= \frac{1}{\sqrt{\mathbf{n}_{iA\uparrow}\mathbf{n}_{iA\downarrow}(1-\mathbf{n}_{jB\uparrow})(1-\mathbf{n}_{jB\downarrow})}}. \end{aligned} \tag{2.50}$$

In the calculation of Gutzwiller factors for the trimer terms, the intermediate step is unimportant, only the initial and final states are used to calculate the probabilities. The

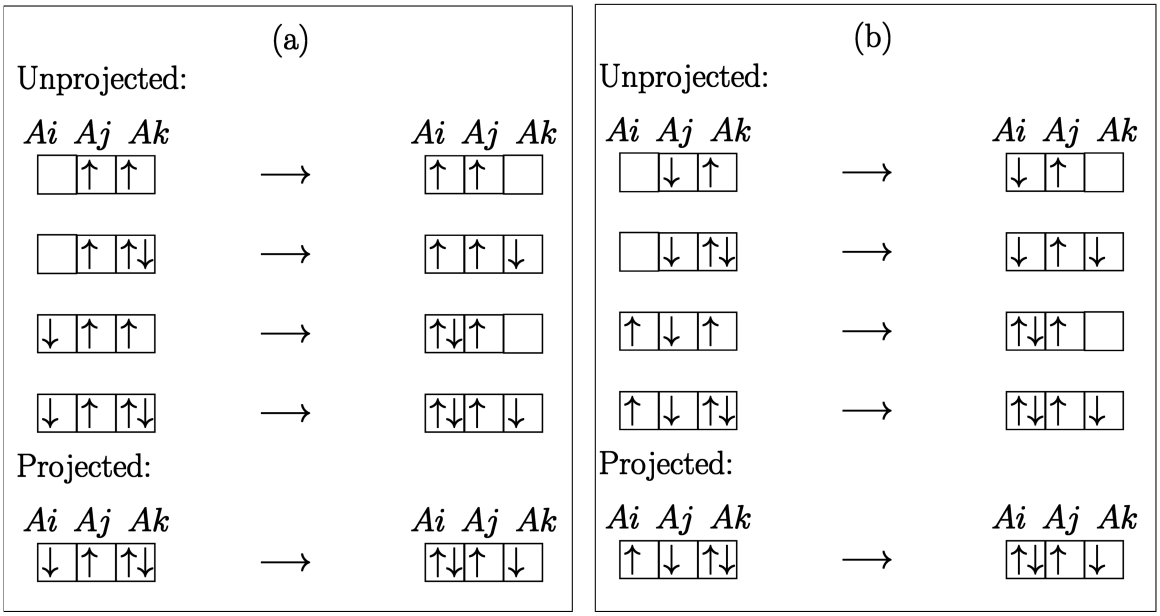

Figure 2.19: Processes involved in the calculation of $g_{1\sigma}$ and $g_{2\sigma}$ which are renormalization Gutzwiller factors for AAA trimer terms.

renormalized form of the AAA trimer term which is written in Eq. (2.41) is given below,

$$H_{trimer}^{A_i,A_j,A_k} = \frac{t^2}{U}\sum_{\sigma}(g_{1\sigma}^{AAA}(i,j,k)c_{iA\sigma}^{\dagger}(1-n_{jA\bar{\sigma}})c_{kA\sigma} + g_{2\sigma}^{AAA}(i,j,k)c_{iA\bar{\sigma}}^{\dagger}c_{jA\sigma}^{\dagger}c_{jA\bar{\sigma}}c_{kA\sigma} + h.c.). \tag{2.51}$$

The processes in projected and unprojected spaces for the calculation of $g_{1\uparrow}$ are shown in Fig. [2.19(a)]. The probability of the process in the unprojected basis is $(1-\mathbf{n}_{iA\uparrow})\mathbf{n}_{iA\uparrow}(1-\mathbf{n}_{jA\downarrow})^2\mathbf{n}_{kA\uparrow}(1-\mathbf{n}_{kA\uparrow})$ and in the projected basis it is $(\mathbf{n}_{iA}-1)(1-\mathbf{n}_{iA\uparrow})(1-\mathbf{n}_{jA\downarrow})^2(\mathbf{n}_{kA}-1)(1-\mathbf{n}_{kA\uparrow})$. The Gutzwiller factor then comes out to be,

$$g_{1\uparrow}^{AAA}(i,j,k) = \sqrt{\frac{(\mathbf{n}_{iA}-1)(\mathbf{n}_{kA}-1)}{\mathbf{n}_{iA\uparrow}\mathbf{n}_{kA\uparrow}}}. \tag{2.52}$$

In Fig. [2.19(b)], the processes in unprojected and projected spaces required for the cal-

culation of $g_{2\sigma}$ are shown for which the total probability in the unprojected basis is $(1-\mathbf{n}_{iA\downarrow})\mathbf{n}_{jA\downarrow}(1-\mathbf{n}_{jA\uparrow})\mathbf{n}_{kA\uparrow}(1-\mathbf{n}_{kA\uparrow})\mathbf{n}_{jA\uparrow}(1-\mathbf{n}_{jA\downarrow})\mathbf{n}_{iA\downarrow}$ and in the projected basis is $(1-\mathbf{n}_{iA\downarrow})(1-\mathbf{n}_{jA\uparrow})(\mathbf{n}_{kA}-1)(1-\mathbf{n}_{kA\uparrow})(1-\mathbf{n}_{jA\downarrow})(\mathbf{n}_{iA}-1)$. The Gutzwiller factor then comes out to be,

$$g_{2\sigma}^{AAA}(i,j,k)=\sqrt{\frac{(\mathbf{n}_{kA}-1)(\mathbf{n}_{iA}-1)}{\mathbf{n}_{jA\uparrow}\mathbf{n}_{jA\downarrow}\mathbf{n}_{kA\sigma}\mathbf{n}_{iA\bar{\sigma}}}}. \tag{2.53}$$

Similarly, the BBB trimer terms of Eq. (2.42) can be obtained by replacing $\mathbf{n}_{A\sigma}$ with $(1-\mathbf{n}_{B\sigma})$ and $(\mathbf{n}_A-1)$ with $(1-\mathbf{n}_B)$ in the above two equations.

Now we consider the trimer terms of ABA and BAB types for which we also calculated the Gutzwiller factors in the section on IHM. The renormalized form of these terms under the Gutzwiller approximation is,

$$H_{trimer}^{Ai,Bj,Ak}=-\frac{t^2}{V}\sum_{\sigma}c_{kA\sigma}^{\dagger}[g_{1\sigma}^{ABA}(i,j,k)n_{jB\bar{\sigma}}c_{iA\sigma}-g_{2\sigma}^{ABA}(i,j,k)c_{iA\bar{\sigma}}c_{jB\bar{\sigma}}^{\dagger}c_{jB\sigma}], \tag{2.54}$$

$$H_{trimer}^{Bj,Ai,Bl}=-\frac{t^2}{V}\sum_{\sigma}c_{lB\sigma}[g_{1\sigma}^{BAB}(j,i,l)(1-n_{iA\bar{\sigma}})c_{jB\sigma}^{\dagger}+g_{2\sigma}^{BAB}(j,i,l)c_{iA\sigma}^{\dagger}c_{iA\bar{\sigma}}c_{jB\bar{\sigma}}^{\dagger}] \tag{2.55}$$

Now we will calculate Gutzwiller factors for these trimer terms shown in Fig.[2.7] and Fig. [2.8]. Fig.[2.10(a)] shows hopping of an $\uparrow$ electron from an A site to its next nearest neighbor A sites with a spin ($\downarrow$) on the intermediate B site being preserved. In the unprojected basis, the probability for this process to happen is $\mathbf{n}_{iA\uparrow}\mathbf{n}_{jB\downarrow}^2(1-\mathbf{n}_{kA\uparrow})(1-\mathbf{n}_{iA\uparrow})\mathbf{n}_{kA\uparrow}$. It is to be noted that processes with either a down type particle or a doublon at the intermediate B site have been considered in the unprojected space. Like wise, the probability for the process to happen in the projected basis is $(\mathbf{n}_{iA}-1)(1-\mathbf{n}_{kA\uparrow})\mathbf{n}_{jB\downarrow}^2(\mathbf{n}_{kA}-1)(1-\mathbf{n}_{iA\uparrow})$.

Therefore, the Gutzwiller factor for this process is,

$$g_{1\uparrow}^{ABA}(i,j,k) = \sqrt{\frac{(\mathbf{n}_{iA}-1)(\mathbf{n}_{kA}-1)}{\mathbf{n}_{iA\uparrow}\mathbf{n}_{kA\uparrow}}}. \tag{2.56}$$

Fig. [2.10(b)] depicts hopping processes on A sublattice in which spin on the intermediate B site gets flipped. The probability in the unprojected basis for this process to occur is $\mathbf{n}_{iA\downarrow}\mathbf{n}_{jB\uparrow}(1-\mathbf{n}_{jB\downarrow})(1-\mathbf{n}_{kA\uparrow})(1-\mathbf{n}_{iA\downarrow})\mathbf{n}_{jB\downarrow}(1-\mathbf{n}_{jB\uparrow})\mathbf{n}_{kA\uparrow}$ where as that in the projected basis is $(\mathbf{n}_{iA}-1)\mathbf{n}_{jB\uparrow}(1-\mathbf{n}_{kA\uparrow})(1-\mathbf{n}_{iA\downarrow})\mathbf{n}_{jB\downarrow}(\mathbf{n}_{kA}-1)$ resulting in the Gutzwiller factor,

$$g_{2\sigma}^{ABA}(i,j,k) = \sqrt{\frac{(\mathbf{n}_{iA}-1)(\mathbf{n}_{kA}-1)}{\mathbf{n}_{iA\bar{\sigma}}\mathbf{n}_{kA\sigma}(1-\mathbf{n}_{jB\uparrow})(1-\mathbf{n}_{jB\downarrow})}}. \tag{2.57}$$

Similarly, we can obtain the Gutzwiller factors $g_{1\sigma}^{BAB}(j,i,l)$ and $g_{2\sigma}^{BAB}(j,i,l)$ from above two equations by replacing $\mathbf{n}_{A\sigma}$ with $(1-\mathbf{n}_{B\sigma})$ and $(\mathbf{n}_A-1)$ with $(1-\mathbf{n}_B)$.

Now we will focus on the Gutzwiller factors of the new trimer terms which arise out of the AAB and BBA processes. The renormalized AAB and BBA trimer terms can be expressed as,

$$\begin{aligned} H_{trimer}^{A_i,A_k,B_j} &= K\sum_{\sigma}(g_{1\sigma}^{AAB}(i,k,j)c_{iA\sigma}^{\dagger}(1-n_{kA\bar{\sigma}})c_{jB\sigma}, + g_{2\sigma}^{AAB}(i,k,j)c_{iA\sigma}^{\dagger}c_{kA\bar{\sigma}}^{\dagger}c_{kA\sigma}c_{jB\bar{\sigma}}), \\ H_{trimer}^{B_j,B_l,A_i} &= -K\sum_{\sigma}(g_{1\sigma}^{BBA}(j,l,i)c_{iA\sigma}^{\dagger}n_{lB\bar{\sigma}}c_{jB\sigma} - g_{2\sigma}^{BBA}(j,l,i)c_{iA\sigma}^{\dagger}c_{lB\bar{\sigma}}^{\dagger}c_{lB\sigma}c_{jB\bar{\sigma}}). \end{aligned} \tag{2.58}$$

The AAB and BBA spin preserving hopping as depicted in Fig. [2.20(a)] and [2.21(a)] are effective next nearest neighbor hopping processes, the Gutzwiller factors for which are like nearest neighbor AB hopping. If we look at Fig. [2.20(a)] for the processes involved in the calculation of the Gutzwiller factor $g_{1\uparrow}^{AAB}$, we see that the probability of the process in the

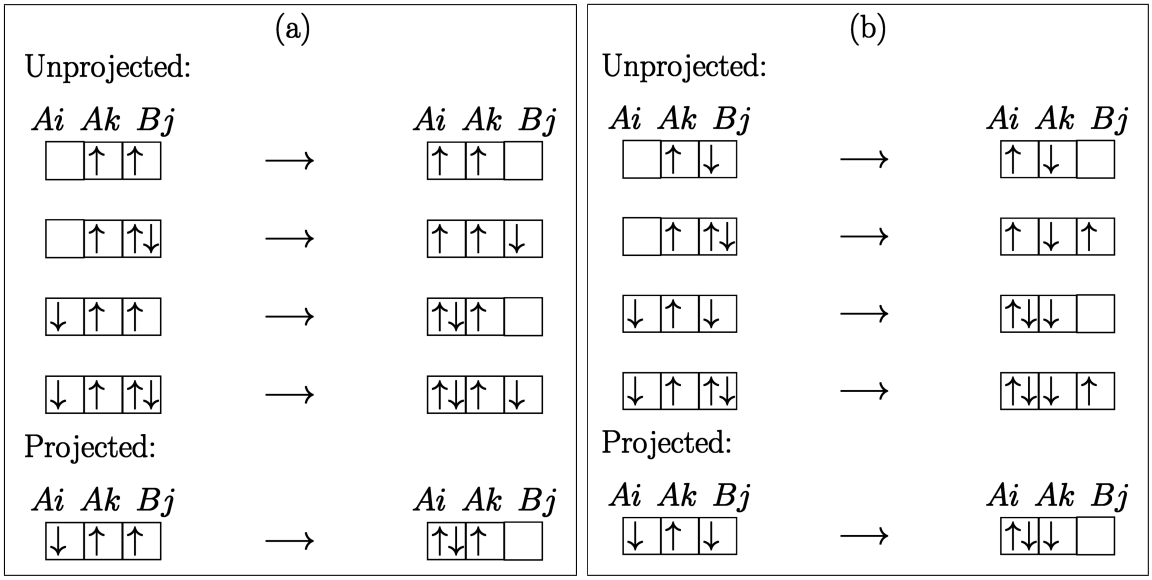

Figure 2.20: (a) Processes involved in the calculation of $g_{1\sigma}^{AAB}$. Similar AAB physical processes with hole at intermediate A site in the unprojected basis are considered in the calculation. (b) Processes involved in calculation of $g_{2\sigma}^{AAB}$.

unprojected basis is $(1-\mathbf{n}_{iA\uparrow})\mathbf{n}_{iA\uparrow}(1-\mathbf{n}_{kA\downarrow})^2(1-\mathbf{n}_{jB\uparrow})\mathbf{n}_{jB\uparrow}$ and in the projected basis it is $(1-\mathbf{n}_{iA\uparrow})(\mathbf{n}_{iA}-1)(1-\mathbf{n}_{kA\downarrow})^2\mathbf{n}_{jB\uparrow}(1-\mathbf{n}_{jB})$ resulting in the Gutzwiller factor,

$$g_{1\uparrow}^{AAB}(i,k,j)=\sqrt{\frac{(\mathbf{n}_{iA}-1)(1-\mathbf{n}_{jB})}{\mathbf{n}_{iA\uparrow}(1-\mathbf{n}_{jB\uparrow})}}. \tag{2.59}$$

It is to be remembered that in the unprojected basis, processes with either up spin or hole at the intermediate A site have been considered. In Fig. [2.21(a)], processes involved in the calculation of $g_{1\uparrow}^{BBA}$ has been depicted. The probability of the process in the unprojected basis is $(1-\mathbf{n}_{iA\uparrow})\mathbf{n}_{iA\uparrow}\mathbf{n}_{lB\downarrow}^2(1-\mathbf{n}_{jB\uparrow})\mathbf{n}_{jB\uparrow}$ and in the projected basis is $(1-\mathbf{n}_{iA\uparrow})(\mathbf{n}_{iA}-1)\mathbf{n}_{lB\downarrow}^2(1-\mathbf{n}_{jB})n_{jB\uparrow}$. Then, the Gutzwiller factor is,

$$g_{1\uparrow}^{BBA}(j,l,i)=\sqrt{\frac{(\mathbf{n}_{iA}-1)(1-\mathbf{n}_{jB})}{\mathbf{n}_{iA\uparrow}(1-\mathbf{n}_{jB\uparrow})}}, \tag{2.60}$$

which is the same as $g^{AAB}_{1\uparrow}(i,k,j)$. The Gutzwiller factors for spin flip terms depicted in

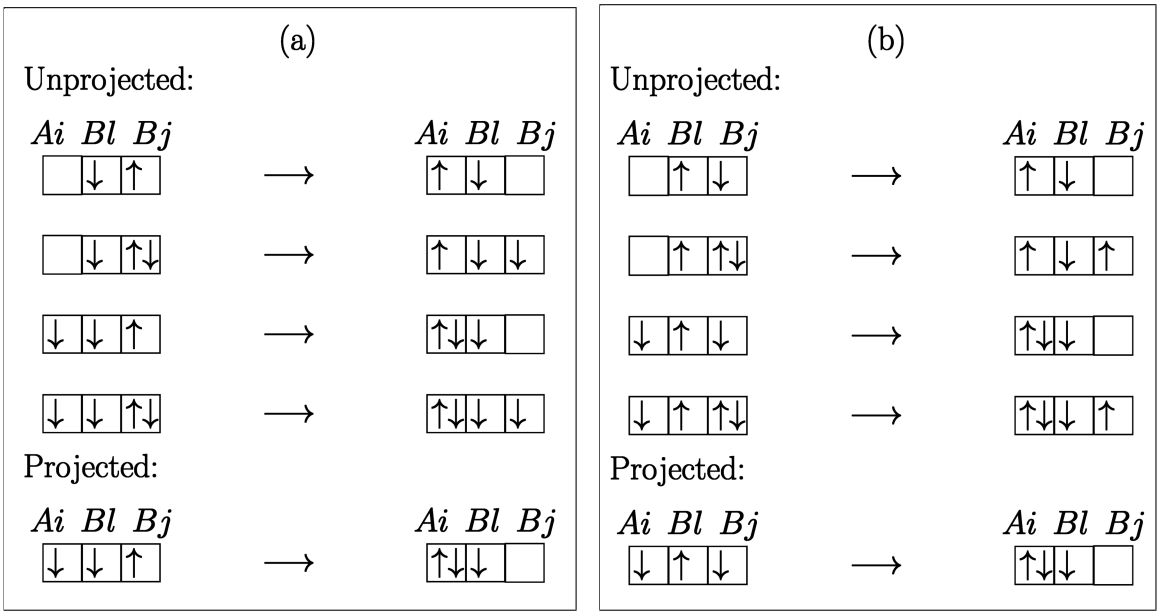

Figure 2.21: (a) Processes involved in the calculation of $g^{BBA}_{1\sigma}$. Similar BBA physical processes with doublon at intermediate B site in the unprojected basis are considered in the calculation. (b) Processes involved in calculation of $g^{BBA}_{2\sigma}$.

Fig. [2.20(b)] and [2.21(b)] can be found out similarly. For $g^{AAB}_{2\uparrow}(i,k,j)$, the probability in the unprojected space is $(1-\mathbf{n}_{iA\uparrow})\mathbf{n}_{iA\uparrow}(1-\mathbf{n}_{kA\uparrow})(1-\mathbf{n}_{kA\downarrow})\mathbf{n}_{kA\uparrow}\mathbf{n}_{kA\downarrow}\mathbf{n}_{jB\downarrow}(1-\mathbf{n}_{jB\downarrow})$ and in the projected space is $(1-\mathbf{n}_{iA\uparrow})(\mathbf{n}_{iA}-1)(1-\mathbf{n}_{kA\uparrow})(1-\mathbf{n}_{kA\downarrow})\mathbf{n}_{jB\downarrow}(1-\mathbf{n}_{jB})$ resulting in the Gutzwiller factor,

$$g^{AAB}_{2\uparrow}(i,k,j)=\sqrt{\frac{(\mathbf{n}_{iA}-1)(1-\mathbf{n}_{jB})}{\mathbf{n}_{kA\uparrow}\mathbf{n}_{kA\downarrow}\mathbf{n}_{iA\uparrow}(1-\mathbf{n}_{jB\downarrow})}}. \tag{2.61}$$

For $g^{BBA}_{2\uparrow}(j,l,i)$, the probability in the unprojected space is $(1-\mathbf{n}_{iA\uparrow})\mathbf{n}_{iA\uparrow}\mathbf{n}_{lB\uparrow}\mathbf{n}_{lB\downarrow}(1-\mathbf{n}_{lB\uparrow})(1-\mathbf{n}_{lB\downarrow})\mathbf{n}_{jB\downarrow}(1-\mathbf{n}_{jB\downarrow})$ and that in the projected space is $(1-\mathbf{n}_{iA\uparrow})(\mathbf{n}_{iA}-1)\mathbf{n}_{lB\uparrow}\mathbf{n}_{lB\downarrow}\mathbf{n}_{jB\downarrow}(1-$

$\mathbf{n}_{jB}$) leading to the Gutzwiller factor,

$$g_{2\uparrow}^{BBA}(j,l,i) = \sqrt{\frac{(\mathbf{n}_{iA}-1)(1-\mathbf{n}_{jB})}{(1-\mathbf{n}_{lB\uparrow})(1-\mathbf{n}_{lB\downarrow})\mathbf{n}_{iA\uparrow}(1-\mathbf{n}_{jB\downarrow})}}. \tag{2.62}$$

2.4.4 Insights into correlated binary alloy from the renormalized Hamiltonian

The renormalized Hamiltonian derived above brings deep insight towards the possible phase diagram of the strongly correlated binary alloy. Let us first focus at the projected hopping terms given in Eq. (2.47) and the corresponding Gutzwiller factors in Eq. (2.48). At half-filling for $U \gg t$, if the disorder is weak, the system will be an antiferromagnetic Mott insulator because the hopping term is completely projected out. As disorder increases and becomes comparable to U, the local particle density does not remain close to one on all the sites and the Gutzwiller factors $g_{t\sigma}^{\alpha\beta}$ for various hopping processes become finite resulting in finite kinetic energy of the electrons. Also the Mott gap reduces with increase in V. This indicates the possibility of a metallic phase in the system for $V \sim U$. This is consistent with what has been shown within DMFT + coherent potential approximation [99]. In the metallic phase, the quasiparticle weight will be given by the most probable value of the Gutzwiller factors for hopping terms (in Eq. (2.48)). Since $V \sim U$, the local electron densities will not deviate much from unity. Hence the Gutzwiller factors $g_{t\sigma}^{\alpha\beta}$ are very small resulting in very small quasiparticle weight in the metallic phase.

Let us now turn our attention to the spin exchange terms in the low energy Hamiltonian. For the parameter regime $V \sim U \gg t$, since the effective hopping in the projected Hilbert space becomes finite, and the electron density on each site is not one, spin exchange terms

might give rise to disordered superconductivity with either d wave pairing or $d+is$ pairing. Due to the presence of large binary disorder, we might get a disordered superconducting phase coexisting with an incommensurate/dis-commensurate charge density wave which is a topic of great interest in context of high T_c superconductors [100, 101].

2.5 Conclusions

In this chapter, we have extended the idea of inhomogeneous Gutzwiller projection for excluding holes from the low energy Hilbert space from some sites while projecting out doublons from the other sites of the lattice, which so far has been developed only for exclusion of doublons, e.g., in context of the hole doped $t-J$ model. We have discussed variants of the Hubbard model with large onsite potentials because of which, in the limit of strong correlations and comparable potential terms, on some sites doublons are projected out from low energy Hilbert space while from some other sites holes are projected out from the low energy Hilbert space. In order to understand the physics of these systems, it becomes essential to understand how to carry out Gutzwiller projection for holes. We defined new fermionic operators in the case of hole projected Hilbert space and derived effective low energy Hamiltonian for these models by carrying out systematic similarity transformation. We further carried out rescaling of couplings in the effective Hamiltonian using the Gutzwiller approximation to implement the effect of site dependent projection of holes and doublons. To be specific, we provided details of the similarity transformation and Gutzwiller approximation for IHM and Hubbard model with binary disorder.

The effective low energy Hamiltonian derived in both the cases shines light on the possibility of exotic phases. In the half filled IHM, our renormalized Hamiltonian predicts a half-metal phase followed up by a metal with increase in Δ for $U \sim \Delta$ and a superconduct-

ing phase for higher dimensional ($d \geq 2$) systems. Our effective Hamiltonian also explains the non-monotonic behavior of the Néel temperature as a function of Δ in the AFM phase of the IHM realized for $U \gg t$. In the correlated binary alloy model, for both disorder and e-e interactions being much larger than the hopping amplitude ($V \sim U \gg t$), there is a possible metallic phase which might turn into a very narrow disordered superconducting phase coexisting with a dis-commensurate charge density wave in two or higher dimensional systems with the help of effective next nearest neighbor hopping. The nature of Gutzwiller factors indicate that the metallic phase intervening between the two insulating phases in the IHM or the correlated binary alloy model will be a bad metal with very high effective mass of the quasiparticles.

Although we have considered so far the case of the strongly correlated Hubbard model in the presence of large binary disorder, the formalism can be easily used even in the case of fully random disorder $V(i) \in [-V, V]$. The strongly correlated Hubbard model in the presence of fully random disorder has been mostly studied in the limit of weak disorder mainly in context of high T_c cuprates [19, 96–98]. The case of strong disorder has been studied in order to understand the effect of impurities like Zn in high T_c cuprates [67, 68] but that too keeping $V \leq U$ so that the constraint of no double occupancy remains intact. But for the limit of strong correlation as well as strong disorder such that $U \sim V \gg t$ the formalism of hole projection is essential and has not been studied before. For $V(i) < 0$ and $|V(i)| > V_c$, where $V_c \gg t$, holes will not be allowed in the low energy Hilbert space. But due to the limit of strong correlations for the hole-doped case, doublons will not be energetically allowed at other sites of the system which have either $V(i) > 0$ or $V(i) < 0$ but $|V(i)| < V_c$. Hence, even in the case of fully random disorder there will be effectively two type of sites A where holes are projected out from low energy Hilbert space and B type sites where doublons are projected out from low energy Hilbert space and one can

easily use the formalism we have provided for strongly correlated binary alloys. Another situation where this physics is of relevance is a strongly correlated Hubbard model with large attractive impurities randomly distributed over the lattice with $V(i) = -V$ at the impurity sites and $V(i) = 0$ at other sites of the lattice. For $V \sim U \gg t$, at the impurity sites energetics will not allow holes in the low energy Hilbert space while at all other sites of the lattice for which $V(i) = 0$ large U will not allow for doublons in the low energy sector for the hole doped case. Again in this situation one can use the formalism developed here for the case of strongly correlated binary alloys.

To conclude, in this chapter we have provided an essential tool which has been missing so far in the field of stongly correlated electron systems, that is, the Gutzwiller projection for holes allowing for doublons which happens in many correlated systems in various possible scenarios explained above. We have described its implementation at the level of the Gutzwiller approximation. We would like to mention that so far we have evaluated Gutzwiller factors under the simplest assumption of spin resolved densities being the same in the projected and unprojected state. It will be interesting to find Gutzwiller factors in more general scenarios.

CHAPTER 3

PHASE DIAGRAM OF THE HALF-FILLED IONIC HUBBARD MODEL IN THE LIMIT OF STRONG CORRELATIONS

3.1 Introduction

Doping a strongly correlated Mott insulator (MI) away from commensurate filling results in a superconducting phase [16] as known from high T_c cuprates and the recently discovered superconductivity in magic angle twisted bilayer graphene [14]. The minimal model to describe this physics is the strongly correlated Hubbard model, which at half-filling maps onto an effective Heisenberg model having an antiferromagnetic (AF) insulating ground state and doping holes or electrons into this system results in a superconducting state.

In this chapter, we study the half-filled ionic Hubbard model (IHM) and explore the possibility of superconducting phase. As mentioned in the Introduction chapter, the IHM

is basically the Hubbard model defined on a bipartite lattice with an additional staggered potential Δ. The physics of IHM is governed by the competition between the staggered potential Δ and the Hubbard U [5, 51, 78, 79]. At half-filling, in the large U limit, the system is a MI while for large Δ regime, the system is a band insulator (BI) due to doubling of the unit cell. The physics of the intermediate regime in which $U \sim \Delta$, straddling the two insulating phases, has been of interest to the condensed matter community. Here we focus on the limit when $U \sim \Delta$ but both are much larger than the hopping amplitude t, that is, $U \sim \Delta \gg t$ and explore the possibility of a superconducting phase in this limit of the IHM at half-filling.

The IHM has been realized for ultracold fermions on an optical honeycomb lattice [8]. Due to recent developments in layered materials and heterostructures, it is indeed possible to think of many scenarios where the IHM can be used as a minimal model to understand the qualitative physics. Some of these examples are graphene on h-BN substrate where due to the difference in energy of B and N sites, electrons in the graphene sheet also feel a staggered potential. Also for a bilayer graphene in the presence of a transverse electric field, a potential difference is induced between the two layers [66] which plays the role of the staggered potential. Interactions are inevitably present in all real materials.

The IHM has been studied in various dimensions by a variety of numerical and analytical tools [5–7, 9, 41–44, 51, 58–61, 78, 79]. In one-dimension [9, 51, 78, 79] it has been shown to have a spontaneously dimerized phase which separates the weakly coupled BI from the strong coupling MI. In higher dimensions ($d > 1$), this model has been mostly studied in the weak to intermediate coupling regime for $\Delta \sim t$ by many groups using the dynamical mean field theory (DMFT) [5, 7, 43, 58–61], determinantal quantum Monte carlo [41, 42], and coherent potential approximation [44]. The solution of the DMFT self consistent equations for intermediate strength of U and $\Delta \sim t$, in the paramagnetic (PM)

sector at half filling at zero temperature shows an intervening correlation induced metallic phase [5, 41–44]. When one allows for spontaneous spin symmetry breaking the transition from paramagnetic BI to AF insulator preempts the formation of the para-metallic phase [6, 59], except, as shown in Ref [60] using DMFT with iterated perturbation theory (IPT) as the impurity solver, for a sliver of a half-metallic AF phase. Upon doping the IHM in the intermediate coupling regime for $\Delta \sim t$, one gets a broad ferrimangetic half-metal phase [60] sandwiched between a weakly correlated PM metal for small U and a strongly correlated metal for large U. Recently the IHM was solved at half-filling within DMFT using continuous time Monte Carlo (CTQMC) as an impurity solver [7, 61]. In the large U limit $U \gg (\Delta, t)$ it maps onto an effective Heisenberg model with the spin-exchange coupling $\tilde{J} = t^2 U/(U^2 - \Delta^2)$ [7, 61]. At any finite T, for $\Delta \sim t$, as U increases, first the magnetic order turns on via a first order phase transition followed up by a continuous transition back to the PM phase. There is a line of tricritical point T_{tcp} that separates the two surfaces of first and second order phase transitions [7].

In this chapter we study the half-filled IHM in the limit where *both* the Hubbard U and the staggered potential Δ are much larger than the hopping amplitude. Cluster DMFT study in this limit [6] demonstrated a direct transition between the AF MI and the BI as Δ is increased for a fixed large value of U. Recently this limit has been explored using slave-boson mean field theory [80] which demonstrated a transition from MI to BI as Δ increases followed up by a transition to a broad superconducting phase as Δ is increased further. Clearly there is no clear consensus on the phase diagram of the IHM in this limit. In order to develop some understanding of the IHM in this limit, here we solve it using a Gutzwiller projected renormalized mean field theory as well as using the DMFT+CTQMC technique. Below we summarize our main findings from this analysis.

The IHM we study is on a 2-dimensional square lattice, at zero temperature. We find

that within a spin symmetric Gutzwiller projected mean field theory, the d-wave pairing does indeed turn on for a small range of $\Delta \sim U$ sandwiched between a paramagnetic MI and a BI. Though the extended s-wave pairing amplitude is also non zero for a small Δ range, it is always a little higher in energy than the d-wave superconducting (SC) phase. But in a generic calculation, where the system is allowed to have phases with broken spin symmetry as well, the AF Mott insulating phase wins over the superconducting phase, and the system does not have any stable superconducting ground state. There occurs a transition from the AF MI to the paramagnetic BI, with a thin half-metallic phase intervening between the two insulators close to the transition point. This phase diagram shows consistency with the earlier analysis [5,7] in weak to intermediate U and Δ regime, where a metallic phase is observed within a spin symmetric calculation; however, once spin-ordering is allowed for, the AF MI preempts the formation of metal, except for a thin half-metallic phase close to the transition between the MI and the BI. Hence there is a continuity in the phase diagram along the $U \sim \Delta$ line as U increases. Surprisingly, the phase diagram obtained from the Gutzwiller projected mean field calculation differs from the one obtained from the slave boson mean field theory calculation [80] where a broad SC phase appears beyond the BI phase as Δ increases. We have benchmarked the AF transition point obtained within the Gutzwiller projected mean field theory calculation against the DMFT+CTQMC calculation which has earlier been shown to capture the correct strongly correlated limit of IHM [7,61] within a mean field description of the AF order.

The rest of this chapter is organized as follows. In section 3.2, we describe the model, the low energy Hilbert space which is relevant to the limit $U \sim \Delta \gg t$, and the effective low energy Hamiltonian , obtained using a similarity transformation. Furthermore, we describe the Gutzwiller approximation used to solve this low energy Hamiltonian. In section 3.3, we briefly describe the Gutzwiller projected renormalized mean field theory

(RMFT) for the AF phase and then benchmark our results against the DMFT+CTQMC calculations. In section 3.4, we describe the spin symmetric RMFT calculation which allows for superconducting pairing amplitude followed up by the generic RMFT calculation where we include the pairing amplitude as well as the magnetic order. At the end we conclude and summarize.

3.2 Model and Method: Low energy effective Hamiltonian and Gutzwiller Approximation

The IHM is described on a bipartite lattice by the Hamiltonian,

$$H = -t \sum_{<i,j>,\sigma} (c^{\dagger}_{i\sigma} c_{j\sigma} + h.c.) - \frac{\Delta}{2} \sum_{i \in A} \hat{n}_i + \frac{\Delta}{2} \sum_{i \in B} \hat{n}_i + U \sum_i \hat{n}_{i\uparrow} \hat{n}_{i\downarrow} - \frac{U}{2} \sum_i \hat{n}_i. \quad (3.1)$$

Here t is the nearest neighbor hopping amplitude, Δ is the staggered one body potential and U is the onsite Hubbard repulsion. At half-filling, corresponding to $(\langle \hat{n}_A \rangle + \langle \hat{n}_B \rangle)/2 = 1$, the Hamiltonian is particle-hole symmetric, with $\mu = \frac{U}{2}$.

In the limit $U \sim \Delta \gg t$, the $t = 0$ model can be thought of as the unperturbed model and the hopping can be treated perturbatively. For $t = 0$, and $U \sim \Delta$, from the energies associated with all possible configurations at each site, it is easy to see that holes on the A sublattice are energetically expensive and doublons are energetically unfavorable on the B sites. Hence holes on A and doublons on B sublattice get eliminated from the low energy Hilbert space. As shown in Chapter 2, the effective low energy Hamiltonian in the limit $U \sim \Delta \gg t$, obtained by a similarity transformation which eliminates processes which

inter-connect the high and low energy sector of the Hilbert space is given by,

$$\mathcal{H}_{eff} = H_0 + H_{t,low} + H_d + H_{tr} + H_{ex}. \tag{3.2}$$

Here $H_{t,low}$ is the hopping process in the low energy Hilbert space. As an effect of projection of holes and doublons from A and B sublattice, respectively, many of the nearest neighbor hopping processes between sites of sublattice A and B, where either the initial or the final state has holes on A sublattice and/or doublons on B sublattice, belong to the high energy sector of the Hilbert space and hence get projected out from low energy Hamiltonian. But interestingly, in the half filled IHM there are hopping processes which belong only to the low energy Hilbert space, e.g., $|d_A 0_B\rangle \Leftrightarrow |\uparrow_A\downarrow_B\rangle$. This is in contrast to the half-filled Hubbard model [30], where hopping is completely projected out of the low energy Hilbert space. Hence we have the following expression for $H_{t,low}$,

$$\begin{aligned} H_{t,low} &= -t \sum_{<ij>,\sigma} \tilde{c}^{\dagger}_{iA\sigma}\tilde{\tilde{c}}_{jB\sigma} + \tilde{\tilde{c}}^{\dagger}_{jB\sigma}\tilde{c}_{iA\sigma} \\ &= -t \sum_{<ij>,\sigma} \mathcal{P}[c^{\dagger}_{iA\sigma}c_{jB\sigma} + h.c.]\mathcal{P}. \end{aligned} \tag{3.3}$$

Here $\mathcal{P}$ is the projection operator that projects out holes from sublattice A and doublons from sublattice B. The new fermionic operators in the projected Hilbert space are defined as,

$$\tilde{c}^{\dagger}_{A\sigma} \equiv \eta(\sigma) X_A^{d\leftarrow\bar{\sigma}} = c^{\dagger}_{A\sigma}\hat{n}_{A\bar{\sigma}}, \tag{3.4}$$

$$\tilde{\tilde{c}}^{\dagger}_{B\sigma} \equiv X_B^{\sigma\leftarrow 0} = c^{\dagger}_{B\sigma}(1-\hat{n}_{B\bar{\sigma}}). \tag{3.5}$$

A second order hopping process starting from and returning to the sector of states with single occupancies on two neighboring sites, where the first hopping results in a virtual

hole on A and a doublon on B, results in an effective spin exchange process H_{ex} given by,

$$H_{ex} = -\frac{J_1}{2} \sum_{<ij>,\sigma} [\tilde{c}_{iA\bar{\sigma}} \tilde{c}^{\dagger}_{iA\bar{\sigma}} \tilde{\tilde{c}}^{\dagger}_{jB\bar{\sigma}} \tilde{\tilde{c}}_{jB\bar{\sigma}} - \tilde{c}_{iA\sigma} \tilde{c}^{\dagger}_{iA\bar{\sigma}} \tilde{\tilde{c}}^{\dagger}_{jB\sigma} \tilde{\tilde{c}}_{jB\bar{\sigma}}]$$

$$= J_1 \sum_{<ij>} \mathcal{P}(S_{iA}.S_{jB} - (2 - \hat{n}_{iA})\hat{n}_{jB}/4)\mathcal{P}, \tag{3.6}$$

with $J_1 = \frac{2t^2}{U+\Delta}$. There are dimer processes H_d where a spin from an A site hops to an empty B site, and then hops back to the same A site, creating a virtual state with a hole on the A site. In another dimer process, a spin σ from a doubly occupied A site hops to a B site which has $\bar{\sigma}$ and then hops back to A site, resulting in a virtual state with a doublon on B site. Both these processes are of order t^2/Δ and can be written as,

$$H_d = -\frac{t^2}{\Delta} \sum_{\sigma,<ij>} \left[\tilde{c}_{iA\bar{\sigma}} \tilde{c}^{\dagger}_{iA\bar{\sigma}} \tilde{\tilde{c}}_{jB\sigma} \tilde{\tilde{c}}^{\dagger}_{jB\sigma} + \tilde{c}^{\dagger}_{iA\sigma} \tilde{c}_{iA\sigma} \tilde{\tilde{c}}^{\dagger}_{jB\bar{\sigma}} \tilde{\tilde{c}}_{jB\bar{\sigma}}\right]$$

$$= -\frac{t^2}{\Delta} \sum_{<ij>,\sigma} \mathcal{P}\big[(1 - \hat{n}_{iA\bar{\sigma}})(1 - \hat{n}_{jB}) + (\hat{n}_{iA} - 1)\hat{n}_{jB\bar{\sigma}}\big]\mathcal{P}. \tag{3.7}$$

Trimer terms, leading to H_{tr}, correspond to the hopping of a doublon or a hole from a site on the A(B) sublattice to its second neighbor site in the same sublattice via a two hop process. Effectively, there is a doublon hopping which is intra A sublattice, where as the hole hopping is intra B sublattice. In terms of projected operators, these are represented as,

$$H_{tr} = -\frac{t^2}{\Delta} \sum_{\sigma,<ijk>} (\tilde{c}^{\dagger}_{kA\sigma} \tilde{\tilde{c}}^{\dagger}_{jB\bar{\sigma}} \tilde{\tilde{c}}_{jB\bar{\sigma}} \tilde{c}_{iA\sigma} + \tilde{c}_{iA\bar{\sigma}} \tilde{\tilde{c}}^{\dagger}_{jB\bar{\sigma}} \tilde{\tilde{c}}_{jB\sigma} \tilde{c}^{\dagger}_{kA\sigma})$$

$$-\frac{t^2}{\Delta} \sum_{\sigma,<jil>} (\tilde{\tilde{c}}_{lB\sigma} \tilde{c}_{iA\bar{\sigma}} \tilde{c}^{\dagger}_{iA\bar{\sigma}} \tilde{\tilde{c}}^{\dagger}_{jB\sigma} + \tilde{\tilde{c}}^{\dagger}_{jB\sigma} \tilde{c}_{iA\sigma} \tilde{c}^{\dagger}_{iA\bar{\sigma}} \tilde{\tilde{c}}_{lB\bar{\sigma}})$$

$$= -\frac{t^2}{\Delta} \sum_{\sigma,<ijk>} \mathcal{P}(c^\dagger_{kA\sigma} \hat{n}_{jB\bar{\sigma}} c_{iA\sigma} + c_{iA\bar{\sigma}} c^\dagger_{jB\bar{\sigma}} c_{jB\sigma} c^\dagger_{kA\sigma})\mathcal{P}$$

$$-\frac{t^2}{\Delta} \sum_{\sigma,<jil>} \mathcal{P}(c_{lB\sigma}[(1-\hat{n}_{iA\bar{\sigma}})c^\dagger_{jB\sigma} + c^\dagger_{iA\sigma} c_{iA\bar{\sigma}} c^\dagger_{jB\bar{\sigma}}])\mathcal{P}. \tag{3.8}$$

The effective low energy Hamiltonian mentioned above cannot be solved using regular perturbation theory because the projected fermionic operators $\tilde{c}_A$ and $\tilde{\tilde{c}}_B$ do not satisfy the standard anti-commutation relations of canonical fermions and hence Wick's theorem can not be applied. The possible approaches to solve H_{eff} are either fully numerical, like variational Monte-Carlo (VMC) [34] where the projection constraints can be handled exactly in each configuration but is computationally very expensive, or one can use the Gutzwiller approximation in the same spirit as it is used for doublon projection in the tJ model [1,2,19,36–40,76,77]. Within the Gutzwiller approximation, the effect of projection is treated approximately by renormalizing the coefficients of the various terms in H_{eff} by corresponding Gutzwiller factors and calculating the expectation value of the renormalized Hamiltonian in the unprojected basis. The Gutzwiller factors, for the half-filled IHM in the limit $U \sim \Delta \gg t$, for the hole projection from the A sublattice and the doublon projection from the B sublattice have been calculated in chapter 2. The renormalized Hamiltonian obtained is of the form,

$$\tilde{H} = H_0 - t \sum_{\sigma,<ij>} g_{t\sigma}[c^\dagger_{iA\sigma} c_{jB\sigma} + c^\dagger_{jB\sigma} c_{iA\sigma}]$$

$$-g_1 \frac{t^2}{\Delta} \sum_{<ij>,\sigma} [(1-\hat{n}_{iA\bar{\sigma}})(1-\hat{n}_{jB}) + (\hat{n}_{iA}-1)\hat{n}_{jB\bar{\sigma}}]$$

$$-\frac{t^2}{\Delta} \sum_{\sigma,<ijk>} (g_{t\sigma} c^\dagger_{kA\sigma} \hat{n}_{jB\bar{\sigma}} c_{iA\sigma} + g_2 c_{iA\bar{\sigma}} c^\dagger_{jB\bar{\sigma}} c_{jB\sigma} c^\dagger_{kA\sigma}) + h.c.$$

$$-\frac{t^2}{\Delta}\sum_{\sigma,<jil>}(g_{t\sigma}c_{lB\sigma}(1-\hat{n}_{iA\bar{\sigma}})c^{\dagger}_{jB\sigma}+g_2 c_{lB\sigma}c^{\dagger}_{iA\sigma}c_{iA\bar{\sigma}}c^{\dagger}_{jB\bar{\sigma}})$$

$$+J_1\sum_{<i,j>}[g_s S_{iA}.S_{jB}-\frac{1}{4}(2-\hat{n}_{iA})\hat{n}_{jB}]. \tag{3.9}$$

Here $g_{t\sigma}, g_1, g_s$ and g_2 are the Gutzwiller renormalization factors. The factors for various processes in H_{eff} were calculated under the approximation that the local densities before and after the projection are the same. Table 3.1 provides expressions for the various Gutzwiller factors in terms of the mean field quantities, namely, $\delta = (n_A - n_B)/2$, the density difference between the two sublattices, and $m_s = (m_A - m_B)/2$, the staggered magnetization in the symmetry broken antiferromagnetic phase.

Gutzwiller Factors	Expressions
$g_{t\sigma}$	$\frac{2\delta}{1+\delta+\sigma m_s}$
g_s	$\frac{4}{(1+\delta)^2-m_s^2}$
g_1	1
g_2	$\frac{4\delta}{(1+\delta)^2-m_s^2}$

Table 3.1: Gutzwiller factors for various terms in H_{eff} at half-filling in the antiferromnagnetically ordered phase [10].

Note that for $m_s = 0$, the expressions for g_t and g_s become similar to that of the familiar hole-doped tJ model with δ in IHM playing the role of doping in tJ model [1, 36–40] although the projection constraints in the two situations are completely different.

H_0, the unperturbed part of the Hamiltonian in the projected space is equivalent to $H_0 = \sum_i \frac{U-\Delta}{2}[\hat{n}_{iA\uparrow}\hat{n}_{iA\downarrow} + (1-\hat{n}_{iB\uparrow})(1-\hat{n}_{iB\downarrow})]$. To see this, consider first the A sublattice, where holes are not allowed in the low energy Hilbert space. The unperturbed Hamiltonian can be written as $H_{0,A} = \mathcal{P}_h\left[U(1-\hat{n}_{A\uparrow})(1-\hat{n}_{A\downarrow}) + \left(\frac{U-\Delta}{2}\right)\hat{n}_A\right]\mathcal{P}_h$. Since holes are

projected out, only the second term survives under the projection. Using the completeness relation in the hole projected Hilbert space, $\hat{n}_{A\uparrow}(1-\hat{n}_{A\downarrow})+\hat{n}_{A\downarrow}(1-\hat{n}_{A\uparrow})+\hat{n}_{A\uparrow}\hat{n}_{A\downarrow}=1$, one can show that $\mathcal{P}_h\hat{n}_A\mathcal{P}_h \equiv (1+\hat{n}_{A\uparrow}\hat{n}_{A\downarrow})$. Similarly, on the B sublattice where doublons are not energetically favourable $H_{0,B} = \mathcal{P}_d\left[U\hat{n}_{B\uparrow}\hat{n}_{B\downarrow} - \left(\frac{U-\Delta}{2}\right)\hat{n}_B\right]\mathcal{P}_d$ where only the second term survives. Using the completeness relation on the B sublattice, $H_{0,B} = (U-\Delta)/2[(1-\hat{n}_{B\uparrow})(1-\hat{n}_{B\downarrow})-1]$.

We have solved the renormalized low energy effective Hamiltonian within a mean field theory. Before we go into details of this renormalized mean field theory (RMFT) and the phase diagram obtained from it, below we first benchmark the results obtained from RMFT against DMFT+CTQMC.

3.3 Benchmarking the renormalized Hamiltonian and Gutzwiller Approximation

The Gutzwiller approximation for the projection of doublons done for the hole-doped t-J model has shown qualitative and quantitative consistency with results obtained from VMC [2]. Hence we expect that the Gutzwiller approximation for the projection of holes and doublons from A and B sublattice sites, respectively, will also capture the physics qualitatively correctly. To check the validity of this expectation, in this section we compare the results obtained within RMFT against those obtained from DMFT+CTQMC. DMFT+CTQMC has been shown to capture the physics of strong correlations and the projection correctly in the limit $U \gg \Delta, t$ as demonstrated by the correct dependence of Néel temperature for the AF order as a function of Δ [7, 61].

However, within a single site DMFT, we cannot explore the possibility of d-wave or

extended s-wave superconductivity. Hence our comparison of the results of RMFT with the DMFT+CTQMC calculations is without including the superconducting pairing amplitude as a mean field. To be precise, we give nonzero expectation values only to (a) the staggered magnetization $m_\alpha = \langle c^\dagger_{i\alpha\uparrow} c_{i\alpha\uparrow} - c^\dagger_{i\alpha\downarrow} c_{i\alpha\downarrow} \rangle$, (b) the density difference between two sublattices $\delta = \langle (\hat{n}_A - \hat{n}_B) \rangle / 2$, (c) the inter-sublattice Fock shift $\chi_{AB,\sigma} = \langle c^\dagger_{iA\sigma} c_{jB\sigma} \rangle$, and (d) the intra-sublattice Fock shifts $\chi_{\alpha\alpha,\sigma} = \langle c^\dagger_{i\alpha\sigma} c_{j\alpha\sigma} + h.c. \rangle$. Here α is the sublattice index and σ is the spin index. The mean field quadratic Hamiltonian can be written as,

$$H_{MF} = \sum_{k,\sigma} h_{1\sigma}(k)[c^\dagger_{kA\sigma} c_{kA\sigma} - c^\dagger_{kB\sigma} c_{kB\sigma}] + h_{2\sigma}(k)[c^\dagger_{kA\sigma} c_{kB\sigma} + h.c.], \tag{3.10}$$

$$\begin{aligned} \text{where } h_{1\sigma}(k) &= \tfrac{U-\Delta}{2}\left(\tfrac{1+\delta-\sigma m}{2}\right) - \tfrac{t^2}{\Delta}\left[4(1-2\delta) + g_{t\bar{\sigma}}(2\chi_{BB\bar{\sigma}} + 4\chi_{BBxy\bar{\sigma}}) + g_{t\sigma}\tfrac{1-\delta+\sigma m}{2}\gamma'_k\right] - \\ &\tfrac{2t^2}{U+\Delta} g_s \sigma m + \tfrac{2t^2}{U+\Delta}(1-\delta) \\ h_{2\sigma}(k) &= \left[-t g_{t\sigma} - \tfrac{t^2}{\Delta}(-2\chi_{AB\sigma} + 6 g_2 \chi_{AB\bar{\sigma}}) - \tfrac{t^2}{U+\Delta}[g_s(\tfrac{1}{2}\chi_{AB\sigma} + \chi_{AB\bar{\sigma}}) + \tfrac{1}{2}\chi_{AB\sigma}] \right] \gamma_k. \end{aligned} \tag{3.11}$$

Here, $\gamma_k = 2[\cos(k_x) + \cos(k_y)]$ and $\gamma'_k = 2[\cos(2k_x) + \cos(2k_y)] + 4[\cos(k_x + k_y) + \cos(k_x - k_y)]$.

The mean field Hamiltonian H_{MF} can be diagonalized using standard canonical transformation $c_{kA\sigma} = \alpha_{k\sigma} d_{k1\sigma} + \beta_{k\sigma} d_{k2\sigma}$ and $c_{kB\sigma} = \alpha_{k\sigma} d_{k2\sigma} - \beta_{k\sigma} d_{k1\sigma}$ where α and β are fixed such that the off-diagonal part of Hamiltonian written in terms of the d operators vanishes. This results in $2\alpha^2_{k\sigma} = (1 - h_{1\sigma}(k)/E_\sigma(k))$ and $2\beta^2_{k\sigma} = (1 + h_{1\sigma}(k)/E_\sigma(k))$ with $E_\sigma(k) = \sqrt{h_{1\sigma}(k)^2 + h_{2\sigma}(k)^2}$.

At half filling, the magnetization on A and B sublattices are equal and opposite to each other owing to the particle-hole symmetry. Hence $m_s = (m_A - m_B)/2 = m_A$. Self-

consistent equations for various mean field order parameters are,

$$\begin{aligned} m_s =& \langle \hat{n}_{iA\uparrow} \rangle - \langle \hat{n}_{iA\downarrow} \rangle = \frac{1}{N} \sum_k (\alpha^2_{k\uparrow} - \alpha^2_{k\downarrow}), \\ \delta =& \frac{1}{2N} \sum_{k\sigma} (\alpha^2_{k\sigma} - \beta^2_{k\sigma}), \\ \chi_{AB\sigma} =& -\frac{1}{4N} \sum_k \gamma_k \alpha_{k\sigma} \beta_{k\sigma}, \\ \chi_{BB\sigma} =& \frac{1}{N} \sum_k [\cos(2k_x) + \cos(2k_y)] \beta^2_{k\sigma}, \\ \chi_{BBxy\sigma} =& \frac{1}{N} \sum_k 2\beta^2_{k\sigma} \cos(k_x) \cos(k_y). \end{aligned} \tag{3.12}$$

The DMFT is done using CTMQC as an impurity solver using the hybridization expansion method, details of which can be found in our earlier work [7]. Below we compare the staggered magnetization and the density difference obtained from the RMFT at $T = 0$ for a half-filled IHM on the 2D-square lattice with those obtained from the DMFT+CTQMC at $\beta = 50/t$ where β is the inverse temperature. Fig. 3.1 shows good qualitative consistency between the Gutzwiller projected RMFT and the DMFT+CTQMC calculations. The transition in both the calculations is first order, as reflected in the jump in the magnetization at the transition point. Furthermore, the consistency between the RMFT and DMFT+CTQMC calculations improves for larger values of U and Δ, as expected. For large values of U and Δ, where the doublon density on B sublattice and the hole density on A sublattice within the CTQMC calculations become really small (less than 0.01 or so, as shown in Fig. 3.2), then even quantitative consistency is seen between the two calculations at least deep in the ordered state or away from the transition point in the disordered state, as shown in the lower right panel of Fig. 3.1. In contrast, in slave boson mean field calculations [80] in the same limit one obtains the staggered magnetization transition point at $\sim 15.8t$ for $U = 20t$ and

also the value of m_s is much smaller as compared to what is obtained within the RMFT or the DMFT+CTQMC calculations.

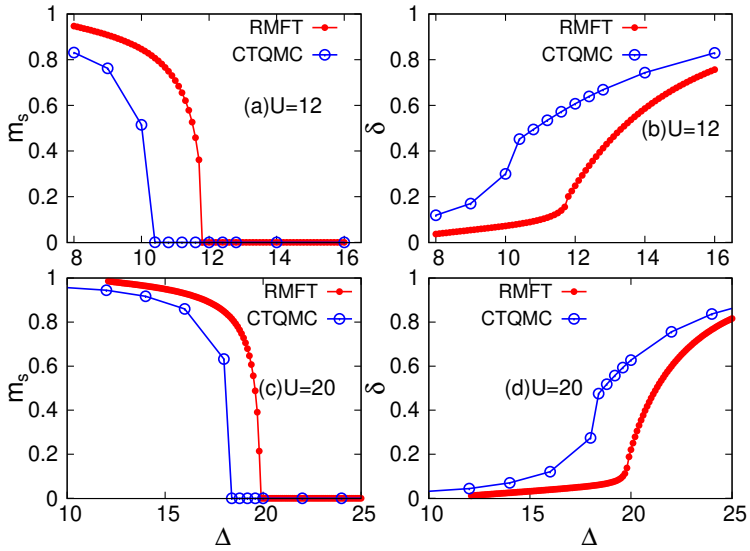

Figure 3.1: Staggered magnetization, m_s and the density difference, δ vs Δ for $U = 12t$ and $20t$. Blue circles show the data obtained in a DMFT+CTQMC calculation and the red data points are obtained within a Gutzwiller projected RMFT calculation respectively.

We have also calculated the density of holes $h_A = \langle(1-\hat{n}_{A\uparrow})(1-\hat{n}_{A\downarrow})\rangle$ and doublons $d_A = \langle\hat{n}_{A\uparrow}\hat{n}_{A\downarrow}\rangle$ on A sublattice within DMFT+CTQMC. Due to the $p-h$ symmetry at half-filling, $h_A = \langle\hat{n}_{B\uparrow}\hat{n}_{B\downarrow}\rangle = d_B$ and $h_B = d_A$. Fig. 3.2 shows the density of holes and doublons on the A sublattice. As shown, sublattice A has negligible fraction of holes for $U \sim \Delta \geq 12t$. The density of holes decreases as U increases and also for a fixed $U \geq 8t$, as Δ increases h_A decreases becoming eventually less than one percent. This explains why a better consistency is observed at higher values of U and Δ between the DMFT+CTQMC calculation and the Gutzwiller projected RMFT theory, where holes from A sublattice and doublons from B sublattice have been fully projected out in the process of obtaining the low energy Hamiltonian.

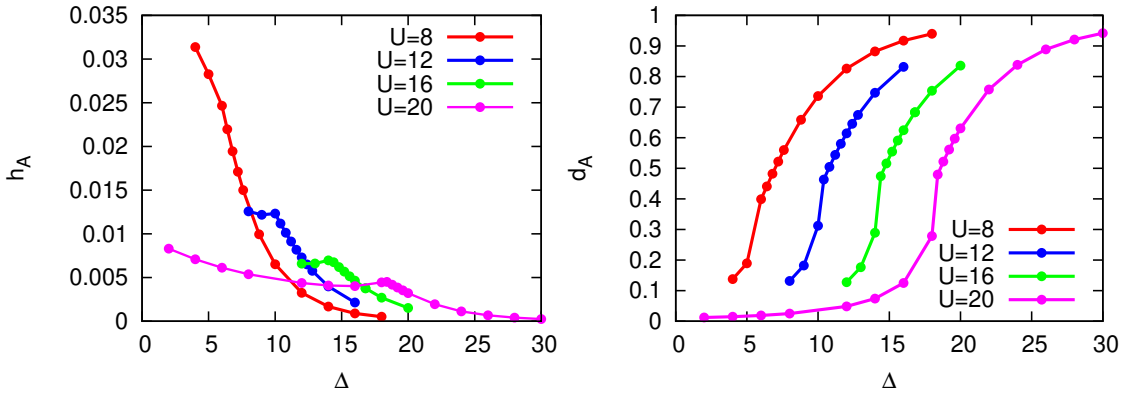

Figure 3.2: Hole occupancy and double occupancy on A sites as a function of Δ obtained from the DMFT+CTQMC calculation for the IHM at half-filling on a 2D square lattice.

3.4 Phase Diagram within Renormalised Mean Field Theory

In this section, we provide details of two versions of the Gutzwiller projected RMFT calculations for the low energy Hamiltonian in Eq. 3.9 allowing for the presence of a superconducting order parameter. One is the spin symmetric calculation where we do allow for a d-wave (or extended s-wave) pairing amplitude to have nonzero expectation value but $n_{\alpha\uparrow} = n_{\alpha\downarrow}$ is imposed. The other is a less restricted calculation where we allow for superconductivity as well as symmetry breaking in the spin sector.

Our solution of the mean field Hamiltonian involves a two step transformation. The Hamiltonian obtained after the first step of the transformation has both interband and intraband pairing terms. The results presented below are obtained by ignoring the interband pairing term, as it is smaller than the gap between the two bands at most of the points in the Brillouin zone, whence the second step of the transformation can be done analytically. Details of these calculations are given in Appendix B.1. In Appendix B.2, we have shown a

comparison of these results with the calculations where the interband pairing term is kept, in which case the mean field Hamiltonian needs to be diagonalized numerically. As shown in Appendix B.2, at zero temperature, the contribution of the interband pairing term is negligible for most of the physical quantities of interest. Hence to obtain the zero temperature phase diagram it is a reasonably good approximation to ignore the interband pairing terms.

3.4.1 Results from Spin-symmetric RMFT

In the spin symmetric RMFT, along with the mean fields mentioned earlier, we allow for a non zero value of the superconducting pairing amplitude $\Delta_{AB}(i,j) = \langle c^{\dagger}_{iA\uparrow} c^{\dagger}_{jB\downarrow} - c^{\dagger}_{iA\downarrow} c^{\dagger}_{jB\uparrow} \rangle$ looking for d-wave and extended s-wave pairing in the $U \sim \Delta \gg t$ limit of the half-filled IHM on a 2d square lattice. For d-wave pairing $\Delta_{AB}(i, i\pm x) = \Delta_d = -\Delta_{AB}(i, i\pm y)$ while for the extended s-wave $\Delta_{AB}(i, i \pm x) = \Delta_{AB}(i, i \pm y) = \Delta_s$. This implies $\Delta_{AB}(k) = 2\Delta_d[cos(k_x) - cos(k_y)]$ for the d-wave pairing while for the extended s-wave $\Delta_{AB}(k) = 2\Delta_s[cos(k_x)+cos(k_y)]$. We impose the spin symmetry $\langle \hat{n}_{i\uparrow} \rangle = \langle \hat{n}_{i\downarrow} \rangle$, which further implies that all the inter- sublattice and intra sublattice Fock shifts are spin independent. Details of the mean-field calculations are given in Appendix B.1.

Fig. 3.3 shows the pairing amplitude with the d-wave and the extended s-wave symmetry as a function of Δ for four values of U. Both the pairing amplitudes are nonzero for a finite range of Δ close to but less than U. For most of U values of interest, the range of Δ over which the extended s-wave pairing appears is much smaller than the Δ range over which the d-wave pairing amplitude is non-zero. Note that though the pairing amplitude $\Delta_{d,s}$ remains nonzero for values of Δ smaller than the range shown in Fig. 3.3, the density difference δ becomes close to zero for these smaller values of Δ. This, as shown below, results in a vanishing SC order parameter for these smaller values of Δ.

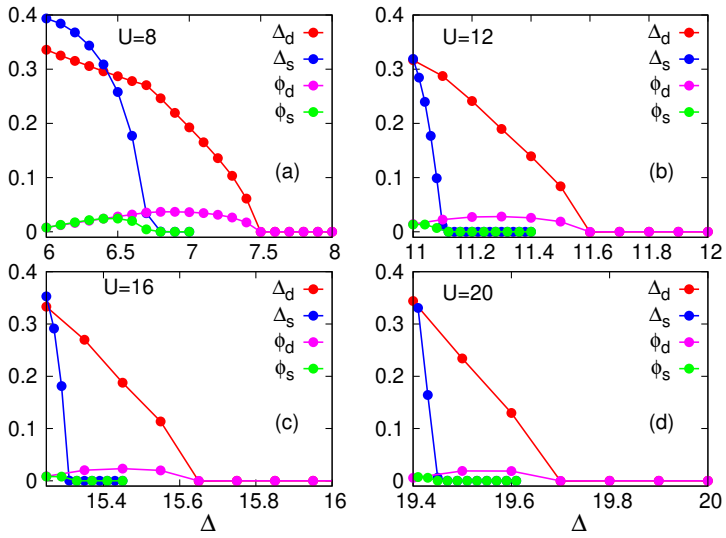

Figure 3.3: The superconducting pairing amplitude for d-wave and extended s-wave symmetry vs Δ obtained from spin symmetric RMFT. The pink curves shows the d-wave order parameter ϕ_d vs Δ while the green data points represent the extended s-wave order parameter ϕ_s. Different panels show results for different values of U ranging from $U = 8t$ to $U = 20t$. The extended s-wave pairing is observed for a smaller Δ regime while there is nonzero d-wave pairing amplitude for a comparatively broader range of Δ.

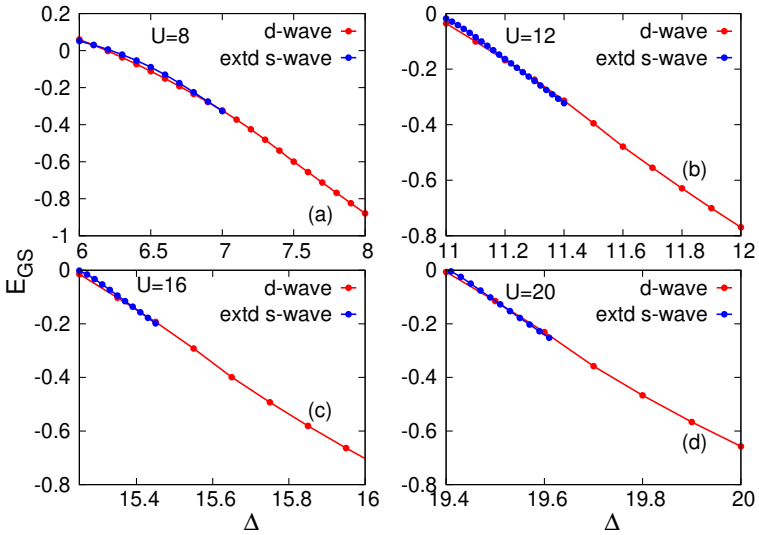

Figure 3.4: Ground state energy, E_{GS} vs Δ for extended s-wave pairing and d-wave pairing. For Δ ranges where the extended s-wave pairing amplitude is non zero, the ground state energy for the extended s-wave solution is higher than the ground state energy for the d-wave pairing superconducting phase.

Fig. 3.4 further shows the comparison of the ground state energies for the self-consistent solutions with d-wave pairing and extended s-wave pairing. For almost the entire Δ regime where extended s-wave superconductivity is seen, the ground state energy of the extended s-wave superconducting phase is higher than that of the d-wave superconducting phase, making the latter the stable phase in the spin symmetric calculation.

The superconducting order parameter ϕ_d and ϕ_s for the d-wave and extended s-wave channel respectively is defined as $\phi^2_{d,s} = g_t^2 \lim_{r\to\infty}\langle c^\dagger_{i\uparrow} c^\dagger_{j\downarrow} c_{i+r\uparrow} c_{j+r\downarrow}\rangle$. For a given U, though the pairing amplitude is larger for smaller values of Δ, because probability for formation of a singlet is larger for smaller Δ, these singlets can hop around coherently only when there are sufficient number of doublons on A sublattice and holes on B sublattice. This can happen only when n_A is sufficiently larger than and n_B is sufficiently smaller than the average density of one. This is exactly what is indicated in the definition of the SC order parameter $\phi_{d,s}$ where g_t is the Gutzwiller renormalization parameter for the kinetic energy. Fig. 3.5 shows the behavior of Gutzwiller factor g_t as a function of Δ for d-wave pairing SC. For a given U, the density difference δ between two sublattices increases with increase in Δ. This enhances the hopping between two sublattices through increase of g_t. On the other hand, the pairing amplitude Δ_{AB} decreases with increase in Δ, resulting in a dome shaped non monotonic behavior of ϕ as a function of Δ as shown in Fig. 3.3.

Fig. 3.5 also shows the antinodal gap $Gap_d = h_3(0,\pi)$ for the d-wave SC, which is also the energy scale at which coherence peaks appear in the single particle density of states. Here $h_3(k)$ is the off-diagonal part of the mean-field Hamiltonian as shown in Appendix B.1. The antinodal gap monotonically decreases with increase in Δ as both the pairing amplitude Δ_d and the dominating Gutzwiller factor g_s involved in $h_3(k)$ are monotonically decreasing functions of Δ.

The superconducting phase is sandwiched between two insulating phases. For $\Delta < \Delta_1$,

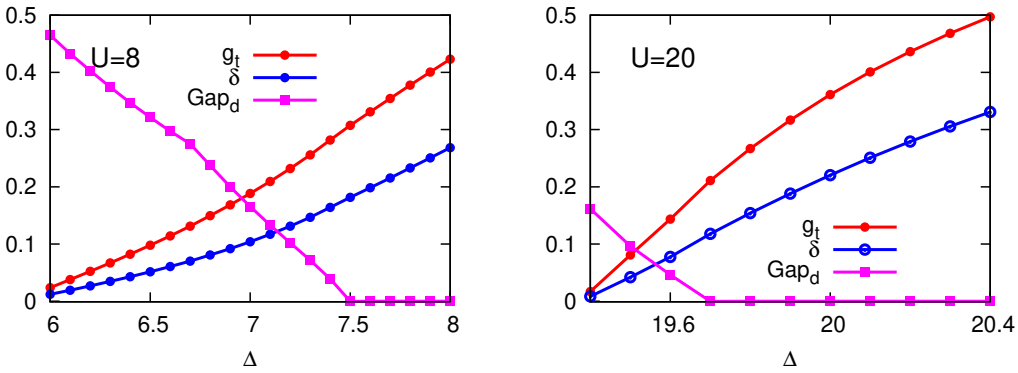

Figure 3.5: Gutzwiller renormalization factor g_t and the density difference δ vs Δ for the d-wave pairing SC phase. With increase in Δ, the density difference between two sublattices increases, which results in enhanced coherent hopping of singlets. Gap_d is the anti-nodal gap for the d-wave SC which, in contrast to the SC order parameter ϕ_d, decreases monotonically with increase in Δ.

where the SC order-parameter ϕ becomes nonzero first, the system is a paramagnetic MI with the gap in the single particle spectrum increasing monotonically with U. SC survives for $\Delta_1 < \Delta < \Delta_2$, and for $\Delta > \Delta_2$ the system goes into a trivial BI phase. The range in Δ for which the system shows the SC phase decreases with increase in U. Note that the range of Δ for which the system shows the SC phase in this spin symmetric RMFT is much smaller than what is obtained using SBMFT [80].

3.4.2 Results from Spin-asymmetric RMFT

In the last section we showed that the half-filled IHM in the limit $U \sim \Delta \gg t$ has a d-wave superconducting phase on a 2D square lattice, provided the system is constrained to have spin symmetry. In this section, we carry out a less restricted calculation allowing for symmetry breaking in the spin sector and explore the fate of the SC phase in competition with the magnetic order in the system. Thus we give non zero values to the AF order

m_s as well as to the superconducting pairing amplitude Δ_{AB} along with other mean fields like δ and the Fock shifts. The mean field Hamiltonian is then a 4×4 matrix for each allowed momentum $\vec{k}$ and requires a canonical transformation followed up by a Bogoliubov transformation to diagonalize it. Details of the mean field Hamiltonian, the transformations and the self-consistent equations for various order parameters are given in Appendices B.1 and B.2.

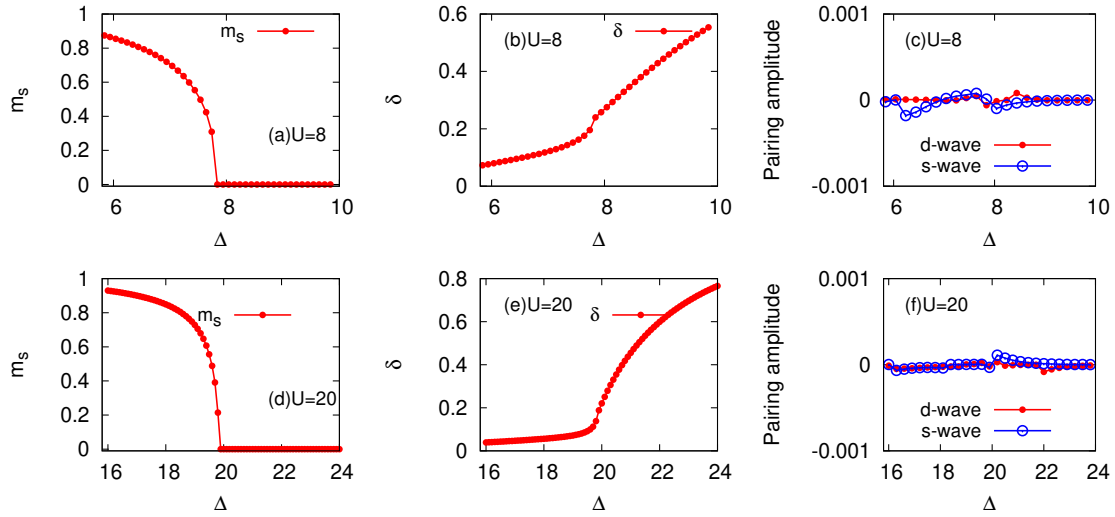

Figure 3.6: The staggered magnetization m_s, the density difference δ between the two sublattices and the d-wave and extended s-wave pairing amplitudes from the spin asymmetric calculation vs Δ. The pairing amplitude remains vanishingly small for both the symmetries considered. Thus, the AF order is energetically more stable than the SC order in the spin-asymmetric calculation.

Fig. 3.6 shows the staggered magnetization m_s, the density difference between the two sublattices δ and the pairing amplitude with d-wave and extended s-wave symmetry for $U = 8t$ and $U = 20t$. Comparing with Fig. 3.3, we see that, for a fixed U, as Δ decreases from a large value the development of AF order preempts the formation of SC order, and hence the SC does not appear either with d-wave or extended s-wave symmetry. The system undergoes a direct transition from an AF MI into a paramagnetic insulator with possibility

of only a thin half-metallic phase near the transition point, which we will discuss in a little while. Thus, though the recent SBMFT treatment of the half-filled IHM for $U \sim \Delta \gg t$ showed a broad SC phase, our Gutzwiller projected RMFT suggests that the system has only a metastable d-wave SC phase, which is hidden under the AF ordered phase. The SC phase is likely to get stablised only if the AF order is frustrated somehow.

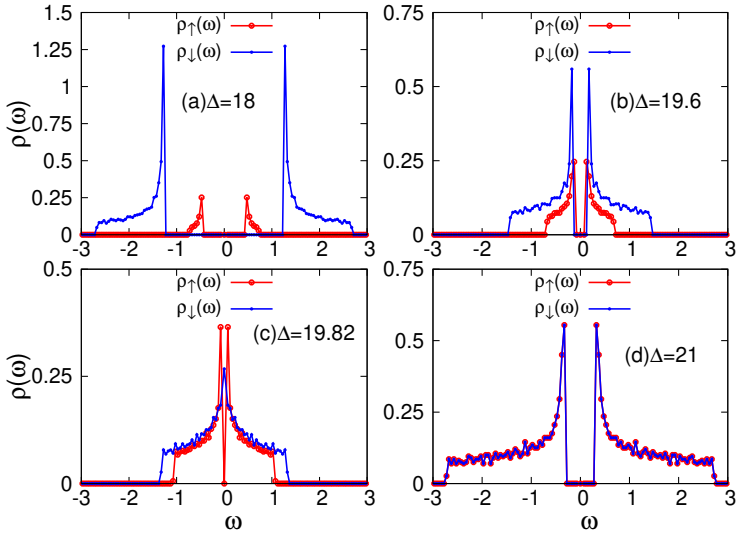

Figure 3.7: The single particle DOS for $U = 20t$. (a) At $\Delta = 18t$, the system has spin asymmetry with $gap_\downarrow > gap_\uparrow$. (b) Very near to $\Delta = 19.6t$, the gaps are equal in both the spin channels but $\rho_\uparrow \neq \rho_\downarrow$.(c) At $\Delta = 19.82t$, the system is a half-metal with down spin electrons conducting and up spin electrons insulating. (d) At $\Delta = 21t$, the gaps are spin-symmetric with $\rho_\uparrow = \rho_\downarrow$.

Fig. 3.7 shows the average single particle density of states (DOS) $\rho_\sigma(\omega) = 1/2 \sum_\alpha \rho_{\alpha\sigma}(\omega)$. The spin-resolved sublattice single particle DOS is defined as

$$\rho_{\alpha\sigma}(\omega) = -\frac{1}{\pi} \sum_k \text{Im}\, G_{\alpha\sigma}(k, \omega^+)$$

where, α represents the sublattice A or B and σ is the spin index. Note that the Green's function in the projected Hilbert space is related to the Green's function $G^0_{\alpha\sigma}(k, \omega)$ in the unprojected space with appropriate Gutzwiller factor such that $G_{\alpha\sigma}(k, \omega) = g_{t\sigma} G^0_{\alpha\sigma}(k, \omega)$ [19]. As shown in Fig. 3.7, for $\Delta = 18t$, $\rho_\sigma(\omega)$ is spin asymmetric with the gap in the down

spin DOS being more than that in the up spin DOS. As we increase Δ, the gaps in both channels as well as the asymmetry in the DOS for up and down spin channels decrease. Finally, at a particular Δ the gaps in both the channels become equal to each other, even though $\rho_\uparrow \neq \rho_\downarrow$, as is suggested by panel (b) of Fig. 3.7. After this the asymmetry in the gaps in the up and down spin channels opens up again but now the gap in the up spin channel is more than that in the down spin channel [see panel (d) of Fig. 3.8]. As shown in panel (c) of Fig. 3.7, there is a sliver of Δ for which $\rho_\downarrow(\omega = 0)$ is non-zero indicating the metallic behavior of the down-spin electrons while $\rho_\uparrow(\omega = 0)$ is still zero with a small gap around $\omega = 0$. This is the half-metallic point. With a further finite increment in Δ the system makes a transition at $\Delta = \Delta_c$ to the band insulating phase with full spin symmetry in the DOS.

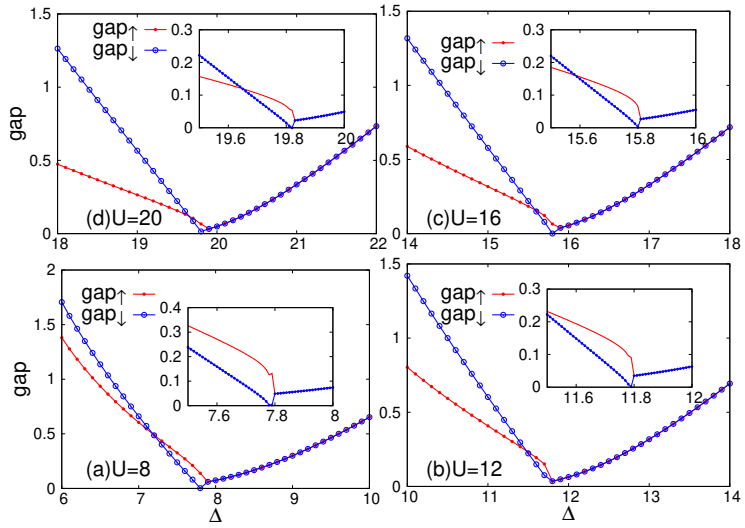

Figure 3.8: The gap in the single particle excitation spectrum for the up and down spin channels. For small Δ, where the system has AF order, $gap_\downarrow > gap_\uparrow$. On increasing Δ, the gaps become equal and after that, $gap_\uparrow > gap_\downarrow$. Inset shows existence of a half-metallic state where $gap_\downarrow = 0$. On further increase in Δ, there is a transition to the paramagnetic BI phase, where the gaps are equal for the two spin components and increase with Δ.

Fig. 3.8 shows that this behavior of the gaps in the single particle excitation spectrum

for the up and down spin channels is similar for various values of U. For $\Delta < U$, the gaps are spin-asymmetric with the gap in the down spin channel being more than that in the up spin channel until at some $\Delta < \Delta_c$, the gaps cross and become equal. Post this crossing point, for Δ still below the transition point Δ_c, the gap in the up spin sector is more than that in the down spin sector. There occurs a point where gap in the down spin channel diminishes to zero (less than 0.001 within our numerical calculations of the self-consistent mean field equations), where as there is a finite gap in the up spin channel as shown in the inset. This indicates a half-metallic point within the AF phase but close to the transition into the BI phase. After the transition, for $\Delta > \Delta_c$, the system is in the spin-symmetric band-insulating phase where $gap_\uparrow = gap_\downarrow$.

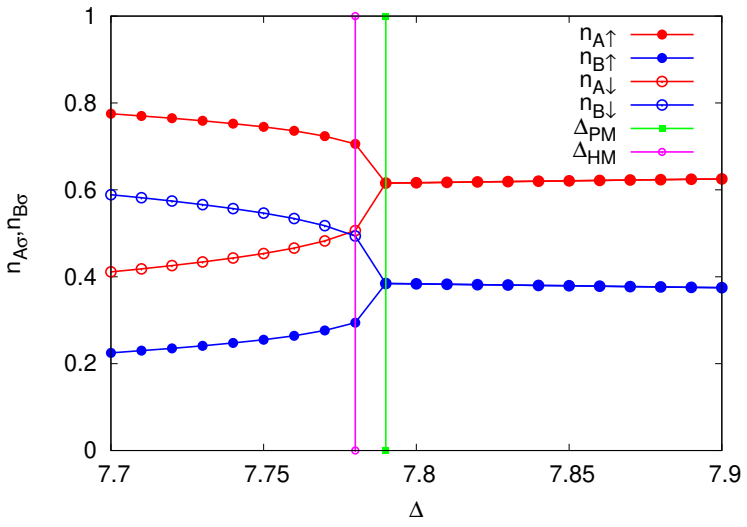

Figure 3.9: Spin resolved densities on A and B sublattices as a function of Δ for $U = 8t$. Δ_{HM} shows the half-metallic point and Δ_{PM} is the point where AFM order is lost and the system enters into the paramegnetic (PM) phase.

Some insights into the nature of half-metal phase can be gleaned by looking at the spin-resolved densities on A and B sites, shown in Fig. 3.9. For a given U, for smaller values of Δ, when the system is in an AF ordered Mott insulating phase, the density of up electrons

on A sites, $n_{A\uparrow}$, decreases with increase in Δ, while its density on B sites, $n_{B\uparrow}$, increases with increase in Δ, as shown in Fig. 3.9. Thus, the density difference for the up-spin electrons $\delta_\uparrow = n_{A\uparrow} - n_{B\uparrow}$ decreases with increase in Δ. However, the density of down spins on the A sites, $n_{A\downarrow}$, increases while $n_{B\downarrow}$ decreases as Δ increases, which implies that the density difference for the downspin electrons $\delta_\downarrow = n_{B\downarrow} - n_{A\downarrow}$ also decreases as Δ increases. Note that $\delta = (\delta_\uparrow - \delta_\downarrow)/2$, still increases as Δ increases. At Δ_{HM}, $n_{A\downarrow} = n_{B\downarrow}$ leading to the metallic nature of the down spin electrons while the up spin electrons continue to show density modulation on A and B sublattices, with $n_{A\uparrow} > n_{B\uparrow}$, and hence continue to show a gap in the single particle density of states. Thus, the half-metal phase can be visualized as the density modulation of up-spin electrons only, while the AF ordered insulating state has density modulations for both the up and the down spins electrons.

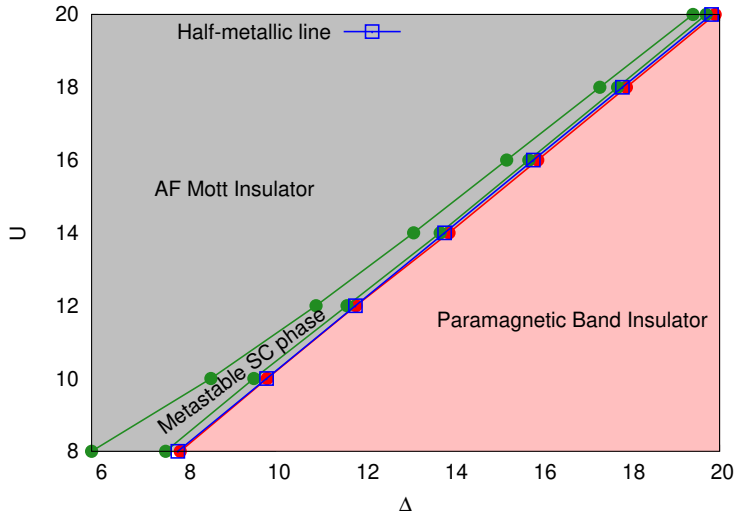

Figure 3.10: Complete phase diagram of the IHM in the $U \sim \Delta \gg t$ limit at half-filling on a two dimensional square lattice, obtained within the Gutzwiller projected RMFT analysis. The system shows only one first order transition from an AF ordered phase to a paramagnetic insulating phase. Most of the AF ordered phase is a MI. Inside the AF phase, there is a metastable d-wave SC phase. Very close to the transition line between AF and the paramagnetic BI, the system shows a line of AF ordered half-metallic phase.

Fig. 3.10 shows the complete phase diagram of the IHM at half-filling in the $U \sim \Delta \gg t$ limit on a 2D square lattice obtained within the Gutzwiller projected RMFT. The system undergoes a first order transition from an AF ordered state into the paramagnetic BI phase which is shown by the red line. Most of the AF phase is also Mott insulating in nature except for the thin half-metallic sliver close to the transition line, inside the AF phase. Therefore, at the parameter values along this sliver there will be spin polarized conductivity in the system at half-filling. Inside the AF phase, over the limited region shown, there also exists a metastable d-wave SC phase though the AF order is stabler than the SC order. Therefore, there is no stable superconducting phase in the IHM at half-filling in $U \sim \Delta \gg t$ regime within the Gutzwiller projected RMFT. This is in contrast to Ref [80], where a robust extended s-wave SC phase is obtained within slave boson mean field theory.

The phase diagram we have obtained here using Gutzwiller projected RMFT in the limit $U \sim \Delta \gg t$ is adiabatically connected to the phase diagram obtained within DMFT (solved using CTQMC and iterative perturbative theory (IPT) as an impurity solver), for intermediate ranges of U and Δ [7], where also a direct transition between AF MI and the paramagnetic insulator is obtained except for a sliver of half-metallic phase. It is also consistent with the phase diagram obtained from cluster DMFT [6] where results were shown upto large values of U and Δ and a direct transition between the MI and the paramagnetic BI is obtained.

3.5 Conclusions

In summary, in this chapter we have studied the IHM at half-filling in the limit $U \sim \Delta \gg t$. The low energy effective Hamiltonian in this limit is defined on a projected Hilbert space

where holes are projected out from one sublattice and the doublons are projected out from the other sublattice. Since the projected fermionic operators on either sublattice do not satisfy the algebra of canonical fermions, Wick's theorem does not hold for these operators and hence the effective low energy Hamiltonian can not be solved using standard perturbation theory. We implemented the Gutzwiller projection approximately by renormalizing the coefficients of the various terms in the effective Hamiltonian and solved the renormalized Hamiltonian within a mean field theory. On a 2D square lattice, we showed that the system has a d-wave superconducting phase sandwiched between a paramagnetic MI and a BI, provided the spin symmetry is enforced. But in a more general RMFT where the spin symmetry breaking is allowed, the AF order wins over the d-wave superconductivity. The system undergoes a transition from an AF MI to a paramagnetic BI with a thin sliver of a half-metallic phase in between, inside the AF insulating region.

It is surprising that though the Gutzwiller projected RMFT finds only a metastable SC phase, that too over a limited regime in the $U - \Delta$ plane, slave boson mean field theory (SBMFT) on the other hand shows a broad stable SC region [80]. The RMFT treatment of the IHM gives AF order and the AF transition point which show consistency, both qualitatively and quantitatively, with the results obtained within DMFT+CTQMC; and the latter has been earlier shown to capture the correct physics of strong correlations and Gutzwiller projection in the limit $U \gg \Delta, t$ [7,61]. Hence we expect that our RMFT results yield the correct strong correlation physics in the limit $U \sim \Delta \gg t$. Furthermore our study based on Gutzwiller projected RMFT is consistent with CDMFT study of IHM [6]. Also the phase diagram within the RMFT is adiabatically continuous with the phase diagram obtained within DMFT (using IPT as well as CTQMC as impurity solver) for the weak to intermediate values of U and Δ [7].

It will be interesting to explore the possibility of the explicit addition of a term to the

IHM which can frustrate the AF order and can stablise the SC phase. Also IHM has recently been implemented in the context of ultracold atoms [8] where the relative strengths of U and Δ can be tuned controllably. It will be really interesting to study this system in the limit $U \sim \Delta \gg t$ and to look for the superconducting phase experimentally.

CHAPTER 4

UNCONVENTIONAL SUPERCONDUCTIVITY IN A STRONGLY CORRELATED BAND-INSULATOR WITHOUT DOPING

4.1 Introduction

In this chapter, we present how sufficient frustration against magnetic order helps in stabilizing a spin-exchange mediated superconducting phase at half filling in a strongly correlated band insulator. The discovery of unconventional superconductivity in a variety of materials, such as high T_c superconductivity in cuprates [11], iron pnictides and chalcogenides [12], in organic superconductors [3], in heavy fermions [102] and very recently in magic angle twisted bilayer graphene [14, 15], has always ignited worldwide interest owing

to their rich phenomenonology, the theoretical challenges they pose, scientific implications and broad application potential. In almost all of these examples, superconductivity appears upon chemically doping the parent compound away from commensurate filling [11–16], though in some cases inducing charge fluctuations by changing pressure also leads to the superconducting phase [3, 13]. An important experimental fact is that chemical doping inevitably induces disorder, as is clearly the case in high T_c superconductors (SCs), which makes these materials very inhomogeneous [17–20]. It is a theoretical and experimental challenge to come up with new mechanisms and materials for clean high T_c SCs.

Theoretical analysis has shown that strong e-e correlations are crucial to achieve unconventional superconductivity. In most of the known unconventional SCs [3, 11–16] the low temperature phase of the parent compound is either a strongly correlated AF Mott insulator where charge dynamics is completely frozen, or a AF spin-density-wave phase with at least moderately strong correlations. The unconventional superconductivity in many of these materials can be understood, at least qualitatively, in terms of the strongly correlated limit of the paradigmatic Hubbard model (single or multi band) doped away from half-filling [2, 13, 16, 69, 103, 104]. But the possibility of a SC phase in a *strongly correlated band-insulator* has been explored very little so far, either theoretically or experimentally.

In this chapter, we show how a spin-exchange mediated SC can be realized *without doping* in a simple model of a strongly correlated band insulator (BI), where the bare band gap and the e-e interactions both dominate over the kinetic energy. As e-e interactions are increased (but still remain of the order of the band-gap), the single particle excitation gap in the BI closes, resulting in a metallic phase. Upon further increasing the e-e interactions, superconductivity develops by the formation of a coherent macroscopic quantum condensation of electron pairs, provided the metal has enough low energy quasiparticles and the system has enough frustration against the magnetic order. The superconductivity, which

survives for a broad range of e-e interactions, features tightly bound short coherence length Cooper pairs with a T_c well separated from the energy scale at which the pairing amplitude builds up. The phase diagram, whose section with all model parameters fixed except for the interaction to band-gap ratio is shown in Fig. 4.1, presents a plethora of exoctic phases, that we discuss further below, in the vicinity of a broad region of the SC phase.

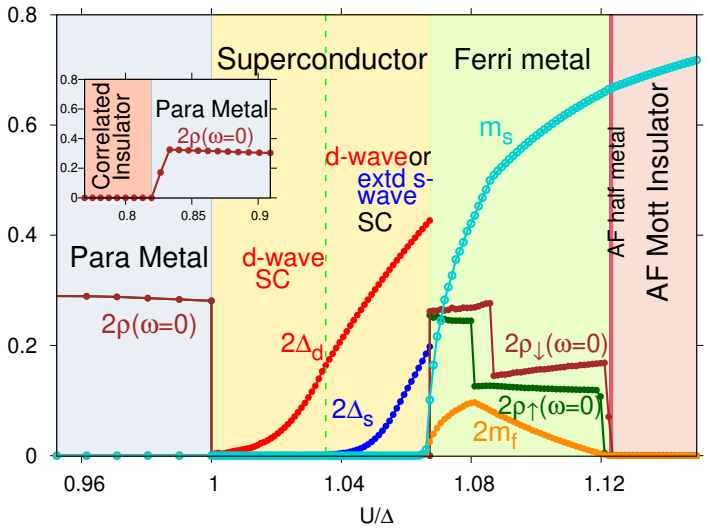

Figure 4.1: **Phase Diagram at a fixed** t' . The zero temperature phase diagram for the 2d square lattice for $U = 10t$ and $t' = 0.4t$. For $\Delta \gg U \gg t$, the system is a correlated band insulator without any magnetic order which is adiabatically connected to the BI at $U = 0$. On increasing U, first the gap in the single particle excitation spectrum closes, as shown by the non-zero single particle density of states (DOS) at the Fermi energy $\rho(\omega = 0)$, resulting in a metallic phase. On further increasing U/Δ, superconductivity sets in and lasts over a broad range ($\Delta \in [9.3 : 10]t$) before the ferrimagnetic order with a non-zero staggered magnetization (m_s) and non zero uniform magnetization (m_f) sets in via a first order transition. This is a Ferri metal phase with $\rho_\uparrow(\omega = 0) \neq \rho_\downarrow(\omega = 0) > 0$. As U/Δ increases further, $m_f \to 0$ whence the magnetic order becomes AF. Furthermore, a spectral gap opens up for the up-spin electrons such that $\rho_\uparrow(\omega = 0) = 0$ while the down-spin electrons are still conducting with $\rho_\downarrow(\omega = 0)$ being finite, resulting in a sliver of AF half-metal. Eventually the system becomes a AF Mott insulator as U/Δ increases further. *Note that the SC phase is surrounded by metallic phases on both the sides.*

4.2 Ionic Hubbard model and the limit of strong correlations

Our starting point is a variant of the Hubbard model, known as the *ionic* Hubbard model (IHM), where, on a bipartite lattice with sub-lattices A and B, a staggered ionic potential $\Delta/2$ is present in addition to electron hopping and coulomb repulsion (U):

$$\begin{aligned}\mathcal{H} = \quad & -\sum_{i,j\sigma}(t_{ij}c^{\dagger}_{i\sigma}c_{j\sigma} + h.c.) - \mu\sum_i n_i \\ & -\tfrac{\Delta}{2}\sum_{i\in A} n_i + \tfrac{\Delta}{2}\sum_{i\in B} n_i + U\sum_i n_{i\uparrow}n_{i\downarrow}\end{aligned} \tag{4.1}$$

The amplitude for electrons with spin σ to hop between sites i and j is $t_{ij} = t$ for near-neighbors and $t_{ij} = t'$ for second neighbors. The chemical potential μ is chosen to fix the average site occupancy at $n = 1$, corresponding to half-filling. The staggered potential doubles the unit cell, and (for $t' < \Delta/4$) induces a gap between the two electronic bands that result, making the system a BI at half-filling when the Hubbard on-site interaction U is zero.

The parameter range of interest here is $U \sim \Delta \gg t, t'$, where a theoretical solution can be obtained based on a generalization of the projected wavefunctions method [1,2,4,10,38–40, 105]. In this limit and at half-filling, holons are energetically expensive on the A sites (with onsite potential $-\frac{\Delta}{2}$) and doublons are expensive on the B sites (with onsite potential $\frac{\Delta}{2}$); i.e., in the low energy subspace h_A and d_B are constrained to be zero (with d representing a doublon and h a holon). Consequently, we can carry out a similarity transformation to eliminate all hopping processes connecting the low and high energy sectors of the Hilbert space. Nevertheless, and unlike in the Hubbard model, in the half-filled IHM the system

still has charge dynamics through hopping processes which take place entirely within the low-energy Hilbert space, e.g., first neighbor processes such as $|d_A h_B\rangle \Leftrightarrow |\uparrow_A\downarrow_B\rangle$ and second neighbor hopping processes which allow doublons to hop on the A sublattice and holons to hop on the B sublattice. Further details can be found in Appendix C.1.

The effective low energy Hamiltonian at half-filling, H_{eff}, is an extended $t-t'-J-J'$ model acting on a projected Hilbert space:

$$\begin{aligned} H_{eff} &= -t\sum_{<ij>,\sigma}\mathcal{P}[c^{\dagger}_{iA\sigma}c_{jB\sigma}+h.c.]\mathcal{P} - t'\sum_{<<ij>>,\alpha,\sigma}\mathcal{P}[c^{\dagger}_{i\alpha\sigma}c_{j\alpha\sigma}+h.c.]\mathcal{P} \\ &+J'\sum_{<<ij>>}\mathcal{P}\left[S_{iA}.S_{jA}-\frac{1}{4}(2-n_{iA})(2-n_{jA})\right]+\left[S_{iB}.S_{jB}-\frac{1}{4}n_{iB}n_{jB}\right]\mathcal{P} \\ &+J\sum_{<ij>}\mathcal{P}(S_{iA}.S_{jB}-(2-n_{iA})n_{jB}/4)\mathcal{P}+H_0+H_d+H_{tr}-\mu\sum_i n_i+... \end{aligned} \tag{4.2}$$

Here $J = 2t^2/(U+\Delta)$ and $J' = 4t'^2/U$. H_0 is the rescaled Hubbard interaction term in the projected Hilbert space. $H_d(H_{tr})$ indicates other dimer (trimer) processes. We treat the projection constraint in H_{eff} using the generalized Gutzwiller approximation [10] and solve it using a renormalized Bogoliubov mean field theory. Gutzwiller approximations [1, 10, 39] of the sort we use have been well vetted against quantum Monte Carlo calculations [2, 4, 105] and dynamical mean field theory [106]. Details of the Gutzwiller approximation and the various terms in H_{eff} are given in Appendices C.1, C.2 and C.3.

4.3 Phase diagram and the order parameters

We solve the renormalized effective low energy Hamiltonian using three different versions of the renormalized mean field theory (RMFT). (1) To explore the SC phase, we use a generalized spin-symmetric Bogoliubov mean field theory, which basically maps

onto a two-site Bogoliubov-deGennes (BdG) mean field theory for each allowed k point in the BZ. We do a mean field decomposition of the various terms in the Hamiltonian, and self-consistently solve for the following mean fields : (a) pairing amplitude, $\Delta_{AB}^{\gamma} \equiv \langle c_{iA\uparrow}^{\dagger} c_{i+\gamma B\downarrow}^{\dagger} - c_{iA\downarrow}^{\dagger} c_{i+\gamma B\uparrow}^{\dagger} \rangle$, where γ is x or y, considering d-wave pairing symmetry ($\Delta_{AB}^{x} = -\Delta_{AB}^{y} \equiv \Delta_d$) and extended s-wave pairing symmetry ($\Delta_{AB}^{x} = \Delta_{AB}^{y} \equiv \Delta_s$) separately; (b) density difference between two sublattices, $\delta = (n_A - n_B)/2$; (c) inter sublattice Fock shifts, $\chi_{AB\sigma}^{(1)} = \langle c_{iA\sigma}^{\dagger} c_{jB\sigma} \rangle, j = i \pm x, i \pm y, \chi_{AB\sigma}^{(2)} = \langle c_{iA\sigma}^{\dagger} c_{jB\sigma} \rangle, j = i \pm 2x \pm y$ or $i \pm 2y \pm x$; and (d) intra sublattice Fock shift on A(B) sublattice, with $\chi_{\alpha\alpha\sigma} = \langle c_{i\alpha\sigma}^{\dagger} c_{i\pm 2x/2y\alpha\sigma}$+h.c.$\rangle$, and $\chi_{\alpha\alpha\sigma}^{'} = \langle c_{i\alpha\sigma}^{\dagger} c_{i\pm x\pm y\alpha\sigma}$+h.c.$\rangle$. (2) To explore the magnetic order and the phase transitions involved, we solve the renormalized Hamiltonian using standard mean field theory allowing non-zero values of the sublattice magnetization $m_\alpha = n_{\alpha\uparrow} - n_{\alpha\downarrow}$ with $\alpha = A, B$, from which one gets the staggered magnetization $m_s = (m_A - m_B)/2$ and the uniform magnetisation $m_f = (m_A + m_B)/2$, along with all other mean-fields mentioned above except for the SC pairing amplitudes $\Delta_{s/d}$. (3) The third calculation, where we allow for both the SC pairing amplitudes and the magnetization along with all other mean fields metioned above, uses a standard canonical transformation followed up by the Bogoliubov transformation to diagonalize the mean field Hamiltonian neglecting the inter-band pairing as weak. We solve the resulting RMFT self-consistent equations on the square lattice for various values of U, Δ and t' to obtain the phase diagram shown in Fig. 4.1 and Fig. 4.2 (See Appendix C.5 for details). In the parameter regime where solutions with nonzero SC pairing amplitudes and magnetization (from the first two calculations) are both viable, we compare the ground state energy of the two mean-field solutions to determine the stabler ground state. We finally compare the energy of this state with the one obtained in the third calculation to determine the true ground state.

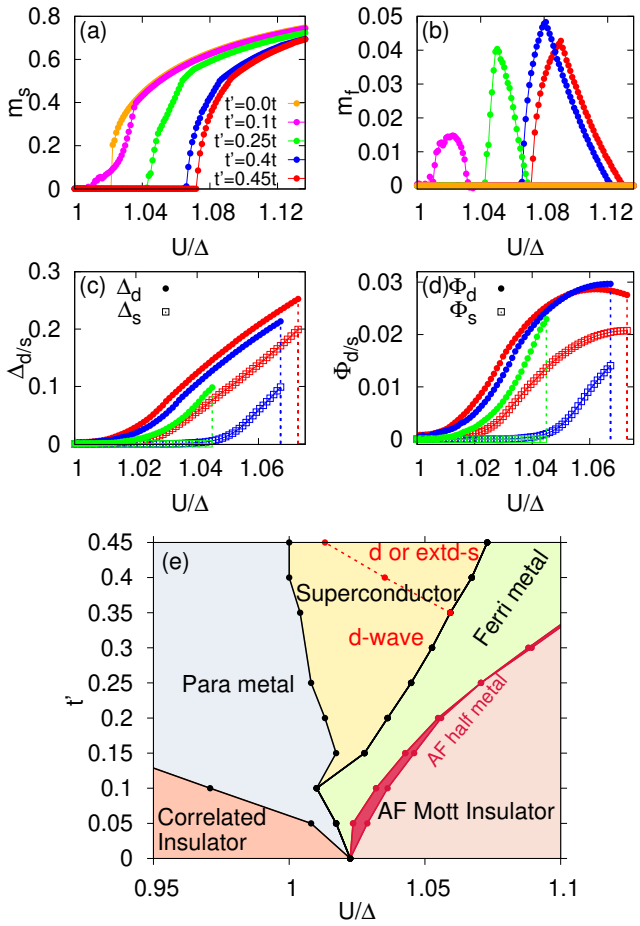

Figure 4.2: **Order Parameters and Complete Phase diagram.** Top panels show the staggered magnetization, m_s and the uniform magnetization, m_f as functions of U/Δ for several values of t' and $U = 10t$. With increasing t', the transition point at which the magnetic order turns on first decreases for $t' \leq 0.12$ and then starts increasing again. The magnetic transition is of first order for $t' = 0$ as well as for large values of t', though for intermediate values of t' the magnetization tuns on continuously. Panel (c) shows the SC pairing amplitude $\Delta_{d/s}$, for the d-wave and extended s-wave pairing symmetry. With increasing t' the range in U/Δ over which the superconductivity is stable gets wider, and the amplitudes of both d-wave and extended s-wave pairings get enhanced. Note that the extended s-wave order turns on only for $t' > 0.35t$. Panel (d) shows the SC order parameter $\Phi_{d/s}$, which also gives an estimate of the SC transition temperature, T_c. The bottom panel (e) shows the complete zero temperature phase diagram for $U = 10t$ in the t'-U/Δ plane. As we approach the SC phase from either the correlated band insualtor or the MI phase, the charge fluctuations build up gradually through metallic phases, and the superconductivity develops by the formation of coherent Cooper pairs between electrons which reside on the Fermi pockets of these metallic phases.

Our main findings are summarised in the phase diagram of Fig. 4.1, which shows a linear section (along the U/Δ axis) of the full phase diagram in Fig. 4.2[e], for the IHM on a 2d square lattice. The unconventional SC phase is sandwiched between paramagnetic and ferrimagnetic metallic phases, which in turn are sandwiched between a correlated band insulator and an AF Mott insulator (MI), along with an intervening sliver of AF half-metal. The correlated band insulator, stable for $\Delta \gg U \gg t$, is paramagnetic and adiabatically connected to the BI phase of the non-interacting IHM. As Δ approaches U, the low energy hopping processes ($|d_A h_B\rangle \Leftrightarrow |\uparrow_A \downarrow_B\rangle$) become more prominent, increasing charge-fluctuations such that the gap in the single particle excitation spectrum closes, leading to a finite density of states (DOS) $\rho(\omega = 0)$ at the Fermi energy, though for most of the parameter regime the resulting paramagnetic metallic (PM) phase is a compensated semi-metal with small Fermi pockets as shown in detail in Fig. 4.6. This PM phase is adiabatically connected to the metallic phase observed for weak to intermediate strength of U/t as long as $U \sim \Delta$ and the system is constrained to be paramagnetic, as shown in earlier work on the IHM using DMFT and other approaches [5, 41, 43, 44]. On further increasing U/Δ, in the presence of sufficiently large t', superconductivity sets in for $U \sim \Delta$ (irrespective of the strength of U/t, as shown in Fig. 4.3) due to the formation of coherent Cooper pairs of quasi-particles which live near the Fermi pockets, and survives for a broad range of U/Δ.

The pairing amplitude $\Delta_{d/s}$ for both the pairing symmetries we have studied, namely, the d-wave and the extended s-wave, increases monotonically with U/Δ and drops to zero via a first order transition at the transition to the ferrimagnetic metal. Though there is a metastable state in which the SC phase coexists along with the ferrimagnetic order for a range of U/Δ after the transition (see Appendix C.5 for details), due to the really tiny Zeeman splitting ($\leq 0.035t$ for $U = 10t$) produced by the small uniform magnetization m_f the possibility of a Fulde-Ferrel-Larkin-Ovchinnikov (FFLO) state seems unlikely [107–

109].

The ferrimagnetic metal (FM) phase is characterised by non-zero values of the staggered magnetization m_s as well as the uniform magnetization m_f, along with a finite DOS $\rho_\sigma(\omega = 0)$ at the Fermi energy. With further increase in U/Δ the FM evolves into an AF *half-metal* phase in which the system has only staggered magnetization (i.e., $m_f = 0$) and the single particle excitation spectrum for up-spin electrons is gapped while the down-spin electrons are still in a semi- metal phase. Eventually, for a large enough U/Δ, both the spin spectra become gapped, and the system becomes an AF MI. Though we have studied the IHM on a square lattice, a qualitatively similar phase diagram is expected on any bipartite lattice, but with changes involving appropriate symmetries, e.g., $d + id$ pairing symmetry on a honeycomb lattice.

We next discuss the changes in behavior of the system with increasing U/Δ for varying values of t', as depicted in Fig. 4.2. For $t' = 0$, the system shows a direct first order transition from an AF ordered phase to a correlated band insulator with a sliver of a half-metallic AF phase close to the AF transition point. This is consistent with a variational quantum Monte Carlo study of the half-filled IHM for $t' = 0$ [110] as well as with most other earlier work [6, 7]. When t' is non-zero, due to the breaking of particle-hole symmetry as well as the frustration induced by the second neighbor spin-exchange coupling J', the system first attains ferrimagnetic order characterized by non-zero values of both the staggered (m_s) and the uniform (m_f) magnetizations, for a range of U/Δ, beyond which it has pure AF order as shown in panel (a) of Fig. 4.2. The magnetic transition occurs at increasingly larger values of U/Δ with increasing t' (except for an initial decrease for small values of t') which helps in the development of a stable SC phase.

To stabilize the superconducting phase, a minimum threshold value of t' (which is a function of U) is required, partly in order to frustrate the magnetic order as mentioned

above, but more importantly to gain sufficient kinetic energy by intra-sublattice hopping of holons and doublons on their respective sublattices where they are energetically allowed. While a stable d-wave SC phase turns on for $t' > 0.1t$ for $U = 10t$, as shown in Fig. 4.2 , superconductivity in the extended s-wave channel gets stabilized for the much larger value of $t' > 0.35t$. In an intermediate regime of U/Δ and t', states with both d-wave and extended s-wave symmetry are viable solutions with energies that are very close (See Appendix C.5 for details). As t' increases, the pairing amplitude increases and the range of U/Δ over which the SC phase exists becomes broader for both the pairing symmetries studied. Though t' helps in the formation of the SC phase with pairing amplitudes living on the nearest neighbor bonds, there is no significant second neighbor pairing induced by J'.

The pairing amplitude discussed above signals the strength of Cooper pairing on a bond, but the SC order parameter $\Phi_{d/s}$ is defined in terms of the off-diagonal long-range order in the correlation function $F_{\gamma_1\gamma_2}(\mathbf{r}_i - \mathbf{r}_j) = \langle B^\dagger_{i\gamma_1} B_{j\gamma_2} \rangle$ where $B^\dagger_{i\gamma}$ creates a singlet on the bond $(i, i+\gamma)$. Fig. 4.2 shows the SC order parameter, which has been obtained after taking care of renormalization required in $F_{\gamma_1\gamma_2}(\mathbf{r}_i - \mathbf{r}_j)$ in the projected wavefunction scheme (see Methods section). Since the SC order parameter for this system is much smaller than the strength of the pairing amplitude, with increase in temperature the superconductivity will be destroyed at T_c by the loss of coherence among the Cooper pairs, leaving behind a pseudo-gap phase with a soft gap in the single particle density of states due to the Cooper pairs which will exist even for $T > T_c$. Thus $\Phi_{d/s}$ also provides an estimate of the SC transition temperature T_c. The maximum estimated T_c for $U = 10t$ on a square lattice is approximately $0.03t$ for the d-wave SC phase, which for a hopping amplitude comparable to that in cuprates ($t \sim 0.4eV$) gives a $T_c \sim 150K$, and there is a considerable scope for enhancing T_c by tuning U/Δ as well as t'.

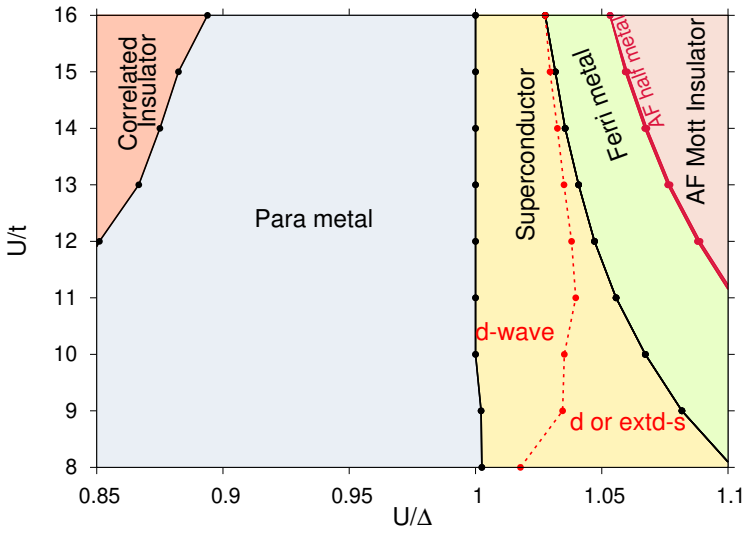

Figure 4.3: **Phase diagram in $\mathbf{U/t - U/\Delta}$ plane**. Phase diagram of the half-filled IHM on a 2d square lattice in $U/t - U/\Delta$ plane for $t' = 0.4t$. Note that the SC phase always turns on for $U \sim \Delta$ irrespective of the value of U/t within the range of validity of the calculation. As U/t increases, the range of U/Δ over which both the s-wave and the d-wave SC phases are viable solutions and almost degenerate shrinks rapidly while the range of U/Δ over which only the d-wave SC phase is stable reduces rather slowly.

Earlier in this chapter we have shown and discussed the phase-diagrams for the IHM on a 2d square lattice for a fixed value of U/t. Fig. 4.2[e] shows the phase diagram in $t'/t - U/\Delta$ plane for a fixed U and Fig. 4.1 shows a section of this phase diagram for $t' = 0.4t$. In order to understand how the different phases and the phase boundaries between them evolve with varying U, here we show in Fig. 4.3 the phase diagram in $U/t - U/\Delta$ plane for a fixed t'/t. As is clear from the figure, superconductivity always turns on for $U \sim \Delta$ irrespective of the value of U/t though with increase in U/t, the range of U/Δ over which both pairing symmetries are almost degenerate solutions shrinks rapidly such that eventually, for large enough values of U/t, the system has only a d-wave SC phase.

All the results presented so far in the chapter are for the 2d square lattice. We would like to emphasize that within the renormalized mean field theory the phase diagram is

qualitatively similar for higher dimensional systems as well. This is clear from Fig. 4.4 which shows the phase diagram for a cubic lattice.

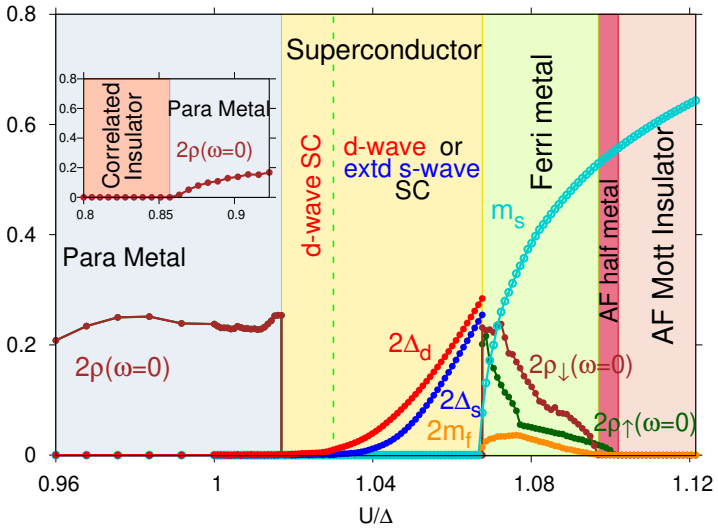

Figure 4.4: **Phase diagram for cubic lattice**. Phase diagram of the half-filled IHM on a 3d cubic lattice for $U = 12t$ and $t' = 0.35t$. Note that the phase diagram obtained for cubic lattice is qualitatively similar to the one obtained for a 2d square lattice.

We note that, in an earlier work [80] on the strongly correlated half-filled IHM with $t' = 0$, (i.e., in the absence of any of the frustration effects we have discussed above,) using slave bosons to represent the projection processes in Eq. 4.2, and using a slave-boson mean field theory approach to treat the problem, SC was shown to exist when $U \sim \Delta >> t$. However, this result is not consistent with the variational quantum Monte-Carlo study mentioned above [110] where no SC phase was reported at half-filling in the absence of frustration against the magnetic order. Within the Gutzwiller projection approach, while we do find regions of parameter space inside the AFI region where SC pairing is viable even in the $t' = 0$ case, the SC phase has higher energy than the AFI phase and is therefore metastable [106]; and as we have demonstrated above, only in the presence of sufficient frustration against the magnetic order does SC exist in this simple model of a band-insulator

at *half-filling*.

4.4 Low energy spectral functions

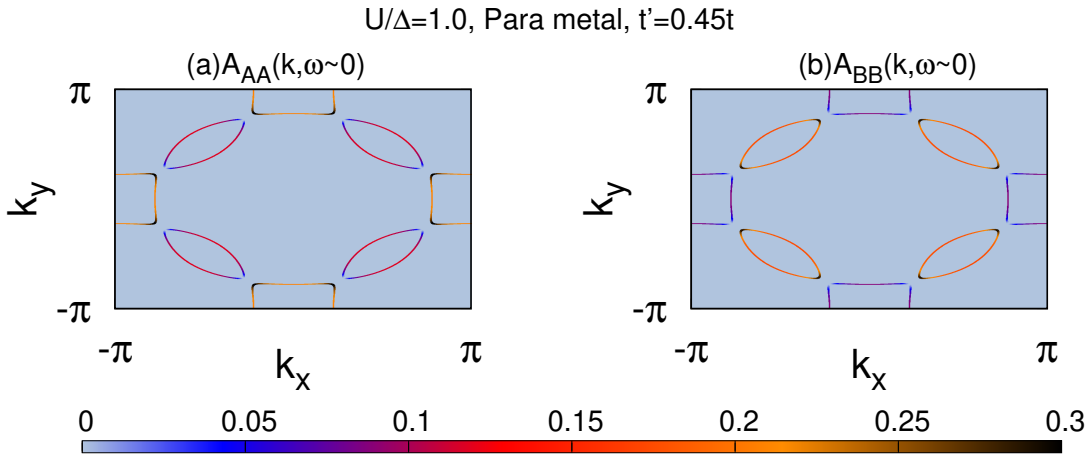

Figure 4.5: **Sublattice specific spectral functions.** $A_{AA}(k, \omega \sim 0)$ and $A_{BB}(k, \omega \sim 0)$ in the para metallic phase. The non-zero quasiparticle weights have k-dependence along the Fermi pockets.

A striking feature of the phase diagram in Fig. 4.2 is that, though the origin of superconductivity in this model lies predominantly in the spin-exchange interactions (with a weaker contribution from other dimer and trimer terms), superconductivity sets in only after the system has evolved to a para metallic or a FM phase. Here, we first show the sublattice specific low energy spectral functions, $A_{AA}(k, \omega \sim 0)$ and $A_{BB}(k, \omega \sim 0)$ in the para metallic phase which are obtained from the retarded Green's functions in the case of the calculation where pairing has not been allowed (Refer to Eq. C.28 of Appendix C.4.1). As shown in Fig. 4.5, the sublattice specific spectral functions vary over the Fermi contours to a large extent. However, the experimentally relevant quantity is the sublattice averaged

single particle spectral function, $A(k,\omega) = \frac{1}{2}(A_{AA}(k,\omega) + A_{BB}(k,\omega))$. In this case in the para metallic phase, the non-zero quasiparticle weight will have no k-dependence and is constant over the Fermi pockets where as in the ferri metallic phase there will be very weak k-dependence along the Fermi pockets (Refer to Eq. C.26 of Appendix C.4.1 for details). Henceforth, we will be looking at only the sublattice averaged spectral functions.

In order to understand the charge dynamics as the system approaches the SC phase with the tuning of U/Δ, we have analysed the single particle spectral functions which can be directly measured in angle resolved photoemission spectroscopy (ARPES). Fig. 4.6 shows the low energy spin resolved spectral functions $A_\sigma(k,\omega \sim 0)$, the non-zero value of which determine the energy contour on which low energy quasiparticles live in the Brillouin zone (BZ) (see Appendices C.1, C.4.1, C.4.2 for details). Panels (a-c) show $A_\sigma(k,w \sim 0)$ in the FM phase for which the up-spin channel has electron pockets around the points $\mathbf{K} = (\pm\pi/2, \pm\pi/2)$ in the BZ and the down spin spectrum has small hole pockets around the points $\mathbf{K}' = (\pm\pi, 0), (0, \pm\pi)$ in the BZ as shown in panel (a). As U/Δ decreases within the FM phase, and approaches the SC phase, the electron pockets (hole-pockets) in the up-spin (down-spin) spectral function become bigger, the down-spin channel gets additional electron pockets while the up-spin channel gets additional hole pockets as shown in panel (c).

In the PM phase, the low energy spectral functions have both electron pockets (around $\mathbf{K}$) as well as the hole pockets (around $\mathbf{K}'$). As U/Δ increases through the PM phase, these Fermi pockets slowly expand such that they almost touch each other before the system enters into the SC phase. Similar behavior is seen with an increase of t' in the PM or the FM phases.

In order to understand the charge dynamics as the system approaches the SC phase with the tuning of second neighbor hopping, t', we have analysed the single particle spectral

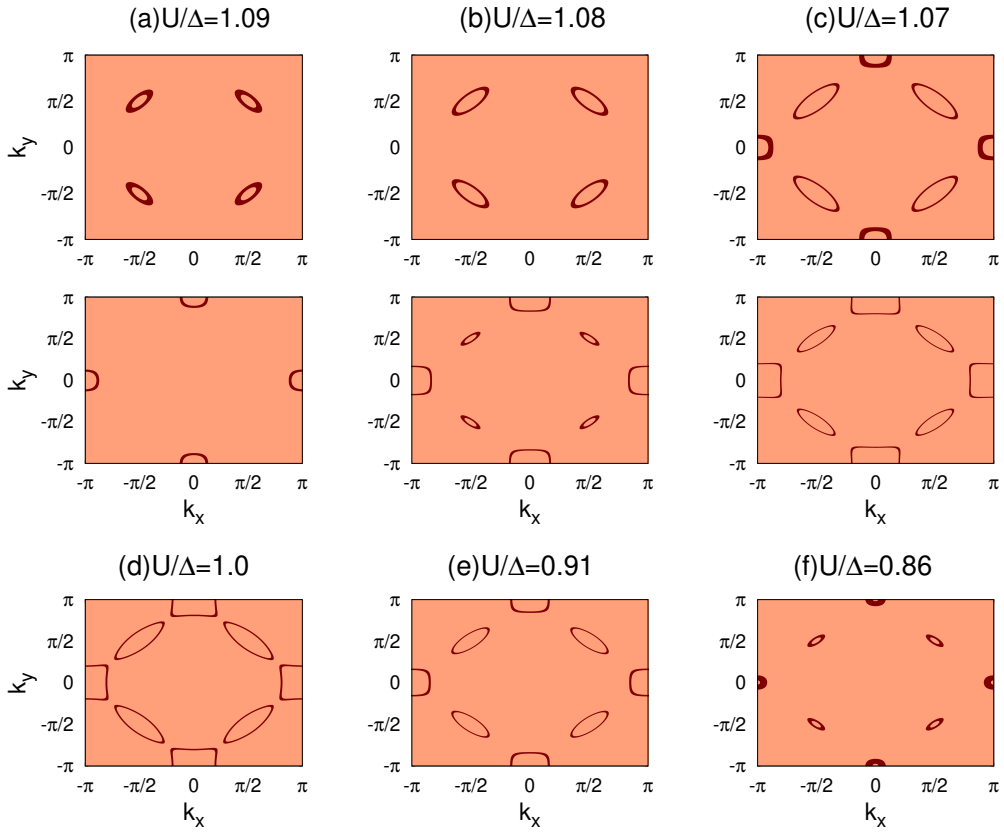

Figure 4.6: **Spectral Functions.** The top two rows show the spin resolved low energy spectral functions $A_\sigma(k, \omega \sim 0)$ (integrated over $|\omega| \leq (0.01 - 0.02)t$ for a 3000×3000 system) in the full Brillouin Zone (BZ) for $t' = 0.35t, U = 10t$, to emphasize how the charge fluctuations evolve as we approach the SC regime from the ferri metal side, with $A_\uparrow(k, \omega \sim 0)(A_\downarrow(k, \omega \sim 0))$ shown in the first (second) row. At $U/\Delta = 1.09$, the up spin channel has electron pockets while the down spin channel has small hole pockets. As U/Δ decreases, these Fermi pockets become bigger, the down spin spectral function gets additional electron pockets and the up-spin spectral functions get additional hole pockets. The last row shows $A(k, \omega \sim 0)$ (same for up or down spins) for the para metal phase. Moving towards the SC phase by increasing U/Δ, Fermi pockets in the para metallic state go on expanding until they almost start touching each other, at which point the superconductivity sets in by formation of Cooper pairs between electrons close to the Fermi energy.

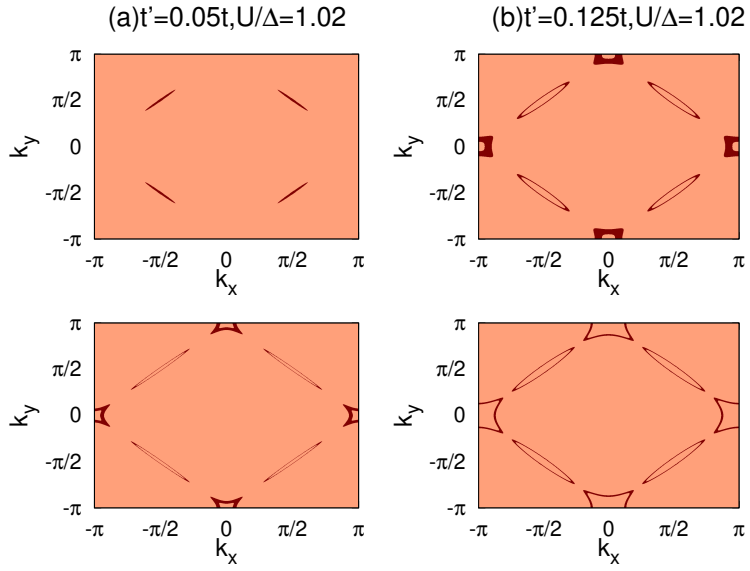

Figure 4.7: **Spectral functions for varying t'**. Here we show the low energy spectral functions $A_\sigma(k, \omega \sim 0)$ (integrated over $|\omega| \leq (0.01 - 0.02)t$ on a 3000×3000 lattice) in the full Brillouin zone (BZ) for the ferrimagnetic phase at a fixed $U/\Delta = 1.02$ and for two values of t'. Upper panels show $A_\uparrow(k, \omega \sim 0)$, and the bottom panels $A_\downarrow(k, \omega \sim 0)$.

functions for a fixed U/Δ in the ferrimagnetic metallic phase. We can understand why the SC phase does not get stabilized for small values of t' by looking at the evolution of $A_\sigma(k, \omega \sim 0)$ for a fixed U/Δ as one tunes t'. Fig. 4.7 shows $A_\sigma(k, \omega \sim 0)$ close to the magnetic transition point of $t' = 0$, that is, for $U/\Delta = 1.02$. For small values of t', at this value of U/Δ the system is in the ferrimagnetic metal phase. As we increase t' inside the ferrimagnetic metal phase, the up spin spectral functions get bigger electron pockets around $\mathbf{K} = (\pm\pi/2, \pm\pi/2)$ points while the down spin spectral functions get bigger hole pockets around $\mathbf{K}' = (\pm\pi, 0), (0, \pm\pi)$ points. In addition to this, as t' increases even the up-spin spectral functions get hole pockets and the down spin spectral functions get electron pockets. As a result of both these effects, an almost connected contour of Fermi pockets is formed, whence superconductivity emerges by the formation of Cooper pairs of

the corresponding low energy quasiparticles.

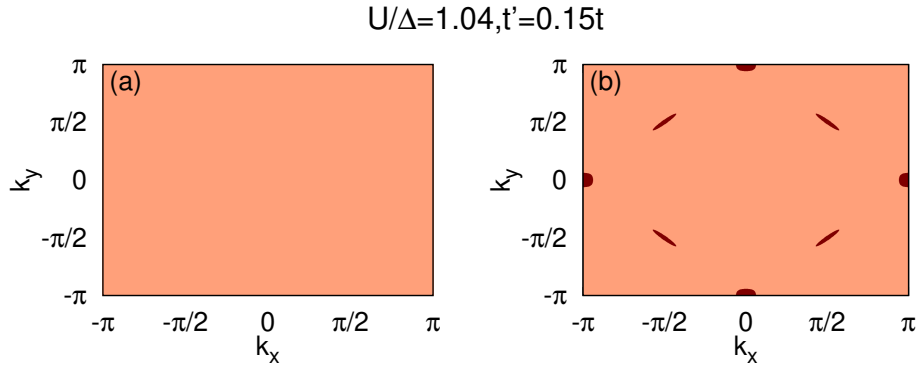

Figure 4.8: **Spectral functions in the AF half-metal phase**. Spin resolved low energy spectral function $A_\sigma(k, \omega \sim 0)$ (integrated over $|\omega| \leq 0.01t$) in the AF half-metal phase. Left (right) panel shows the spectral function for the up-spin (down-spin) channel.

We also show the low energy spectral function $A_\sigma(k, \omega \sim 0)$ for the AF half-metal phase (see Fig. 4.8), which is fully consistent with the band-dispersions shown above. The up-spin channel is gapped while $A_\downarrow(k, \omega \sim 0)$ has tiny electron pockets at the $\mathbf{K}$ points and hole pockets at the $\mathbf{K}'$ points in the BZ.

The electron and hole pockets mentioned above, are best identified based on the momentum distribution function $n_\sigma(k)$ as defined in Appendix C.1. $n_\sigma(k)$ is uniformly half in the entire BZ for any insulating phase of the model studied here. When the system goes into a metallic phase, at least one of the bands cross the Fermi level resulting in filled or empty Fermi pockets depending on the curvature of the band. Filled Fermi pockets, also called electron pockets, have $n_\sigma(k) > 1/2$, while empty Fermi pockets, also called hole pockets, have $n_\sigma(k) < 1/2$. Fig. 4.9 shows $n_\sigma(k)$ for $t' = 0.35t$ for two values of U/Δ. Panel (a) shows the result for the ferrimagnetic metal phase and panel (b) shows the results in the para metal phase. In the ferri-metal phase, $n_\uparrow(k)$ has filled pockets around the $\mathbf{K}$

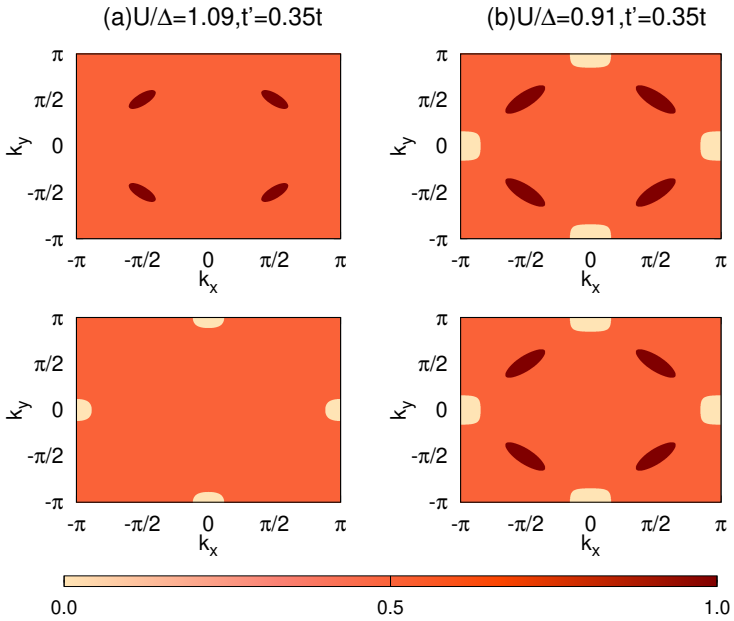

Figure 4.9: **Momentum Distribution Function**. Momentum distribution function $n_\sigma(k)$ in the ferrimagnetic metal and the para metal phases for $t' = 0.35t$. In the ferrimagnetic metal phase shown in panel (a) $n_\uparrow(k) > 1/2$ on (electron) pockets centered around the $\mathbf{K}$ points while $n_\downarrow(k) < 1/2$ on (hole) pockets centered around the $\mathbf{K}'$ points in the BZ. Panel (b) shows the results for the paramagnetic metal phase, where the systen has spin symmetry and $n_\sigma(k) < 1/2$ around the $\mathbf{K}'$ points while $n_\sigma(k) > 1/2$ around the $\mathbf{K}$ points for both the spin components. Everywhere else in the BZ $n_\sigma(k) = 1/2$ in all the panels.

points while the down-spin component has hole pockets around the $\mathbf{K}'$ points in the BZ. In the para-metal phase, shown in panel (b), there is a spin symmetry and $n_\sigma(k)$ has electron and hole pockets for both the spin channels.

Nature of Fermi pockets

Fig. 4.10 shows the band dispersion $E_{n\sigma}(k)$ for both the bands on paths along high symmetry directions in the BZ. In the AF half-metal phase, the down spin channel has small hole pockets around $\mathbf{K}'$ and tiny electron pockets around $\mathbf{K}$. In the Ferrimagnetic metal

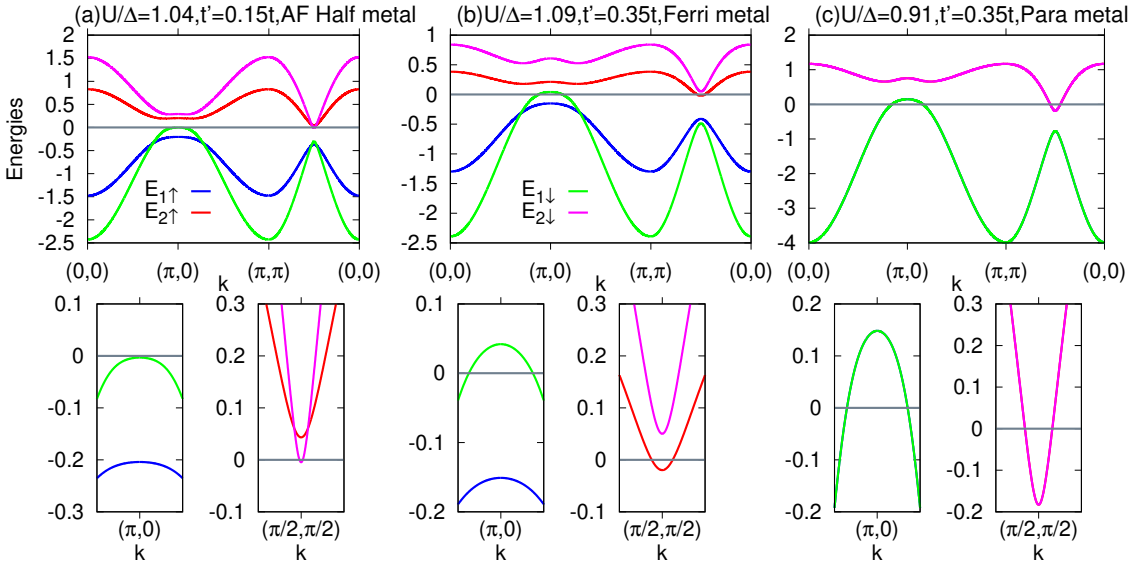

Figure 4.10: **Band Dispersion**. Band dispersion $E_{n\sigma}(k)$ on paths along high symmetry directions in the BZ. Panel (a) shows bands in the AF half-metal phase where both the down spin bands cross the Fermi level near the $\mathbf{K}$ and $\mathbf{K}'$ points while the up spin bands are fully gapped. Panel (b) shows bands in the ferrimagnetic metal phase, where one down-spin band crosses the Fermi level near the $\mathbf{K}'$ points while one up-spin band crosses the Fermi level near the $\mathbf{K}$ point and the other two bands are gapped. Panel (c) shows bands in the paramagnetic metal phase where there is a spin symmetry and all the bands cross the Fermi level. The lower panels zoom in close to the band crossing at the Fermi energy.

phase, the down spin band $E_{1\downarrow}(k)$ crosses the Fermi energy around the $\mathbf{K}'$ points resulting in small hole pockets and $E_{2\uparrow}(k)$ crosses the Fermi energy near the $\mathbf{K}$ points resulting in small electron pockets. In the paramagnetic metal phase, $E_1(k)$ crosses the Fermi energy around the $\mathbf{K}'$ points resulting in hole pockets and $E_2(k)$ crosses the Fermi level around $\mathbf{K}$ resulting in electron pockets, where, because of the spin symmetry, we have suppressed the spin indices.

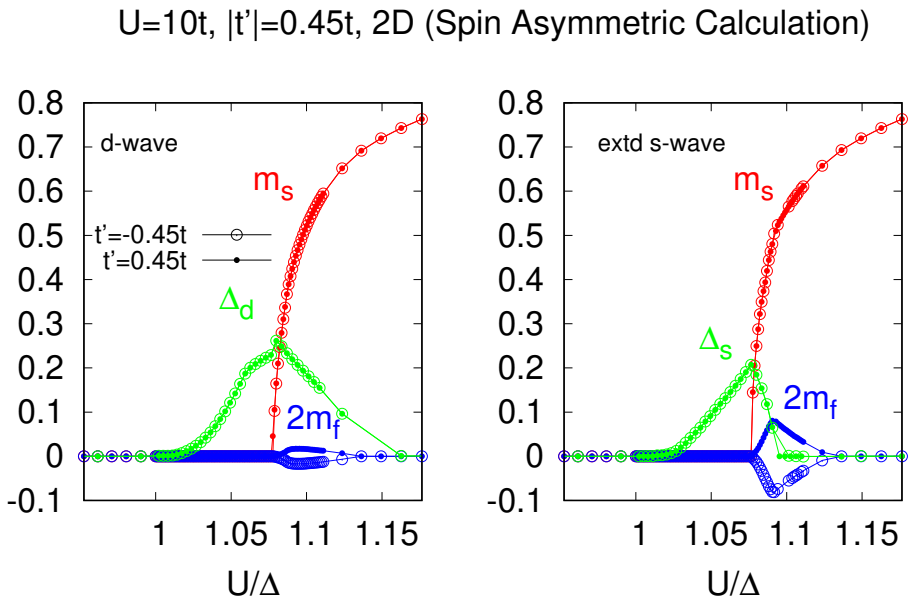

Figure 4.11: **Comparison between +ve and -ve t'.** The pairing amplitude and magnetic order parameters for $t' = 0.45t$ and $t = 0.45t$. As shown only m_f changes due to related particle hole symmetry between the model with +ve and ve values of t'.

Sign of t' and related p-h symmetry

Although the analysis so far presented is for positive values of t', we would like to emphasize that the phase diagram is invariant under the reflection symmetry of the next neighbor hopping amplitude. The Hamiltonians in the two cases are simply related through a particle hole transformation (as described in chapter 1),

$$\begin{aligned} c^{\dagger}_{iA\sigma} &\rightarrow c_{jB\sigma}, \\ c^{\dagger}_{jB\sigma} &\rightarrow -c_{iA\sigma}. \end{aligned} \tag{4.3}$$

Under this transformation the Hamiltonian of the IHM with positive value of t' gets mapped to the Hamiltonian with negative value of t', the other terms remaining invariant

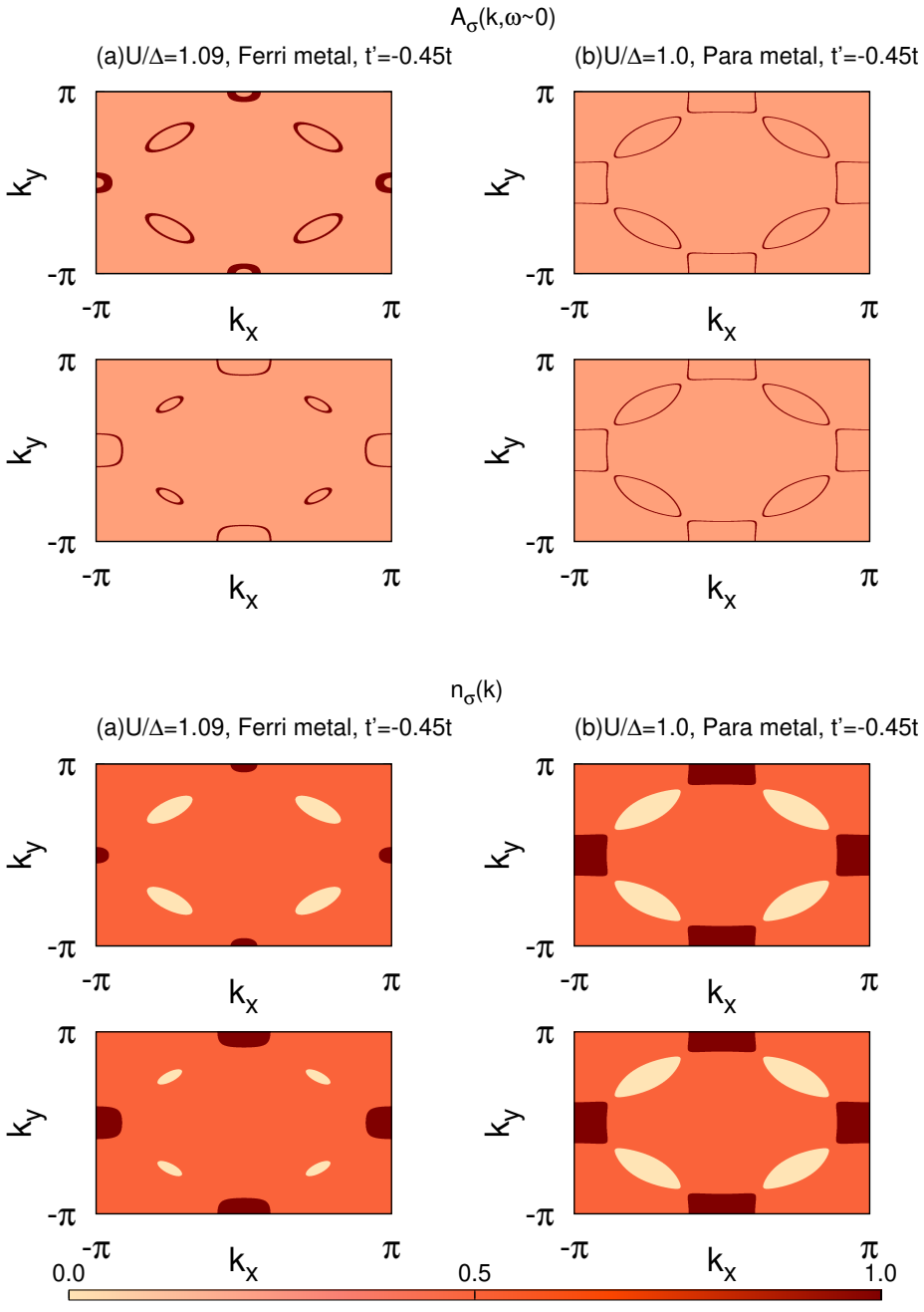

Figure 4.12: **Spectral functions and momentum distribution functions for -ve t'.** Top panel shows the spectral functions in the metallic phases for $t' = 0.45t$. First row is for spin-up and the second row is for the spin-down component. The bottom panel shows the momentum distribution function $n_{k\sigma}$ in the metallic phases for $t' = 0.45t$. Comparison of this plot with Fig. 4.9 shows that the hole and electron pockets get interchanged for negative values of t'. For negative values of t', we have electron pockets around $(\pm\pi, 0)$ and symmetrically related points while we have hole pockets around $(\pm\pi/2, \pm\pi/2)$ points.

under the transformation.

Accordingly, in the spin asymmetric phase $m_A \rightarrow -m_B$ and vice-versa such that the staggered magnetisation, m_s remains invariant. However, the uniform magnetisation, m_f flips in sign. The pairing amplitude, Δ_{AB} remains invariant under this transformation. These are shown in Fig. 4.11. Also, shown in Fig. 4.12 are the spectral functions in the case of negative t'. Under this transformation the electron and hole pockets switch i.e., the electron pockets now appear at $K' = (0, \pm\pi), (\pm\pi, 0)$ and the hole pockets appear at $K = (\pm\pi/2, \pm\pi/2)$.

4.5 Single particle density of states

Fig. 4.13. shows the spin-resolved single particle density of states (DOS) $\rho_\sigma(\omega)$ which can be measured directly in scanning tunneling spectroscopy (STS) experiments and provides additional evidence for the existence of various metallic phases as in the phase diagram in Fig. 4.2. The DOS at $\omega = 0$ for these phases was presented in Fig. 4.1 as a function of U/Δ, and here we present the full $\rho_\sigma(\omega)$ vs ω. The para metal, ferri-metal and the AF half-metal phases are all compensated semi metals, which is reflected in the depletion in the DOS at the Fermi energy and is consistent with the small Fermi pockets shown in Fig. 4.6. We have also analysed the DOS in the SC phase. As shown in Fig. 4.13[d], $\rho(\omega \sim 0) \sim |\omega|$ which is a signature of the gapless nodal excitations in the d-wave SC phase. Interestingly, even for the extended s-wave SC phase $\rho(\omega \sim 0) \sim |\omega|$ as the pairing takes place around small Fermi pockets which are centered at $\mathbf{K}$ or $\mathbf{K}'$ points in the BZ where the pairing amplitude $\Delta_s(k) = \Delta_s(\cos(k_x) + \cos(k_y))$ has nodes as well, resulting in gapless excitations. The gap, which is the peak to peak distance in the DOS, is much larger in the d-wave SC phase than in the extended s-wave phase, consistent with the former being the stable phase. Infact

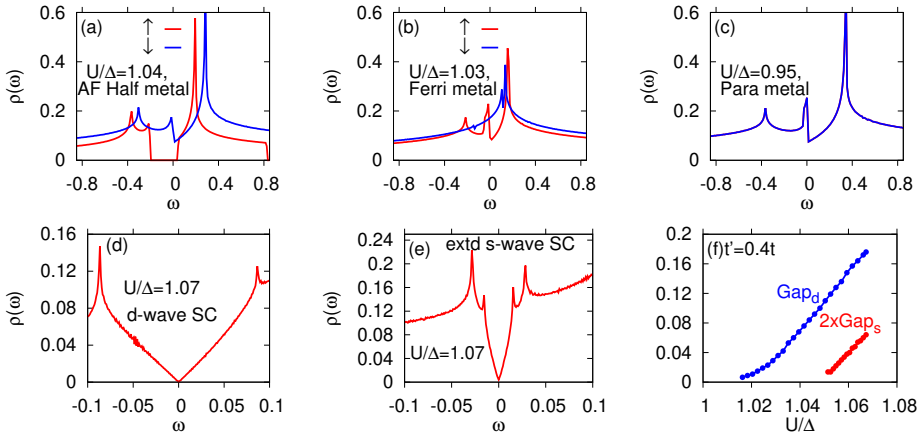

Figure 4.13: **Single particle Density of states.** Panels (a)-(c) show the spin resolved single particle density of states (DOS) $\rho_\sigma(\omega)$ for $t' = 0.15t$ and $U = 10t$. At $U/\Delta \sim 1.04$, $\rho_\downarrow(\omega = 0)$ is finite where as $\rho_\uparrow(\omega = 0) = 0$ with a finite spectral gap, corresponding to the AF half-metal phase. At $U/\Delta = 1.03$, the DOS at the Fermi energy is finite in both the spin channels but $\rho_\uparrow(\omega) \neq \rho_\downarrow(\omega)$ corresponding to the ferri metal phase. At $U/\Delta = 0.95$, the DOS is spin symmetric with a finite weight $\rho_\sigma(\omega = 0)$ at the Fermi energy and the system is a para metal. Panel (d) shows $\rho(\omega)$ for the d-wave SC phase while panel (e) shows that for the extended s-wave SC phase for $U = 10t$ and $t' = 0.4t$. $\rho(\omega)$ shows a linear increase with $|\omega|$ for $\omega \sim 0$ for both the SC phases. Panel (f) shows the gap in the DOS, which is basically the peak to peak distance in $\rho_\sigma(\omega)$, for both the d-wave and the extended s-wave pairing symmetries.

for the extended s-wave phase, Gap_s is only slightly larger than the SC order parameter Φ_s, which indicates that the extended s-wave SC phase will have a narrower pseudogap phase above T_c, compared to the d-wave case. The gaps in the d-wave and extended s-wave pairing channels are proportional to the Gutzwiller renormalized pairing amplitudes in the respective channels.

4.6 Conclusions

As mentioned in the introduction, the origin as well as the basic features of unconventional SC in most of the superconducting materials known today [3, 13, 14, 16] can be understood,

at least at the broad qualitative level [2, 13, 16, 69, 103, 104], in terms of the strongly correlated limit of the Hubbard model (single or multi band), but only upon doping the system away from half-filling. In the theoretical model we have studied here, superconductivity appears even at half-filling, and therefore without the disorder that inevitably accompanies doping, in the special strongly correlated limit where $U, \Delta \gg t, t'$ and the second neighbor hopping is sufficiently strong. A remarkable feature is that the SC phase in this model of a correlated band insulator is sandwiched between paramagnetic metallic and ferrimagnetic metallic phases (Fig. 4.2[e]), which makes the zero temperature phase diagram very different from that of the known unconventional superconductors like high T_c cuprates [16] or the more recent magic angle twisted bilayer graphene [14]. We expect that the SC phase in this model has transition temperatures comparable to those of cuprates and that it also has a pseudogap phase like in cuprates.

The question as to what are the possible experimental situations where this mechanism of superconductivity at half-filling, with its promise of large transition temperatures and no intrinsic disorder, can be realized is of obvious importance. Since the IHM has been realized for ultracold fermions on an optical honeycomb lattice [8], where the state-of-the art engineering allows the parameters in the Hamiltonian to be tuned with great control, it will be interesting and perhaps the easiest to explore our theoretical proposal in these systems. Due to the recent developments in layered materials and heterostructures, it is indeed possible to think of many scenarios where the IHM can be used as a minimal model, for example, graphene on h-BN substrate and bilayer graphene in the presence of a transverse electric field [66], which plays the role of the staggered potential. The limit of strong correlation, crucial for realizing the SC phase, can be achieved in these materials by applying a strain or twist. Band insulating systems with two inequivalent strongly correlated atoms per unit cell, frustration in hopping and antiferromagnetic exchange, and lack of

particle-hole symmetry, are likely tantalizing candidate materials as well. The work presented in this chapter suggests that further theoretical and experimental exploration of such novel possibilities where superconductivity can be realized with sufficiently high transition temperatures without doping in strongly correlated band insulators is an exciting and worthwhile pursuit.

APPENDIX A

APPENDIX

A.1 Derivation of the tJ model

In the strong correlation limit of the Hubbard model, double occupancies belong to the high energy sector. Through a Schrieffer Wolff transformation, all hopping processes connecting low and high energy sectors are eliminated and finally if we confine to the low energy space, we obtain the low enrgy effective Hamiltonian in the projected space known as the tJ model. In this section, we go through the steps for deriving the effective Hamiltonian.

As a first step for finding the effective Hamiltonian, we have to do a similarity transformation given by,

$$\tilde{H} = e^{-iS} H e^{iS}, \tag{A.1}$$

where S is the similarity operator. Upon expanding the exponentials, the effective Hamiltonian $\tilde{H}$ looks like,

$$\tilde{H} = H_0 + H_t^{low} + H_t^{high} + H_t^{low\leftrightarrow high} + i[S, H_0] + i[S, H_t] + \frac{i^2}{2}[S, [S, H_0]] + ..., \quad \text{(A.2)}$$

where H_0 is the unperturbed part of the Hamiltonian consisting of the Coulomb and the chemical potential terms, H_t is the hopping term which is introduced perturbatively into the system and is a sum of H_t^{low}, H_t^{high} and $H_t^{low\leftrightarrow high}$. H_t^{low} is confined to the low energy Hilbert space in the sense that doublons are not involved in this process whereas H_t^{high} is the process which involves doublons in both the initial and final states. $H_t^{low\leftrightarrow high}$ are processes which connect the low and high energy Hilbert spaces in the sense that doublons, which belong to the high energy sector, are present either in the initial or final state. Below we pictorially show the classification of hopping processes and their expression in terms of fermionic operators.

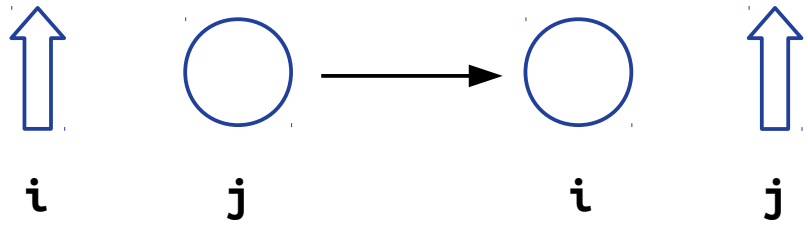

Figure A.1: Figure shows the effective hopping of a hole and lies in the low energy Hilbert space. We call it H_t^{low}.

Fig. A.1 represents the low energy hopping of holes which can be expressed in fermionic language as,

$$H_t^{low} = -t \sum_{<ij>,\sigma} c_{j\sigma}^{\dagger}(1 - n_{j\bar{\sigma}})(1 - n_{i\bar{\sigma}})c_{i\sigma} + H.c. \quad \text{(A.3)}$$

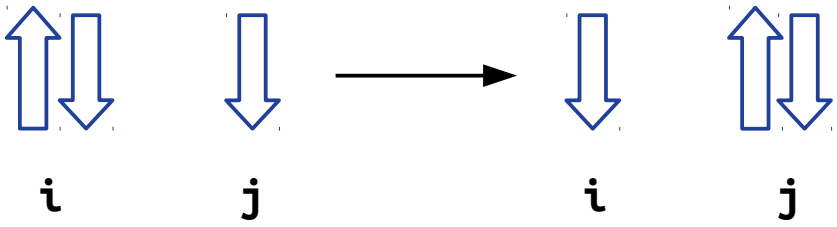

Figure A.2: Figure shows the effective hopping of a doublon and lies in the high energy Hilbert space. We call it H_t^{high}.

Fig. A.2 represents the high energy hopping of doublons which can be expressed in fermionic language as,

$$H_t^{high} = -t \sum_{<ij>,\sigma} c_{j\sigma}^{\dagger} n_{j\bar{\sigma}} n_{i\bar{\sigma}} c_{i\sigma} + H.c. \tag{A.4}$$

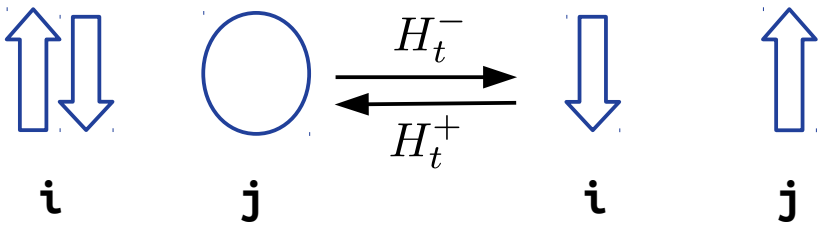

Figure A.3: Figure shows the unpairing of a doublon into single occupancies and vice-versa. It connects the high energy Hilbert space (left) to low energy Hilbert space (right). We call it $H_t^{low \leftrightarrow high}$.

Fig. A.3 represents hopping processes which connect the low energy Hilbert space to the high energy Hilbert space. Doublons either unpair or form through hopping, mixing low energy configurations like the single occupancies to the high energy configuration which in this case is the doublon. These two conjugate processes are expressed in the fermionic language as,

$$H_t^{low\leftrightarrow high} = -t \sum_{<ij>,\sigma} c_{j\sigma}^{\dagger}(1 - n_{j\bar{\sigma}})n_{i\bar{\sigma}}c_{i\sigma} + i \leftrightarrow j + H.c. \tag{A.5}$$

We choose the similarity operator, S in such a way that,

$$i[S, H_0] = -H_t^{low\leftrightarrow high}. \tag{A.6}$$

Therefore, the parts of the hopping that mixes the low and high energy Hilbert spaces are thus eliminated from the effective Hamiltonian. In this case,

$$S = -\frac{i}{U}(H_t^{+} - H_t^{-}), \tag{A.7}$$

where H_t^{+} are processes which increase the number of doublons and holes by one and is represented by the process given by the backward arrow of Fig. A.3. On the other hand, H_t^{-} are processes which decrease the number of doublons and holes by one and is represented by the process given by the forward arrow of Fig. A.3.

If we plug in S in rest of the terms of the Hamiltonian we get,

$$\tilde{H} = H_t^0 + H_0 + \frac{1}{U}[H_t^{+}, H_t^{-}], \tag{A.8}$$

where $H_t^0 = H_t^{low} + H_t^{high}$ represent processes which do not change the number of double occupancies or holes.

We now introduce Hubbard operators $X^{\phi\leftarrow\psi} = |\phi\rangle\langle\psi|$ which represents a process in which state ϕ is created from state ψ. ϕ and ψ belong to the configuration space of a spin $\frac{1}{2}$ particle. The hopping terms in language of these Hubbard operators are expressed as,

$$H_t^0 = -t \sum_{<ij>,\sigma} [X_i^{0\leftarrow\sigma} X_j^{\sigma\leftarrow 0} + X_i^{\bar{\sigma}\leftarrow d} X_j^{d\leftarrow\bar{\sigma}} + H.c.], \tag{A.9}$$

$$H_t^+ = -t \sum_{<ij>,\sigma} \eta(\sigma)[X_i^{d\leftarrow\bar{\sigma}} X_j^{0\leftarrow\sigma} + X_j^{d\leftarrow\bar{\sigma}} X_i^{0\leftarrow\sigma}], \tag{A.10}$$

$$H_t^- = -t \sum_{<ij>,\sigma} \eta(\sigma)[X_i^{\sigma\leftarrow 0} X_j^{\bar{\sigma}\leftarrow d} + X_j^{\sigma\leftarrow 0} X_i^{\bar{\sigma}\leftarrow d}], \tag{A.11}$$

where d represents the double occupancy state and $\eta(\uparrow) = 1$ and $\eta(\downarrow) = -1$ are introduced to account for the fact that if we create a doublon starting from a up spin particle, it will result in $-|d\rangle = c_\downarrow^\dagger c_\uparrow^\dagger |0\rangle$ state.

In the projected state, the density of doublons is zero. So, we can define a creation operator in the projected space $\tilde{c}_{i\sigma}^\dagger$ which is a non-canonical operator which creates a σ spin particle on a site when there is no $\bar{\sigma}$ particle already sitting on that site or else it would have created a doublon which is prohibited. This is evident from the definition,

$$\tilde{c}_{i\sigma}^\dagger = c_{i\sigma}^\dagger (1 - n_{i\bar{\sigma}}) = X_i^{\sigma\leftarrow 0}. \tag{A.12}$$

The low energy hopping H_t^{low} is the part of H_t^0 which does not involve double occupancies and can be expressed in terms of the projected operators like this,

$$H_t^{low} = -t \sum_{<ij>,\sigma} \tilde{c}_{i\sigma}^\dagger \tilde{c}_{j\sigma} + H.c. = \mathcal{P}_d - t(c_{i\sigma}^\dagger c_{j\sigma} + H.c.)\mathcal{P}_d, \tag{A.13}$$

where $\mathcal{P}_d = \prod_i (1 - n_{i\uparrow} n_{i\downarrow})$ is the projection operator which projects out doublons.

The dimer term which arises from the commutator $\frac{1}{U}[H_t^+, H_t^-]$ in the effective Hamiltonian is the Heisenberg term and is derived as follows:

$$\frac{1}{U}[H_t^+, H_t^-] \sim -\frac{1}{U}\sum_{<ij>} {H_t^-}_{ij}{H_t^+}_{ij} \tag{A.14}$$

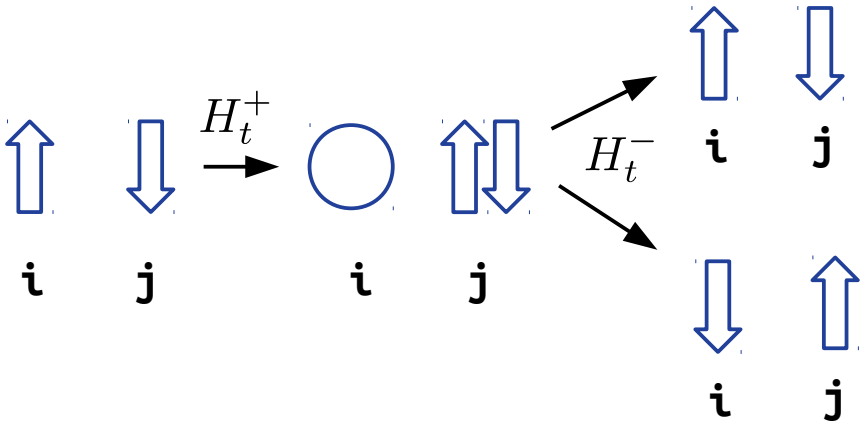

Figure A.4: Figure shows the dimer term in the low energy space which consists of either preservation of spins or flipping of spins on neighboring sites through an intermediate virtual high energy state consisting of a doublon.

The first term in the commutator requires a doublon in the initial state to operate and since doublon density is zero in low energy Hilbert space, the term does not contribute. If $H_t^{\pm}$ are now expressed in terms of the Hubbard operators then it contributes two terms (pictorially shown in Fig. A.4) like,

$$-\frac{1}{U}\sum_{<ij>} {H_t^-}_{ij}{H_t^+}_{ij} \sim -\frac{t^2}{U}\sum_{\sigma} X_i^{\bar{\sigma}\leftarrow\bar{\sigma}} X_j^{\sigma\leftarrow\sigma} + \frac{t^2}{U}\sum_{\sigma} X_i^{\sigma\leftarrow\bar{\sigma}} X_j^{\bar{\sigma}\leftarrow\sigma}. \tag{A.15}$$

In doublon projected space, $X_i^{\sigma\leftarrow\sigma} = \frac{n_i}{2} + \sigma S_i^z$ such that the first term is nothing but $\frac{2t^2}{U}(S_i^z S_j^z - \frac{n_i n_j}{4})$. The second term can be written as $\frac{t^2}{U}(S_i^+ S_j^- + S_i^- S_j^+)$ which is simply the spin flip part. The low energy effective Hamiltonian is then,

$$H_{tJ} = \mathcal{P}_d \Bigg(\sum_{<ij>} -t(\sum_{\sigma} c^{\dagger}_{i\sigma} c_{j\sigma} + H.c.) + J\left(S_i.S_j - \frac{n_i n_j}{4} \right) + \text{trimer terms} \Bigg) \mathcal{P}_d, \quad \text{(A.16)}$$

where $J = \dfrac{4t^2}{U}$. An extra factor of 2 comes in the coupling of the Heisenberg term because we have to consider both processes $i \leftrightarrow j$. Infact, there can be 3-site hopping terms arising from the commutator of H_t^+ and H_t^- which belong to the low energy sector but we leave it as an exercise for the reader to find those terms. Also, there will be terms which still mixes the low energy and high energy Hilbert spaces arising from the same commutator but they will be of order $\dfrac{t^2}{U}$ and can be eliminated by considering a second similarity operator.

A.2 Renormalized mean field theory

The mean field Hamiltonian corresponding to the renormalized tJ model in the spin symmetric case on a square lattice is expressed as,

$$\begin{aligned} H_{MF} = & \sum_{k\sigma} \Bigg[-tg_t\Gamma_k - \mu - \frac{3}{4}Jg_s\tilde{\xi}\Gamma_k + \frac{J}{4}\tilde{\xi}\Gamma_k - J(1-x) \Bigg] c^{\dagger}_{k\sigma} c_{k\sigma} \\ & + \sum_{k} \Bigg[\left(\frac{3}{4}Jg_s + \frac{J}{4} \right) \tilde{\Delta}(\cos(k_x) - \cos(k_y)) \Bigg] c^{\dagger}_{-k\downarrow} c^{\dagger}_{k\uparrow} + H.c., \end{aligned} \quad \text{(A.17)}$$

where, $\Gamma_k = 2(\cos(k_x) + \cos(k_y))$. For homogeneous case $\tilde{\xi}_x = \tilde{\xi}_y = \tilde{\xi}$. And d-wave pairing symmetry imposes $\tilde{\Delta}_x = -\tilde{\Delta}_y = \tilde{\Delta}$. We have choosen d-wave pairing symmetry here because experimentally the pairing symmetry observed in Cuprates is of d-wave nature, the phase diagram of which this renormalized mean field theory qualitatively explains.

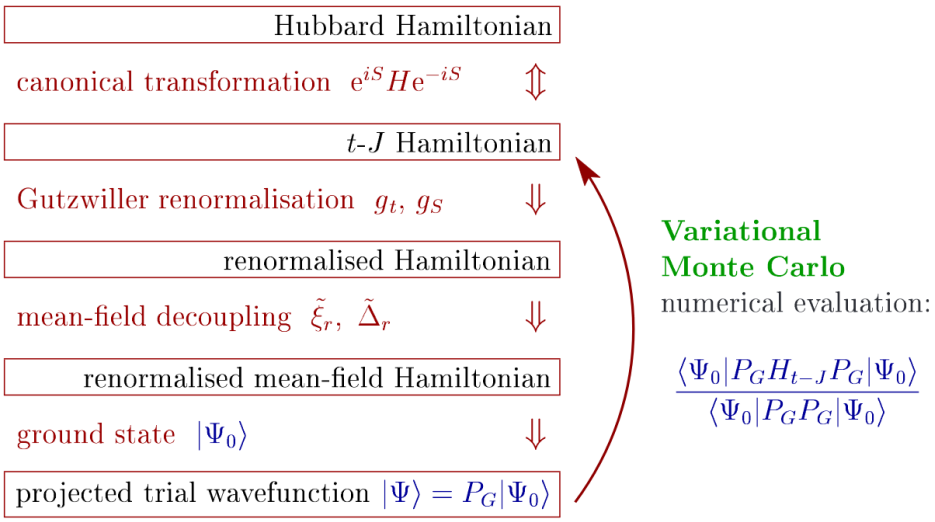

Figure A.5: Schematic showing steps involved in solving the effective Hamiltonian which has been incorporated from Ref [1]. Note P_G here is in our notation $\mathcal{P}_d$.

This quadratic mean field Hamiltonian can be diagonalized easily by Bogoluibov transformation given by,

$$\begin{aligned} c_{k\uparrow} &= u_k \gamma_{k0} + v_k \gamma_{k1}^\dagger, \\ c_{-k\downarrow}^\dagger &= -v_k \gamma_{k0} + u_k \gamma_{k1}^\dagger, \end{aligned} \tag{A.18}$$

where $v_k^2 = \frac{1}{2}\left(1 - \frac{\xi_k}{E_k}\right)$ and $u_k^2 = \frac{1}{2}\left(1 + \frac{\xi_k}{E_k}\right)$. Here, $E_k = \sqrt{\xi_k^2 + \Delta_k^2}$ where $\xi_k = \left[-tg_t\Gamma_k - \mu - \frac{3}{4}Jg_s\tilde{\xi}\Gamma_k + \frac{J}{4}\tilde{\xi}\Gamma_k - J(1-x)\right]$ and $\Delta_k = \left[\left(\frac{3}{4}Jg_s + \frac{J}{4}\right)\tilde{\Delta}(\cos(k_x) - \cos(k_y))\right]$.

The self-consistent equations as shown,

$$\tilde{\xi} = \frac{1}{4N} \sum_k v_k^2 \Gamma_k, \tag{A.19}$$

$$\tilde{\Delta} = \frac{1}{N} \sum_k u_k v_k (\cos(k_x) - \cos(k_y)), \tag{A.20}$$

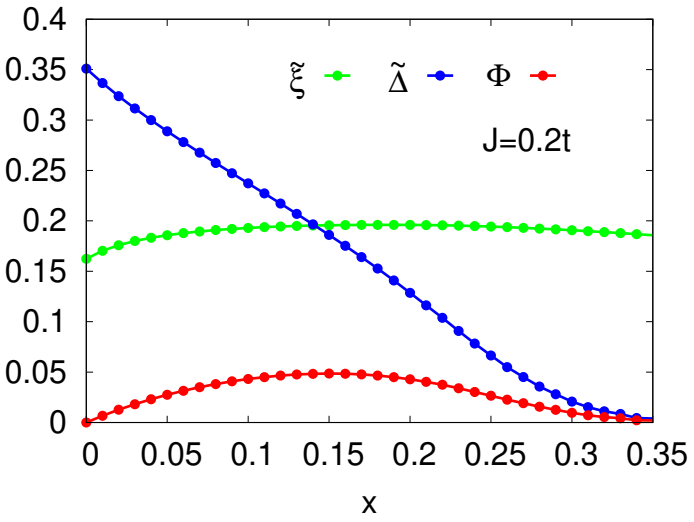

Figure A.6: Figure shows mean field parameters like pairing amplitude $\tilde{\Delta}$, Fock shift $\tilde{\xi}$ and the superconducting order parameter Φ for $J = 0.2t$ on a square lattice.

are solved self-consistently to find $|\psi_0\rangle$ which is the unprojected state. This state can be used as a variational ansatz for the VMC calculation and this is how RMFT can be incorporated into VMC calculations. However, our target state is $P_d|\psi_0\rangle$ which is the approximate ground state of the tJ model in the projected Hilbert space. A schematic flow chart is shown in Fig. A.5 which shows the steps for solving the low energy effective Hamiltonian. The physical quantities of interest should be calculated with respect to the projected state. The superconducting order parameter, Φ is one such quantity which is defined as,

$$\Phi \equiv \langle\psi_0|\mathcal{P}_d(c^\dagger_{i\uparrow}c^\dagger_{i+r\downarrow} - c^\dagger_{i\downarrow}c^\dagger_{i+r\uparrow})\mathcal{P}_d|\psi_0\rangle. \tag{A.21}$$

It is nothing but $g_t\tilde{\Delta}$ and represents superconducting order in the projected state. It is to be noted that two times the maximum value of Δ_k represents the superconducting gap in the projected state and ξ_k gives the renormalized dispersion in the absence of pairing.

The superconducting gap is proportional to $\tilde{\Delta}$ which decreases monotonically with x as can be seen in Fig. A.6. The probability of formation of singlets is more for low doping but the pairs also need enough kinetic energy to propagate through the system so as to make the system superconducting. Φ captures this effect very well in the sense it goes to zero at half-filling (where the system consists of frozen singlets), reaches a maxima and then again decays. Thus it has a non-monotonic dome like dependence.

APPENDIX B

APPENDIX

B.1 Details of RMFT

In this Appendix, we provide details of the renormalized mean field theory used in chapter 3 where both, the SC order and the magnetic order, are allowed. We diagonalize the mean field Hamiltonian using a two step transformation. After the first step of the transformation, the effective Hamiltonian obtained has both interband and intra-band pairing terms. The interband pairing terms are much smaller than the gap between the two bands for most of the points on the Brilluion zone and should not contribute significantly at zero temperature. Hence we ignore the interband pairing terms which allows us to carry out the second step of the transformation also analytically. Below, we provide details of these transformations and the self consistent equations obtained for various order parameters. We also give results for the inter-sublattice and intra-sublattice Fock-shifts calculated within this mean field theory which were not presented in the section on results.

Details of the renormalized mean field theory: The mean field quadratic Hamiltonian,

where we have allowed for nearest neighbor spin-singlet pairing as well as spin ordering, is as follows,

$$\mathcal{H} = \sum_k \begin{pmatrix} c^\dagger_{kA\uparrow} & c_{-kA\downarrow} & c^\dagger_{kB\uparrow} & c_{-kB\downarrow} \end{pmatrix} \tilde{h} \begin{pmatrix} c_{kA\uparrow} \\ c^\dagger_{-kA\downarrow} \\ c_{kB\uparrow} \\ c^\dagger_{-kB\downarrow} \end{pmatrix} \tag{B.1}$$

where, $\tilde{h} = \begin{pmatrix} h_{1\uparrow}(k) & 0 & h_{2\uparrow}(k) & -h_3(k) \\ 0 & -h_{1\downarrow}(k) & -h_3(k) & -h_{2\downarrow}(k) \\ h_{2\uparrow}(k) & -h_3(k) & -h_{1\uparrow}(k) & 0 \\ -h_3(k) & -h_{2\downarrow}(k) & 0 & h_{1\downarrow}(k) \end{pmatrix}$.

The expressions for $h_{1\sigma}(k)$ and $h_{2\sigma}(k)$ are the same as given in Sec. 3.3. For the d-wave symmetry the expression for $h_3(k)$ is $h_3(k) = \left[\frac{4t^2}{\Delta}(1-g_2) + \frac{4t^2}{U+\Delta}\left(\frac{3g_s}{4} - \frac{1}{4}\right) - \frac{2t^2}{\Delta}(g_{t\downarrow}+g_{t\uparrow})\right]\frac{\Delta_{AB}}{2}[\cos(kx) - \cos(ky)]$. For the extended s-wave symmetry the expression is $h_3(k) = \left[\frac{4t^2}{\Delta}(1+3g_2) + \frac{4t^2}{U+\Delta}\left(\frac{3g_s}{4} - \frac{1}{4}\right) + \frac{6t^2}{\Delta}(g_{t\downarrow}+g_{t\uparrow})\right]\frac{\Delta_{AB}}{2}[\cos(kx) + \cos(ky)]$.

As mentioned earlier, here we need to do a two step canonical transformation to diagonalize the Hamiltonian. The first set of transformations are the same as mentioned in Sec. 3.3. We neglect the interband pairing terms from the Hamiltonian obtained after the first set of transformations and perform a regular two band Bogoluibov transformation which is given by,

$$\begin{aligned} d_{k1\uparrow} &= u_{k1} f_{1k} + v_{k1} f^\dagger_{2k}, \\ d^\dagger_{-k1\downarrow} &= -v_{k1} f_{1k} + u_{k1} f^\dagger_{2k}, \\ d_{k2\uparrow} &= u_{k2} f_{3k} + v_{k2} f^\dagger_{4k}, \\ d^\dagger_{-k2\downarrow} &= -v_{k2} f_{3k} + u_{k2} f^\dagger_{4k}. \end{aligned} \tag{B.2}$$

Here, $u_{k1}^2 = \frac{1}{2}\left(1+\frac{\omega_\uparrow+\omega_\downarrow}{\sqrt{(\omega_\uparrow+\omega_\downarrow)^2+4\nu^2}}\right) = v_{k2}^2$ and $u_{k2}^2 = \frac{1}{2}\left(1-\frac{\omega_\uparrow+\omega_\downarrow}{\sqrt{(\omega_\uparrow+\omega_\downarrow)^2+4\nu^2}}\right)$ $= v_{k1}^2$ where, $\omega_\sigma = h_{1\sigma}(k)(\alpha_{k\sigma}^2-\beta_{k\sigma}^2)-2h_{2\sigma}(k)\alpha_{k\sigma}\beta_{k\sigma}$ and $\nu = -h_3(k)(\alpha_{k\uparrow}\beta_{k\downarrow}+\alpha_{k\downarrow}\beta_{k\uparrow})$.

The self-consistent equations for various order-parameters are given below:

$$\begin{aligned}\Delta_{AB} =&\langle c_{iA\uparrow}^\dagger c_{jB\downarrow}^\dagger\rangle - \langle c_{iA\downarrow}^\dagger c_{jB\uparrow}^\dagger\rangle \\ =& \frac{1}{N}\sum_k(\alpha_{k\downarrow}\beta_{k\uparrow}u_{k2}v_{k2} - \alpha_{k\uparrow}\beta_{k\downarrow}u_{k1}v_{k1})\gamma_{sc}(k),\end{aligned} \tag{B.3}$$

with $\gamma_{sc}(k) = \cos(k_x) \pm \cos(k_y)$. The plus sign is for the extended s-wave symmetry while the minus sign is for the d-wave symmetry in the pairing amplitude.

The magnetization on the A sublattice is equal and opposite to the magnetization on the B sublattice owing to particle-hole symmetry of the Hamiltonian at half-filling. Hence the staggered magnetization $m_s = (m_A - m_B)/2 = m_A$,

$$\begin{aligned}m_s =&\langle \hat{n}_{A\uparrow} - \hat{n}_{A\downarrow}\rangle \\ =&\frac{1}{N}\sum_k[(\alpha_{k\uparrow}^2 - \alpha_{k\downarrow}^2)v_{k1}^2 + (\beta_{k\uparrow}^2 - \beta_{k\downarrow}^2)v_{k2}^2].\end{aligned} \tag{B.4}$$

The density difference between A and B sublattices, also equal to the doublon density on the A sublattice and the hole density on the B sublattice, is given by,

$$\begin{aligned}\delta =&\frac{\langle \hat{n}_A\rangle - \langle \hat{n}_B\rangle}{2} \\ =&\frac{1}{2N}\sum_{k\sigma}[\alpha_{k\sigma}^2(v_{k1}^2 - v_{k2}^2) + \beta_{k\sigma}^2(v_{k2}^2 - v_{k1}^2)].\end{aligned} \tag{B.5}$$

$\chi_{AB\sigma}$, defined below, gives the intersublattice Fock shift which comes from the mean field decomposition of the exchange term and the trimer terms in the low energy effective Hamil-

tonian in Eq. 3.9,

$$\begin{aligned}\chi_{AB\sigma} &= \langle c^{\dagger}_{iA\sigma} c_{jB\sigma} \rangle \\ &= \frac{1}{4N} \sum_{k} \alpha_{k\sigma} \beta_{k\sigma} (v^2_{k2} - v^2_{k1}) \gamma_k. \end{aligned} \tag{B.6}$$

Similarly, $\chi_{BB\sigma}$ and $\chi_{BBxy\sigma}$ represent second neighbor hoppings within the B sublattice obtained by the mean-field decomposition of the trimer terms and are given by,

$$\begin{aligned}\chi_{BB\sigma} &= \langle c^{\dagger}_{iB\sigma} c_{jB\sigma} + h.c. \rangle \qquad \text{j=i}\pm\text{2x or i}\pm\text{2y} \\ &= \frac{1}{N} \sum_{k} [\cos 2k_x + \cos 2k_y] (\alpha^2_{k\sigma} v^2_{k2} + \beta^2_{k\sigma} v^2_{k1}), \end{aligned} \tag{B.7}$$

$$\begin{aligned}\chi_{BBxy\sigma} &= \langle c^{\dagger}_{iB\sigma} c_{jB\sigma} + h.c. \rangle \quad \text{j=i}\pm\text{ x}\pm\text{ y} \\ &= \frac{1}{N} \sum_{k} 2 \cos(k_x) \cos(k_y) (\alpha^2_{k\sigma} v^2_{k2} + \beta^2_{k\sigma} v^2_{k1}). \end{aligned} \tag{B.8}$$

The spin symmetric RMFT can be obtained from the generic equations, described above, by imposing the spin symmetry.

Results for Fock Shift: Fig. B.1 shows the variation of the inter and intra sublattice Fock shifts as a function of Δ for $U = 20t$. The inter sublattice Fock shift first increases with increase in Δ with $\chi_{AB\downarrow} > \chi_{AB\uparrow}$, reaches a maximum near the AF transition point, and then decreases with increase in Δ in the paramagnetic phase. This is because in the AF ordered regime, the density difference between the two sublattices is very near to zero but increases slowly with increasing Δ due to the presence of some doublons on the A sublattice and holes on the B sublattice. χ_{AB} in both the spin channels increase due to the increased hopping probability. But beyond the magnetic transition point, densities of

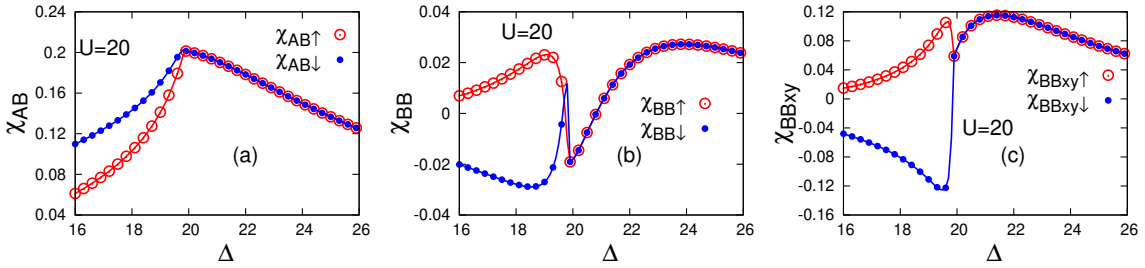

Figure B.1: Inter and intra sublattice fock shifts obtained from the generic RMFT which allows for spin symmetry breaking. Panel (a) shows inter sublattice fock shifts $\chi_{AB\sigma}$ vs Δ while panel (b) shows intra sublattice fock shift $\chi_{BB\sigma}$ along the $2x$ or $2y$ bond. Panel (c) shows intra sublattice Fock shift $\chi_{BBxy\sigma}$. Effects due to the phase transitions from the AF-MI to the paramagnetic BI phase [see Fig. 3.6] are clearly present here as well.

doublons on the A sublattice and holes on the B sublattice increase quite rapidly, resulting in an increasing charge density wave insulating behavior with increasing Δ; hence χ_{AB} in the paramagnetic regime decreases with increase in Δ. This is shown in panel (a) of Fig. B.1. Panel (b) shows the intra sublattice Fock shift on the B sublattice, with two B sites separated by next neighbor spacings in either the x or y direction on the square lattice. While $\chi_{BB\uparrow}$ initially increases and then decreases in the magnetically ordered phase, $\chi_{BB\downarrow}$ decreases and then increases and finally the two become equal to each other in the paramagnetic phase. Panel (c) shows the behavior of χ_{BBxy} with Δ which is the B sublattice fock shift for the two B sites separated by one unit spacing along the x direction and one unit spacing along the y direction. It shows a behavior qualitatively similar to χ_{BB}.

B.2 Numerical Diagonalization

In this Appendix, we provide details of the full numerical diagonalization of the mean field Hamiltonian. We also show a comparison of the results of this calculation with our earlier calculations where interband terms were ignored. The comparison shows that the

interband terms have a very weak effect on all physical quantities of interest at zero temperature. Thus the phase-diagram we have obtained remains same both qualitatively and quantitatively even in this full numerical calculation. In the following discussion, we will refer to these calculations as the calculation with interband pairing terms and without the interband pairing terms.

We diagonalize the mean field Hamiltonian by a transformation

$$\begin{pmatrix} c_{kA\uparrow} \\ c_{kB\uparrow} \\ c^{\dagger}_{-kA\downarrow} \\ c^{\dagger}_{-kB\downarrow} \end{pmatrix} = \begin{pmatrix} u_{1k\uparrow} & u_{2k\uparrow} & v_{1k\uparrow} & v_{2k\uparrow} \\ u_{3k\uparrow} & u_{4k\uparrow} & v_{3k\uparrow} & v_{4k\uparrow} \\ -v_{1k\downarrow} & -v_{2k\downarrow} & u_{1k\downarrow} & u_{2k\downarrow} \\ -v_{3k\downarrow} & -v_{4k\downarrow} & u_{3k\downarrow} & u_{4k\downarrow} \end{pmatrix} \begin{pmatrix} f_{1k} \\ f_{3k} \\ f^{\dagger}_{2k} \\ f^{\dagger}_{4k} \end{pmatrix} \tag{B.9}$$

After the transformation, the diagonalized Hamiltonian is assumed to have the form $\mathcal{H} = \sum_{k,\alpha=1,4} E_{\alpha}(k) f^{\dagger}_{\alpha k} f_{\alpha k} + const.$ We calculate the commutators of the fermionic $c_{kA,B}$ operators with the mean field Hamiltonian and the diagonalized Hamiltonian and equate the coefficients of the Bogoluibov operators $f_{\alpha k}$ for $\alpha = 1, 4$ to obtain the eigenvalue equations. Finally we solve the eigenvalue equation numerically for every k-value in the Brillouin zone to get the eigenvectors and obtain various physical quantities using the following self-consistent equations:

$$\begin{aligned} \chi_{AB\sigma} =& \frac{1}{4N} \sum_{k} (v_{1k\sigma} v_{3k\sigma} + v_{2k\sigma} v_{4k\sigma}) \gamma_k, \\ \chi_{BB\sigma} =& \frac{1}{N} \sum_{k} (v^2_{3k\sigma} + v^2_{4k\sigma}) (\cos(2k_x) + \cos(2k_y)), \\ \chi_{BBxy\sigma} =& \frac{1}{N} \sum_{k} (v^2_{3k\sigma} + v^2_{4k\sigma}) (2\cos(k_x)\cos(k_y)), \\ \delta =& \frac{1}{2N} \sum_{k,\sigma} (v^2_{1k\sigma} + v^2_{2k\sigma} - v^2_{3k\sigma} - v^2_{4k\sigma}), \end{aligned} \tag{B.10}$$

$$m_s = \frac{1}{N}\sum_k (v^2_{1k\uparrow} - v^2_{1k\downarrow} + v^2_{2k\uparrow} - v^2_{2k\downarrow}),$$
$$\Delta_{d,s} = \frac{1}{N}\sum_k (v_{1k\uparrow}u_{3k\downarrow} + v_{2k\uparrow}u_{4k\downarrow})\gamma_{sc}(k).$$

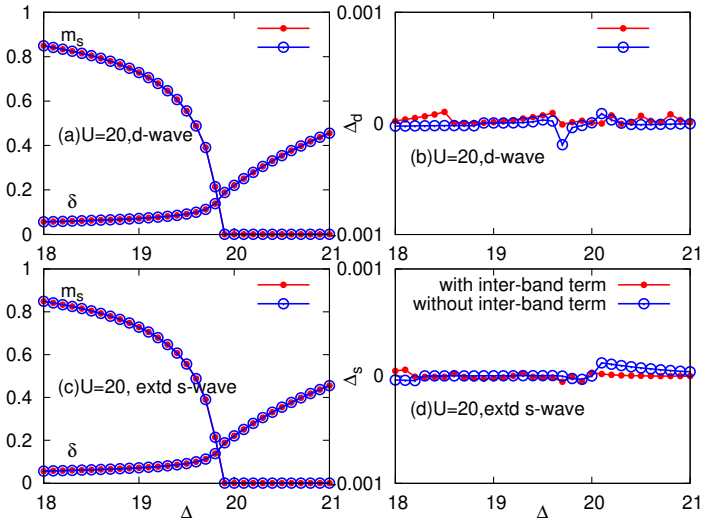

Figure B.2: The staggered magnetization m_s and the density difference δ as functions of Δ for $U = 20t$. The top left panel shows the data for d-wave pairing and the bottom left panel for the extended s-wave case. Right panels show the pairing amplitudes for the d-wave and extended s-wave pairing for $U = 20t$. As shown, the effect of including inter band pairing in the spin-asymmetric case is negigible.

Comparison of results: We first compare the results of the two calculations with and without interband pairing terms for the case where magnetic order is allowed along with the SC order. As shown in Fig. B.2, the staggered magnetization and the density difference in the two calculations are exactly the same. The pairing amplitudes for the d-wave and the extended s-wave pairing are shown in right panels of Fig. B.2. Superconductivity does not turn on even in the calculation with interband pairing and the pairing amplitude for both the d-wave and the extended s-wave symmetry remains zero.

We have also compared the results for the case where the spin symmetry is enforced

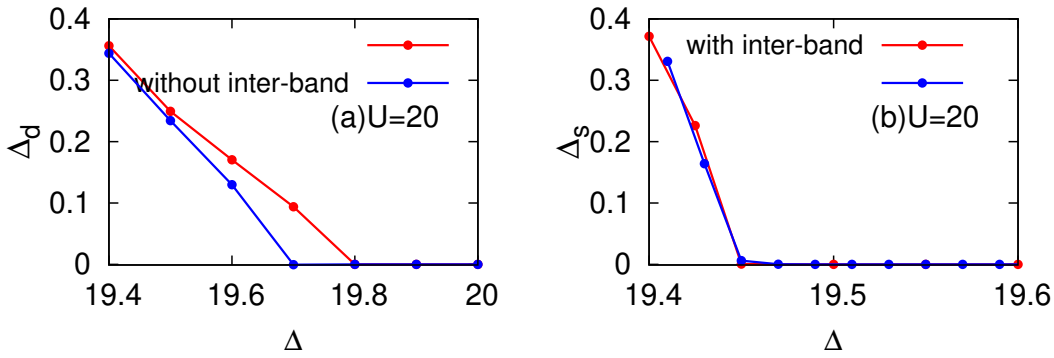

Figure B.3: The left panel shows the d-wave pairing amplitude for $U = 20t$ in the spin-symmetric calculation. There is a small change in the d-wave pairing amplitude due to the interband pairing terms which lead to a small enhancement of the pairing amplitude. The right panel shows the pairing amplitude for the extended s-wave symmetry. Inter band pairing terms have an even weaker effect on the extended s-wave pairing amplitude than on the d-wave pairing amplitude.

and only the SC order is allowed. In this case, the transformation used to diagonalize the mean field Hamiltonian gets simplified due to the smaller number of variables involved. Here, due to spin symmetry $v_{ik\uparrow} = v_{ik\downarrow}$ and $u_{ik\uparrow} = u_{ik\downarrow}$ for $i = 1, 4$. Fig. B.3 shows the d-wave pairing amplitude as a function of Δ for the calculations with and without interband pairing terms. There is a weak effect of the interband pairing term on the d-wave pairing amplitude though the range in Δ over which Δ_d remains non-zero is more or less same in the two calculations. The effect of the interband pairing on the extended s-wave pairing amplitude is even weaker as shown in the right panel of Fig. B.3.

APPENDIX C

APPENDIX

C.1 Details of strong correlation limit and Gutzwiller projection

We first describe the similarity transformation used to obtain the different terms in the low energy effective Hamiltonian (Eq. 4.2). We then describe the generalized Gutzwiller projection for obtaining the projected Hilbert space on which the low energy effective Hamiltonian acts, along with the details of Gutzwiller factors which renormalize the various couplings in the low energy Hamiltonian when the projection is implemented approximately.

We solve the model in Eq. 4.1, in the limit $U \sim \Delta \gg t, t'$. In this limit and at half-filling, holons are energetically expensive on the A sites (with onsite potential $-\frac{\Delta}{2}$) and doublons are expensive on the B sites (with onsite potential $\frac{\Delta}{2}$); i.e., in the low energy subspace h_A and d_B are constrained to be zero. We do a generalized similarity transformation on this Hamiltonian, $\tilde{H} = e^{-iS} H e^{iS}$, such that all first and second neighbor hopping processes connecting the low energy sector to the high energy sector of the Hilbert space

are eliminated. The similarity operator of this transformation is $S = -\frac{i}{U+\Delta}(H^+_{t\ A\to B} - H^-_{t\ B\to A}) - \frac{i}{\Delta}(H^0_{t\ A\to B} - H^0_{t\ B\to A}) - \frac{i}{U}(H^+_{t'\ A\to A} - H^-_{t'\ A\to A}) - \frac{i}{U}(H^+_{t'\ B\to B} - H^-_{t'\ B\to B})$ where $H^+_{t/t'}$ represents first or second neighbor hopping processes which involve an increase in h_A or d_B by one and $H^-_{t/t'}$ on the other hand represent hopping processes which involve a decrease in h_A or d_B by one. H^0_t processes do not involve a change in h_A and d_B. The low energy effective Hamiltonian obtained by this transformation is given in Eq. 4.2, with $H_0 = \frac{U-\Delta}{2}\sum_i[n_{iA\uparrow}n_{iA\downarrow} + (1-n_{iB\uparrow})(1-n_{iB\downarrow})]$. Further details can be found in chapter 2. H_{eff} acts on a projected Hilbert space which consists of states $|\Phi\rangle = \mathcal{P}|\Phi_0\rangle$ where the projection operator $\mathcal{P}$ eliminates components with $h_A \geq 1$ or $d_B \geq 1$ from $|\Phi_0\rangle$. We use here the Gutzwiller approximation [1, 2, 10] to handle the projection, by writing the expectation value of an operator Q in a state $\mathcal{P}|\Phi_0\rangle$ as the product of a Gutzwiller factor g_Q times the expectation value in $|\Phi_0\rangle$ so that $\langle Q\rangle \simeq g_Q\langle Q\rangle_0$. The standard procedure [1] for calculating g_Q has been generalised by us for the case where holons are projected out from one sublattice and doublons from the other [10] as described in chapter 2.

We thus obtain the renormalized effective Hamiltonian with the inter-sublattice kinetic energy $\langle c^\dagger_{iA\sigma}c_{jB\sigma}\rangle \approx g_{t\sigma}\langle c^\dagger_{iA\sigma}c_{jB\sigma}\rangle_0$, and intra-sublattice kinetic energy $\langle c^\dagger_{i\alpha\sigma}c_{j\alpha\sigma}\rangle \approx g_{\alpha\sigma}\langle c^\dagger_{i\alpha\sigma}c_{j\alpha\sigma}\rangle_0$. The inter-sublattice spin correlation $\langle \mathbf{S}_{iA}\cdot\mathbf{S}_{jB}\rangle \approx g_{sAB}\langle \mathbf{S}_{iA}\cdot\mathbf{S}_{jB}\rangle_0$ while the intra-sublattice spin exchange term gets renormalized with a different factor of $g_{s\alpha\alpha}$. The only other dimer term which does not get rescaled under the Gutzwiller projection is,

$$H_d = -\frac{t^2}{\Delta}\sum_{<ij>,\sigma}[(1-n_{iA\bar{\sigma}})(1-n_{jB}) + (n_{iA}-1)n_{jB\bar{\sigma}}] \tag{C.1}$$

as it consists of only density operators [1, 10].

Then we have the important trimer terms:

$$
\begin{aligned}
H_{tr} = & -\frac{t^2}{\Delta} \sum_{<ijk>,\sigma} [g_{A\sigma} c^\dagger_{kA\sigma} n_{jB\bar{\sigma}} c_{iA\sigma} + g_2 c_{iA\bar{\sigma}} c^\dagger_{jB\bar{\sigma}} c_{jB\sigma} c^\dagger_{kA\sigma}] \\
& -\frac{t^2}{\Delta} \sum_{<jil>,\sigma} [g_{B\sigma} c_{lB\sigma} (1 - n_{iA\bar{\sigma}}) c^\dagger_{jB\sigma} + g_2 c_{lB\sigma} c^\dagger_{iA\sigma} c_{iA\bar{\sigma}} c^\dagger_{jB\bar{\sigma}}] \\
+\frac{tt'(U+\Delta)}{2U\Delta} & \sum_{<kj>,<<ik>>\sigma} \Big[g_{t\sigma} c^\dagger_{iA\sigma} (1 - n_{kA\bar{\sigma}}) c_{jB\sigma} - g_{t\sigma} c^\dagger_{jA\sigma} n_{kB\bar{\sigma}} c_{iB\sigma} + \\
& g_{AAB\sigma} c^\dagger_{iA\sigma} c^\dagger_{kA\bar{\sigma}} c_{kA\sigma} c_{jB\bar{\sigma}} + g_{BBA\sigma} c^\dagger_{jA\sigma} c^\dagger_{kB\bar{\sigma}} c_{kB\sigma} c_{iB\bar{\sigma}} \Big] + h.c.
\end{aligned} \tag{C.2}
$$

The various Gutzwiller factors involved (see chapter 2 and Appendix C.3 for details) are as follows:

- $g_{A\sigma} = 2\delta/(1+\delta+\sigma m_A)$, $g_{B\sigma} = 2\delta/(1+\delta-\sigma m_B)$ and $g_{t\sigma} = \sqrt{g_{A\sigma} g_{B\sigma}}$;
- $g_{s\alpha_1\alpha_2} = 4/\sqrt{((1+\delta)^2 - m^2_{\alpha_1})((1+\delta)^2 - m^2_{\alpha_2})}$, and $g_2 = \delta g_{sAB}$;
- $g_{\alpha_1\alpha_1\alpha_2\sigma} = 4\delta/\sqrt{((1+\delta)^2 - m^2_{\alpha_1})(1+\delta+\sigma m_{\alpha_1})(1+\delta+\sigma m_{\alpha_2})}$.

Superconducting order parameter $\Phi_{d/s}$:

The SC correlation function is the two particle reduced density matrix defined by $F_{\gamma_1\gamma_2}(\mathbf{r}_i - \mathbf{r}_j) = \langle B^\dagger_{i\gamma_1} B_{j\gamma_2} \rangle$ where $B^\dagger_{i\gamma}$, defined above, creates a singlet on the bond $(i, i+\gamma)$. The SC order parameter $\Phi_{d/s}$ is defined in terms of the off-diagonal long-range order in this correlation $F_{\gamma_1,\gamma_2}(\mathbf{r}_i - \mathbf{r}_j) \to \langle B^\dagger_{i\gamma_1} \rangle \langle B_{j\gamma_2} \rangle = \Phi_{\gamma_1} \Phi_{\gamma_2}$ as $|\mathbf{r}_i - \mathbf{r}_j| \to \infty$. Since $F_{\gamma_1\gamma_2}(\mathbf{r}_i - \mathbf{r}_j)$ also corresponds to hopping of two electrons from $(j, j+\gamma_2)$ to sites $(i, i+\gamma_1)$, in the projected wavefunction scheme it scales just like the product of two hopping terms such that $F_{\gamma_1\gamma_2} \approx g_{A\uparrow} g_{B\downarrow} F^0_{\gamma_1\gamma_2}$. Hence the rescaled form of the superconducting order parameter is $\Phi_{d/s} \approx \sqrt{g_{A\uparrow} g_{B\downarrow}} \Phi^0_{d/s}$ where $\Phi^0_{d/s} \equiv \Delta_{d/s}$ is the order parameter calculated in the unprojected wavefunction of the low energy effective Hamiltonian in Eq. 4.2.

Spectral Functions and Density of States:

In chapter 4 we also discuss the single particle density of states (DOS) and the spectral functions. In the Gutzwiller projection method, the Green's function is rescaled with the appropriate Gutzwiller factor such that $G_{\alpha\sigma}(k,\omega) = g_{\alpha\sigma}G^0_{\alpha\sigma}(k,\omega)$ where $G^0_{\alpha\sigma}(k,\omega)$ is calculated in the unprojected basis. Here α represents the sublattice A or B and σ is the spin index. The spectral function, $A_{\alpha\sigma}(k,\omega)$ which is imaginary part of the Green's function also get rescaled with the same Gutzwiller factors. The results presented in chapter 4 are for the spectral functions averaged over the two sublattices $A_\sigma(k,\omega) = \frac{1}{2}\sum_\alpha A_{\alpha\sigma}(k,\omega)$ which can be expressed as $A_\uparrow(k,\omega) = (|u_{1\uparrow k}|^2 + |u_{2\uparrow k}|^2)\delta(\omega - E_{1\uparrow}(k)) + (|u_{3\uparrow k}|^2 + u_{4\uparrow k}|^2)\delta(\omega - E_{2\uparrow}(k)) + (|v_{1\uparrow k}|^2 + |v_{2\uparrow k}|^2)\delta(\omega + E_{1\downarrow}(k)) + (|v_{3\uparrow k}|^2 + |v_{4\uparrow k}|^2)\delta(\omega + E_{2\downarrow}(k))$. The down spin spectral function can be obtained by replacing $u_{i\uparrow k} \leftrightarrow v_{i\downarrow k}$ (and vice-versa) and by replacing $E_{i\sigma}(k)$ by $-E_{i\sigma}(k)$. Here $E_{1,2,\uparrow}(k)$ are the eigenvalues of the BdG equation for a given k in the BZ with eigenvectors $(u_{1\uparrow k}, u_{2\uparrow k}, -v_{1\downarrow k}, -v_{2\downarrow k})$ and $(u_{3\uparrow k}, u_{4\uparrow k}, -v_{3\downarrow k}, -v_{4\downarrow k})$ respectively and $-E_{1,2\downarrow}$ are eigenvalues corresponding to eigenvectors obtained by $u_{i\sigma k} \to v_{i\sigma k}$ and $v_{i\sigma k} \to -u_{i\sigma k}$. In order to get the low energy spectral functions, we integrate $A_\sigma(k,\omega)$ over a small ω range such that $|\omega| \leq (0.01 - 0.02)t$.

The single particle density of states is defined as, $\rho_{\alpha\sigma}(\omega) = \sum_k A_{\alpha\sigma}(k,\omega)$. The results presented in chapter 4 are for the single particle density of states (DOS) in the up spin and down spin channels, defined as $\rho_\sigma(\omega) = (\rho_{A\sigma}(\omega) + \rho_{B\sigma}(\omega))/2$. The zero temperature momentum distribution function, which helps in identifying whether a Fermi pocket is an electron pocket or a hole pocket can also be obtained from the spectral function using $n_\sigma(k) = \int_{-\infty}^{0} d\omega A_\sigma(k,\omega)$.

C.2 Details of the calculation of the terms in effective Hamiltonian arising from t'

In chapter 2, we have elaborately discussed about how to get the low energy effective Hamiltonian when there is only nearest neighbor hopping processes present. Here we shall focus on the terms in the effective Hamiltonian that arise from the next nearest neighbor hopping terms as discussed in chapter 4. The hopping term has now two parts : nearest neighbor and next nearest neighbor terms such that $H_{hopp} = H_t + H_{t'}$.

$$H_t = {H_t^+}_{A\to B} + {H_t^+}_{B\to A} + {H_t^-}_{A\to B} + {H_t^-}_{B\to A} + {H_t^0}_{A\to B} + {H_t^0}_{B\to A}, \tag{C.3}$$

$$H_{t'} = \sum_{\alpha\in A,B} {H_{t'}^+}_{\alpha\to\alpha} + {H_{t'}^-}_{\alpha\to\alpha} + {H_{t'}^0}_{\alpha\to\alpha}. \tag{C.4}$$

As already mentioned, out of these ${H_t^+}_{A\to B}, {H_t^-}_{B\to A}, {H_t^0}_{A\to B}, {H_t^0}_{B\to A}$ from the nearest neighbor hopping sector and ${H_{t'}^+}_{\alpha\to\alpha}, {H_{t'}^-}_{\alpha\to\alpha}$ from the next nearest neighbor sector, connect the low and high energy sectors and must be eliminated through suitable similarity transformation. The total similarity operator is perturabative in both $t/(U+\Delta)$ and t/U and is of the following form,

$$\begin{aligned} S = &-\frac{i}{U+\Delta}({H_t^+}_{A\to B} - {H_t^-}_{B\to A}) - \frac{i}{\Delta}({H_t^0}_{A\to B} - {H_t^0}_{B\to A}) \\ &-\frac{i}{U}({H_{t'}^+}_{A\to A} - {H_{t'}^-}_{A\to A}) - \frac{i}{U}({H_{t'}^+}_{B\to B} - {H_{t'}^-}_{B\to B}). \end{aligned} \tag{C.5}$$

If we consider now the commutators $[S, H_{hopp}]$ and $[S,[S,H_0]]$, where H_0 is the unper-

turbed term of the Hamiltonian, we find terms which again connect the low and high energy sectors and should be suitably eliminated through a second similarity transformation to get the effective Hamiltonian. The effective Hamiltonian is of the form,

$$\begin{aligned}
\mathcal{H}_{eff} &= H_0 + H^0_{t'\,A\to A} + H^0_{t'\,B\to B} + H^+_{t\ B\to A} + H^-_{t\ A\to B} \\
&+ \frac{1}{U}[H^+_{t'\,A\to A}, H^-_{t'\,A\to A}] + \frac{1}{U}[H^+_{t'\,B\to B}, H^-_{t'\,B\to B}] \\
&+ \frac{1}{U+\Delta}[H^+_{t\ A\to B}, H^-_{t\ B\to A}] + \frac{1}{\Delta}[H^0_{t\ A\to B}, H^0_{t\ B\to A}] \\
&+ \frac{1}{2}\left(\frac{1}{U}+\frac{1}{\Delta}\right)\left([H^+_{t'\,A\to A} + H^+_{t'\,B\to B}, H^0_{t\ B\to A}]\right) \\
&- \frac{1}{2}\left(\frac{1}{U}+\frac{1}{\Delta}\right)\left([H^-_{t'\,A\to A} + H^-_{t'\,B\to B}, H^0_{t\ A\to B}]\right).
\end{aligned} \tag{C.6}$$

Let us now consider the terms in the effective Hamiltonian arising from the next nearest neighbor hopping and express them in terms of fermionic operators on A and B lattice sites. The next neighbor hopping in the low energy space, shown in Fig. C.1, is of the form,

$$\begin{aligned}
H_{t',low} &= H^0_{t'\,A\to A} + H^0_{t'\,B\to B} \\
&= -t' \sum_{<<i,j>>,\sigma} [\tilde{c}^\dagger_{iA\sigma}\tilde{c}_{jA\sigma} + \tilde{\tilde{c}}^\dagger_{iB\sigma}\tilde{\tilde{c}}_{jB\sigma} + h.c.].
\end{aligned} \tag{C.7}$$

Here, the projected operators on A and B sublattice are $\tilde{c}^\dagger_{A\sigma} = c^\dagger_{A\sigma} n_{A\bar{\sigma}}$ and $\tilde{c}^\dagger_{B\sigma} = c^\dagger_{B\sigma}(1 - n_{B\bar{\sigma}})$.

O(t'^2/U) Dimer terms:

Now we consider $\mathcal{O}(t'^2/U)$ dimer terms coming from $\frac{1}{U}[H^+_{t'\,\alpha\to\alpha}, H^-_{t'\,\alpha\to\alpha}]$ terms where $\alpha = A, B$. For A sublattice, $\frac{1}{U}[H^+_{t'\,A\to A}, H^-_{t'\,A\to A}] \sim -\frac{1}{U} H^-_{t'\,A\to A} H^+_{t'\,A\to A}$ since the first

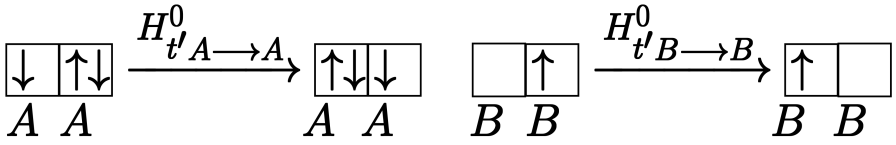

Figure C.1: Next neighbor hopping processes in low energy space.

term in the commutator requires a hole to start with which is forbidden on the A sites. The dimer term corresponding to this commutator is,

$$H^{AA}_{t',dimer} = -\frac{t'^2}{U} \sum_{<<i,j>>\sigma} [X_{iA}{}^{\sigma\leftarrow\sigma} X_{jA}{}^{\bar{\sigma}\leftarrow\bar{\sigma}} - X_{iA}{}^{\sigma\leftarrow\bar{\sigma}} X_{jA}{}^{\bar{\sigma}\leftarrow\sigma} + j \leftrightarrow i]. \tag{C.8}$$

Here, $X^{a\rightarrow b} = |a\rangle\langle b|$.

In terms of projected operators this can be expressed as

$$\begin{aligned} &\frac{J'}{2} \sum_{<ij>,\sigma} [\tilde{c}_{iA\bar{\sigma}} \tilde{c}^{\dagger}_{iA\sigma} \tilde{c}_{jA\sigma} \tilde{c}^{\dagger}_{jA\bar{\sigma}} - \tilde{c}_{iA\bar{\sigma}} \tilde{c}^{\dagger}_{iA\bar{\sigma}} \tilde{c}_{jA\sigma} \tilde{c}^{\dagger}_{jA\sigma}] \\ &= J' \mathcal{P}_h \left(S_{iA}.S_{jA} - \frac{(2-n_{iA})(2-n_{jA})}{4} \right) \mathcal{P}_h, \end{aligned} \tag{C.9}$$

with $J' = 4t'^2/U$. Spin summation and hoppings from i to j site first or vice versa contribute a factor of $4 = 2 \times 2$. A similar analysis can be extended for the B sublattice. $\frac{1}{U}[H^{+}_{t'\ B\rightarrow B}, H^{-}_{t'\ B\rightarrow B}] \sim -\frac{1}{U} H^{-}_{t'\ B\rightarrow B} H^{+}_{t'\ B\rightarrow B}$ since the first term in the commutator requires a doublon to start with which belongs to the high energy sector for the B sublattice. The dimer term corresponding to this commutator is,

$$H^{B,B}_{t',dimer} = -\frac{t'^2}{U}\sum_{<ij>,\sigma}[X_{iB}{}^{\sigma\leftarrow\sigma}X_{jB}{}^{\bar{\sigma}\leftarrow\bar{\sigma}} - X_{iB}{}^{\sigma\leftarrow\bar{\sigma}}X_{jB}{}^{\bar{\sigma}\leftarrow\sigma} + j \leftrightarrow i]. \tag{C.10}$$

In terms of projected operators this becomes,

$$\begin{aligned} -\frac{J'}{2}\sum_{\sigma}[\tilde{\tilde{c}}^{\dagger}_{iB\sigma}\tilde{\tilde{c}}_{iB\sigma}\tilde{\tilde{c}}^{\dagger}_{jB\bar{\sigma}}\tilde{\tilde{c}}_{jB\bar{\sigma}} - \tilde{\tilde{c}}^{\dagger}_{iB\sigma}\tilde{\tilde{c}}_{iB\bar{\sigma}}\tilde{\tilde{c}}^{\dagger}_{jB\bar{\sigma}}\tilde{\tilde{c}}_{jB\sigma}] \\ = J'\mathcal{P}_d\left(S_{iB}.S_{jB} - \frac{n_{iB}n_{jB}}{4}\right)\mathcal{P}_d. \end{aligned} \tag{C.11}$$

$\mathcal{P}_h$ and $\mathcal{P}_d$ represent the hole and double projection operators respectively. The process underlying these Heisenberg terms are shown in Fig. C.2.

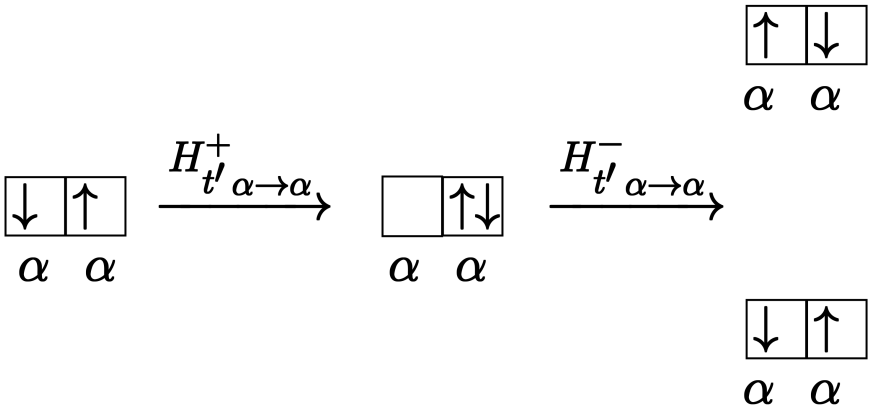

Figure C.2: Pictorial representation of the Heisenberg terms on A and B sublattices. Sublattices are indicated by α.

We have not considered the $\mathcal{O}(t'^2/U)$ trimer terms within our approximate calculation as evidently their contibutions will be small.

AAB and BBA trimer terms:

Due to the presence of next neighbor hopping in the Hamiltonian, AAB and BBA type three site hoppings become possible which live in the low energy sector of the hilbert space.

The AAB trimer terms, shown in Fig. C.3, arise from the commutator $\frac{(U+\Delta)}{2U\Delta}[H^{+}_{t'\ A\to A}, H^{0}_{t\ B\to A}] \sim -\frac{K}{tt'}H^{0}_{t\ B\to A}H^{+}_{t'\ A\to A}$ where the coupling strength $K = \frac{tt'(U+\Delta)}{2U\Delta}$. The first term of the commutator requires a hole at the intermediate A site to begin with which is energetically not favourable. Fig. C.3 shows usual spin preserving and spin flip terms. In the first case, the spin at the intermediate site remains the same as the initial state where as in the second case it flips.

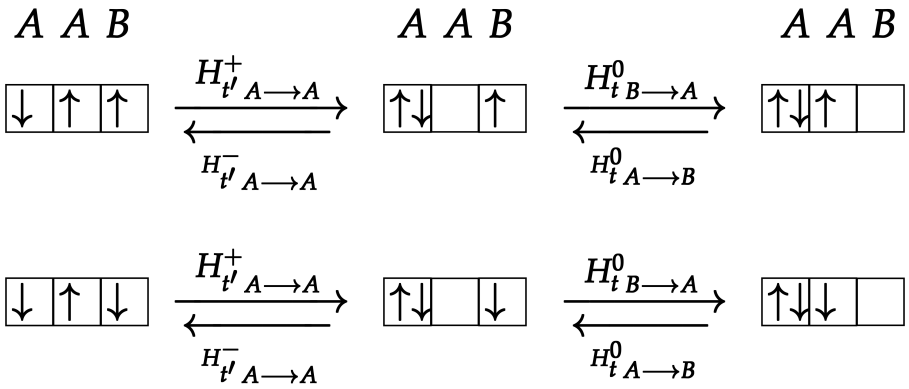

Figure C.3: AAB trimer processes which involve spin preservation or spin flip at the intermediate A site.

The fermionic representation of these terms $H^{A,A,B}_{t',trimer}$ is as follows,

$$-K \sum_{\substack{<<ik>>\\<kj>,\sigma}} \eta(\sigma)[X^{\sigma\leftarrow 0}_{kA}X^{0\leftarrow\sigma}_{jB}X^{d\leftarrow\bar{\sigma}}_{iA}X^{0\leftarrow\sigma}_{kA} + X^{\bar{\sigma}\leftarrow 0}_{kA}X^{0\leftarrow\bar{\sigma}}_{jB}X^{d\leftarrow\bar{\sigma}}_{iA}X^{0\leftarrow\sigma}_{kA}]$$

$$= K \sum_{\substack{<<ik>>\\<kj>,\sigma}} (\tilde{c}^{\dagger}_{iA\sigma}\tilde{c}_{kA\bar{\sigma}}\tilde{c}^{\dagger}_{kA\bar{\sigma}}\tilde{\tilde{c}}_{jB\sigma} - \tilde{c}^{\dagger}_{iA\sigma}\tilde{c}_{kA\sigma}\tilde{c}^{\dagger}_{kA\bar{\sigma}}\tilde{\tilde{c}}_{jB\bar{\sigma}})$$

$$= K \sum_{\substack{<<ik>> \\ <kj>,\sigma}} \mathcal{P}(c^{\dagger}_{iA\sigma}(1 - n_{kA\bar{\sigma}})c_{jB\sigma} + c^{\dagger}_{iA\sigma}c^{\dagger}_{kA\bar{\sigma}}c_{kA\sigma}c_{jB\bar{\sigma}})\mathcal{P}. \tag{C.12}$$

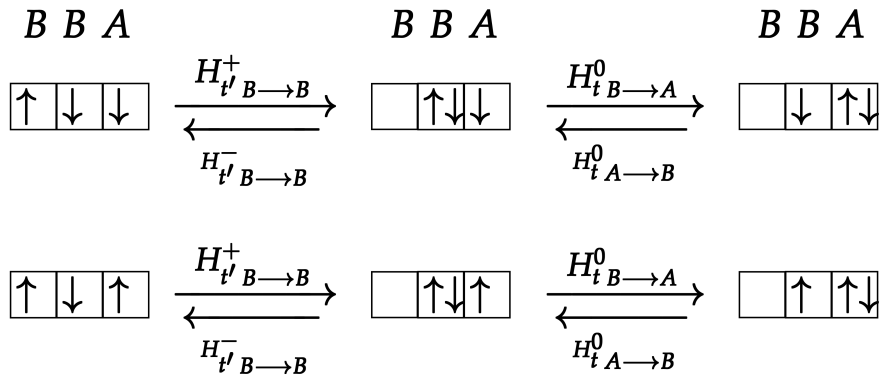

Figure C.4: BBA trimer processes showing spin preservation and spin flip at intermediate B site.

Similarly, the BBA trimer terms appear from the commutator $\frac{K}{tt'}[H^{+}_{t'\ B\to B}, H^{0}_{t\ B\to A}] \sim -\frac{K}{tt'}H^{0}_{t\ B\to A}H^{+}_{t\ B\to B}$. The first term in the commutator requires a doublon at the intermediate B site to start with which is energetically not favourable. As shown in Fig. C.4, these terms also come in two variants, spin preserving and spin flip at the intermediate site.

Below we represent them in terms of X operators and then in terms of projected operators $H^{B,B,A}_{t',trimer}$ as,

$$-K \sum_{\substack{<<lj>> \\ <il>,\sigma}} \eta(\sigma)[X^{d\leftarrow\bar{\sigma}}_{iA}X^{\bar{\sigma}\leftarrow d}_{lB}X^{d\leftarrow\bar{\sigma}}_{lB}X^{0\leftarrow\sigma}_{jB} + X^{d\leftarrow\sigma}_{iA}X^{\sigma\leftarrow d}_{lB}X^{d\leftarrow\bar{\sigma}}_{lB}X^{0\leftarrow\sigma}_{jB}]$$

$$= -K \sum_{\substack{<<lj>> \\ <il>,\sigma}} (\tilde{c}^{\dagger}_{iA\sigma}\tilde{\tilde{c}}^{\dagger}_{lB\bar{\sigma}}\tilde{\tilde{c}}_{lB\bar{\sigma}}\tilde{\tilde{c}}_{jB\sigma} - \tilde{c}^{\dagger}_{iA\sigma}\tilde{\tilde{c}}^{\dagger}_{lB\bar{\sigma}}\tilde{\tilde{c}}_{lB\sigma}\tilde{\tilde{c}}_{jB\bar{\sigma}})$$

$$= -K \sum_{\substack{<<lj>> \\ <il>,\sigma}} \mathcal{P}(c^{\dagger}_{iA\sigma}n_{lB\bar{\sigma}}c_{jB\sigma} - c^{\dagger}_{iA\sigma}c^{\dagger}_{lB\bar{\sigma}}c_{lB\sigma}c_{jB\bar{\sigma}})\mathcal{P}. \tag{C.13}$$

The terms from the commutators $[H^{-}_{t'\ A\to A}, H^{0}_{t\ A\to B}]$ and $[H^{-}_{t'\ B\to B}, H^{0}_{t\ A\to B}]$ are the hermitian conjugate terms of the trimer terms in Eq. (C.12) and (C.13) and are represented by the lower arrows in Fig. C.3 and C.4.

C.3 Gutzwiller factors for the t' terms

The Gutzwiller factors for the terms in the Hamiltonian when we consider only the nearest neighbor hopping have been calculated in details in chapter 2. Here, we will calculate the Gutzwiller factors for the terms arising on introducing next neighbor hopping in the Hamiltonian under the approximation that the spin resolved densities before and after the projection are equal.

Let us first look at the next neighbor hopping renormalization factor. The probability of the hopping in the unprojected space is $n^2_{\alpha\sigma}(1-n_{\alpha\sigma})^2$, where $\alpha \in A, B$. The probability of the hopping process on the A sublattice is $(n_A-1)^2(1-n_{A\sigma})^2$ where as on the B sublattice is $(1-n_B)^2 n^2_{B\sigma}$ in the projected space. Then, the Gutzwiller factor, which is the square root of the ratio of probabilities in the projected and unprojected space becomes,

$$g^{AA}_{t'\sigma} = \frac{(n_A-1)}{n_{A\sigma}} = g_{A\sigma}, \tag{C.14}$$

$$g^{BB}_{t'\sigma} = \frac{(1-n_B)}{(1-n_{B\sigma})} = g_{B\sigma}. \tag{C.15}$$

$g^{\alpha\alpha}_{t'\sigma}$ comes out to be nothing but the Gutzwiller factors of trimer terms involving effective hopping between $\alpha\alpha$ sites. These hopping processes are shown in Fig. C.5(a).

The process of spin exchange is shown in Fig. C.5(b). The probability of the process in unprojected basis is $n^2_{\alpha\uparrow}n^2_{\alpha\downarrow}(1-n_{\alpha\uparrow})^2(1-n_{\alpha\downarrow})^2$. The probabilities in the projected space

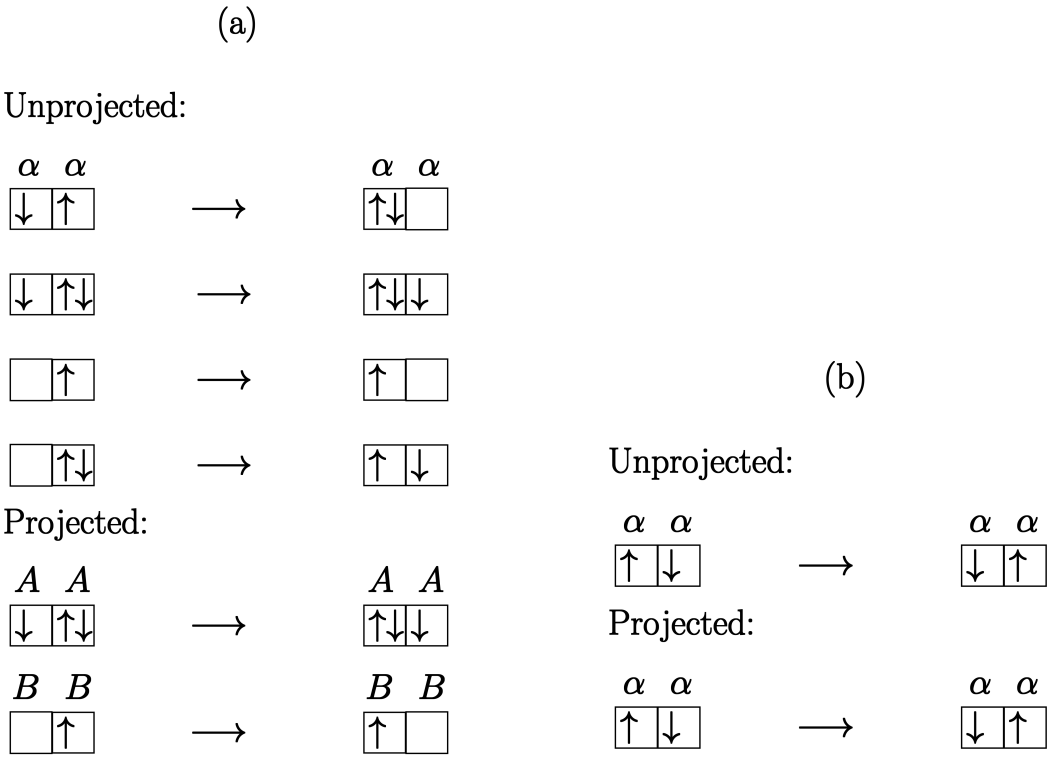

Figure C.5: (a) Next neighbor hoppings in the unprojected and projected spaces on the A and B sublattices. (b) Processes in the unprojected and projected spaces for the Heisenberg terms on A and B sublattices.

for A and B sublattices are $(1-n_{A\uparrow})^2(1-n_{A\downarrow})^2$ and $n_{B\uparrow}^2 n_{B\downarrow}^2$ respectively. The Gutzwiller factors for the Heisenberg term for the two sublattices then become,

$$g_{sAA} = \frac{1}{n_{A\uparrow}n_{A\downarrow}}, \tag{C.16}$$

$$g_{sBB} = \frac{1}{(1-n_{B\uparrow})(1-n_{B\downarrow})}. \tag{C.17}$$

Let us now calculate the Gutzwiller factors for the tt' trimer terms involving a pair of next nearest neighbor sites and a pair of nearest neighbor sites. Let us look at the AAB terms. Fig. C.6(a) represents the processes in the unprojected basis and in the projected

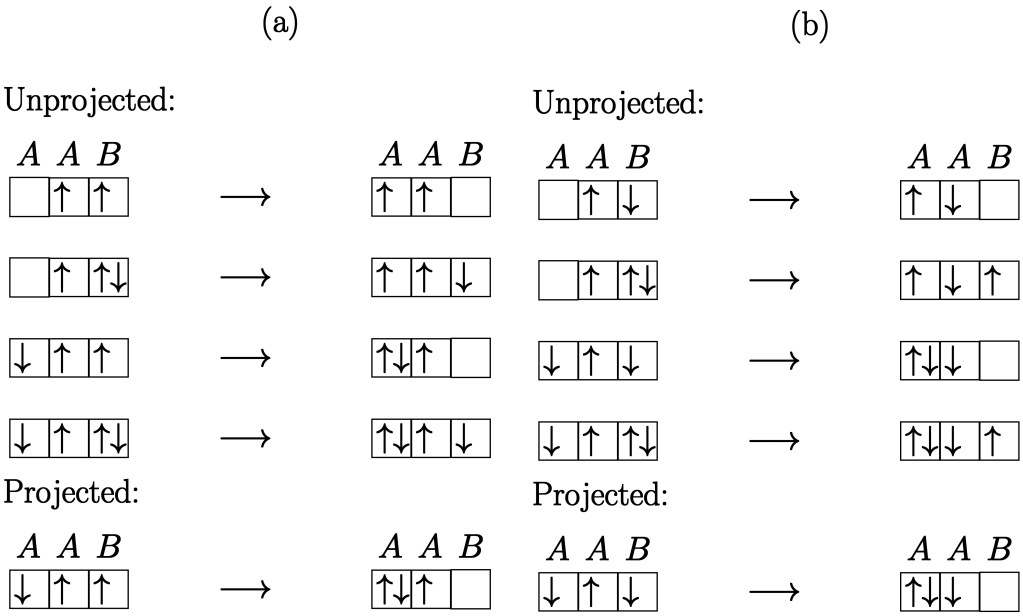

Figure C.6: The tt' trimer terms on AAB sites: (a) with spin preservation at the intermediate site and (b) spin flip at the intermediate site. It is to be noted that in (a), processes with hole at the intermediate site are not shown and must be considered in the calculation.

basis for the spin preserving term. In the unprojected basis, the probability of the process is $(1-n_{A\uparrow})n_{A\uparrow}(1-n_{IA\downarrow})^2(1-n_{B\uparrow})n_{B\uparrow}$ and in the projected basis it is $(1-n_{A\uparrow})(n_A-1)(1-n_{IA\downarrow})^2 n_{B\uparrow}(1-n_B)$ resulting in the Gutzwiller factor,

$$g_{1\uparrow}^{AAB} = \sqrt{\frac{(n_A-1)(1-n_B)}{n_{A\uparrow}(1-n_{B\uparrow})}}. \tag{C.18}$$

This is nothing but the gutzwiller renormalization factor for the nearest neighbor hopping of an up-spin electron. It is to be remembered that in the unprojected basis, processes with either an up-spin or a hole at the intermediate A site have to be considered. Fig C.6(a) shows only the processes with up-spin at the intermediate site in the unprojected space. Here, I stands for the intermediate site. The Gutzwiller factor for the spin preserving hopping on the BBA sites has the same expression as for the AAB term since both of them

connect A and B type sites via an intermediate site and is nothing but $g_{t\sigma}$.

The Gutzwiller factor for the spin flip term on the AAB sites can be calculated similarly. The probability of the process in the unprojected space is $(1-n_{A\uparrow})n_{A\uparrow}n_{IA\uparrow}(1-n_{IA\uparrow})(1-n_{IA\downarrow})n_{IA\downarrow}n_{B\downarrow}(1-n_{B\downarrow})$ and in the projected space is $(1-n_{A\uparrow})(n_A-1)(1-n_{IA\uparrow})(1-n_{IA\downarrow})n_{B\downarrow}(1-n_B)$ resulting in the Gutzwiller factor,

$$g_{2\uparrow}^{AAB} = \sqrt{\frac{(n_A-1)(1-n_B)}{n_{IA\uparrow}n_{IA\downarrow}n_{A\uparrow}(1-n_{B\downarrow})}}. \tag{C.19}$$

We get $g_{2\uparrow}^{BBA}$ if for the intermediate A site in the AAB term we replace $n_{IA\uparrow}n_{IA\downarrow}$ by $(1-n_{IB\uparrow})(1-n_{IB\downarrow})$ for the intermediate B site in the BBA term which results into,

$$g_{2\uparrow}^{BBA} = \sqrt{\frac{(n_A-1)(1-n_B)}{(1-n_{IB\uparrow})(1-n_{IB\downarrow})n_{A\uparrow}(1-n_{B\downarrow})}}. \tag{C.20}$$

Here, I stands for intermediate site. $g_{2\sigma}^{\alpha_1\alpha_1\alpha_2}$ has been simply referred as $g_{\alpha_1\alpha_1\alpha_2\sigma}$ in Appendix C.1.

C.4 Mean field Hamiltonian and self-consistent equations

The mean field quadratic Hamiltonian is expressed as,

$$\mathcal{H} = \sum_k \begin{pmatrix} c_{kA\uparrow}^\dagger & c_{kB\uparrow}^\dagger & c_{-kA\downarrow} & c_{-kB\downarrow} \end{pmatrix} \tilde{H} \begin{pmatrix} c_{kA\uparrow} \\ c_{kB\uparrow} \\ c_{-kA\downarrow}^\dagger \\ c_{-kB\downarrow}^\dagger \end{pmatrix}, \tag{C.21}$$

where, $\tilde{H} = \begin{pmatrix} H_{A\uparrow}(k) & H_{AB\uparrow}(k) & 0 & H_D(k) \\ H_{AB\uparrow}(k) & H_{B\uparrow}(k) & -H_C(k) & 0 \\ 0 & -H_C(k) & -H_{A\downarrow}(k) & -H_{AB\downarrow}(k) \\ H_D(k) & 0 & -H_{AB\downarrow}(k) & -H_{B\downarrow}(k) \end{pmatrix}$.

Here,

$H_{A\sigma}(k) = T^0_{A\sigma}(k) + T^1_{A\sigma}(k)$

$H_{B\sigma}(k) = T^0_{B\sigma}(k) - T^1_{B\sigma}(k)$

$T^0_{\alpha\sigma}(k) = -\frac{U-\Delta}{4}\sigma m_\alpha + \frac{t^2}{\Delta}\left[g_{\alpha\sigma}\gamma_{k2}\sigma\frac{m_{\bar{\alpha}}}{2} - g_{\bar{\alpha}\bar{\sigma}}(d\chi_{\bar{\alpha}\bar{\alpha}\bar{\sigma}} + 4^d C_2\chi'_{\bar{\alpha}\bar{\alpha}\bar{\sigma}})\right] + \frac{t^2}{U+\Delta}dg_{sAB}\sigma m_{\bar{\alpha}} - t'\gamma_{k3}g_{\alpha\sigma} + \frac{4t'^2}{U}{}^dC_2 g_{s\alpha\alpha}\sigma m_\alpha - \frac{t'^2}{2U}\left[g_{s\alpha\alpha}\chi'_{\alpha\alpha\sigma} + 2g_{s\alpha\alpha}\chi'_{\alpha\alpha\bar{\sigma}} - \chi'_{\alpha\alpha\sigma}\right]\gamma_{k3} - \frac{tt'(U+\Delta)}{2U\Delta}\left[16^dC_2 g_{t\bar{\sigma}}\sum_{i=1}^{d}\chi^{(i)}_{AB\bar{\sigma}} + 4dG(\alpha)\chi^{(1)}_{AB\bar{\sigma}}\gamma_{k3}\right] - \mu$

where, $G(A) = g_{AAB\sigma}$ and $G(B) = g_{BBA\bar{\sigma}}$.

$T^1_{\alpha\sigma}(k) = \frac{U-\Delta}{4}(1+\delta) - \frac{t^2}{\Delta}\left[2d(1-2\delta) + g_{\alpha\sigma}\gamma_{k2}\frac{(1-\delta)}{2}\right] + \frac{t^2}{U+\Delta}d(1-\delta) + \frac{4t'^2}{U}{}^dC_2(1-\delta)$

$H_{AB\sigma}(k) = \left[-tg_{t\sigma} - \frac{t^2}{\Delta}\left(-2\chi^{(1)}_{AB\sigma} + 2(2d-1)g_2\chi^{(1)}_{AB\bar{\sigma}}\right) - \frac{t^2}{2(U+\Delta)}g_{sAB}\chi^{(1)}_{AB\sigma} - \frac{t^2}{U+\Delta}g_{sAB}\chi^{(1)}_{AB\bar{\sigma}} - \frac{t^2}{2(U+\Delta)}\chi^{(1)}_{AB\sigma} + \frac{tt'(U+\Delta)}{2U\Delta}\left(g_{t\sigma}\frac{m_A+m_B}{2}\gamma_{k3} - 2^dC_2 g_{AAB\bar{\sigma}}\chi'_{AA\bar{\sigma}} - 2^dC_2 g_{BBA\sigma}\chi'_{BB\bar{\sigma}}\right)\right]\gamma_{k1}$

$H_C(k) = T^{\pm}_{\uparrow}(\cos(k_x) \pm \cos(k_y))$

$H_D(k) = -T^{\pm}_{\downarrow}(\cos(k_x) \pm \cos(k_y))$

where,

$$T_{\sigma}^{-} = \Bigg[\Bigg\{\frac{2t^2}{\Delta} - \frac{2t^2}{U+\Delta}\Bigg(-\frac{3g_{sAB}}{4} + \frac{1}{4}\Bigg) - \frac{t^2}{\Delta}\Bigg(g_{A\bar{\sigma}} + g_{B\sigma}\Bigg) - \frac{2t^2}{\Delta}g_2\Bigg\}\Delta_{AB}^{-}\Bigg]$$

$$T_{\sigma}^{+} = \Bigg[\Bigg\{\frac{2t^2}{\Delta} - \frac{2t^2}{U+\Delta}\Bigg(-\frac{3g_{sAB}}{4} + \frac{1}{4}\Bigg) + \frac{3t^2}{\Delta}\Bigg(g_{A\bar{\sigma}} + g_{B\sigma}\Bigg) + \frac{6t^2}{\Delta}g_2\Bigg\}\Delta_{AB}^{+}\Bigg]$$

For cubic lattice, pairing terms will have an extra contribution for extended s-wave pairing symmetry which is $\frac{4t^2}{\Delta}\cos(k_z)(g_{A\downarrow} + g_{B\uparrow} + 2g_2)\Delta_{AB}^{+}$ and will have to be added to $H_C(k)$ and the opposite spin version will have to be subtracted from $H_D(k)$. Here, $\gamma_{k1} = 2\sum_i \cos(k_i)$, $\gamma_{k2} = 2\sum_i \cos(2k_i) + 4\sum_{\substack{i,j \\ i\neq j}}[\cos(k_i + k_j) + \cos(k_i - k_j)]$ and $\gamma_{k3} = 2\sum_{\substack{i,j \\ i\neq j}}[\cos(k_i + k_j) + \cos(k_i - k_j)]$ where i, j can take x,y or x,y,z values depending upon whether it is square or cubic lattice. Also, d refers to the number of dimensions in the above Hamiltonian. If $\alpha = A$, then $\bar{\alpha} = B$ and vice-versa.

We diagonalize the Hamiltonian in three routes: (1) Diagonalize the block diagonal Hamiltonian keeping pairing terms zero (2) Full numerical diagonalization in the spin symmetric case keeping pairing (3) Two step diagonalization in spin asymmetric phase keeping pairing. The self-consistent equations of the mean field parameters are as follows,

$$
\left.
\begin{aligned}
\chi^{(1)}_{AB\sigma} =& \frac{1}{2dN}\sum_k \langle c^\dagger_{kA\sigma} c_{kB\sigma}\rangle \gamma_{k1}, \\
\chi^{(2)}_{AB\sigma} =& \frac{1}{2^d C_2 N}\sum_k \langle c^\dagger_{kA\sigma} c_{kB\sigma}\rangle \sum_{\substack{i,j \\ i\neq j}} \cos(2k_i)\cos(k_j), \\
\chi^{(3)}_{AB\sigma} =& \frac{1}{N}\sum_k \langle c^\dagger_{kA\sigma} c_{kB\sigma}\rangle \cos(kx)\cos(ky)\cos(kz), \\
\chi_{BB\sigma} =& \frac{1}{dN}\sum_k \langle c^\dagger_{kB\sigma} c_{kB\sigma}\rangle \sum_i 2\cos(2k_i), \\
\chi'_{BB\sigma} =& \frac{1}{2^d C_2 N}\sum_k \langle c^\dagger_{kB\sigma} c_{kB\sigma}\rangle \sum_{\substack{i,j \\ i\neq j}} 4\cos(k_i)\cos(k_j), \\
\chi_{AA\sigma} =& \frac{1}{dN}\sum_k \langle c^\dagger_{kA\sigma} c_{kA\sigma}\rangle \sum_i 2\cos(2k_i), \\
\chi'_{AA\sigma} =& \frac{1}{2^d C_2 N}\sum_k \langle c^\dagger_{kA\sigma} c_{kA\sigma}\rangle \sum_{\substack{i,j \\ i\neq j}} 4\cos(k_i)\cos(k_j), \\
\delta =& \frac{1}{2N}\sum_{k,\sigma} (\langle c^\dagger_{kA\sigma} c_{kA\sigma}\rangle - \langle c^\dagger_{kB\sigma} c_{kB\sigma}\rangle), \\
m_A =& \frac{1}{N}\sum_k (\langle c^\dagger_{kA\uparrow} c_{kA\uparrow}\rangle - \langle c^\dagger_{kA\downarrow} c_{kA\downarrow}\rangle), \\
m_B =& \frac{1}{N}\sum_k (\langle c^\dagger_{kB\uparrow} c_{kB\uparrow}\rangle - \langle c^\dagger_{kB\downarrow} c_{kB\downarrow}\rangle), \\
\Delta^{\pm}_{AB} =& \frac{1}{2N}\sum_k (\langle c^\dagger_{kA\uparrow} c^\dagger_{-kB\downarrow}\rangle - \langle c^\dagger_{-kA\downarrow} c^\dagger_{kB\uparrow}\rangle)(\cos(k_x) \pm \cos(k_y)).
\end{aligned}
\right\} \tag{C.22}
$$

The ground state energy is in general a sum of a k-dependent term (which will be specified for each case) and the constant terms which come from the mean field decomposition. It has the following general structure,

$$
\begin{aligned}
&E_{GS}/N \\
&= \Bigg[\frac{1}{2}\sum_{k\in FBZ} F(k) + \frac{1}{8}(U-\Delta)\left(\frac{m_A^2+m_B^2}{2}+1-\delta^2\right) - \frac{2dt^2}{\Delta}(\delta^2 + {\chi^{(1)}_{AB\uparrow}}^2 + {\chi^{(1)}_{AB\downarrow}}^2) + \\
&\frac{t^2}{2(U+\Delta)} d[g_{sAB}(-m_A m_B + {\chi^{(1)}_{AB\uparrow}}^2 + {\chi^{(1)}_{AB\downarrow}}^2 + 4\chi^{(1)}_{AB\uparrow}\chi^{(1)}_{AB\downarrow}) - (1-\delta^2 - {\chi^{(1)}_{AB\uparrow}}^2 - {\chi^{(1)}_{AB\downarrow}}^2)] + \\
&\frac{t^2}{4\Delta}\sum_{\sigma}[g_{A\sigma}(1-\delta-\sigma m_B)(d\chi_{AA\sigma} + 4^d C_2 \chi'_{AA\sigma}) + g_{B\sigma}(1+\delta-\sigma m_A)(d\chi_{BB\sigma} + 4^d C_2 \chi'_{BB\sigma})] + \\
&\frac{4t^2}{\Delta} g_2 (4^d C_2 + d)\chi^{(1)}_{AB\uparrow}\chi^{(1)}_{AB\downarrow} - \frac{t'^2}{U}\sum_{\alpha\in A,B} g_{s\alpha\alpha}\, {}^d C_2 m_\alpha^2 + \frac{t'^2}{U}\sum_{\alpha\in A,B} {}^d C_2 \Bigg[g_{s\alpha\alpha}\Bigg(\frac{{\chi'_{\alpha\alpha\uparrow}}^2 + {\chi'_{\alpha\alpha\downarrow}}^2}{4} + \\
&\chi'_{\alpha\alpha\uparrow}\chi'_{\alpha\alpha\downarrow}\Bigg) - \frac{{\chi'_{\alpha\alpha\uparrow}}^2 + {\chi'_{\alpha\alpha\downarrow}}^2}{4}\Bigg] - \frac{4t'^2}{U}{}^d C_2 + \frac{2t'^2}{U}{}^d C_2(1+\delta^2) + \frac{tt'(U+\Delta)}{2U\Delta}{}^d C_2 \sum_{\sigma}\Bigg[8g_{t\sigma} \\
&\left(1 - \frac{\sigma(m_A+m_B)}{2}\right)\sum_{i=1}^{d}\chi^{(i)}_{AB\sigma} + 4d g_{AAB\sigma}\chi'_{AA\sigma}\chi^{(1)}_{AB\bar{\sigma}} + 4d g_{BBA\sigma}\chi'_{BB\bar{\sigma}}\chi^{(1)}_{AB\sigma}\Bigg] \\
&+ \textit{Pairing term contribution}
\end{aligned}
\tag{C.23}
$$

Pairing term contribution for d-wave:

$$\left[\frac{t^2}{U+\Delta}[\frac{3}{2}g_{sAB} - \frac{1}{2}] + \frac{2t^2}{\Delta} - \frac{t^2}{2\Delta}[(g_{A\uparrow}+g_{A\downarrow}+g_{B\uparrow}+g_{B\downarrow})] - \frac{2t^2}{\Delta}g_2\right]{\Delta^-_{AB}}^2$$

Pairing term contribution for extended s-wave:

$$\left[\frac{t^2}{U+\Delta}[\frac{3}{2}g_{sAB} - \frac{1}{2}] + \frac{2t^2}{\Delta} + \frac{3t^2}{2\Delta}[(g_{A\uparrow}+g_{A\downarrow}+g_{B\uparrow}+g_{B\downarrow})] + \frac{6t^2}{\Delta}g_2\right]{\Delta^+_{AB}}^2$$

C.4.1 Calculation without pairing

In this case, we put $H_{C,D} = 0$ i.e., we turn off pairing. The mean field Hamiltonian in Eq. C.21 is then block diagonal. The following transformation diagonalizes the Hamiltonian,

$$
\begin{aligned}
c_{kA\sigma} &= \alpha_{k\sigma} d_{k1\sigma} + \beta_{k\sigma} d_{k2\sigma} \\
c_{kB\sigma} &= \alpha_{k\sigma} d_{k2\sigma} - \beta_{k\sigma} d_{k1\sigma}
\end{aligned}
\tag{C.24}
$$

where,

$$
\alpha_{k\sigma}^2 = \frac{1}{2}\left(1 - \frac{(H_{A\sigma}(k) - H_{B\sigma}(k))}{\zeta_\sigma}\right),
$$

$$
\beta_{k\sigma}^2 = \frac{1}{2}\left(1 + \frac{(H_{A\sigma}(k) - H_{B\sigma}(k))}{\zeta_\sigma}\right).
$$

Here, $\zeta_\sigma = \sqrt{(H_{A\sigma}(k) - H_{B\sigma}(k))^2 + 4H_{AB\sigma}(k)^2}$. The energy eigenvalues of the Hamiltonian in Eq. C.21 are $E_{1\uparrow}, -E_{1\downarrow}, E_{2\uparrow}, -E_{2\downarrow}$ where $E_{1\sigma}(k) = \dfrac{(H_{A\sigma}(k) + H_{B\sigma}(k)) - \zeta_\sigma}{2}$ and $E_{2\sigma}(k) = \dfrac{(H_{A\sigma}(k) + H_{B\sigma}(k)) + \zeta_\sigma}{2}$.

The appropriate self-consistent equations in Eq. C.22 should be substituted by the following,

$$
\left.
\begin{aligned}
n_{kA\sigma} &= [\alpha_{k\sigma}^2 \langle d_{k1\sigma}^\dagger d_{k1\sigma}\rangle + \beta_{k\sigma}^2 \langle d_{k2\sigma}^\dagger d_{k2\sigma}\rangle], \\
n_{kB\sigma} &= [\beta_{k\sigma}^2 \langle d_{k1\sigma}^\dagger d_{k1\sigma}\rangle + \alpha_{k\sigma}^2 \langle d_{k2\sigma}^\dagger d_{k2\sigma}\rangle], \\
\langle c_{kA\sigma}^\dagger c_{kB\sigma}\rangle &= [-\alpha_{k\sigma}\beta_{k\sigma} \langle d_{k1\sigma}^\dagger d_{k1\sigma}\rangle + \alpha_{k\sigma}\beta_{k\sigma} \langle d_{k2\sigma}^\dagger d_{k2\sigma}\rangle].
\end{aligned}
\right\}
\tag{C.25}
$$

Here, $\langle d_{ki\sigma}^\dagger d_{ki\sigma}\rangle, i \in 1, 2$ is the Fermi-Dirac distribution function at absolute zero temperature which means all those states will be summed over which are below the Fermi level. In the ground state energy expression, $F(k) = \sum_\sigma E_{1\sigma}(k)\langle d_{k1\sigma}^\dagger d_{k1\sigma}\rangle + E_{2\sigma}(k)\langle d_{k2\sigma}^\dagger d_{k2\sigma}\rangle$ in this case.

In chapter 4, we have shown the spectral functions in the non-superconducting phase viz, the ferrimagnetic metallic phase and the paramagnetic metallic phase. The relevant expression of the single particle spectral function is shown below,

$$A_\sigma(k,w)=\frac{1}{2}[(g_{A\sigma}\alpha_{k\sigma}^2+g_{B\sigma}\beta_{k\sigma}^2)\delta(\omega-E_{1\sigma})+(g_{A\sigma}\beta_{k\sigma}^2++g_{B\sigma}\alpha_{k\sigma}^2)\delta(\omega-E_{2\sigma})], \quad \text{(C.26)}$$

which can be obtained from the definition of the retarded Green's functions defined on A and B sublattices,

$$G_{\alpha\alpha\sigma}(t)=-i\theta(-t)\langle\{c_{\alpha\sigma}(0),c_{\alpha\sigma}^\dagger(t)\}\rangle. \quad \text{(C.27)}$$

Here,

$$\begin{aligned} G_{AA\sigma}(k,\omega)&=\frac{\alpha_{k\sigma}^2}{\omega-E_{1\sigma}+i\eta}+\frac{\beta_{k\sigma}^2}{\omega-E_{2\sigma}+i\eta},\\ G_{BB\sigma}(k,\omega)&=\frac{\beta_{k\sigma}^2}{\omega-E_{1\sigma}+i\eta}+\frac{\alpha_{k\sigma}^2}{\omega-E_{2\sigma}+i\eta}, \end{aligned} \quad \text{(C.28)}$$

where, $g_{A\sigma}=2\delta/(1+\delta+\sigma m_A)$, $g_{B\sigma}=2\delta/(1+\delta-\sigma m_B)$ which are different for ferrimagnetic phase but equal in para phases.

C.4.2 Spin-symmetric calculation with pairing

We do the following generalized Bogoluibov transformation on the mean field Hamiltonian:

$$\begin{pmatrix} c_{kA\uparrow}\\ c_{kB\uparrow}\\ c_{-kA\downarrow}^\dagger\\ c_{-kB\downarrow}^\dagger \end{pmatrix}=\begin{pmatrix} u_{1k} & u_{2k} & v_{1k} & v_{2k}\\ u_{3k} & u_{4k} & v_{3k} & v_{4k}\\ -v_{1k} & -v_{2k} & u_{1k} & u_{2k}\\ -v_{3k} & -v_{4k} & u_{3k} & u_{4k} \end{pmatrix}\begin{pmatrix} f_{1k}\\ f_{3k}\\ f_{2k}^\dagger\\ f_{4k}^\dagger \end{pmatrix} \quad \text{(C.29)}$$

We impose that the above transformation diagonalizes the Hamiltonian in the form $\mathcal{H} = \sum_k E_1(k) f^\dagger_{1k} f_{1k} - E_2(k) f_{2k} f^\dagger_{2k} + E_3(k) f^\dagger_{3k} f_{3k} - E_4(k) f_{4k} f^\dagger_{4k} + const.$ Next we calculate commutators of the fermionic 'c_{kA}, c_{kB}' operators with the mean field Hamiltonian and the diagonalized Hamiltonian and equate the coefficients of the bogoluibov operators to get the eigenvalue equations. Then, we diagonalize the Hamiltonian matrix for every k-value in the Brillouin zone to get 4 eigenvectors which are nothing but the columns of the transformation matrix.

The excitation energies $E_{ik}, i \in \{1, 4\}$ are all positive for the Bogoluibov spectrum. Hence, to get the self-consistent equations in this case, we substitute the following in Eq. C.22,

$$\left.\begin{aligned} n_{kA\sigma} =& [v^2_{1k} + v^2_{2k}], \\ n_{kB\sigma} =& [v^2_{3k} + v^2_{4k}], \\ \langle c^\dagger_{kA\sigma} c_{kB\sigma} \rangle =& [v_{1k} v_{3k} + v_{2k} v_{4k}], \\ \langle c^\dagger_{kA\uparrow} c^\dagger_{-kB\downarrow} \rangle =& [v_{1k} u_{3k} + v_{2k} u_{4k}], \\ \langle c^\dagger_{-kA\downarrow} c^\dagger_{kB\uparrow} \rangle =& -[v_{1k} u_{3k} + v_{2k} u_{4k}]. \end{aligned}\right\} \tag{C.30}$$

In the ground state energy, $F(k) = H_A(k) + H_B(k) - E_2(k) - E_4(k)$ in this case of spin symmetric numerical diagonalization calculation.

The spin symmetric spectral function obtained from the retarded Green's function, $G_{\alpha\alpha}(t) = -i\theta(-t)\langle\{c_\alpha(0), c^\dagger_\alpha(t)\}\rangle$ in this case is,

$$\begin{aligned} A(k,\omega) =& \frac{1}{2}[(g_A v^2_{1k} + g_B v^2_{3k})\delta(\omega - E_1(k)) + (g_A v^2_{2k} + g_B v^2_{4k})\delta(\omega - E_3(k)) + \\ & (g_A u^2_{1k} + g_B u^2_{3k})\delta(\omega + E_2(k)) + (g_A u^2_{2k} + g_B u^2_{4k})\delta(\omega + E_4(k))], \end{aligned} \tag{C.31}$$

where, $E_1 = E_2$ and $E_3 = E_4$.

C.4.3 Two step spin asymmetric calculation

In this calculation, we do a spin asymmetric calculation keeping pairing as a mean field parameter. Firstly we do the transformation as in Eq. C.24. Subsequently, we do a second Bogoluibov transformation to diagonalize the Hamiltonian. Here, we have neglected the interband pairing terms considering them as weak.

The Hamiltonian after first set of transformation (neglecting interband pairing terms) is,

$$H_1 = \sum_{k,\sigma}[\omega_\sigma d^\dagger_{k1\sigma} d_{k1\sigma} + \phi_\sigma d^\dagger_{k2\sigma} d_{k2\sigma}] + \sum_k [\nu d^\dagger_{-k1\downarrow} d^\dagger_{k1\uparrow} + \lambda {d^\dagger}_{-k2\downarrow} d^\dagger_{k2\uparrow} + H.c.] \quad \text{(C.32)}$$

where,

$\omega_\sigma = \dfrac{H_{A\sigma}(k) + H_{B\sigma}(k) - \zeta_\sigma(k)}{2}$,

$\phi_\sigma = \dfrac{H_{A\sigma}(k) + H_{B\sigma}(k) + \zeta_\sigma(k)}{2}$,

$\zeta_\sigma(k) = \sqrt{(H_{A\sigma}(k) - H_{B\sigma}(k))^2 + 4H_{AB\sigma}(k)^2}$,

$\nu = -(H_C(k)\alpha_{k\downarrow}\beta_{k\uparrow} - H_D(k)\alpha_{k\uparrow}\beta_{k\downarrow})$,

$\lambda = (H_C(k)\alpha_{k\uparrow}\beta_{k\downarrow} - H_D(k)\alpha_{k\downarrow}\beta_{k\uparrow})$.

The second transformation to diagonalize the above Hamiltonian is,

$$\begin{aligned} d_{k1\uparrow} &= u_{k1} f_{k1} + v_{k1} f^\dagger_{k2}, \\ d^\dagger_{-k1\downarrow} &= -v_{k1} f_{k1} + u_{k1} f^\dagger_{k2}, \\ d_{k2\uparrow} &= u_{k2} f_{k3} + v_{k2} f^\dagger_{k4}, \\ d^\dagger_{-k2\downarrow} &= -v_{k2} f_{k3} + u_{k2} f^\dagger_{k4}. \end{aligned} \quad \text{(C.33)}$$

Here, $u_{k1}^2 = \frac{1}{2}\left(1 + \frac{\omega_\uparrow + \omega_\downarrow}{\sqrt{(\omega_\uparrow + \omega_\downarrow)^2 + 4\nu^2}}\right)$,

$v_{k1}^2 = \frac{1}{2}\left(1 - \frac{\omega_\uparrow + \omega_\downarrow}{\sqrt{(\omega_\uparrow + \omega_\downarrow)^2 + 4\nu^2}}\right)$,

$u_{k2}^2 = \frac{1}{2}\left(1 + \frac{\phi_\uparrow + \phi_\downarrow}{\sqrt{(\phi_\uparrow + \phi_\downarrow)^2 + 4\lambda^2}}\right)$,

$v_{k2}^2 = \frac{1}{2}\left(1 - \frac{\phi_\uparrow + \phi_\downarrow}{\sqrt{(\phi_\uparrow + \phi_\downarrow)^2 + 4\lambda^2}}\right)$.

The diagonalized Hamiltonian is of the form,

$$H_d = \sum_k E_1^+(k) f_{k1}^\dagger f_{k1} + E_1^-(k) f_{k2}^\dagger f_{k2} + E_2^+(k) f_{k3}^\dagger f_{k3} + E_2^-(k) f_{k4}^\dagger f_{k4} + \text{Constant terms.} \tag{C.34}$$

where,

$$E_1^\pm(k) = \pm\frac{\omega_\uparrow - \omega_\downarrow}{2} + \frac{1}{2}\sqrt{(\omega_\uparrow + \omega_\downarrow)^2 + 4\nu^2}$$
$$E_2^\pm(k) = \pm\frac{\phi_\uparrow - \phi_\downarrow}{2} + \frac{1}{2}\sqrt{(\phi_\uparrow + \phi_\downarrow)^2 + 4\lambda^2}$$

In this case, $F(k) = \left(\frac{\omega_\uparrow(k) + \omega_\downarrow(k)}{2} - \frac{1}{2}\sqrt{(\omega_\uparrow(k) + \omega_\downarrow(k))^2 + 4\nu(k)^2} + \frac{\phi_\uparrow(k) + \phi_\downarrow(k)}{2} - \frac{1}{2}\sqrt{(\phi_\uparrow(k) + \phi_\downarrow(k))^2 + 4\lambda(k)^2}\right) + E_1^+(k)\langle f_{k1}^\dagger f_{k1}\rangle + E_1^-(k)\langle f_{k2}^\dagger f_{k2}\rangle + E_2^+(k)\langle f_{k3}^\dagger f_{k3}\rangle + E_2^-(k)\langle f_{k4}^\dagger f_{k4}\rangle$ in the ground state energy calculation.

The following expectation values should be substituted in Eq. C.22 to get the self-consistent equations which are solved iteratively,

$$
\left.
\begin{aligned}
&n_{kA\uparrow} = \alpha_{k\uparrow}^2(u_{k1}^2\langle f_{k1}^\dagger f_{k1}\rangle + v_{k1}^2\langle f_{k2}f_{k2}^\dagger\rangle) + \beta_{k\uparrow}^2(u_{k2}^2\langle f_{k3}^\dagger f_{k3}\rangle + v_{k2}^2\langle f_{k4}f_{k4}^\dagger\rangle),\\
&n_{kA\downarrow} = \alpha_{k\downarrow}^2(v_{k1}^2\langle f_{k1}f_{k1}^\dagger\rangle + u_{k1}^2\langle f_{k2}^\dagger f_{k2}\rangle) + \beta_{k\downarrow}^2(v_{k2}^2\langle f_{k3}f_{k3}^\dagger\rangle + u_{k2}^2\langle f_{k4}^\dagger f_{k4}\rangle),\\
&n_{kB\uparrow} = \alpha_{k\uparrow}^2(u_{k2}^2\langle f_{k3}^\dagger f_{k3}\rangle + v_{k2}^2\langle f_{k4}f_{k4}^\dagger\rangle) + \beta_{k\uparrow}^2(u_{k1}^2\langle f_{k1}^\dagger f_{k1}\rangle + v_{k1}^2\langle f_{k2}f_{k2}^\dagger\rangle),\\
&n_{kB\downarrow} = \alpha_{k\downarrow}^2(v_{k2}^2\langle f_{k3}f_{k3}^\dagger\rangle + u_{k2}^2\langle f_{k4}^\dagger f_{k4}\rangle) + \beta_{k\downarrow}^2(v_{k1}^2\langle f_{k1}f_{k1}^\dagger\rangle + u_{k1}^2\langle f_{k2}^\dagger f_{k2}\rangle),\\
&\langle c_{kA\uparrow}^\dagger c_{kB\uparrow}\rangle = -\alpha_{k\uparrow}\beta_{k\uparrow}(u_{k1}^2\langle f_{k1}^\dagger f_{k1}\rangle + v_{k1}^2\langle f_{k2}f_{k2}^\dagger\rangle) +\\
&\alpha_{k\uparrow}\beta_{k\uparrow}(u_{k2}^2\langle f_{k3}^\dagger f_{k3}\rangle + v_{k2}^2\langle f_{k4}f_{k4}^\dagger\rangle),\\
&\langle c_{kA\downarrow}^\dagger c_{kB\downarrow}\rangle = -\alpha_{k\downarrow}\beta_{k\downarrow}(v_{k1}^2\langle f_{k1}f_{k1}^\dagger\rangle + u_{k1}^2\langle f_{k2}^\dagger f_{k2}\rangle) +\\
&\alpha_{k\downarrow}\beta_{k\downarrow}(v_{k2}^2\langle f_{k3}f_{k3}^\dagger\rangle + u_{k2}^2\langle f_{k4}^\dagger f_{k4}\rangle),\\
&\langle c_{kA\uparrow}^\dagger c_{-kB\downarrow}^\dagger\rangle = -\alpha_{k\uparrow}\beta_{k\downarrow}(-u_{k1}v_{k1}\langle f_{k1}^\dagger f_{k1}\rangle + u_{k1}v_{k1}\langle f_{k2}f_{k2}^\dagger\rangle) +\\
&\alpha_{k\downarrow}\beta_{k\uparrow}(-u_{k2}v_{k2}\langle f_{k3}^\dagger f_{k3}\rangle + u_{k2}v_{k2}\langle f_{k4}f_{k4}^\dagger\rangle),\\
&\langle c_{-kA\downarrow}^\dagger c_{kB\uparrow}^\dagger\rangle = -\alpha_{k\downarrow}\beta_{k\uparrow}(-u_{k1}v_{k1}\langle f_{k1}f_{k1}^\dagger\rangle + u_{k1}v_{k1}\langle f_{k2}^\dagger f_{k2}\rangle) +\\
&\alpha_{k\uparrow}\beta_{k\downarrow}(-u_{k2}v_{k2}\langle f_{k3}f_{k3}^\dagger\rangle + u_{k2}v_{k2}\langle f_{k4}^\dagger f_{k4}\rangle).
\end{aligned}
\right\} \quad \text{(C.35)}
$$

If we do a spin symmetric two step calculation keeping intraband pairing but neglecting inter-band pairing then we can get analytical expressions for the superconducting gap in the d-wave and extended s-wave pairing channels.

The gap in case of d-wave turns out to be

$$Gap_d = 2Max\left(\sqrt{H_C(k)^2\left(1-\left(\frac{H_A(k)-H_B(k)}{H_A(k)+H_B(k)}\right)^2\right)}\delta(\phi(k))\right)$$

Where as the gap for extended s-wave is,

$$Gap_s = 2Max\left(\sqrt{H_C(k)^2\left(1-\left(\frac{H_A(k)-H_B(k)}{H_A(k)+H_B(k)}\right)^2\right)}\delta(\omega(k))\right)$$

The absolute value of eigenvalues in the spin symmetric case from 2 step transformation are $\sqrt{\omega^2+\nu^2}$ and $\sqrt{\phi^2+\nu^2}$. The gap then will become the maximum value of ν on the

countour in the Brillouin zone where $\omega = 0$ or $\phi = 0$.

The expression of ν^2 in this case is $\nu^2 = 4H_{AB}^2 H_C^2/\zeta^2$. Since for $\omega = 0$ or $\phi = 0$, $4H_{AB}^2 = (H_A + H_B)^2 - (H_A - H_B)^2$ and $\zeta^2 = (H_A + H_B)^2$, we have substituted these in the expression of ν under the constraint that these quantities are calculated on the contour where $\omega = 0$ or $\phi = 0$, while finding the gap.

C.5 Competing order-parameters and ground state energy comparison

We solve the effective low energy Hamiltonian using three different versions of renormalized mean field theory (RMFT) (as explained in Appendix C.4), the first which allows for superconductivity but not magnetic order, the second which allows for the magnetic order but not superconductivity, and the third which allows for both, along with various other mean fields, as discussed in Section 4.3 of chapter 4. When we compare the results from the first two calculations, we find that there is a significantly broad regime of parameters over which the SC and magnetic orders both exist and compete with each other. In order to determine the true nature of the ground state in this parameter regime, we compare the ground state energies of the different RMFT solutions.

As shown in Fig. C.7 , even for small values of t', the SC pairing amplitudes, in both the pairing channels studied, turn on but the magnetic transition precedes the transition into the SC phase. Once the magnetic order turns on, the ground state energy of the non-superconducting solution becomes lower than that of both the SC phases studied as shown in the right panels of Fig. C.7. Thus for $t' < 0.1t$ there is no stable SC phase, as shown in Fig. 4.2[e] of chapter 4. For larger values of t', as U/Δ increases superconductivity turns

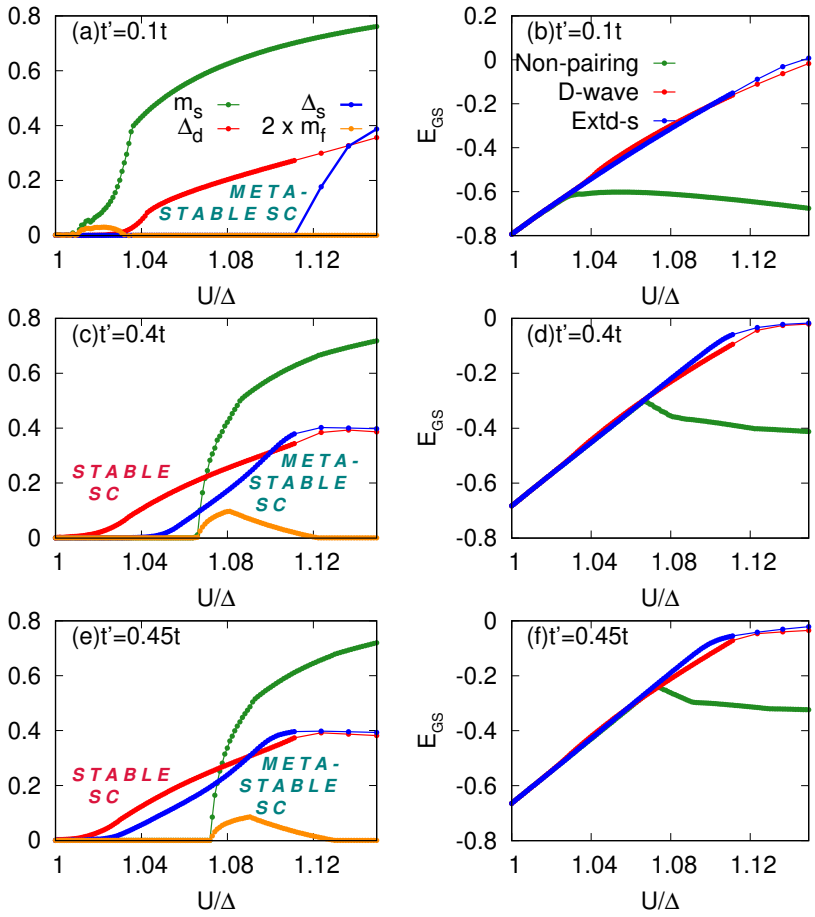

Figure C.7: **Order parameters and the ground state energy**. Left panels show various mean fields, namely, the staggered magnetization m_s, uniform magnetization m_f, d-wave pairing amplitude Δ_d and the extended s-wave pairing amplitude Δ_s as functions of U/Δ for different values of t' at $U = 10t$ for the 2d square lattice. Right panels show the ground state energies for the d-wave SC phase, extended s-wave SC phase and the non-superconducting phase where only magnetic order is allowed, as functions of U/Δ.

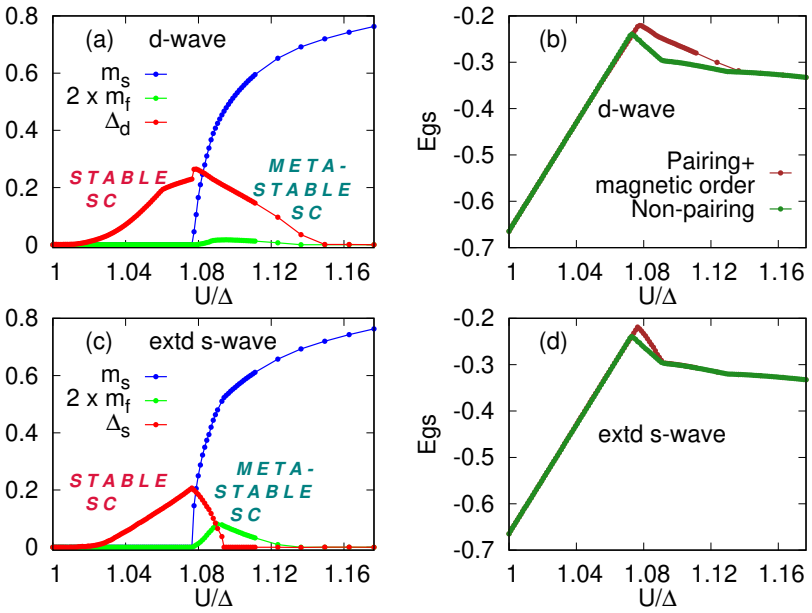

Figure C.8: **Comparison of different renormalized mean field theories**. Top left panel shows several mean fields obtained from the third solution of the RMFT where both SC pairing and magnetic order are allowed, namely, the staggered magnetization m_s, uniform magnetization m_f, and the d-wave pairing amplitude Δ_d as functions of U/Δ for $t' = 0.45t$ and $U = 10t$. Top right panel shows the ground state energy of the non-superconducting phase where only magnetic order is allowed and the energy for the third solution as functions of U/Δ. Note that the phase with both orders coexisting is only a metastable phase. Lower panels show similar results for the extended s-wave SC order.

on before the magnetic order sets in. There continues to be a solution of the RMFT with pairing amplitudes, in either of the symmetry channels, non zero even in the magnetically ordered regime, but the non-superconducting magnetically ordered solution is lower in energy here. Thus the pure SC phase is a stable phase only before the magnetic transition point.

There is a third scenario possible where one can do a RMFT allowing for non-zero values of both SC and magnetic order parameters along with other mean fields. Before the magnetic order turns on, this theory is consistent with the spin-symmetric Bogoliubov the-

ory described above. After the magnetic order sets in, differences between the two calculations become visible. In the third calculation, the SC order coexists with the ferrimagnetic order for a range of parameters as shown in Fig. C.8 though the pairing amplitudes decrease with increasing U/Δ. Comparing the energy of this phase with that of the ferrimagnetic metal phase, which was found to be the stabler phase by comparing the energies in the first two calculations in this regime, we find that the coexistence phase is also a metastable phase, and the system actually stabilizes into the ferrimagnetic metallic phase as shown in Fig. 4.2 of chapter 4.

BIBLIOGRAPHY

[1] B. Edegger, V. N. Muthukumar and C. Gros, *Gutzwiller-RVB theory of high-temperature superconductivity: Results from renormalized mean-field theory and variational Monte Carlo calculations*, *Advances in Physics* **56** (2007) 927–1033, [https://doi.org/10.1080/00018730701627707]. iii, xiv, 2, 13, 16, 33, 50, 90, 91, 112, 113, 144, 156

[2] P. W. Anderson, P. A. Lee, M. Randeria, T. M. Rice, N. Trivedi and F. C. Zhang, *The physics behind high-temperature superconducting cuprates: the plain vanilla version of RVB*, *Journal of Physics: Condensed Matter* **16** (jun, 2004) R755–R769. iii, 3, 4, 32, 90, 92, 110, 112, 113, 132, 156

[3] S. Lefebvre, P. Wzietek, S. Brown, C. Bourbonnais, D. Jérome, C. Mézière et al., *Mott Transition, Antiferromagnetism, and Unconventional Superconductivity in Layered Organic Superconductors*, *Phys. Rev. Lett.* **85** (Dec, 2000) 5420–5423. iii, 1, 5, 109, 110, 131

[4] M. Randeria, R. Sensarma and N. Trivedi, *Projected Wavefunctions and High T_c Superconductivity in Doped Mott Insulators*, pp. 29–64. Springer Berlin

Heidelberg, Berlin, Heidelberg, 2012. 10.1007/978-3-642-21831-6-2. iv, 20, 112, 113

[5] A. Garg, H. R. Krishnamurthy and M. Randeria, *Can Correlations Drive a Band Insulator Metallic?*, *Phys. Rev. Lett.* **97** (Jul, 2006) 046403. iv, 22, 24, 34, 59, 84, 85, 86, 116

[6] S. S. Kancharla and E. Dagotto, *Correlated Insulated Phase Suggests Bond Order between Band and Mott Insulators in Two Dimensions*, *Phys. Rev. Lett.* **98** (Jan, 2007) 016402. iv, 24, 34, 35, 59, 84, 85, 106, 107, 117

[7] S. Bag, A. Garg and H. R. Krishnamurthy, *Phase diagram of the half-filled ionic Hubbard model*, *Phys. Rev. B* **91** (Jun, 2015) 235108. iv, 21, 24, 25, 26, 34, 35, 58, 62, 84, 85, 86, 92, 94, 106, 107, 117

[8] M. Messer, R. Desbuquois, T. Uehlinger, G. Jotzu, S. Huber, D. Greif et al., *Exploring Competing Density Order in the Ionic Hubbard Model with Ultracold Fermions*, *Phys. Rev. Lett.* **115** (Sep, 2015) 115303. v, 27, 28, 35, 84, 108, 132

[9] Y. Anusooya-Pati, Z. G. Soos and A. Painelli, *Symmetry crossover and excitation thresholds at the neutral-ionic transition of the modified Hubbard model*, *Phys. Rev. B* **63** (May, 2001) 205118. vi, 57, 58, 60, 84

[10] A. Chattopadhyay and A. Garg, *Gutzwiller projection for exclusion of holes: Application to strongly correlated ionic Hubbard model and binary alloys*, *Phys. Rev. B* **97** (Jun, 2018) 245114. xvii, 26, 91, 112, 113, 156

[11] J. G. Bednorz and K. A. Müller, *Possible high T_c superconductivity in the $BaLaCuO$ system*, *Zeitschrift für Physik B Condensed Matter* **64** (Jun, 1986) 189–193. 1, 2, 109, 110

[12] Y. Kamihara, T. Watanabe, M. Hirano and H. Hosono, *Iron-Based Layered Superconductor $La[O_{1-x}F_x]FeAs(x = 0.05{-}0.12)$ with T_c = 26 K*, *Journal of the American Chemical Society* **130** (Mar, 2008) 3296–3297. 1, 2, 6, 109, 110

[13] Q. Si, R. Yu and E. Abrahams, *High-temperature superconductivity in iron pnictides and chalcogenides*, *Nature Reviews Materials* **1** (Mar, 2016) 16017. 1, 2, 6, 110, 131, 132

[14] Y. Cao, V. Fatemi, S. Fang, K. Watanabe, T. Taniguchi, E. Kaxiras et al., *Unconventional superconductivity in magic-angle graphene superlattices*, *Nature* **556** (Apr, 2018) 43–50. 1, 2, 6, 7, 83, 109, 110, 131, 132

[15] E. Codecido, Q. Wang, R. Koester, S. Che, H. Tian, R. Lv et al., *Correlated insulating and superconducting states in twisted bilayer graphene below the magic angle*, *Science Advances* **5** (2019) , [https://advances.sciencemag.org/content/5/9/eaaw9770.full.pdf]. 1, 2, 6, 7, 109, 110

[16] P. A. Lee, N. Nagaosa and X.-G. Wen, *Doping a Mott insulator: Physics of high-temperature superconductivity*, *Rev. Mod. Phys.* **78** (Jan, 2006) 17–85. 2, 3, 32, 83, 110, 131, 132

[17] S. H. Pan, J. P. O'Neal, R. L. Badzey, C. Chamon, H. Ding, J. R. Engelbrecht et al., *Microscopic electronic inhomogeneity in the high-T_c superconductor $Bi_2Sr_2CaCu_2O_{8+x}$*, *Nature* **413** (Sep, 2001) 282–285. 4, 35, 110

[18] K. McElroy, J. Lee, J. A. Slezak, D.-H. Lee, H. Eisaki, S. Uchida et al., *Atomic-Scale Sources and Mechanism of Nanoscale Electronic Disorder in* $Bi_2Sr_2CaCu_2O_{8+\delta}$, *Science* **309** (2005) 1048–1052, [https://science.sciencemag.org/content/309/5737/1048.full.pdf]. 4, 110

[19] A. Garg, M. Randeria and N. Trivedi, *Strong correlations make high-temperature superconductors robust against disorder*, *Nature Physics* **4** (Oct, 2008) 762–765. 4, 81, 90, 102, 110

[20] S. Tang, V. Dobrosavljević and E. Miranda, *Strong correlations generically protect d-wave superconductivity against disorder*, *Phys. Rev. B* **93** (May, 2016) 195109. 4, 110

[21] J. Hubbard and B. H. Flowers, *Electron correlations in narrow energy bands*, *Proceedings of the Royal Society of London. Series A. Mathematical and Physical Sciences* **276** (1963) 238–257, [https://royalsocietypublishing.org/doi/pdf/10.1098/rspa.1963.0204]. 8

[22] J. Hubbard and B. H. Flowers, *Electron correlations in narrow energy bands. II. The degenerate band case*, *Proceedings of the Royal Society of London. Series A. Mathematical and Physical Sciences* **277** (1964) 237–259, [https://royalsocietypublishing.org/doi/pdf/10.1098/rspa.1964.0019]. 8

[23] J. Hubbard and B. H. Flowers, *Electron correlations in narrow energy bands III. An improved solution*, *Proceedings of the Royal So-*

ciety of London. Series A. Mathematical and Physical Sciences **281** (1964) 401–419, [https://royalsocietypublishing.org/doi/pdf/10.1098/rspa.1964.0190]. 8

[24] J. Hubbard and B. H. Flowers, *Electron correlations in narrow energy bands - IV. The atomic representation*, *Proceedings of the Royal Society of London. Series A. Mathematical and Physical Sciences* **285** (1965) 542–560, [https://royalsocietypublishing.org/doi/pdf/10.1098/rspa.1965.0124]. 8

[25] M. Ogata and H. Shiba, *Bethe-ansatz wave function, momentum distribution, and spin correlation in the one-dimensional strongly correlated Hubbard model*, *Phys. Rev. B* **41** (Feb, 1990) 2326–2338. 9

[26] N. Bulut, $d_{x^2-y^2}$ *superconductivity and the Hubbard model*, *Advances in Physics* **51** (2002) 1587–1667, [https://doi.org/10.1080/00018730210155142]. 10

[27] E. Dagotto, *Correlated electrons in high-temperature superconductors*, *Rev. Mod. Phys.* **66** (Jul, 1994) 763–840. 10

[28] M. Keller, W. Metzner and U. Schollwöck, *Dynamical Mean-Field Theory for Pairing and Spin Gap in the Attractive Hubbard Model*, *Phys. Rev. Lett.* **86** (May, 2001) 4612–4615. 10

[29] G. Hager, G. Wellein, E. Jeckelmann and H. Fehske, *Stripe formation in doped Hubbard ladders*, *Phys. Rev. B* **71** (Feb, 2005) 075108. 10

[30] P. Fazekas, *Lecture Notes on Electron Correlation and Magnetism*. Series in modern condensed matter physics. World Scientific, 1999. 11, 32, 88

[31] Y. A. Izyumov, *Strongly correlated electrons: the $t - J$ model*, *Physics-Uspekhi* **40** (may, 1997) 445–476. 11

[32] B. S. Shastry, *Extremely correlated Fermi liquids: The formalism*, *Phys. Rev. B* **87** (Mar, 2013) 125124. 12, 32

[33] B. S. Shastry, *Theory of extreme correlations using canonical Fermions and path integrals*, *Annals of Physics* **343** (2014) 164 – 199. 12, 32

[34] C. Gros, *Physics of projected wavefunctions*, *Annals of Physics* **189** (1989) 53 – 88. 13, 32, 90

[35] H. Matsukawa and H. Fukuyama, *Antiferromagnetism of the $t - J$ model in the Slave Boson Mean Field Approximation*, *Journal of the Physical Society of Japan* **61** (1992) 1882–1885, [https://doi.org/10.1143/JPSJ.61.1882]. 14

[36] T. Ogawa, K. Kanda and T. Matsubara, *Gutzwiller Approximation for Antiferromagnetism in Hubbard Model*, *Progress of Theoretical Physics* **53** (02, 1975) 614–633, [https://academic.oup.com/ptp/article-pdf/53/3/614/6866280/53-3-614. 16, 33, 50, 90, 91

[37] D. Vollhardt, *Normal ^{3}He: an almost localized Fermi liquid*, *Rev. Mod. Phys.* **56** (Jan, 1984) 99–120. 16, 33, 50, 90, 91

[38] F. C. Zhang, C. Gros, T. M. Rice and H. Shiba, *A renormalised Hamiltonian approach to a resonant valence bond wavefunction*, *Superconductor Science and Technology* **1** (jun, 1988) 36–46. 16, 33, 50, 90, 91, 112

[39] M. Ogata and A. Himeda, *Superconductivity and Antiferromagnetism in an Extended Gutzwiller Approximation for t-J Model: Effect of Double-Occupancy Exclusion*, *Journal of the Physical Society of Japan* **72** (2003) 374–391, [https://doi.org/10.1143/JPSJ.72.374]. 16, 33, 50, 90, 91, 112, 113

[40] W.-H. Ko, C. P. Nave and P. A. Lee, *Extended Gutzwiller approximation for inhomogeneous systems*, *Phys. Rev. B* **76** (Dec, 2007) 245113. 16, 33, 50, 90, 91, 112

[41] N. Paris, K. Bouadim, F. Hebert, G. G. Batrouni and R. T. Scalettar, *Quantum Monte Carlo Study of an Interaction-Driven Band-Insulator–to–Metal Transition*, *Phys. Rev. Lett.* **98** (Jan, 2007) 046403. 22, 24, 34, 59, 84, 85, 116

[42] K. Bouadim, N. Paris, F. Hébert, G. G. Batrouni and R. T. Scalettar, *Metallic phase in the two-dimensional ionic Hubbard model*, *Phys. Rev. B* **76** (Aug, 2007) 085112. 22, 24, 34, 59, 84, 85

[43] L. Craco, P. Lombardo, R. Hayn, G. I. Japaridze and E. Müller-Hartmann, *Electronic phase transitions in the half-filled ionic Hubbard model*, *Phys. Rev. B* **78** (Aug, 2008) 075121. 22, 24, 34, 84, 85, 116

[44] A. T. Hoang, *Metal–insulator transitions in the half-filled ionic Hubbard model*, *Journal of Physics: Condensed Matter* **22** (feb, 2010) 095602. 22, 24, 34, 84, 85, 116

[45] J. Hubbard and J. B. Torrance, *Model of the Neutral-Ionic Phase Transformation*, *Phys. Rev. Lett.* **47** (Dec, 1981) 1750–1754. 23

[46] N. Nagaosa and J.-i. Takimoto, *Theory of Neutral-Ionic Transition in Organic Crystals. I. Monte Carlo Simulation of Modified Hubbard Model*, *Journal of the Physical Society of Japan* **55** (1986) 2735–2744, [https://doi.org/10.1143/JPSJ.55.2735]. 23

[47] T. Egami, S. Ishihara and M. Tachiki, *Lattice Effect of Strong Electron Correlation: Im-*
plication for Ferroelectricity and Superconductivity, *Science* **261** (1993) 1307–1310, [https://science.sciencemag.org/content/261/5126/1307.full.pdf]. 23

[48] S. Ishihara, T. Egami and M. Tachiki, *Enhancement of the electron-lattice interaction due to strong electron correlation*, *Phys. Rev. B* **49** (Apr, 1994) 8944–8954. 23

[49] R. Resta and S. Sorella, *Many-Body Effects on Polarization and Dynamical Charges in a Partly Covalent Polar Insulator*, *Phys. Rev. Lett.* **74** (Jun, 1995) 4738–4741. 23

[50] R. Resta and S. Sorella, *Electron Localization in the Insulating State*, *Phys. Rev. Lett.* **82** (Jan, 1999) 370–373. 23

[51] M. Fabrizio, A. O. Gogolin and A. A. Nersesyan, *From Band Insulator to Mott Insulator in One Dimension*, *Phys. Rev. Lett.* **83** (Sep, 1999) 2014–2017. 23, 34, 84

[52] G. Ortiz and R. M. Martin, *Macroscopic polarization as a geometric quantum phase: Many-body formulation*, *Phys. Rev. B* **49** (May, 1994) 14202–14210. 23

[53] G. Ortiz, P. Ordejón, R. M. Martin and G. Chiappe, *Quantum phase transitions involving a change in polarization*, *Phys. Rev. B* **54** (Nov, 1996) 13515–13528. 23

[54] T. Wilkens and R. M. Martin, *Quantum Monte Carlo study of the one-dimensional ionic Hubbard model*, *Phys. Rev. B* **63** (May, 2001) 235108. 23

[55] Y. Z. Zhang, C. Q. Wu and H. Q. Lin, *Inducement of bond-order wave due to electron correlation in one dimension*, *Phys. Rev. B* **67** (May, 2003) 205109. 23

[56] J. Lou, S. Qin, T. Xiang, C. Chen, G.-S. Tian and Z. Su, *Transition from band insulator to Mott insulator in one dimension: Critical behavior and phase diagram*, *Phys. Rev. B* **68** (Jul, 2003) 045110. 23

[57] C. D. Batista and A. A. Aligia, *Exact Bond Ordered Ground State for the Transition between the Band and the Mott insulator*, *Phys. Rev. Lett.* **92** (Jun, 2004) 246405. 23

[58] T. Jabben, N. Grewe and F. B. Anders, *Charge gaps and quasiparticle bands of the ionic Hubbard model*, *The European Physical Journal B - Condensed Matter and Complex Systems* **44** (Mar, 2005) 47–55. 24, 34, 84

[59] K. Byczuk, M. Sekania, W. Hofstetter and A. P. Kampf, *Insulating behavior with spin and charge order in the ionic Hubbard model*, *Phys. Rev. B* **79** (Mar, 2009) 121103. 24, 34, 35, 59, 84, 85

[60] A. Garg, H. R. Krishnamurthy and M. Randeria, *Doping a Correlated Band Insulator: A New Route to Half-Metallic Behavior*, *Phys. Rev. Lett.* **112** (Mar, 2014) 106406. 24, 25, 34, 35, 84, 85

[61] X. Wang, R. Sensarma and S. Das Sarma, *Ferromagnetic response of a "high-temperature" quantum antiferromagnet*, *Phys. Rev. B* **89** (Mar, 2014) 121118. 24, 34, 35, 84, 85, 86, 92, 107

[62] A. J. Kim, M. Y. Choi and G. S. Jeon, *Finite-temperature phase transitions in the ionic Hubbard model*, *Phys. Rev. B* **89** (Apr, 2014) 165117. 24, 34

[63] S. Bag, A. Garg and H. R. Krishnamurthy, *Correlation driven metallic and half-metallic phases in a band insulator*, 2019. 27

[64] A. Chattopadhyay, H. R. Krishnamurthy and A. Garg, *Unconventional superconductivity in a strongly correlated band-insulator without doping*, 2020. 27

[65] A. Chattopadhyay, *Interplay of mass imbalance and frustration in correlated band insulators*, *Phys. Rev. B* **103** (Jan, 2021) 045125. 27

[66] E. V. Castro, K. S. Novoselov, S. V. Morozov, N. M. R. Peres, J. M. B. L. dos Santos, J. Nilsson et al., *Biased Bilayer Graphene: Semiconductor with a Gap Tunable by the Electric Field Effect*, *Phys. Rev. Lett.* **99** (Nov, 2007) 216802. 28, 84, 132

[67] A. V. Balatsky, I. Vekhter and J.-X. Zhu, *Impurity-induced states in conventional and unconventional superconductors*, *Rev. Mod. Phys.* **78** (May, 2006) 373–433. 32, 81

[68] D. Chakraborty, R. Sensarma and A. Ghosal, *Effects of strong disorder in strongly correlated superconductors*, *Phys. Rev. B* **95** (Jan, 2017) 014516. 32, 81

[69] P. W. ANDERSON, *The Resonating Valence Bond State in La_2CuO_4 and Superconductivity*, *Science* **235** (1987) 1196–1198, [https://science.sciencemag.org/content/235/4793/1196.full.pdf]. 32, 110, 132

[70] S. A. Kivelson, D. S. Rokhsar and J. P. Sethna, *Topology of the resonating valence-bond state: Solitons and high-T_c superconductivity*, *Phys. Rev. B* **35** (Jun, 1987) 8865–8868. 32

[71] G. Baskaran, Z. Zou and P. Anderson, *The resonating valence bond state and high-T_c superconductivity -A mean field theory*, *Solid State Communications* **63** (1987) 973 – 976. 32

[72] G. Kotliar and J. Liu, *Superexchange mechanism and d-wave superconductivity*, *Phys. Rev. B* **38** (Sep, 1988) 5142–5145. 32

[73] C. Gros, *Superconductivity in correlated wave functions*, *Phys. Rev. B* **38** (Jul, 1988) 931–934. 32

[74] F. C. Zhang and T. M. Rice, *Effective Hamiltonian for the superconducting Cu oxides*, *Phys. Rev. B* **37** (Mar, 1988) 3759–3761. 32

[75] A. L. Fetter and J. D. Walecka, *Quantum Theory of Many-Particle Systems*. McGraw-Hill, Boston, 1971. 32

[76] M. C. Gutzwiller, *Effect of Correlation on the Ferromagnetism of Transition Metals*, *Phys. Rev.* **134** (May, 1964) A923–A941. 32, 90

[77] M. C. Gutzwiller, *Correlation of Electrons in a Narrow s Band*, *Phys. Rev.* **137** (Mar, 1965) A1726–A1735. 32, 90

[78] A. P. Kampf, M. Sekania, G. I. Japaridze and P. Brune, *Nature of the insulating phases in the half-filled ionic Hubbard model*, *Journal of Physics: Condensed Matter* **15** (aug, 2003) 5895–5907. 34, 84

[79] S. R. Manmana, V. Meden, R. M. Noack and K. Schönhammer, *Quantum critical behavior of the one-dimensional ionic Hubbard model*, *Phys. Rev. B* **70** (Oct, 2004) 155115. 34, 84

[80] A. Samanta and R. Sensarma, *Superconductivity from doublon condensation in the ionic Hubbard model*, *Phys. Rev. B* **94** (Dec, 2016) 224517. 35, 85, 86, 94, 100, 106, 107, 120

[81] C. Li and Z. Wang, *Mott and Wigner-Mott transitions in doped correlated electron systems: Effects of superlattice potential and intersite correlation*, *Phys. Rev. B* **80** (Sep, 2009) 125130. 35

[82] H. S. Jarrett, W. H. Cloud, R. J. Bouchard, S. R. Butler, C. G. Frederick and J. L. Gillson, *Evidence for Itinerant d-Electron Ferromagnetism*, *Phys. Rev. Lett.* **21** (Aug, 1968) 617–620. 35

[83] G. L. Zhao, J. Callaway and M. Hayashibara, *Electronic structures of iron and cobalt pyrites*, *Phys. Rev. B* **48** (Dec, 1993) 15781–15786. 35

[84] S. K. Kwon, S. J. Youn and B. I. Min, *Itinerant ferromagnetism in half-metallic CoS_2*, *Phys. Rev. B* **62** (Jul, 2000) 357–360. 35

[85] T. Shishidou, A. J. Freeman and R. Asahi, *Effect of GGA on the half-metallicity of the itinerant ferromagnet CoS_2*, *Phys. Rev. B* **64** (Oct, 2001) 180401. 35

[86] K. Günter, T. Stöferle, H. Moritz, M. Köhl and T. Esslinger, *Bose-Fermi Mixtures in a Three-Dimensional Optical Lattice*, *Phys. Rev. Lett.* **96** (May, 2006) 180402. 36

[87] S. Ospelkaus, C. Ospelkaus, O. Wille, M. Succo, P. Ernst, K. Sengstock et al., *Localization of Bosonic Atoms by Fermionic Impurities in a Three-Dimensional Optical Lattice*, *Phys. Rev. Lett.* **96** (May, 2006) 180403. 36

[88] D. Semmler, K. Byczuk and W. Hofstetter, *Mott-Hubbard and Anderson metal-insulator transitions in correlated lattice fermions with binary disorder*, *Phys. Rev. B* **81** (Mar, 2010) 115111. 36, 64

[89] K. Byczuk and M. Ulmke, *Curie temperature in the Hubbard model with alloy disorder*, *The European Physical Journal B - Condensed Matter and Complex Systems* **45** (Jun, 2005) 449–454. 36, 64

[90] K. Byczuk, M. Ulmke and D. Vollhardt, *Ferromagnetism and Metal-Insulator Transition in the Disordered Hubbard Model*, *Phys. Rev. Lett.* **90** (May, 2003) 196403. 36, 64

[91] P. Haldar, M. S. Laad and S. R. Hassan, *Real-space cluster dynamical mean-field approach to the Falicov-Kimball model: An alloy-analogy approach*, *Phys. Rev. B* **95** (Mar, 2017) 125116. 36, 64

[92] D. Basko, I. Aleiner and B. Altshuler, *Metal-insulator transition in a weakly interacting many-electron system with localized single-particle states*, *Annals of Physics* **321** (2006) 1126 – 1205. 36

[93] M. Serbyn, Z. Papić and D. A. Abanin, *Local Conservation laws and the Structure of the Many-Body Localized States*, *Phys. Rev. Lett.* **111** (Sep, 2013) 127201. 36

[94] S. Iyer, V. Oganesyan, G. Refael and D. A. Huse, *Many-body localization in a quasiperiodic system*, *Phys. Rev. B* **87** (Apr, 2013) 134202. 36

[95] S. Nag and A. Garg, *Many-body mobility edges in a one-dimensional system of interacting fermions*, *Phys. Rev. B* **96** (Aug, 2017) 060203. 36

[96] W. A. Atkinson, P. J. Hirschfeld and A. H. MacDonald, *Gap Inhomogeneities and the Density of States in Disordered d-Wave Superconductors*, *Phys. Rev. Lett.* **85** (Oct, 2000) 3922–3925. 50, 81

[97] A. Ghosal, M. Randeria and N. Trivedi, *Spatial inhomogeneities in disordered d-wave superconductors*, *Phys. Rev. B* **63** (Dec, 2000) 020505. 50, 81

[98] T. S. Nunner, B. M. Andersen, A. Melikyan and P. J. Hirschfeld, *Dopant-modulated pair interaction in cuprate superconductors*, *Phys. Rev. Lett.* **95** (Oct, 2005) 177003. 50, 81

[99] M. Balzer and M. Potthoff, *Disorder- and correlation-driven metal-insulator transitions*, *Physica B: Condensed Matter* **359-361** (2005) 768 – 770. 79

[100] E. H. da Silva Neto, P. Aynajian, A. Frano, R. Comin, E. Schierle, E. Weschke et al., *Ubiquitous Interplay Between Charge Ordering and High-Temperature Superconductivity in Cuprates*, *Science* **343** (2014) 393–396, [https://science.sciencemag.org/content/343/6169/393.full.pdf]. 80

[101] I. M. Vishik, M. Hashimoto, R.-H. He, W.-S. Lee, F. Schmitt, D. Lu et al., *Phase competition in trisected superconducting dome*, *Proceedings of the National Academy of Sciences* **109** (2012) 18332–18337, [https://www.pnas.org/content/109/45/18332.full.pdf]. 80

[102] M. Sigrist and K. Ueda, *Phenomenological theory of unconventional superconductivity*, *Rev. Mod. Phys.* **63** (Apr, 1991) 239–311. 109

[103] G. Kotliar and J. Liu, *Superexchange mechanism and d-wave superconductivity*, *Phys. Rev. B* **38** (Sep, 1988) 5142–5145. 110, 132

[104] A. V. Mallik, G. K. Gupta, V. B. Shenoy and H. R. Krishnamurthy, *Surprises in the $t-j$ Model: Implications for Cuprates*, *Phys. Rev. Lett.* **124** (Apr, 2020) 147002. 110, 132

[105] A. Paramekanti, M. Randeria and N. Trivedi, *Projected Wave Functions and High Temperature Superconductivity*, *Phys. Rev. Lett.* **87** (Nov, 2001) 217002. 112, 113

[106] A. Chattopadhyay, S. Bag, H. R. Krishnamurthy and A. Garg, *Phase diagram of the half-filled ionic Hubbard model in the limit of strong correlations*, *Phys. Rev. B* **99** (Apr, 2019) 155127. 113, 120

[107] P. Fulde and R. A. Ferrell, *Superconductivity in a Strong Spin-Exchange Field*, *Phys. Rev.* **135** (Aug, 1964) A550–A563. 116

[108] A. I. Larkin and Y. N. Ovchinnikov, *Nonuniform state of superconductors*, *Zh. Eksp. Teor. Fiz.* **47** (1964) 1136 [Sov. Phys. JETP **20**, 762 (1965)]. 116

[109] A. Datta, K. Yang and A. Ghosal, *Fate of a strongly correlated d-wave superconductor in a Zeeman field: The Fulde-Ferrel-Larkin-Ovchinnikov perspective*, *Phys. Rev. B* **100** (Jul, 2019) 035114. 116

[110] T. Watanabe and S. Ishihara, *Band and Mott Insulators and Superconductivity in Honeycomb-Lattice Ionic-Hubbard Model*, *Journal of the Physical Society of Japan* **82** (2013) 034704, [https://doi.org/10.7566/JPSJ.82.034704]. 117, 120